

Adaptive Millimeter-Wave and THz Antenna Devices Based on Dielectric Elastomer Actuators

THÈSE N° 6743 (2015)

PRÉSENTÉE LE 27 AOÛT 2015

À LA FACULTÉ DES SCIENCES ET TECHNIQUES DE L'INGÉNIEUR
LABORATOIRE D'ÉLECTROMAGNÉTISME ET ANTENNES
PROGRAMME DOCTORAL EN MICROSYSTÈMES ET MICROÉLECTRONIQUE

ÉCOLE POLYTECHNIQUE FÉDÉRALE DE LAUSANNE

POUR L'OBTENTION DU GRADE DE DOCTEUR ÈS SCIENCES

PAR

Pietro ROMANO

acceptée sur proposition du jury:

Prof. A. Kis, président du jury
Prof. H. Shea, Prof. J. R. Mosig, directeurs de thèse
Prof. S. V. Hum, rapporteur
Dr B. Fuchs, rapporteur
Prof. G. Villanueva, rapporteur



ÉCOLE POLYTECHNIQUE
FÉDÉRALE DE LAUSANNE

Suisse
2015

We must not forget that when radium was discovered no one knew that it would prove useful in hospitals. The work was one of pure science. And this is a proof that scientific work must not be considered from the point of view of the direct usefulness of it. It must be done for itself, for the beauty of science, and then there is always the chance that a scientific discovery may become like the radium a benefit for humanity.

— Marie Curie

To the memory of Prof. Julien Perruisseau-Carrier

Acknowledgements

At the end of this journey, started in February 2012, it is a real pleasure to acknowledge all the people who contributed with advice, support, discussions, or a simple smile. This thesis would have never been possible without the initial confidence and encouragement of Prof. Julien Perruisseau-Carrier, to whom this work is dedicated. Julien has been my mentor and supervisor for more than two years, driving me to explore new and exciting challenges in the world of “reconfigurable antennas”. I will always remember with great affection and devotion his creative and genial personality. His enthusiasm, ambition and love for science have always been inspiring and motivational for me. I will always be grateful for the opportunity he gave me and I will keep his precious advice and teachings forever impressed in my mind.

I am very grateful to my thesis directors, Prof. Juan Mosig and Prof. Herbert Shea for their patient guidance and scientific advice. Thanks Juan, for “adopting” me into the LEMA family and for all the confidence and support in the last year. Thanks Herb, for being an invaluable source of insightful ideas and advice since the beginning of my thesis.

I would like to acknowledge the members of the jury who reviewed my thesis and provided me with valuable feedback: Prof. Sean V. Hum from the University of Toronto, Canada, Dr. Benjamin Fuchs from the University of Rennes, France, Prof. Guillermo Villanueva, head of the Advanced NEMS group at EPFL, and Prof. Andras Kis, president of the jury and head of the Laboratory of Nanoscale Electronics and Structures at EPFL.

I wish to express my gratitude to Samuel Rosset for providing me with invaluable help and support since the beginning of the thesis. His expertise and brilliant ideas allowed to solve several technological challenges, leading to the successful completion of this work. It has been a great pleasure to work and interact with him during these years. A big thanks goes to the “other Samuel” (Samuel Schlatter) for the really enjoyable and fruitful collaboration in the last year. I also want to thank Seun Araromi for his fundamental help in the first year of my PhD, which led to the development of my first working device.

I will always be grateful to Santiago Capdevila Cascante, the advisor that every PhD student would like to have in his lab. All the results achieved during the last year would have never been possible without his extensive knowledge, dedication and generosity. I will never forget the endless time he dedicated to me for discussions, advice and measurement campaigns. I would like to thank Tomislav Debogovic for the useful discussions and for the always available help with measurement equipment and instrumentation.

A big thanks goes to Prof. Anja Skrivervik for all the interesting discussions and suggestions

Acknowledgements

during these years, and for stimulating me to speak in French all the time. I also wish to acknowledge Eulalia, Mercedes, Isabelle and Marie. Their kindness and permanent smile have been fundamental to deal with several bureaucratic and organizational matters. And many thanks to David and Raymond for the IT help and support. I would also like to acknowledge the ACI workshop at EPFL, with a special thanks to Manuel Leitos, for all the kind and patient support in the fabrication of my “unconventional” PCBs.

These years at EPFL have been easier thanks to all the colleagues and friends with whom I shared coffee breaks, lunches, barbecues, ski days, and night outings. Many thanks to all the NANOLAB (and related) friends and colleagues who “hosted” me for more than two years: Luca, Livio, Sara, Francesco, Arnab, Wolfgang, Emanuele, Mariazel, Höel, Erick, Cem, Pankaj, Maneesha, Nilay, Clara, Sebastian, Elizabeth, Alex, Montserrat, Antonios, Wladek, Charly, Enver, Oguz. A warm thanks to all the LEMA friends and colleagues: Jovanche, Ioannis, Marc, Mohsen, Eduardo, Sebas, Dani, Baptiste, Joana, Apo, María, Hamed, Anton, Mina, Pedro, Marco, Gabriele, Francesco, Maddalena, Michael, Lei, Sami, Etienne. I would like to thank Michele, my office mate during the last six months, with whom I shared conversations, ideas, achievements, laughs and concerns. His scientific and practical support has been fundamental in the last part of this thesis. I really appreciated his passion for science and his attitude to approach complex challenges with smart and visionary ideas.

I wish to acknowledge Jean-Christophe Angevain from the Antenna and Sub-Millimeter Wave Section of ESA-ESTEC for the interesting discussions and suggestions during these years. A big thanks goes also to Elena Saenz, Luis Rolo and Eric van der Houwen from the Antenna and Sub-Millimeter Wave Section of ESA-ESTEC for their kind help and support with measurements during my stay at ESTEC.

Last but not least, my special thanks go to my parents. They have always supported and encouraged me in all the decision that brought me traveling around the world. They are the real driving force of all my achievements and will always represent a solid anchor in my life. I would like to thank Serena for sharing with me this “Swiss journey”. Her patient support and encouragement have been fundamental for the successful completion of this work.

Pietro

Abstract

Dynamic reconfiguration of antenna devices is becoming a prime need in emerging telecommunication and remote sensing systems operating in the portion of the electromagnetic (EM) spectrum spanning from millimeter-wave (MMW) to terahertz. Different techniques and materials are currently available for the implementation of a given EM reconfiguration in antenna systems at microwaves and MMW, such as semiconductors, RF-MEMS, Liquid Crystal, and ferroelectrics. However, a common feature to all these technologies is the significant increased loss and complexity with regard to the devices fixed counterpart. Both loss and complexity further increase when high-performance reconfiguration capabilities are addressed at MMW and above, constituting a major limitation to the future deployment of dynamically controllable systems.

Advanced performance, low-complexity and low-cost are, therefore, the cornerstones in the development of new technologies for antenna reconfiguration. In this framework, the main objective of this thesis is to contribute to the advancement of low-cost and efficient technologies enabling antenna reconfiguration capabilities from MMW to THz frequencies. Within this scope, it is proposed the analysis, design and implementation of mechanically reconfigurable devices using dielectric elastomer actuators (DEAs). DEAs are an emerging technology that possesses unique properties, and represents a potential alternative to conventional mechanical reconfiguration schemes. DEAs are especially attractive for their large strain combined with low-cost materials and fabrication, analog control and near-zero DC power consumption. These characteristics make them particularly suited to the realization of low-cost and low-loss reconfigurable antennas.

The high potential of DEAs for the realization of adaptive devices is experimentally validated by the development of different prototypes operating at MMW and THz frequencies: i) a very low-loss true-time-delay phase shifter operating at Ka-band; ii) a Ka-band reconfigurable reflectarray with 1-D beam-scanning capability; iii) a stretchable and beam-scanning THz reflectarray exhibiting the uncommon potential for the implementation of conformal or reconfigurable devices based on mechanical stretching. The designs and concepts demonstrated in this thesis pave the way for the evolution of new DEA-based reconfigurable devices resulting in low-cost, low loss and compact structures.

Keywords: reconfigurable antenna, dielectric elastomer actuator (DEA), reflectarray antennas, reconfigurable reflectarray, Ka-band, millimeter-wave (MMW), terahertz, beam-scanning, phase shifter, stretchable reflectarray, Micro-Electro-Mechanical Systems (MEMS).

Résumé

La reconfiguration dynamique d'antennes représente un besoin croissant pour les technologies émergentes en télécommunication et télédétection opérant dans la plage du spectre électromagnétique (EM) qui s'étend des ondes millimétriques au térahertz. Différentes technologies et matériaux sont actuellement disponibles pour implémenter une reconfiguration EM de systèmes d'antennes dans la plage des micro-ondes et des ondes millimétriques, tels que des semi-conducteurs, des microsystèmes électromécaniques, des cristaux liquides, et des matériaux ferroélectriques. Toutefois, un point commun à toutes ces technologies est l'augmentation significative des pertes et de la complexité des systèmes en comparaison avec leurs pendants non-reconfigurables. Les pertes et la complexité augmentent d'autant plus lorsque l'on considère des systèmes avec de hautes performances de reconfiguration dans le domaine des ondes millimétriques et plus haut. Ceci constitue un frein majeur au développement et déploiement futur de systèmes comprenant des fonctionnalités de reconfiguration dynamique.

Performances avancées, complexité et coûts de fabrication réduits forment donc les fondements du développement d'une nouvelle technologie de reconfiguration d'antennes. Dans ce contexte, l'objectif principal de cette thèse est de contribuer à l'avancement de technologies efficaces et à bas-coût permettant la reconfiguration d'antennes dans la gamme des ondes millimétriques, jusqu'au THz. Dans cette optique, l'analyse, le design et l'implémentation de dispositifs reconfigurables mécaniquement et basés sur des actionneurs diélectriques en elastomère (DEA, dielectric elastomer actuators) sont proposés. Les DEAs représentent une technologie émergente qui possède des caractéristiques uniques et qui représentent une alternative aux méthodes conventionnelles de reconfiguration mécanique. L'attractivité des DEAs est due principalement à leur grande déformation, leurs coûts de matériaux et de fabrication réduits, leur contrôle analogique, et une dissipation de puissance quasiment nulle pour maintenir une position statique. Ces caractéristiques les rendent donc particulièrement bien adaptés à la réalisation d'antennes reconfigurables combinant bas coûts et pertes réduites.

Le haut potentiel des DEAs pour la réalisation de dispositifs adaptatifs est validée expérimentalement par le développement de différents prototypes opérants dans la gamme des ondes millimétriques et du THz : i) un déphaseur à très faibles pertes opérant dans la bande Ka ; ii) un réseau réflecteur reconfigurable opérant dans la bande Ka, permettant un balayage 1-D ; iii) un réseau réflecteur THz déformable et capable de balayage, qui présente un potentiel novateur pour l'implémentation de dispositifs conformes ou reconfigurables basé sur la défor-

Résumé

mation mécanique. Les designs et concepts démontrés dans cette thèse ouvrent la voie à de nouveaux dispositifs reconfigurables basés sur des actionneurs en élastomère, résultant en une diminution du prix de fabrication et des pertes EM, ainsi qu'en une diminution de la taille et de la complexité des systèmes.

Mots clés : antennes reconfigurables, actionneurs diélectriques en élastomère (DEA), antennes réseaux réflecteurs, bande Ka, ondes millimétriques, térahertz, balayage de faisceau, déphaseur, réseaux réflecteur extensible, microsystèmes électromécaniques (MEMS).

Contents

Acknowledgements	i
Abstract (English/Français)	iii
List of figures	ix
List of tables	xiii
1 Introduction	1
1.1 Framework and objectives	1
1.2 Dielectric elastomer actuators	3
1.3 Thesis outline	7
2 Millimeter-wave characterization of DEA materials	11
2.1 Bulk materials characterization	11
2.1.1 Basic theory and general approach	12
2.1.2 Dielectric properties extraction from simulated data	16
2.2 Characterization of stretchable conductive membranes	21
2.2.1 Basic theory and general approach	22
2.2.2 Surface impedance extraction from simulated data	24
2.3 Experimental results	28
2.3.1 Dielectric properties of bulk PDMS	28
2.3.2 Conductivity of stretchable metalized membranes	31
2.4 Conclusions	36
3 Reconfigurable phase shifters based on DEAs	41
3.1 Existing technologies for phase shifter reconfiguration	43
3.1.1 MMIC	43
3.1.2 Ferrite	45
3.1.3 MEMS	48
3.1.4 Technology comparison	50
3.2 Preliminary design of DEA-based phase shifters	51
3.3 The first reconfigurable TTD phase shifter using DEAs	58
3.3.1 Design approach	60
3.3.2 Manufacturing and assembly	65

Contents

3.3.3	Experimental characterization	71
3.4	Conclusions	76
4	A beam-scanning DEA reflectarray	85
4.1	Introduction	85
4.1.1	The reflectarray antenna	88
4.1.2	Reconfigurable reflectarray antennas	92
4.1.3	Basics of the reflectarray antenna	94
4.2	Variable-size resonators RA using DEA	98
4.2.1	Motivation	98
4.2.2	Proposed reconfiguration concept	99
4.3	A reconfigurable reflecting surface using DEA	104
4.3.1	Unit cell design and numerical results	105
4.3.2	The first prototype: fabrication and test	108
4.3.3	Prototype optimization: fabrication and test	116
4.4	DEA-based 1-D scanning RA	122
4.5	Conclusions	129
5	Stretchable reflectarray antennas for THz applications	135
5.1	Introduction	135
5.2	Stretchable conductors based on gold ion implantation	137
5.3	A fixed-beam stretchable reflectarray	143
5.3.1	Reflectarray design and fabrication	144
5.3.2	Experimental characterization	152
5.4	A beam-scanning stretchable reflectarray	154
5.5	Conclusions	161
6	Conclusion and perspectives	167
6.1	Summary	167
6.2	Perspectives	169
	List of Publications	171
	Curriculum Vitae	175

List of Figures

1.1	Basic actuation principle of a DEA with free boundary conditions	4
1.2	Comparison between different micro-actuation technologies	6
2.1	Rectangular waveguide loaded by the unknown dielectric material	13
2.2	Transmission line model of the dielectric loaded RWG	13
2.3	Simulated and theoretical S-parameters for different PDMS thickness	17
2.4	Simulated geometry after deembed of the reference planes	18
2.5	Propagation constant and dielectric properties extracted from simulations . . .	19
2.6	Relative error for the retrievals of Fig. 2.5 with respect to the nominal values . .	19
2.7	Error in the extraction due to inaccuracy in the knowledge of the PDMS thickness	20
2.8	Schematic representation of a RWG loaded by the foam-glass-membrane chip under test	23
2.9	Equivalent representation of the RWG configuration depicted in Fig. 2.8	23
2.10	Simulated measurements setup for surface impedance characterization	24
2.11	Extracted impedance Z_S and committed error for the presented simulated ex- periment	26
2.12	Extracted impedance for different errors in the knowledge of the PDMS thickness	26
2.13	Schematic representation of a gap between the conductive membrane and the RWG walls	27
2.14	Effect of a gap δy in the extraction procedure	27
2.15	RWG section filled with the commercial Sylgard 186	29
2.16	Measured scattering parameters for the analyzed PDMS samples	30
2.17	Complex propagation constant retrieved from measured scattering parameters	30
2.18	Permittivity and loss tangent retrieved from measured scattering parameters .	31
2.19	Flexible and stretchable conductive membranes under test	32
2.20	Measured scattering parameters from the considered conductive membranes .	33
2.21	Measured surface impedance before correction of the gap error	33
2.22	Surface impedance Z_S extracted from simulated S-parameters	35
2.23	Extracted surface resistance R_S'' after correction of the gap error	35
3.1	Basic actuation principles of DEAs	42
3.2	Simplified drawing of the proposed phase shifter concepts	53
3.3	Simulated scattering parameters for the concept of Fig. 3.2a	54

List of Figures

3.4	Simulated scattering parameters for the concept of Fig. 3.2b	55
3.5	Calculated phase shift the for the concept of Fig. 3.2c	56
3.6	Simulated scattering parameters for the concept of Fig. 3.2c	57
3.7	Schematic drawing of the DEA-based phase shifter	59
3.8	Simplified drawing of the phase shifter reconfiguration principle	60
3.9	Transmission line model of the selected phase shifter concept	61
3.10	Symbolic representation of the “minimum mismatch” principle	62
3.11	Performance map for the optimization of the proposed phase shifter	63
3.12	Top-view drawing of the basic CPW	64
3.13	Render of the manufactured device	66
3.14	Different steps of the electrodes printing on the PDMS membrane	67
3.15	Bonding procedure of the loading PCB to the actuator membrane	69
3.16	Validation of Δh_{PS} spacing using a digital holographic microscope	70
3.17	Procedure for the horizontal alignment	71
3.18	Picture of the fabricated DEA-based phase shifter	71
3.19	Measurements setup used for the prototype characterization	72
3.20	Displacement characterization as a function of the applied voltage	73
3.21	Measured scattering parameters for different actuation states	74
3.22	Comparison between measurements and simulations at two fixed frequencies	75
3.23	Comparison between measurements and simulations over the complete frequency range	76
4.1	Basic principle of conventional high-gain antenna configurations	87
4.2	Possible implementation of a RA surface using resonant patches	90
4.3	Typical reflection phase and magnitude for an infinite array of rectangular patches	90
4.4	Reference system for a generic reflectarray	95
4.5	Radiation pattern example for a planar array of 30×30 elements	96
4.6	Symbolic illustrations of a reconfigurable RA surface based on mechanically tunable resonating patches	100
4.7	Simulated example of a 1-D scanning reflectarray	101
4.8	Schematic of the DEA-driven reconfigurable reflective surface design	103
4.9	Reconfiguration procedure for the proposed DEA-based reflectarray	103
4.10	Simplified drawing of the proposed implementation of the DEA-driven reconfigurable cell	105
4.11	Reflection phase and magnitude of the designed unit cell	107
4.12	First prototype of reconfigurable reflective surface	109
4.13	Symbolic illustration of three main states of reconfiguration	110
4.14	Free-space quasi-optical setup available at ESA ESTEC	112
4.15	Displacement characterization as a function of the applied voltage for the first prototype	114
4.16	Comparison between measurements and simulations of the first prototype	114
4.17	Comparison between measurements and simulations with air gap	116

4.18 Optimized prototype of reconfigurable reflective surface	117
4.19 Reflection phase and magnitude of the optimized unit cell	119
4.20 Displacement characterization as a function of the applied voltage for the optimized prototype	120
4.21 Comparison between measurements and simulations of the optimized prototype	120
4.22 Simplified drawing of the final concept for independent column reconfiguration	123
4.23 Reflection phase and magnitude of the unit cell for the scanning RA	123
4.24 Final geometry of the DEA actuators integrated in the beam-scanning RA . . .	125
4.25 Render of the 1-D beam-scanning RA	126
4.26 Simulated beam-scanning example for the final RA prototype	128
5.1 Electromagnetic spectrum spanning from microwave to optical frequencies . .	137
5.2 Illustration of the implanted test sample	139
5.3 Picture of the THz TDS measurement setup	139
5.4 Equivalent transmission line model representing the implanted PDMS membrane	139
5.5 Surface resistance extracted from TDS measurements of the implanted samples	142
5.6 Drawing of the unit cell composing the THz stretchable RA	145
5.7 Reflection phase and magnitude of the unit cell designed for the fixed-beam RA	146
5.8 Symbolic illustration of the designed fixed-beam RA	147
5.9 Simulated radiation pattern for the designed fixed-beam RA	147
5.10 Reflection phase profile selected for the fixed-beam RA	148
5.11 Fabrication process for the realization of the stretchable RA	150
5.12 Fabricated fixed-beam reflectarray operating at 1 THz	151
5.13 Schematic of the TDS setup used for the THz RA characterization	153
5.14 Experimental characterization of the fabricated THz RA	153
5.15 Schematic illustration of a generic 1-D RA principle	155
5.16 Deflection angle as a function of the differential phase and the cell stretching .	156
5.17 Reflection phase and magnitude of the unit cell designed for the stretchable scanning RA	157
5.18 Calculated radiation pattern for the designed stretchable RA	158
5.19 Measurement setup of the THz beam-scanning RA	160
5.20 Experimental characterization of the THz beam-scanning RA	160

List of Tables

2.1	Main characteristics of the conductive membranes under test	33
2.2	Surface resistance R_S'' and estimated gap δy	36
3.1	Summary of available technologies for phase shifter reconfiguration	51
3.2	Performance comparison for the proposed phase shifter concepts	58
3.3	Main variable definitions and dimensions of the fabricated phase shifter	65
3.4	Performance comparison with available tunable phase shifters	77
4.1	Optimized dimensions and material properties of the reconfigurable cell shown in Fig. 4.10	107
4.2	Optimized dimensions and material properties of the unit cell constituting the new prototype	119
4.3	Optimized dimensions and material properties of the unit cell constituting the scanning RA	124
5.1	Measurement procedure needed to extract the surface resistance of the implanted layer	141
5.2	Geometric and electromagnetic properties of the first unit cell	146

1 Introduction

1.1 Framework and objectives

The unprecedented expansion of wireless systems and terminals has led to the deployment of a plethora of new services with the consequent increasing demand for higher speed communications. According to the Cisco Visual Networking Index (VNI) Forecast [1], global mobile data traffic grew 69% in 2014 and will be increased nearly tenfold in 2019 with respect to 2014, reaching 24.3 EB¹ per month. Moreover, the average mobile data-rate will pass from 1683 kbit/s to nearly 4 Mbit/s in 2019 owing to the increase of 4G networks that will reach 14 Mbit/s, and will generate significantly higher traffic. This increasing request for higher connection speeds has been so far fulfilled introducing advanced modulation schemes (e.g., OFDM) and particular channel propagation techniques such as multiple-input multiple-output (MIMO).

However, the inherent bandwidth limitations characterizing conventional systems operating between L-band (1–2 GHz, e.g. mobile communications and global navigation satellite systems) and X-band (8–12 GHz, e.g. satellite communications and radars) is encouraging service operators and providers to migrate to higher frequencies. Following this trend, the portion of the electromagnetic (EM) spectrum ranging between millimeter-wave (MMW) and terahertz frequencies has experienced a growing interest justified by the potential for wider bandwidth (consequently higher capacity) and the availability of not allocated frequency slots. This is leading to the deployment of different services at Ku-band (12–18 GHz) and Ka-band (26.5–40 GHz), and the investigation of new applications at higher MMW (e.g., indoor wireless communications and 5G networks at V-band) and sub-THz frequencies (e.g., next generation femto-cellular networks, terabit WLAN and WPAN, and security screening). Despite the advantage offered in terms of channel capacity, additional technological challenges need to be considered with respect to lower frequency systems. Path losses are in fact higher and atmospheric effects (e.g., rain fade) can considerably affect the signal propagation degrading system performance. Moreover, material losses are typically higher, and available technologies

¹ 1 EB (exabyte) corresponds to 10^{18} bytes in SI units

Chapter 1. Introduction

suffer from increased cost and complexity when advanced capabilities are required. Therefore, the development of new technologies and the improvement of existing ones is becoming a prime need to overcome these limitations and allow a faster expansion of new communication services.

Satellite communications, among others, are in rapid evolution and are progressively migrating to higher frequencies of operation. Great interest is currently addressed to Ka-band for the deployment of commercial telecommunication systems such as broadband satellite internet and satcom on the move. At this regard, the new economics generated by high capacity satellites recently launched by Eutelsat and ViaSat has opened new markets attracting over 600 000 new users in US and Europe in less than two years. The Ka-band system, currently implemented in Eutelsat KaSAT and ViaSat-1 satellites, allows to provide broadband services with quality and costs unattainable with previous satellites operating at lower frequencies. In this field, as in the other mobile communication systems mentioned above, antenna reconfiguration capabilities are increasingly demanded, in order to optimize system performance and improve the quality of the service. User terminals with fixed beam or mechanically steerable beam pointing are already available, but the introduction of inertia-free beam steering capabilities (i.e. electronically realized) would greatly improve the exploitation of the network and its economics. Here the main challenge is the development of compact and low-cost terminals able to realize automatic repointing to compensate for undesired misalignment, which can be accidental (e.g., in the case of fixed terminals) or due the intrinsic movement of the holding platform (e.g., oil platform). From the spacecraft perspective, future on-board Ka-band antenna systems should allow for in-flight reconfiguration of the radiation performance, such as beam repointing, coverage reshaping and polarization agility. These capabilities would be highly desired to cope with potential link degradation (e.g., owing to thermoelastic distortions and/or rain fade), and to adapt to changing requirements that might be needed during the satellite lifetime. Also in this segment, the availability of new technologies allowing to improve performance while keeping controlled size, cost and complexity, will have a large impact on the system exploitation.

Different techniques and materials are currently available for the implementation of a given EM reconfiguration in antenna devices, such as semiconductors (i.e., PIN and varactor diodes), RF-MEMS, Liquid Crystal, and ferroelectrics [2]. All these technologies come with different advantages and disadvantages, which also highly depend on the frequency of operation and the addressed reconfiguration concept. However, a common feature to all these technologies is the significant increased loss and complexity with regard to the devices fixed counterpart. Moreover, both loss and complexity further increase when high-performance reconfiguration capabilities are needed at millimeter-waves and above. In particular, loss and complexity can be considered as the two main “universal” problems associated with the implementation of reconfiguration capabilities in antenna systems, and will therefore constitute major limitation to the future deployment of dynamically controllable systems for high-frequency applications.

In this context, the objective of this thesis is to contribute to the development of low-cost

and efficient technologies enabling antenna reconfiguration capabilities from MMW to THz frequencies. Within this scope, this thesis proposes the analysis, design and implementation of mechanically reconfigurable devices using dielectric elastomer actuators (DEAs). This is an emerging micro-technology allowing to achieve large displacement (up to the millimeter-scale) with very compact actuators. DEAs operate by deforming thin elastomer membranes under the application of an electric field via mechanically compliant electrodes, and possess appealing properties for antenna reconfiguration, namely: low cost materials and fabrication, analogue control, low power consumption and large strain outputs. Moreover, the microscale mechanical reconfiguration principle associated with DEA technology is expected to provide losses comparable with those of non-reconfigurable systems, owing to the possibility to completely isolate the actuation part from the EM-active area. This is a crucial aspect for the concerned applications, and represents a significant advantage over competing technologies.

This thesis has been partially carried out in the framework of two research projects aiming at the development of antenna reconfiguration at MMW and above: i) REACT (Reconfigurable millimeter-wave Antennas based on micro-fabricated electroactive Actuators) funded by the European Space Agency (ESA) in the frame of a Network/Partnering Initiative (NPI); ii) AMRA (Artificial Muscles for Reconfigurable Millimeter-wave Antennas) funded by the Swiss Space Center. Additional support has been provided by the Swiss National Science Foundation (SNSF) (grant n. 133583).

1.2 Dielectric elastomer actuators

Dielectric Elastomer Actuators (DEAs) are an attractive and relatively new technology which possesses unique properties, and represents a potential alternative to conventional mechanical reconfiguration schemes. DEAs are stretchable soft transducer consisting of a passive elastomer thin film (Young's modulus in the order of MPa) sandwiched between two compliant electrodes [3–5]. DEAs belong to the electroactive polymer (EAP) family, and are often referred to as “artificial muscles” since they respond to an electrical stimulus and exhibit strain and energy density comparable to natural muscles. Their principle of operation is based on the electrostatic attraction between the two electrodes as symbolically represented in Fig. 1.1. When a voltage is applied between the electrodes, the opposite charges collected on each electrode produce an electrostatic pressure (Maxwell pressure) that squeezes the elastomer modifying its original shape. In the simple case of free boundary conditions, the dielectric contracts in thickness and expands in area (Fig. 1.1b). This behavior is owing to the incompressibility characteristic of the elastomer, which results in the conservation of the original volume. This last condition can be mathematically expressed by the following relation [6]:

$$\lambda_1 \lambda_2 \lambda_3 = 1, \tag{1.1}$$

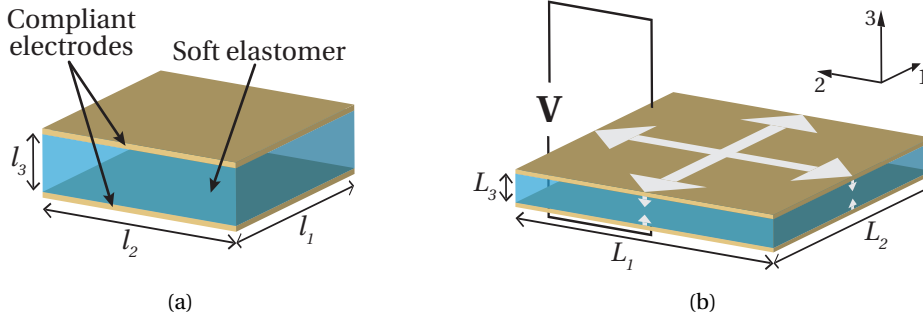


Figure 1.1 – Basic actuation principle of a DEA with free boundary conditions. (a) Inactive actuator consisting of a thin elastomer membrane sandwiched between two compliant electrodes. (b) Actuated state: when a voltage is applied to the compliant electrodes, the electrostatic pressure squeezes the elastomer, which contracts in thickness and expands in area.

where $\lambda_i = L_i / l_i$ ($i = 1, 2, 3$) is the ratio between the deformed and initial size in the i direction (Fig. 1.1). Equation (1.1) hence allows to correlate the thickness compression generated by the electrostatic Maxwell force with the corresponding area expansion. The fundamental relation between the dielectric compression and the applied voltage is obtained starting from the electrostatic energy associated with the DEA capacitor, and adopting an approach similar to that commonly used for parallel plate capacitors. This capacitive model allows to calculate the Maxwell pressure p induced by the external voltage V in the vertical direction [3]:

$$p = -\epsilon_0 \epsilon_r E^2 = -\epsilon_0 \epsilon_r \left(\frac{V}{d} \right)^2, \quad (1.2)$$

where ϵ_0 is the vacuum permittivity, ϵ_r is the dielectric constant of the elastomer, E is the electric field applied between the electrodes and d is the thickness of the membrane. Considering the Hooke's law and introducing the Young's modulus Y of the dielectric, the thickness strain (i.e., compression of the membrane) is given by:

$$s_3 = \frac{L_3}{l_3} - 1 = \frac{p}{Y} = -\frac{\epsilon_0 \epsilon_r V^2}{Y d^2}. \quad (1.3)$$

It is worth noting that the electric field in eq. (1.2) and (1.3) is dependent on the varying dielectric thickness, meaning that the electrostatic force increases during the dielectric compression. However, for small strains, d can be considered almost constant and replaced by the initial thickness l_3 (Fig. 1.1). Under this assumption and considering the elastomer incompressibility expressed by eq. (1.1), the in-plane strain can be calculated from eq. (1.3) using the following

expression [3]:

$$s_1 = s_2 = -\frac{s_3}{2}. \quad (1.4)$$

Typical driving fields are in the order $100 \text{ V}/\mu\text{m}$ (to avoid the dielectric breakdown), resulting in actuation voltages in the kV range for common elastomer membranes with a thickness ranging between 20 and $40 \mu\text{m}$. However, the current is very small, leading to very low DC power consumption. In addition, power is only required to change the device configuration, and not to maintain the actuator in a stable state, which results in a very low-power actuation principle. Common DEA designs targeting stable and long-term operation, typically exhibit strains in the range 10 – 30% , although very large strains larger than 100% (up to 1690%) have been demonstrated for particular actuator configurations [4, 7, 8]. These large achievable strains, in combination with low-cost materials and low-complexity fabrication techniques, make DEAs very attractive for their integration in a broad range of systems.

Since the first demonstration in 1998 [3], the interests in DEA technology has rapidly expanded driving the emergence of several devices and applications in different fields, as appears from comprehensive review papers on the subject [9–11]. The large strains and intrinsic soft nature of these elastomeric actuators allow full flexibility for the realization of unconventional actuator shapes and configurations at different size scales, in contrast to traditional rigid actuators (e.g., piezoelectric, magnetic, electrostatic, pneumatic). This peculiarity has led to the development of a huge number of devices, which include but are not limited to extenders, bow-tie actuators, spring rolls [12], folded DEA [13], hydrostatically coupled [14], and buckling-mode actuators [15]. Owing to their particular properties linking a change in electrical charge to a mechanical deformation, DEAs have also been investigated for the realization of energy harvesting from small (from human movement) [16] to large scale (from ocean waves) [17], capacitive and resistive sensors [18] and switches [19]. Combining so many attributes, in addition to inherent lightweight and compliance, makes them particularly suited for the realization of intelligent deformable machines [11], such as biomimetic robots [20], very lightweight rolling motors [21], and micro-grippers [22]. Commercial applications have also been developed. In this area it is worth mentioning the Optotune's laser speckle reducers and the VivitouchTM system from Bayer MaterialScience.

The particular relation between the actuation force and the elastomer thickness in DEAs represents a distinctive potential for the realization of miniaturized devices such as for instance demonstrated by the biological cell stretcher proposed in [24], where actuators as small as $100 \mu\text{m}$ were demonstrated. Dielectric elastomer actuators present a maximal energy density of $10^5 \text{ J}/\text{m}^3$, comparable to their magnetic and piezoelectric counterparts (Fig. 1.2). With respect to these technologies DEAs exhibit less output force, but larger strain, which can be several order of magnitude higher (especially compared to piezoelectric devices). Although DEAs are also a class of electrostatic devices, they have a higher energy density than

their air-gap counterpart, mainly due to the much larger dielectric strength of elastomers compared to air, which allows driving the devices at higher electric fields. Thermal micro-actuators have a higher energy density, but their performance are typically limited by the maximum temperature change allowed by the specific application, in addition to higher power consumption. Furthermore, DEAs are generally realized using low-cost technology which is highly compatible with standard micro-fabrication techniques. DEAs therefore present the best trade-off in terms of strain-force performance that are difficultly matched by other micro-actuator technologies. These characteristics make them perfect candidates to cope with the large-strain requirements of a wide range of applications, leading to compact solutions with high potential for complexity and cost reduction.

DEAs are particularly suited to generate planar deformation that can be efficiently used to displace objects in-plane, resulting in very thin devices [25]. This approach has been used for instance for the realization of soft tunable gratings [26], rotary micromotors [21], or Optotune's laser speckle reducers. This particular DEA operation (i.e., in-plane displacement) is adopted for the realization of the reconfigurable antenna devices developed during this research, confirming the potential of DEAs for low-cost, low-complexity, and efficient mechanical tuning discussed in this section.

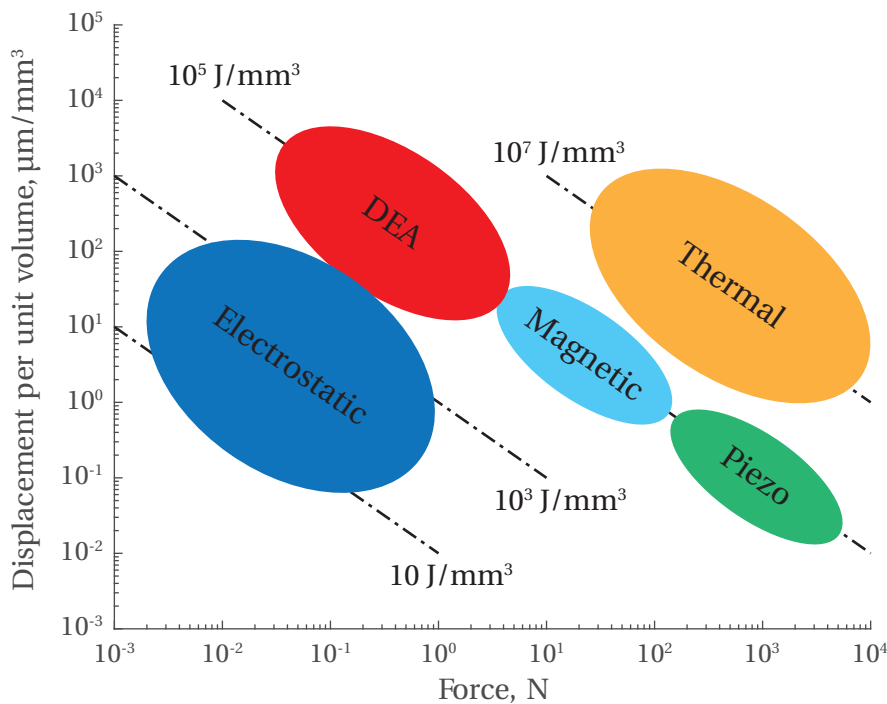


Figure 1.2 – Comparison between different micro-actuation technologies as a function of the energy density, the output force and the achievable displacement. DEAs represent the best trade-off in terms of actuation stroke and produced force. Adapted from [23].

1.3 Thesis outline

The scientific contribution of this work is represented by the development of novel reconfigurable antenna devices based on the in-plane mechanical deformation offered by dielectric elastomer micro-actuators. The devices presented throughout this manuscript have been developed targeting millimeter-wave and THz operation, motivated by the increasing need for advanced antenna reconfiguration required by emerging applications in this frequency range. The research activities carried out during this PhD thesis have been summarized in four main chapters. A brief review of the relevant state-of-the-art is proposed at the beginning of each chapter.

Chapter 2 – Millimeter-wave characterization of DEA materials

The second chapter presents the experimental characterization of the electromagnetic properties of dielectric materials generally used for the implementation of DEAs. The samples under test are made of polydimethylsiloxane (PDMS), that is the soft elastomer used for the realization of the DEAs considered in this thesis. Two different types of measurements are presented: (i) dielectric characterization (permittivity and loss tangent) of bulk PDMS at Ka-band and (ii) electromagnetic characterization (surface impedance) of flexible and stretchable PDMS-based conductive membranes in the same frequency range. The desired material properties are extracted using a transmission/reflection approach based on 2-port rectangular waveguide (RWG) measurements. In particular, a transmission line model and a corresponding extraction algorithm is proposed for the non-contact characterization of thin stretchable conductors, allowing to compensate for tolerances in the measurement setup. The experimental characterization presented in this chapter is crucial to allow an accurate electromagnetic modeling of DEA materials in the design presented in the following chapters.

Chapter 3 – Reconfigurable phase shifters based on DEAs

The third chapter proposes for the first time the application of DEAs to the implementation of MMW reconfigurable phases shifters. Different phases shifter concepts based on DEA mechanical reconfiguration are investigated and their performance evaluated using full-wave simulations. One device is selected to be further optimized, fabricated and tested. The considered concept consists of a conventional coplanar waveguide (CPW) loaded by a suspended perturbing element which is supported and horizontally displaced by a set of planar DEAs. The movement of the loading element over the CPW induces a variation in the effective permittivity of the line, hence generating a change in the insertion phase. The actuation part is completely isolated from the electromagnetic active area resulting in a very low-loss device. A prototype is fabricated using standard and low-cost printed circuit board (PCB) technology, demonstrating state-of-the-art performance in terms of the phase shift to loss figure of merit. The achieved results confirm the attractive potential of DEA micro-actuators for the realization of efficient reconfiguration in high-frequency antenna devices.

Chapter 1. Introduction

Chapter 4 – A beam-scanning DEA reflectarray

The fourth chapter addresses the design and development of a novel reflectarray (RA) concept using DEAs to implement 1-D beam-scanning capabilities. The proposed RA concept uses in-plane DEA expansion to mechanically modify the resonant length of microstrip patches on a grounded dielectric substrate. Although the use of resonant patches to realize RAs is well known, the mechanical reconfiguration of the patch length is proposed for the first time. The tuning approach is first demonstrated and validated through the realization of a periodic reflective surface with uniform phase distribution where the reconfiguration is implemented by a single set of DEAs. The design, fabrication and test of this reconfigurable surface are discussed together with encountered issues and proposed solutions. The experimental characterization of the fabricated prototype highlights very good performance allowing to validate the designed concept. Based on these results, the design of a 1-D beam-scanning reflectarray is proposed. This concept is based on the independent control of each column of cells to implement beam-scanning functionality in the H -plane of the antenna.

Chapter 5 – Stretchable reflectarray antennas for THz applications

The fifth chapter focuses on the realization of stretchable reflectarrays operating in the THz range, targeting the realization of conformal and beam-scanning devices. First it is proposed an efficient approach for the fabrication of flexible and stretchable conductors with high potential for the implementation of adaptive antenna devices. These conductors are realized inheriting the experience gained by the EPFL-LMTS group in the development of compliant electrodes for DEAs, which are based on low-energy gold ion implantation in PDMS thin membranes. Fabricated test samples are characterized using THz time-domain spectroscopy (TDS) to evaluate the change in conductivity associated with an applied stretching. This technique is then used for the realization of the stretchable ground plane in a RA operating at 0.75 THz and using solid-metal resonant patches of different sizes (fabricated using a shadow mask evaporation technique) to deflect the beam to an off-normal direction. Beam-scanning is experimentally demonstrated at THz for the first time. The approach is based on mechanical stretching, which can be implemented by integrated planar DEAs in future designs.

Chapter 6 – Conclusion and perspective

The sixth and last chapter draws the conclusions summarizing the main results achieved during this work and presented in the previous chapters. Furthermore, it includes a discussion about future perspectives and critical aspects that need to be addressed in future research lines to promote a wider application of DEA reconfiguration in antenna devices.

Bibliography

- [1] “Visual Networking Index (VNI),” <http://www.cisco.com/>.
- [2] S. Hum and J. Perruisseau-Carrier, “Reconfigurable Reflectarrays and Array Lenses for Dynamic Antenna Beam Control: A Review,” *IEEE Transactions on Antennas and Propagation*, vol. 62, no. 1, pp. 183–198, 2014.
- [3] R. E. Pelrine, R. D. Kornbluh, and J. P. Joseph, “Electrostriction of polymer dielectrics with compliant electrodes as a means of actuation,” *Sensors and Actuators A: Physical*, vol. 64, no. 1, pp. 77–85, 1998.
- [4] R. Pelrine, R. Kornbluh, Q. Pei, and J. Joseph, “High-Speed Electrically Actuated Elastomers with Strain Greater Than 100%,” *Science*, vol. 287, no. 5454, pp. 836–839, 2000.
- [5] F. Carpi, D. De Rossi, R. Kornbluh, R. Pelrine, and P. Sommer-Larsen, *Dielectric Elastomers as Electromechanical Transducers*. Elsevier, 2008.
- [6] Z. Suo, “Theory of dielectric elastomers,” *Acta Mechanica Solida Sinica*, vol. 23, no. 6, pp. 549–578, 2010.
- [7] S. J. A. Koh, T. Li, J. Zhou, X. Zhao, W. Hong, J. Zhu, and Z. Suo, “Mechanisms of large actuation strain in dielectric elastomers,” *Journal of Polymer Science Part B: Polymer Physics*, vol. 49, no. 7, pp. 504–515, 2011.
- [8] C. Keplinger, T. Li, R. Baumgartner, Z. Suo, and S. Bauer, “Harnessing snap-through instability in soft dielectrics to achieve giant voltage-triggered deformation,” *Soft Matter*, vol. 8, pp. 285–288, 2012.
- [9] A. O’Halloran, F. O’Malley, and P. McHugh, “A review on dielectric elastomer actuators, technology, applications, and challenges,” *Journal of Applied Physics*, vol. 104, no. 7, p. 071101, 2008.
- [10] P. Brochu and Q. Pei, “Advances in dielectric elastomers for actuators and artificial muscles,” *Macromolecular Rapid Communications*, vol. 31, no. 1, pp. 10–36, 2010.
- [11] I. A. Anderson, T. A. Gisby, T. G. McKay, B. M. O’Brien, and E. P. Calius, “Multi-functional dielectric elastomer artificial muscles for soft and smart machines,” *Journal of Applied Physics*, vol. 112, no. 4, p. 041101, 2012.
- [12] R. Kornbluh, R. Pelrine, Q. Pei, M. Rosenthal, S. Stanford, N. Bonwit, R. Heydt, H. Prahald, and S. V. Shastri, “Application of Dielectric Elastomer EAP Actuators,” in *Electroactive Polymer (EAP) Actuators as Artificial Muscles: Reality, Potential, and Challenges*, 2004.
- [13] F. Carpi, C. Salaris, and D. De Rossi, “Folded dielectric elastomer actuators,” *Smart Materials and Structures*, vol. 16, no. 2, p. S300, 2007.

- [14] F. Carpi, G. Frediani, and D. Rossi, "Contractile hydrostatically coupled dielectric elastomer actuators," *IEEE/ASME Transactions on Mechatronics*, vol. 17, no. 5, pp. 987–994, 2012.
- [15] S. Rosset, M. Niklaus, P. Dubois, and H. Shea, "Large-Stroke Dielectric Elastomer Actuators With Ion-Implanted Electrodes," *Journal of Microelectromechanical Systems*, vol. 18, no. 6, pp. 1300–1308, 2009.
- [16] R. Pelrine, R. D. Kornbluh, J. Eckerle, P. Jeuck, S. Oh, Q. Pei, and S. Stanford, "Dielectric elastomers: generator mode fundamentals and applications," in *Proc. SPIE*, vol. 4329, 2001, pp. 148–156.
- [17] R. D. Kornbluh, R. Pelrine, H. Prahlad, A. Wong-Foy, B. McCoy, S. Kim, J. Eckerle, and T. Low, "Dielectric elastomers: Stretching the capabilities of energy harvesting," *MRS Bulletin*, vol. 37, pp. 246–253, 2012.
- [18] T. A. Gisby, B. M. O'Brien, and I. A. Anderson, "Self sensing feedback for dielectric elastomer actuators," *Applied Physics Letters*, vol. 102, no. 19, p. 193703, 2013.
- [19] B. M. O'Brien, E. P. Calius, T. Inamura, S. Q. Xie, and I. A. Anderson, "Dielectric elastomer switches for smart artificial muscles," *Applied Physics A*, vol. 100, no. 2, pp. 385–389, 2010.
- [20] Q. Pei, M. Rosenthal, S. Stanford, H. Prahlad, and R. Pelrine, "Multiple-degrees-of-freedom electroelastomer roll actuators," *Smart Materials and Structures*, vol. 13, no. 5, p. N86, 2004.
- [21] S. Rosset and H. R. Shea, "Towards fast, reliable, and manufacturable deas: miniaturized motor and rupert the rolling robot," in *Proc. SPIE*, vol. 9430, 2015, pp. 943 009–943 009–11.
- [22] O. Araromi, I. Gavrilovich, J. Shintake, S. Rosset, M. Richard, V. Gass, and H. Shea, "Rollable Multisegment Dielectric Elastomer Minimum Energy Structures for a Deployable Microsatellite Gripper," *IEEE/ASME Transactions on Mechatronics*, vol. 20, no. 1, pp. 438–446, 2015.
- [23] S. Rosset, "Metal ion implanted electrodes for dielectric elastomer actuators," Ph.D. dissertation, École Polytechnique Fédérale de Lausanne, 2009.
- [24] S. Akbari and H. R. Shea, "An array of $100\mu\text{m} \times 100\mu\text{m}$ dielectric elastomer actuators with 80% strain for tissue engineering applications," *Sensors and Actuators A: Physical*, vol. 186, pp. 236–241, 2012.
- [25] S. Rosset, O. A. Araromi, and H. R. Shea, "Maximizing the displacement of compact planar dielectric elastomer actuators," *Extreme Mechanics Letters*, *in press*, vol. 3, pp. 72–81, 2015.
- [26] M. Kolloche, S. Döring, J. Stumpe, and G. Kofod, "Voltage-controlled compression for period tuning of optical surface relief gratings," *Opt. Lett.*, vol. 36, no. 8, pp. 1389–1391, 2011.

2 Millimeter-wave characterization of DEA materials

This chapter presents the experimental characterization of dielectric materials generally used for the implementation of dielectric elastomer actuators (DEAs). The samples under test are made of polydimethylsiloxane (PDMS), a silicon-based organic polymer that finds application in several engineering fields. In particular, two different types of measurements are presented: (i) dielectric characterization (permittivity and loss tangent) of bulk PDMS at Ka-band (26.5–40 GHz) and (ii) electromagnetic characterization (surface impedance) of flexible and stretchable PDMS-based conductive membranes in the same frequency range.

A transmission/reflection approach based on 2-port rectangular waveguide (RWG) measurements is used to extract in a simple and accurate way the dielectric properties of the considered test samples. The proposed technique is presented in §2.1: the theoretical formulation is described in §2.1.1 while an experiment based on full-wave electromagnetic simulations is analyzed in §2.1.2. Different bulky PDMS samples have been prepared using commercial materials and their experimental characterization is presented in §2.3.1. In turn, a non-contact measurement technique for the surface impedance characterization of flexible metallizations is discussed in §2.2: the theoretical approach is presented in §2.2.1 and it is validated in §2.2.2 using full-wave simulated data. The experimental characterization of different types of flexible and stretchable conductive membranes is presented in §2.3.2. A discussion on measurements results and open issues is reported in §2.4.

2.1 Bulk materials characterization

The objective of this section is to describe the proposed method for the dielectric characterization of PDMS. This study is especially motivated by the need to accurately know the dielectric properties of any material included in the design of the reconfigurable antenna devices presented in the following chapters. PDMS has a large number of applications including biomedical devices, microfluidics and DEAs, but has been barely used for the implementation of MMW antenna devices. Moreover, dielectric properties are generally provided only at lower frequency (up to 100 kHz) for commercial polymers. Therefore, a dedicated experimental

characterization has been necessary. The considered technique is based on 2-port scattering parameter measurements of a RWG loaded by the unknown material. This method demonstrated to be fast and accurate and can be generally used to measure the complex dielectric constant of any material at microwaves and millimeter-waves.

2.1.1 Basic theory and general approach

The proposed method for the characterization of polymerized PDMS follows a transmission/reflection (T/R) approach, which is commonly used to measure the broadband complex permittivity of dielectric materials. The discussed technique is a formulation of the Nicolson-Ross [1] and Weir [2] procedure. We use a different transmission line (TL) modeling to retrieve the electromagnetic properties of the sample under test from the 2-ports measured scattering parameters. The selected waveguide-based T/R method was mainly preferred to other available techniques (e.g., dielectric and cavity resonators, free-space techniques) [3] for the following reasons: i) test samples are easily prepared filling RWG sections with the unpolymerized PDMS; ii) good accuracy in the extraction over a wide frequency range, which is defined by the single mode operation of the holder RWG (e.g., 26.5–40 GHz for a WR28 waveguide standard); iii) easy connection of the sample under test with the measuring vector network analyzer; iv) no need to involve transcendental equation or numerical solutions in the extraction procedure. Overall, the proposed technique represents the best trade-off between achievable accuracy in the extraction and low-complexity of the measurement setup.

The measurement setup is simple and test samples can be easily prepared. The unknown material is placed within the section of a rectangular waveguide with generic transversal dimensions a and b , as illustrated in Fig. 2.1. The corresponding equivalent transmission line (TL) model is then considered. When the rectangular waveguide is only excited by the fundamental mode TE_{10} , the whole structure can be modeled as the cascade of three different transmission line sections as represented in Fig. 2.2a. Each section, corresponding to a portion of the loaded RWG, is characterized by its length L_i , characteristic impedance Z_i (complex for lossy materials) and complex propagation constant $\gamma_i = \alpha_i + j\beta_i$, and can be fully described through an $ABCD$ transmission model [4]. Considering the previous assumptions (i.e., TE_{10} excitation and TL modeling), the i -th section is exactly represented by the respective transmission or $ABCD$ matrix T_i , given by [4]:

$$T_i = \begin{bmatrix} A_i & B_i \\ C_i & D_i \end{bmatrix} = \begin{bmatrix} \cosh(\gamma_i L_i) & Z_i \sinh(\gamma_i L_i) \\ \frac{1}{Z_i} \sinh(\gamma_i L_i) & \cosh(\gamma_i L_i) \end{bmatrix}. \quad (2.1)$$

In the specific case depicted in Fig. 2.1, the electromagnetic propagation in the rectangular waveguide loaded by the unknown dielectric, is fully described by the concatenation of three transmission matrices: 1) air-filled RWG, 2) dielectric-filled RWG and 3) air-filled RWG. Thus,

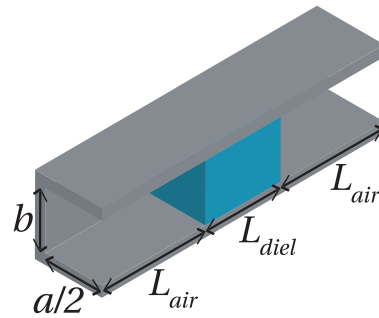
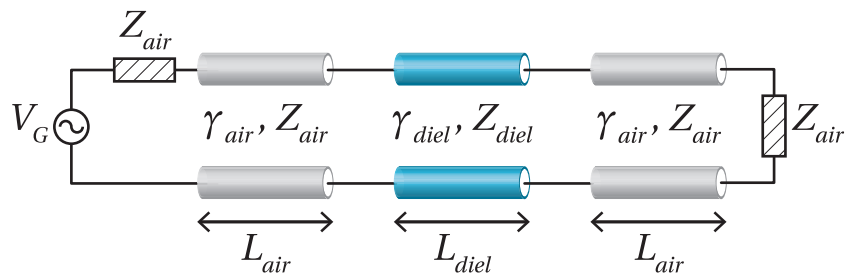
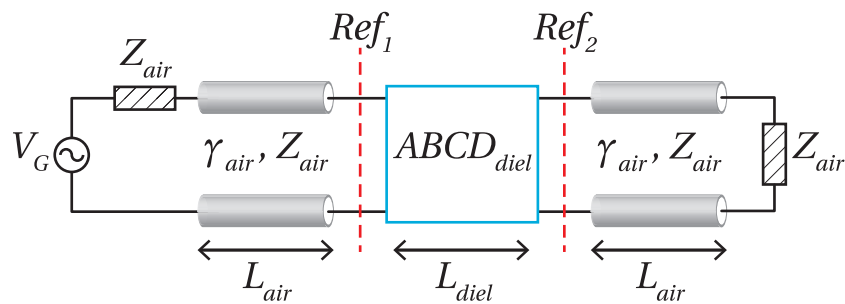


Figure 2.1 – Longitudinal section drawing of a rectangular waveguide loaded by the unknown dielectric material. The dielectric completely fills the central part of the waveguide with generic cross section $a \times b$.



(a)



(b)

Figure 2.2 – Transmission line model of the RWG filled with the dielectric under test. (a) Each TL section is described by its propagation constant γ_i , characteristic impedance Z_i and length L_i . (b) The dielectric-filled TL section is completely described by its equivalent $ABCD$ TL model after deembedded of the air-filled RWG sections.

Chapter 2. Millimeter-wave characterization of DEA materials

considering the general TL theory, the total transmission or $ABCD$ matrix is calculated using a matrix multiplication:

$$T_{tot} = \begin{bmatrix} A_{tot} & B_{tot} \\ C_{tot} & D_{tot} \end{bmatrix} = T_{air} T_{diel} T_{air}. \quad (2.2)$$

T_{tot} is obtained from the measured S-parameters using the following relations:

$$A_{tot} = \frac{(1 + S_{11})(1 - S_{22}) + S_{12}S_{21}}{2S_{21}}, \quad (2.3a)$$

$$B_{tot} = \frac{Z_{ref}(1 + S_{11})(1 + S_{22}) - S_{12}S_{21}}{2S_{21}}, \quad (2.3b)$$

$$C_{tot} = \frac{1}{Z_{ref}} \frac{(1 - S_{11})(1 - S_{22}) - S_{12}S_{21}}{2S_{21}}, \quad (2.3c)$$

$$D_{tot} = \frac{(1 - S_{11})(1 + S_{22}) + S_{12}S_{21}}{2S_{21}}, \quad (2.3d)$$

where Z_{ref} is the reference characteristic impedance of the considered S-parameters. At this point, the $ABCD$ matrix of the dielectric-filled section is given by

$$T_{diel} = \begin{bmatrix} A_{diel} & B_{diel} \\ C_{diel} & D_{diel} \end{bmatrix} = T_{air}^{-1} T_{tot} T_{air}. \quad (2.4)$$

In practical applications it is usually possible to deembed the measured scattering parameters (e.g., using TRL calibration, as discussed in §2.3), in order to place the reference planes of the performed measurement exactly at the faces of the unknown dielectric. The equivalent transmission line model is illustrated in Fig. 2.2b. In this particular case, the parameters A_{diel} , B_{diel} , C_{diel} and D_{diel} can be directly calculated using eq. (2.3), where Z_{ref} corresponds to the characteristic impedance of the air-filled RWG section. Then, eq. (2.1) can be easily inverted to obtain the complex propagation constant and the characteristic impedance of the dielectric-filled RWG section:

$$\gamma_{diel} = \frac{1}{L_{diel}} \operatorname{acosh} \left(\frac{A_{diel} + D_{diel}}{2} \right), \quad (2.5)$$

$$Z_{diel} = \sqrt{\frac{B_{diel}}{C_{diel}}}. \quad (2.6)$$

The unknown complex dielectric constant can be directly retrieved from the propagation constant γ_{diel} . For the fundamental TE_{10} mode, the complex propagation constant and the characteristic impedance are respectively given by:

$$\gamma = \alpha + j\beta = \sqrt{\left(\frac{\pi}{a}\right)^2 - \omega^2 \mu_0 \epsilon}, \quad (2.7)$$

$$Z_0 = \frac{j\omega\mu}{\gamma}, \quad (2.8)$$

and the complex dielectric constant can be generally written as

$$\epsilon = \epsilon' - j\epsilon'' = \epsilon_0 \epsilon_r (1 - j \tan \delta), \quad (2.9)$$

where ϵ_r is the relative dielectric constant and $\tan \delta = \epsilon''/\epsilon'$ is the dielectric loss tangent. In this formulation, the conductivity of the dielectric material is assumed to be zero and only dielectric losses are considered (i.e., $\alpha = \alpha_d$); under this assumption, the loss tangent is directly related to the imaginary part of the propagation constant. Thus, by squaring second and third terms of eq. (2.7) and comparing the respective real and imaginary parts, we obtain the desired dielectric properties

$$\epsilon_r = \frac{\left(\frac{\pi}{a}\right)^2 + \beta^2 - \alpha^2}{\omega^2 \mu_0 \epsilon_0}, \quad (2.10)$$

$$\tan \delta = \frac{2\alpha\beta}{\omega^2 \mu_0 \epsilon_0 \epsilon_r}. \quad (2.11)$$

Equations (2.10) and (2.11) allow to calculate the desired dielectric properties of the unknown elastomer (or generic dielectric material) from the measured 2-port S-parameters. Nevertheless, it is well known from literature that T/R techniques are numerically unstable for low-loss materials when thickness resonances arise, that is when the dielectric thickness correspond to an integer multiple of half guided wavelength [5, 6]. At these frequencies, in fact, the magnitude of S_{11} is very small (thickness resonance peak) and the uncertainty on the phase of S_{11} becomes unacceptable. Different methods have been proposed to overcome this issue (e.g., [5–7]) and could be investigated. However, these techniques would generally increase algorithm and computation complexity, without bringing a significant advantage. For our goal, a simpler solution lied in the preparation of various samples with different thickness, in order to avoid pathological resonance effects in the bandwidth of interest. In the next section the proposed technique is validated using full-wave simulation data. More details about sample

preparation and characterization are given in §2.3.1.

2.1.2 Dielectric properties extraction from simulated data

In order to validate the extraction technique discussed in the previous section, an experiment based on full-wave simulations is reported. A rectangular waveguide loaded by a PDMS sample (Fig. 2.1) was simulated in the range 25–40 GHz using the commercial software *Ansys HFSS*. Dimensions and frequency range of the RWG section were selected in agreement with the commercial standard WR28 ($a = 7.112$ mm and $b = 3.556$ mm). The dielectric properties of the PDMS were chosen according to the results reported in [8] for the commercial Sylgard 184. Therefore, a dielectric permittivity $\epsilon_r = 2.77$ and a loss tangent $\tan \delta = 0.04$ were assigned in the simulator. Different thicknesses for the dielectric inside the RWG were considered (1, 2, 3 and 5 mm), in order to test the sensitivity of the extraction technique to realistic tolerances of the test fixture. Simulated results are also compared with synthetic data calculated using the TL theory discussed in the previous section.

Figure 2.3 shows a comparison between simulated (from HFSS without deembed) and theoretical scattering parameters. Both sets of data corresponds to the geometry depicted in Fig. 2.1 and the related TL model of Fig. 2.2a. Theoretical scattering parameters were calculated using the transmission matrix approach described in the previous section. That is, eq. (2.1) was used to calculate the $ABCD$ parameters for each TL section (*air*, *pdms*, *air*) and the total $ABCD$ matrix was obtained by eq. (2.2). Then, scattering parameters were calculated using the following relations [4]:

$$S_{11} = \frac{A_{tot} + \frac{B_{tot}}{Z_{ref}} - C_{tot}Z_{ref} - D_{tot}}{A_{tot} + \frac{B_{tot}}{Z_{ref}} + C_{tot}Z_{ref} + D_{tot}}, \quad (2.12a)$$

$$S_{12} = \frac{2(A_{tot}D_{tot} - B_{tot}C_{tot})}{A_{tot} + \frac{B_{tot}}{Z_{ref}} + C_{tot}Z_{ref} + D_{tot}}, \quad (2.12b)$$

$$S_{21} = \frac{2}{A_{tot} + \frac{B_{tot}}{Z_{ref}} + C_{tot}Z_{ref} + D_{tot}}, \quad (2.12c)$$

$$S_{22} = \frac{-A_{tot} + \frac{B_{tot}}{Z_{ref}} - C_{tot}Z_{ref} + D_{tot}}{A_{tot} + \frac{B_{tot}}{Z_{ref}} + C_{tot}Z_{ref} + D_{tot}}, \quad (2.12d)$$

where Z_{ref} is the reference characteristic impedance of the air-filled waveguide, obtained from eq. (2.8). As expected, an excellent agreement is obtained for both magnitude and phase

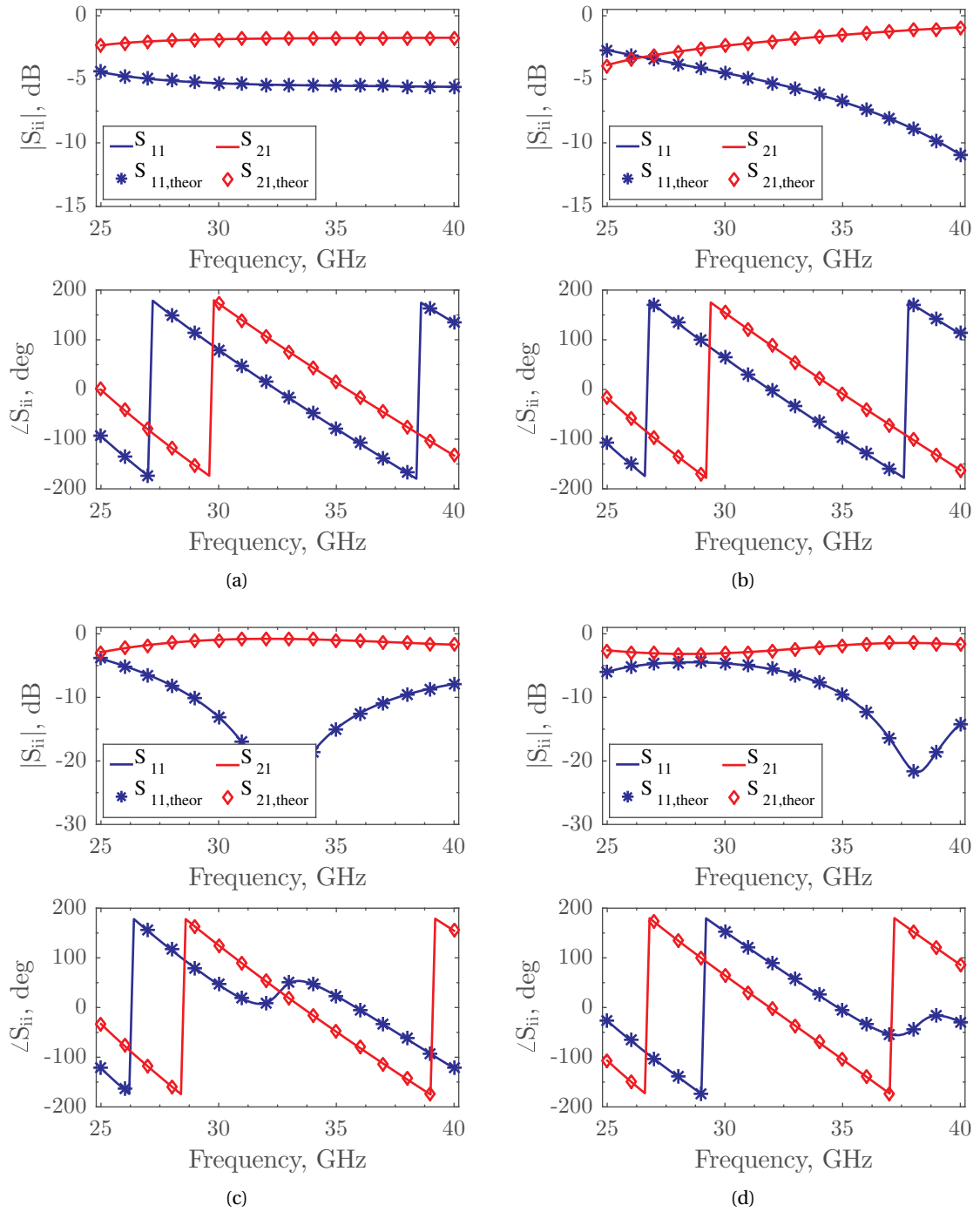


Figure 2.3 – Simulated and theoretical scattering parameters for different thicknesses of the PDMS dielectric inside the hosting RWG: (a) $L_{PDMS} = 1$ mm, (b) $L_{PDMS} = 2$ mm, (c) $L_{PDMS} = 3$ mm, (d) $L_{PDMS} = 5$ mm. Simulated data are obtained using HFSS full-wave simulations, whereas theoretical S-parameters are calculated using eq. (2.1), (2.2) and (2.12).

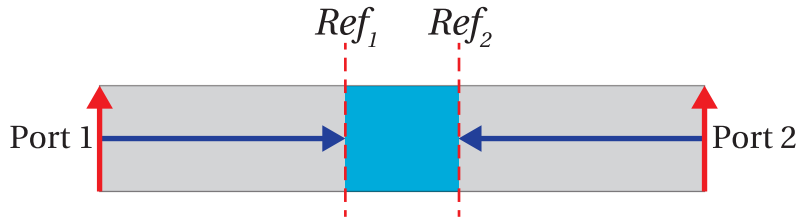


Figure 2.4 – Simulated geometry (HFSS) after deembedding of the reference planes, equivalent to the TL model of Fig. 2.2b. The RWG walls are implemented using PEC boundary conditions and two waveports (Port 1 and Port 2) are used to excite the TE_{10} mode.

between calculated and simulated scattering parameters for the PDMS-filled RWG, since an exact analytical model has been adopted.

The simulated scattering parameters of Fig. 2.3 were then deembedded as illustrated in Fig. 2.4 to remove the effect of the air-filled waveguide sections. The rectangular waveguide was implemented using perfect electric conductor (PEC) boundary conditions in HFSS, and two waveports were used to excite the TE_{10} mode. The deembedding procedure allowed to move the reference planes of the simulated S-parameters to the faces of the dielectric material, corresponding to a realistic 2-ports measurement setup based on TRL calibration (more details in §2.3). The equivalent model of Fig. 2.2b was then considered and equations (2.3)–(2.11) were used to extract the desired dielectric properties. This procedure exactly corresponds to a real experimental characterization, if simulated scattering parameters are replaced with measured ones.

The results of the extraction are shown in Fig. 2.5, where retrieved ϵ_r and $\tan \delta$ are plotted in comparison with the respective nominal values assigned in the simulator. Retrievals and simulations exhibit an excellent agreement, validating the accuracy and efficiency of the proposed technique. This is also confirmed by the error analysis presented in Fig. 2.6: the relative error is always smaller than 0.15% for the permittivity and 0.012% for the loss tangent. Such an error is only due to the numerical precision of the electromagnetic solver and of the extraction software. Moreover, the procedure is not affected by the PDMS thickness since similar results were obtained for all the considered examples. It is worth noting that the extraction experiment presented so far is based on the ideal case where all the parameters and sample properties are well known. However, in a real measurement setup, this assumption is no longer valid since all these properties are known with a finite precision, and a number of tolerances need be considered.

Tolerances in the dielectric thickness, for instance, will certainly affect the measurement accuracy. An error in the knowledge of L_{PDMS} can generate inaccuracy in the extraction of the propagation constant from eq. (2.5) and, thus, incorrect values of the calculated ϵ_r and $\tan \delta$. In order to assess the effect of this error, a sensitivity analysis has been performed introducing a perturbation δL in the extraction procedure. The error was calculated with respect to the

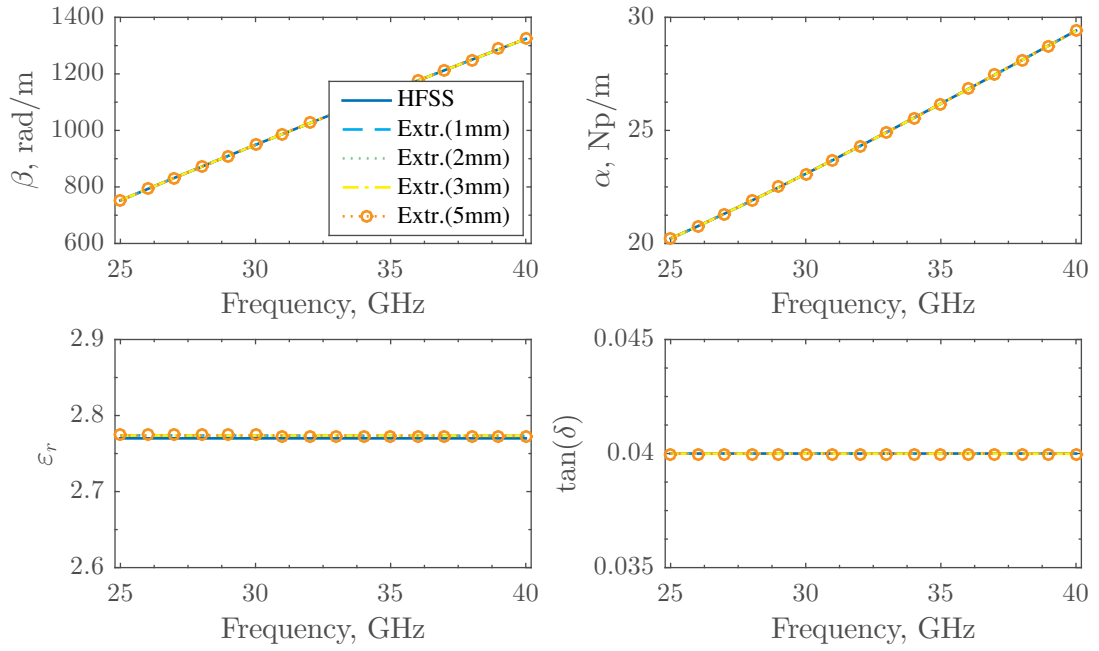


Figure 2.5 – Propagation constant and dielectric properties (permittivity and loss tangent) extracted from full-wave simulations for different thickness of the PDMS material loading the RWG. The extraction technique described in §2.1.1 is applied.

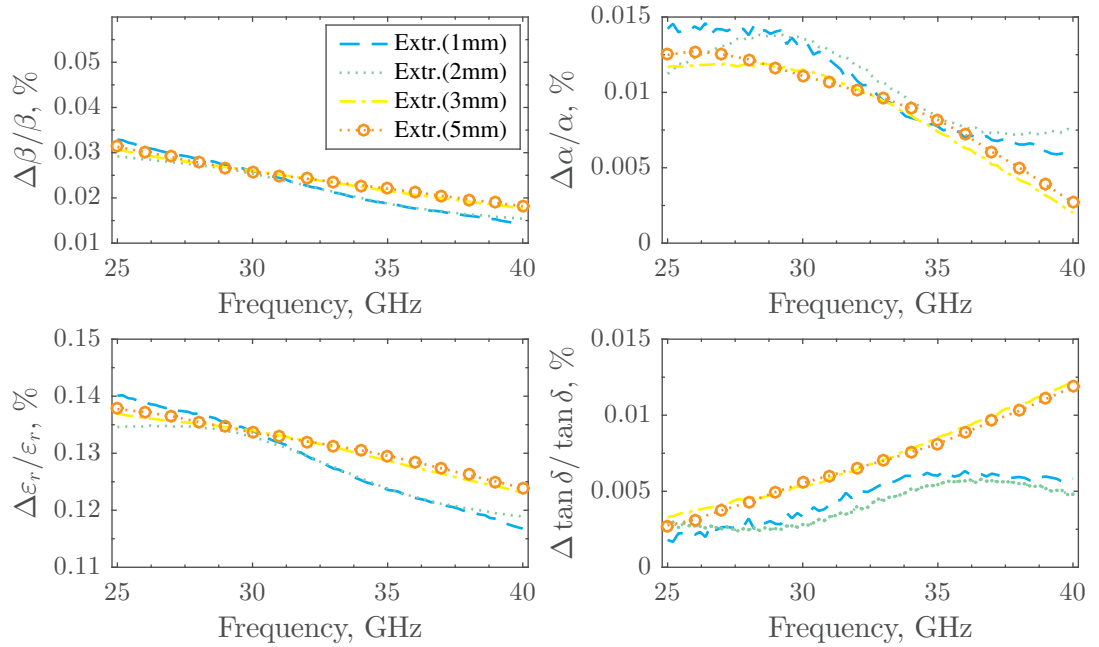


Figure 2.6 – Relative error for the retrievals of Fig. 2.5 with respect to the nominal values assigned in HFSS. Negligible values are found, which are mainly due to the numerical precision of the EM solver and of the extraction software.

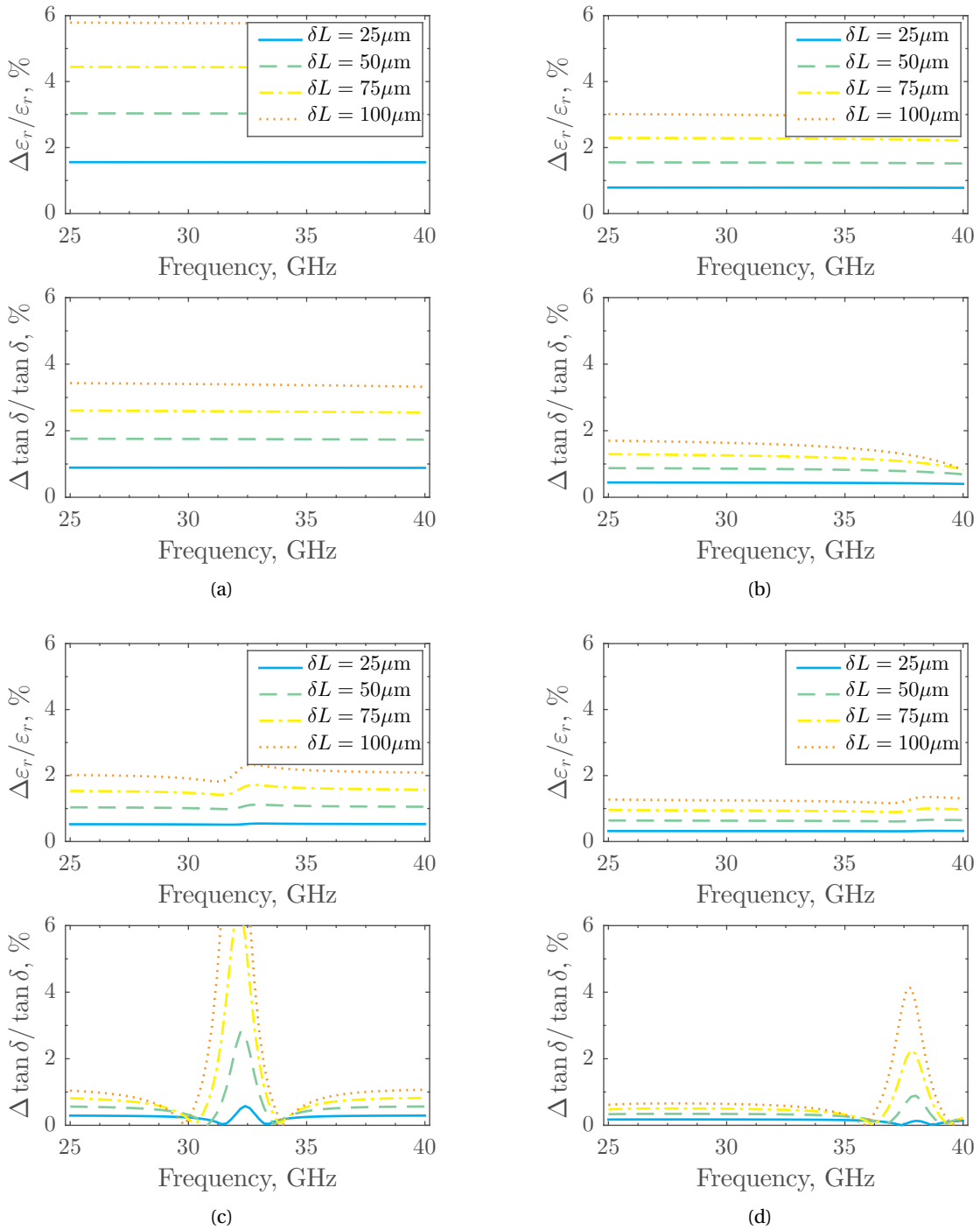


Figure 2.7 – Relative error in the extraction of ϵ_r and $\tan \delta$ due to inaccuracy in the knowledge of the PDMS thickness. A perturbation δL was introduced in the extraction procedure to emulate an incorrect sample thickness. Different dielectric thicknesses are considered: (a) $L_{PDMS} = 1$ mm, (b) $L_{PDMS} = 2$ mm, (c) $L_{PDMS} = 3$ mm, (d) $L_{PDMS} = 5$ mm.

2.2. Characterization of stretchable conductive membranes

nominal extraction when the dielectric thickness is known with infinite precision (i.e., $\delta L = 0$):

$$\frac{\Delta x}{x} = \frac{x|_{\delta L \neq 0} - x|_{\delta L = 0}}{x|_{\delta L = 0}}. \quad (2.13)$$

Figure 2.7 shows the relative error for four different thicknesses of the PDMS sample (1, 2, 3 and 5 mm) and for different perturbations δL . As expected, the smaller is the nominal thickness of the sample, the bigger is the error for the same value δL . The maximum calculated error on the retrieved permittivity is smaller than 6 % when $L_{PDMS} = 1$ mm, while it decreases to 2 % when $L_{PDMS} = 5$ mm. These values were completely acceptable in our setup, considering that in practical applications we were able to know the sample thickness with a 50 μm precision. It is also worth noting that a peak in the error of the extracted loss tangent appears in correspondence of the thickness resonance for the 3 mm and 5 mm samples (cf. Fig. 2.3). From this analysis we can conclude that thicker samples are less sensitive to any small error in the knowledge of their thickness, but present the well-known resonance effect. For this reason, we have considered samples with various thicknesses in our experimental characterization, thereby reducing the uncertainty linked to the extracted values in the whole frequency range.

2.2 Characterization of stretchable conductive membranes

Manufacturing and characterization of *flexible and stretchable* conductors has recently gained sustained interest [9], due to their wide range of applications in wireless communications and biomedical industry, including the realization of wearable antennas [10] and reconfigurable radiofrequency (RF) devices [11]. Design and development of all these components require an accurate knowledge of the electric properties of considered metallizations. Different measurement techniques, based on cavity and planar resonators (e.g., [12]), have been developed in the past to characterize the RF surface impedance of thin metal films. However, these methods require the design and manufacturing of particular resonators based on the unknown conductor and their connection to the measurement system. This increases the complexity of the measurement setup and can be particularly inconvenient for the high frequency characterization of flexible and stretchable membranes based on soft materials (i.e., the contact can be problematic).

The aim of this section is to present the basics of a non-contact characterization technique based on a 2-port transmission/reflection (T/R) approach, allowing to measure the surface impedance of thin flexible and stretchable conductors. In particular, we are especially interested in the characterization of flexible metallization or conductive membranes, in order to understand whether they can be suitable for the design and implementation of reconfigurable MMW devices (mainly tunable phase shifters and antennas). Although the proposed technique is generally applicable to the characterization of any thin-film conductor, here we consider flexible and stretchable metallizations on thin PDMS membranes.

2.2.1 Basic theory and general approach

The general transmission line theory behind the proposed non-contact measurement technique is presented in this section. The basic approach was adapted from the work described in [13], that allows a non-contact characterization of conductive sheets. The method is based on the same transmission line modeling discussed in §2.1.1 for the dielectric characterization of bulk dielectrics, but a particular electrical model for the conductive layer has been considered.

As the considered membranes are very thin, it is necessary to bond them on a rigid and low-loss substrate in order to allow their placement inside the hosting RWG. Therefore, a realistic setup is assumed in this section to present the proposed measurement technique. In particular, for the experimental characterization discussed in §2.3.2, conductive PDMS membranes are transferred to fused silica substrates, previously cut in order to fit the holding RWG section (WR28 standard is considered for Ka-band measurements). Fused silica chips, obtained from a commercial wafer, have thickness $L_{glass} = 525 \pm 50 \mu\text{m}$, permittivity $\epsilon_{glass} = 3.80 \pm 0.15$ and loss tangent $\tan \delta_{glass} = 0.0004$ at the frequencies of interest. Then, each chip (conductive membrane on glass) is pasted on a foam substrate of same cross-section, of thickness $L_{foam} = 1000 \pm 50 \mu\text{m}$ and permittivity $\epsilon_{foam} = 1.05 \pm 0.05$. This foam substrate is used as a physical support to simplify the placement and alignment within the RWG holder employed for measurements. The foam-glass-membrane sample is then placed within a RWG section, as depicted in Fig. 2.8. The corresponding circuit model, assuming a TE_{10} mode excitation, is illustrated in Fig. 2.9a, where the conductive layer is represented by a lumped impedance Z_S , and each uniform dielectric-loaded RWG section by a transmission line of finite length L_i , characteristic impedance Z_i and complex propagation constant γ_i ($i = air; pdms; glass; foam$). This model is a rigorous representation of the considered system under the fundamental TE_{10} mode propagation. Moreover, since the thickness of the conducting layer is electrically very small in our samples ($<100 \text{ nm}$, [14, 15]), a shunt lumped impedance Z_S exactly models the conductive layer [16].

The sheet impedance Z_S is then represented by an $ABCD$ matrix and the corresponding T-model is considered (Fig. 2.9b). According to the previous assumptions (i.e., the conductive layer is electrically small), Z_1 and Z_2 shall be exactly zero [16] and the conductive layer is correctly represented by the shunt impedance Z_S alone. Thus, from measured scattering parameters we can calculate the total network transmission matrix T_{tot} using eq. (2.2) and eq. (2.3). The transmission matrix T_S for the impedance layer is then obtained by matrix inversion and multiplication:

$$T_S = \begin{bmatrix} A_S & B_S \\ C_S & D_S \end{bmatrix} = T_{air}^{-1} T_{tot} T_{foam}^{-1} T_{glass}^{-1} T_{pdms}^{-1}, \quad (2.14)$$

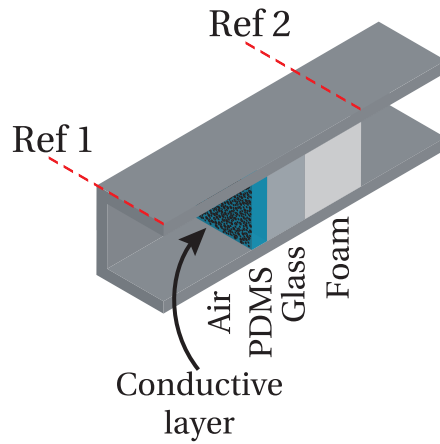


Figure 2.8 – Schematic representation of a RWG loaded by the foam-glass-membrane chip under test. The considered conductive membranes are extremely thin and, therefore, it is necessary to bond them on a rigid and low-loss substrate.

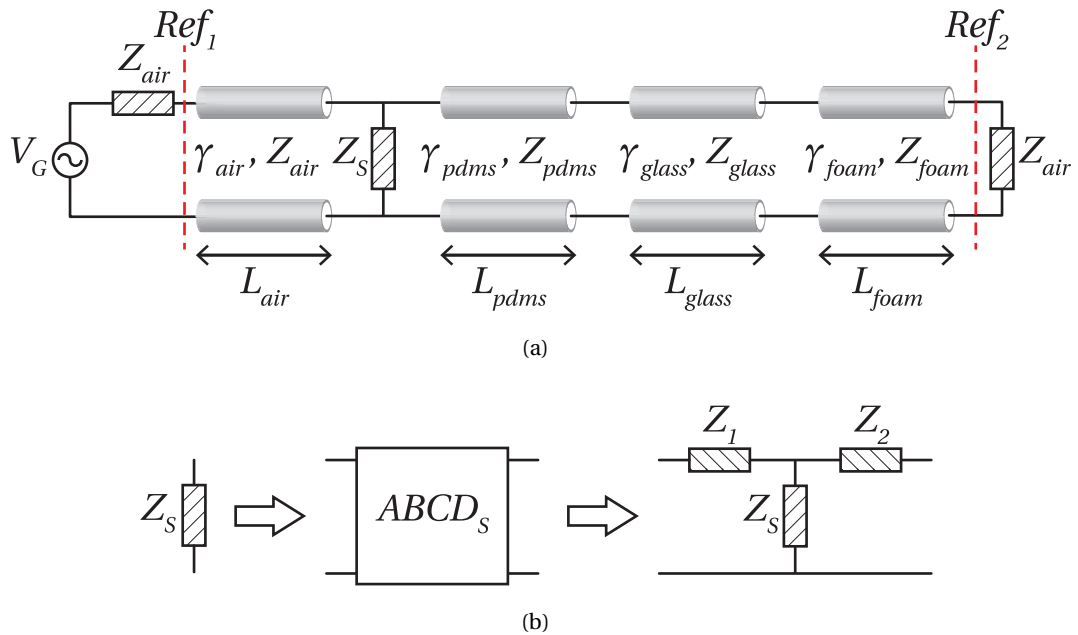


Figure 2.9 – Equivalent representation of the RWG configuration depicted in Fig. 2.8. (a) Complete transmission line model, where each TL section is described by its propagation constant γ_i , characteristic impedance Z_i and length L_i , and the conductive layer by a shunt impedance Z_S . (b) Equivalent circuit of the conductive layer under measurements; the equivalent $ABCD$ model is considered and a T-model circuit is extracted.

where T_{air} , T_{pdms} , T_{glass} , and T_{foam} are the transmission matrices of the respective TL sections depicted in Fig. 2.9a. The elements of the equivalent T-model, in turn, are calculated using the following relations [4]:

$$Z_1 = \frac{A_S - 1}{C}, \quad (2.15a)$$

$$Z_2 = \frac{D_S - 1}{C}, \quad (2.15b)$$

$$Z_S = \frac{1}{C_S}. \quad (2.15c)$$

The series impedances from eq. (2.15a) and eq. (2.15b) must be exactly zero [16] and the flexible membrane is fully described by the shunt impedance Z_S . However, in practical application, non-zero series elements Z_1 and Z_2 are generally retrieved from real measurements, due to the effect of tolerances in the thickness and dielectric properties of the involved substrates (i.e., substrates properties are known with finite accuracy). Based on these observations, the routine used for the extraction of Z_S varies the different substrate parameters (thickness and permittivity) within the manufacturer tolerances so as to minimize the series components. More specifically, Z_1 and Z_2 are used to estimate the error, which is minimized at each iteration. This allows for a more accurate computation of Z_S , reducing the effect of the different tolerances in considered samples.

2.2.2 Surface impedance extraction from simulated data

The extraction technique discussed in the previous section was validated through a full-wave simulation approach, where a realistic measurement setup was considered (Fig. 2.10). An air-filled RWG section was left between the conductive layer and Ref_1 to emulate the real case when the chip under test does not fill completely the waveguide holder. In agreement with §2.1.2, simulations were performed in the range 25–40 GHz using *Ansys HFSS*. The rectan-

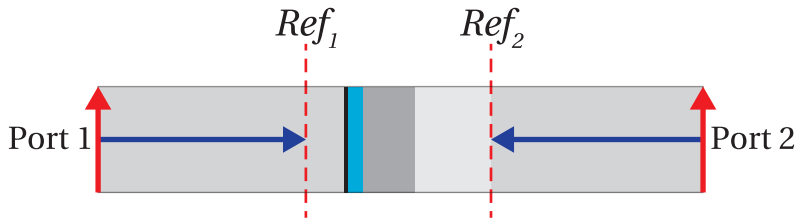


Figure 2.10 – Simulated measurements setup for surface impedance characterization. The rectangular waveguide is implemented using PEC boundary conditions, and two waveports are used to excite the TE_{10} mode. The conductive layer on the PDMS membrane is modeled through an impedance boundary condition.

2.2. Characterization of stretchable conductive membranes

gular waveguide was implemented using PEC boundary conditions in the simulator, and two waveports were used to excite the TE_{10} mode. The conductive layer on the PDMS membrane was considered infinitely thin and modeled through a surface impedance boundary condition. Different values of thickness and surface impedance for the PDMS membrane were simulated and the respective extraction procedure was carried out. In all the analyzed cases, we were able to extract the desired values with negligible errors when all the dimensions and dielectric parameters were assumed to be known. Nevertheless, for the sake of brevity, only one case is presented in this section. This simulated experiment was based on the following realistic parameters for the involved materials: $L_{pdms} = 60\mu\text{m}$, $L_{glass} = 525\mu\text{m}$, $L_{foam} = 1000\mu\text{m}$ and surface impedance $Z_S = 50\Omega/\square$.

The results of the extraction are shown in Fig. 2.11. It is worth observing that the proposed technique is very accurate in the processing of simulated data where all the parameters are precisely known. In fact, as discussed in §2.2.1, Z_1 and Z_2 should be zero and their extracted values can be used to evaluate the committed error (Fig. 2.11), which results to be very small here ($<0.8\Omega$) and most probably due to the numerical precision of the utilized software.

Nevertheless, in real measurements all the parameters (e.g., thicknesses of the glass and foam, and respective dielectric properties) are known with finite precision, thereby introducing errors in the extraction. In order to improve the extraction accuracy, the retrieved values of Z_1 and Z_2 can be used to optimize the procedure. That is, the substrate uncertainties can be varied in the extraction procedure within the manufacturer tolerances in order to minimize Z_1 and Z_2 , since as mentioned above these have to be zero.

A sensitivity analysis has been performed to evaluate the influence of the PDMS thickness accuracy. Since the PDMS thickness is very small compared to the fused silica and foam substrates, an error in its knowledge will marginally affect the extraction. To confirm this assumption, a perturbation δL was introduced in the extraction procedure, as it had been previously done for the bulk PDMS. The extracted values of Z_S , Z_1 and Z_2 are shown in Fig. 2.12 for different realistic values of δL : the extraction of the surface impedance is barely affected by an error in the knowledge of the PDMS thickness. The only visible effect is an increase of the magnitude of Z_2 (increasing error), but its values are still below an acceptable threshold. Moreover, as explained above, this error can be favorably used to improve the extraction accuracy. Different tests related to substrate tolerances were performed and the extraction procedure always managed to correct for any inaccuracy in the knowledge of the permittivity and thickness of involved materials.

A critical aspect to investigate is represented by the effect of the conductive layer size. In fact, when the conductive membrane does not exactly fill the waveguide section, capacitive effects between the conductor edge and the waveguide walls can arise. Two situations can be considered, and are symbolically illustrated in Fig. 2.13: i) a gap δx between the conductive sheet and the vertical metallic walls of the waveguide, and ii) a gap δy between the sheet and the horizontal metallic walls. The former generates negligible effects because the electric field

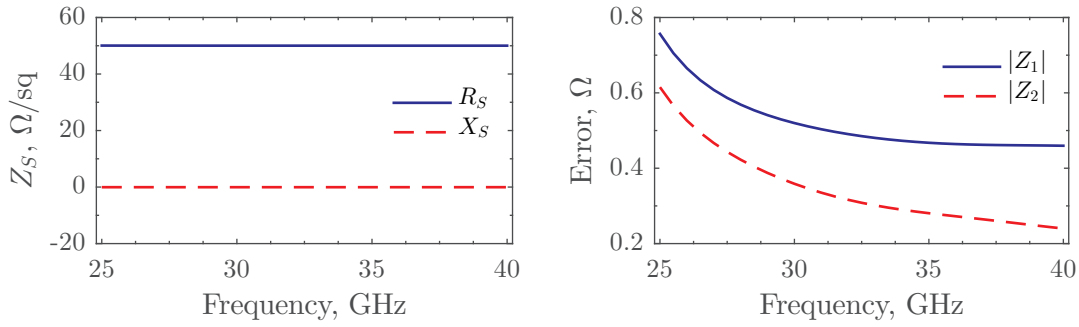


Figure 2.11 – Extracted impedance Z_S (left panel) and committed error (right panel) for the presented simulated experiment. The conductive membrane is bonded to a stack of fused silica and foam and placed inside a RWG. The considered materials have the following characteristics: $L_{pdms} = 60\mu\text{m}$, $L_{glass} = 525\mu\text{m}$, $L_{foam} = 1000\mu\text{m}$ and $Z_S = 50\Omega/\square$.

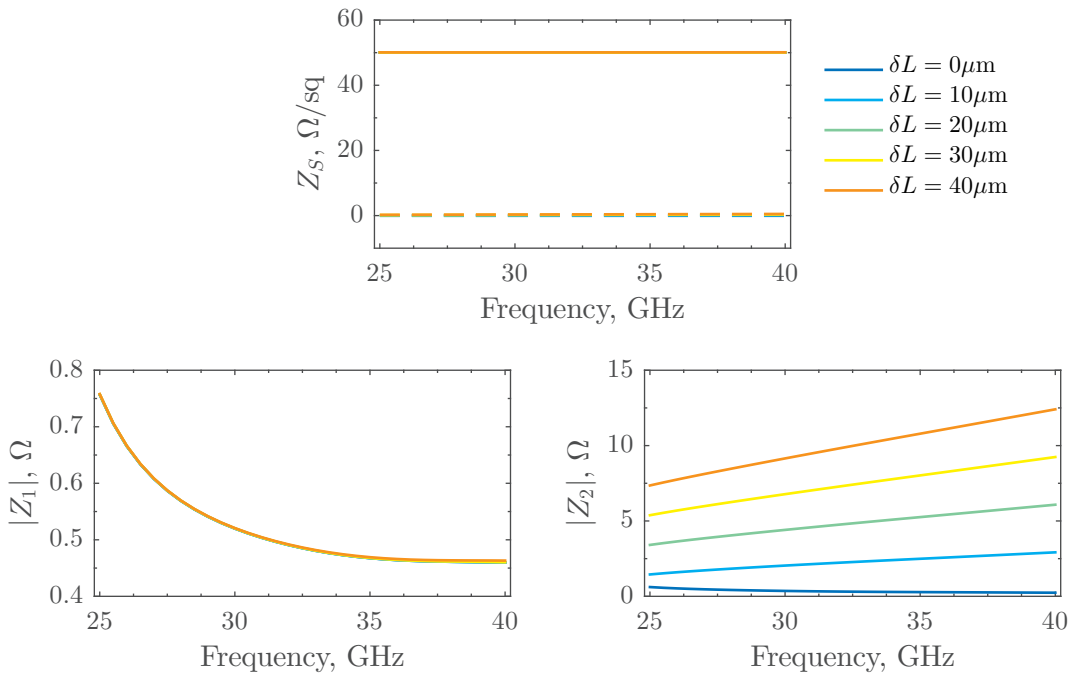


Figure 2.12 – Extracted impedance for different errors in the knowledge of the PDMS thickness: real part in solid line, imaginary part in dashed line. The nominal PDMS thickness assigned in the simulator is $L_{pdms} = 60\mu\text{m}$. A small error, expressed by Z_2 , is generated by the perturbation δL .

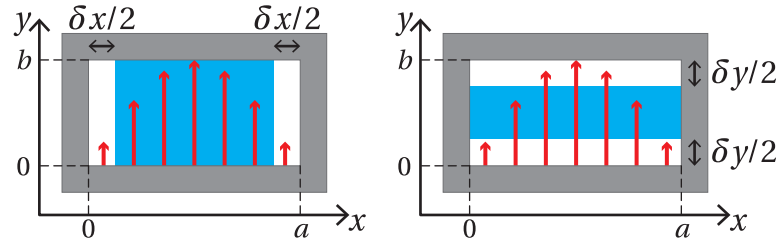


Figure 2.13 – Schematic representation of a gap between the conductive membrane and the RWG walls. A gap δx between the membrane and the vertical metallic wall of the waveguide and a gap δy between the membrane and the horizontal metallic wall of the waveguide are considered. Red arrows depict the electric field distribution of the fundamental TE_{10} mode.

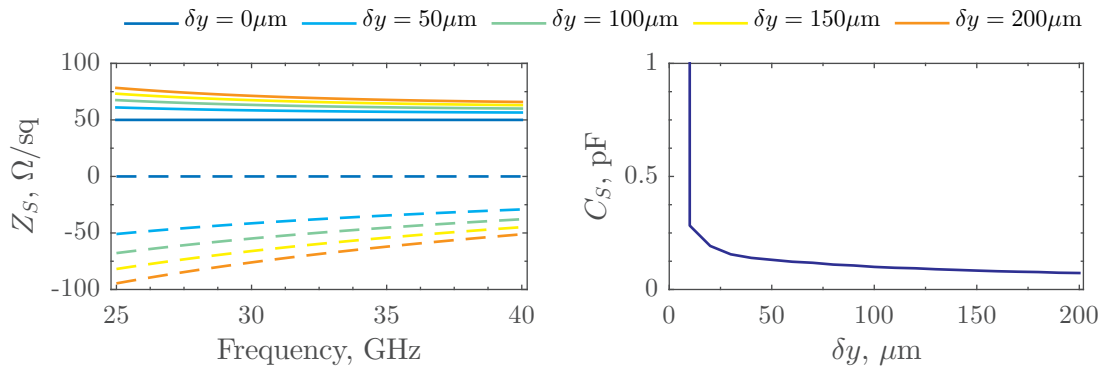


Figure 2.14 – Effect of a gap δy between the conductive membrane and the horizontal wall of the RWG (cf. Fig. 2.13) in the extraction procedure. Left panel shows the extracted surface resistance R_S (solid lines) and reactance X_S (dashed lines). Right panel shows the extracted series capacitive component that accurately models the imaginary part X_S .

of the dominant TE_{10} mode vanishes in correspondence of $x = 0$ and $x = a$, while the latter has to be investigated. Figure 2.13 also shows the electric field distribution (red arrows) of the dominant TE_{10} mode inside the RWG. This simplified illustration clearly highlights the non-negligible coupling between the horizontal edge of the conductive layer and the RWG when a gap δy is present.

A parametric analysis was performed varying δy in the simulator geometry, and the resulting scattering parameters were fed to the extraction procedure. The extracted sheet impedance $Z_S = R_S + jX_S$ for different gaps is reported in the left panel of Fig. 2.14 (R_S in solid lines and X_S in dashed lines): the real part of the extracted impedance increases with δy , and an imaginary part different from zero appears (note that a real impedance was previously assigned in the simulator). It is easy to demonstrate that the extracted impedance can be modeled by a series R - L - C circuit, where the inductive component is almost negligible. The right panel of Fig. 2.14 shows the extracted series capacitance C_S as a function of the vertical gap δy .

This effect has to be carefully studied in real measurements. However, the magnitude of this gap is not easy to quantify, due to the very small sizes of the involved materials, but simulations can be used in post-processing for a better estimate of the desired surface impedance. A post-processing procedure (based on full-wave simulations and least-squared approach) allowing to remove the gap error and to estimate the δy value, will be proposed and discussed in §2.3.2.

2.3 Experimental results

2.3.1 Dielectric properties of bulk PDMS

In this section the experimental dielectric characterization of a commercial PDMS material at Ka-band is presented. The extraction technique described in §2.1.1 was used to retrieve the relative permittivity and loss tangent of the unknown dielectric.

The PDMS under investigation is the commercial Dow Corning Sylgard 186 [17]. This elastomer will be mentioned several time throughout this manuscript, since it is the basic material of all the dielectric elastomer actuators implementing the reconfigurable devices presented in the following chapters. Thus, a dielectric characterization was necessary to extract the material properties needed in the design of any later MMW device. To our best knowledge, no information regarding the Ka-band behavior of this specific material were available in literature, and the manufacturer only provides information up to 100 kHz.

Different brass RWG sections with thickness of 2, 3 and 5 mm were manufactured and completely filled with the unpolymerized PDMS. Therefore, the thickness of each PDMS sample exactly corresponded to the thickness of the hosting RWG section. The PDMS polymer was prepared using a standard procedure: the Sylgard 186 monomer was first mixed together with the curing agent in a 10:1 mass ratio (as suggested by the manufacturer) and then rect-

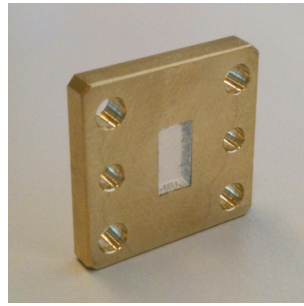


Figure 2.15 – Rectangular waveguide section filled with the PDMS under study. The commercial Dow Corning Sylgard 186 is prepared using a standard procedure and poured inside the RWG holder. The polymerization of the PDMS is then accelerated by two baking phases.

angular waveguide sections were manually filled. Two microscope glass slides were placed and pressed on the two faces of the RWG, in order to assure a flat surface once the PDMS was cured. The polymerization of PDMS was accelerated by two baking phases: the first at 50 °C for 30 minutes to reduce the formation of air bubbles and the second at 105 °C for 60 minutes. The preparation of the PDMS test samples was carried out at the *Microsystems for Space Technologies Laboratory (LMTS)*, EPFL. An example of test sample is shown in Fig. 2.15.

The results corresponding to five different samples are considered in this measurements analysis: two samples with a thickness of 2 mm (*sample1* and *sample2* in the following), two samples with a thickness of 3 mm (*sample3* and *sample4*) and one sample with a thickness of 5 mm (*sample5*).

A full two-port measurement procedure was adopted to characterize the considered samples. To this regard, each RWG section was connected to an Agilent E8361 PNA using two coax-to-waveguide adapters. A Thru-Reflect-Line (TRL) calibration was used for removing the effect of the transitions between the coaxial-based network analyzer and the RWG. TRL calibration allows to locate the reference planes of the measurements exactly at the faces of the waveguide section and to refer the measured S-parameters to the modal impedance of the air-filled waveguide (as described in §2.1.2 for simulations). The measured scattering parameters (magnitude and phase) for the five samples are shown in Fig. 2.16. An excellent agreement is found for S_{21} between samples with equal thickness and a very good agreement for S_{11} . Moreover, for the 3 mm and 5 mm thick samples is also visible the S_{11} thickness resonance effect discussed in §2.1.1; this means that extracted values will diverge at those frequency and cannot be trusted. However, the use of different thicknesses allows to have always a wide frequency range exempt from degrading effects.

Measured scattering parameters (Fig. 2.16) were then processed to obtain the complex propagation constant and the desired dielectric properties using eq. (2.10) and eq. (2.11). The extracted propagation constant $\gamma = \alpha + j\beta$ is shown in Fig. 2.17. A good agreement is achieved between the propagation constant of different samples, while α diverges at frequencies where the resonance thickness appears for *sample3* and *sample4*. This is a well known phenomenon

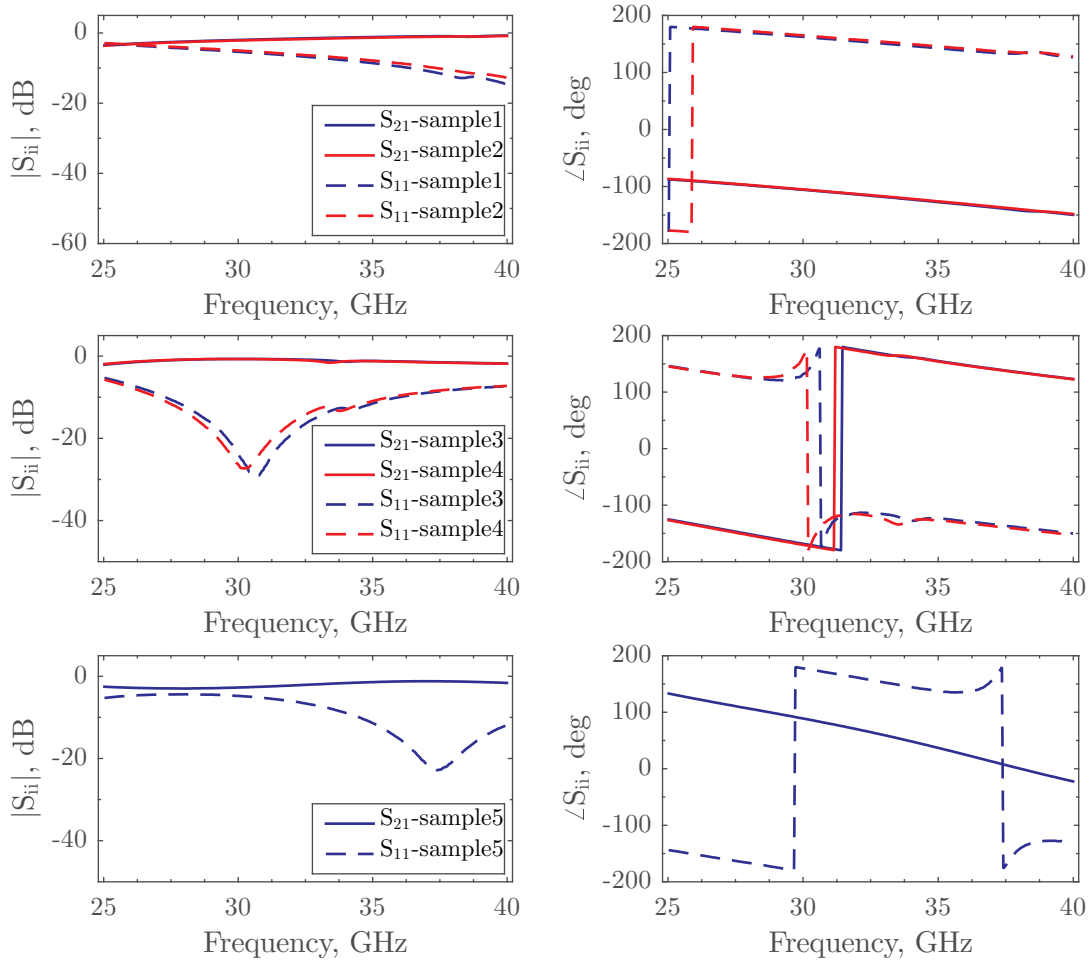


Figure 2.16 – Measured scattering parameters for the analyzed PDMS samples. Five samples with different thickness are characterized: *sample1* and *sample2* (top panels) have a thickness of 2 mm, *sample3* and *sample4* (middle panels) have a thickness of 3 mm and *sample5* (bottom panels) has a thickness of 5 mm.

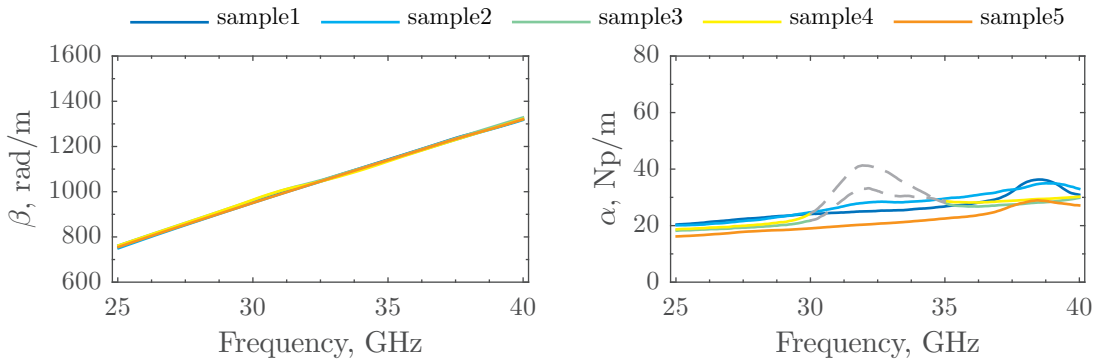


Figure 2.17 – Complex propagation constant retrieved from the measured scattering parameters of Fig. 2.16: phase constant β (left) and attenuation constant α (right). Gray dashed parts are a priori discarded because correspond to a thickness resonance (cf. §2.1.1).

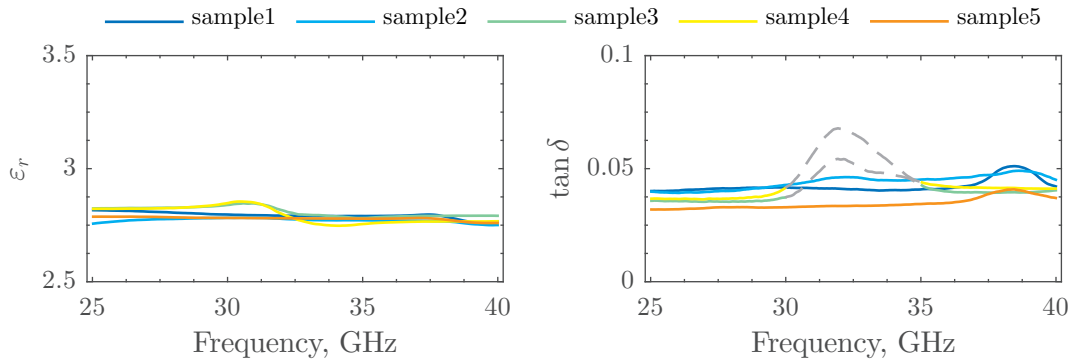


Figure 2.18 – Permittivity ϵ_r (left) and loss tangent $\tan \delta$ (right) retrieved from the measured scattering parameters of Fig. 2.16. Gray dashed parts are a priori discarded because correspond to a thickness resonance (cf. §2.1.1).

(e.g., [5, 6]) and has already been discussed in §2.1.1. The measurement procedure is numerically unstable when the magnitude of S_{11} is too small and the extracted values are discarded (dashed gray lines). More interesting for our scopes are the retrieved dielectric properties shown in Fig. 2.18. All measured samples exhibit a permittivity in the range 2.78–2.82 with a mean value of 2.79. A slightly higher variability is visible for the retrieved loss tangent with extracted values between 0.033 and 0.045 and a mean value of 0.038. Moreover, the values corresponding to the resonance are discarded, because not accurate for the reasons explained above.

2.3.2 Conductivity of stretchable metalized membranes

The measurement technique presented in §2.2 has been applied to characterize two different types of flexible conductive membranes: i) PDMS membranes (both prestretched and non-prestretched) implanted with gold ions using low-energy filtered cathodic vacuum arc (FCVA) [14, 18], and ii) commercial PDMS corrugated films with a thin silver layer deposition provided by Danfoss PolyPower A/S [15, 19].

The selected conductive membranes have been developed addressing the realization of compliant electrodes in dielectric elastomer actuators, where high flexibility and strain capabilities are required. Moreover, these electrodes must remain conductive and sustain high actuation strains without being damaged [9]. These properties result to be very convenient for the realization of flexible and stretchable conductive paths in mechanically reconfigurable MMW devices, where deformations up to the millimeter-range are desired (note that the free-space wavelength is 10 mm at 30 GHz).

The implanted PDMS membranes were prepared at LMTS using a low-energy (2–10 keV) FCVA equipment based on a RHK Technology ARC 20 pulsed arc source [14, 18]. The implantation procedure, described in [14], allows to create a layer of gold nano-clusters embedded into the top 50 nm of the PDMS membrane as shown in Fig. 2.19a. These gold particles are in physical

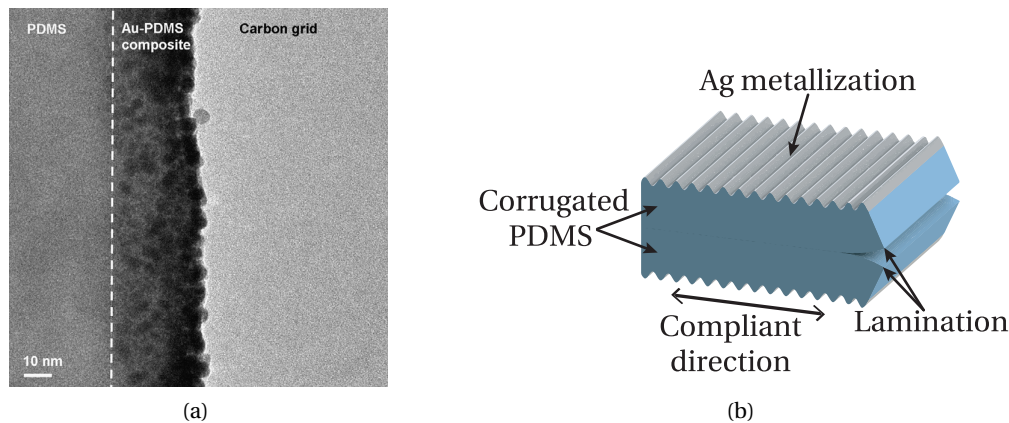


Figure 2.19 – Flexible and stretchable conductive membranes under test. (a) TEM cross-section of a PDMS membrane implanted with gold nano-particles using filtered cathodic vacuum arc; the implantation direction is from right to left. Reproduced from [18]. (b) Illustration of the PolyPower corrugated membrane with thin-film silver evaporated on the corrugated surface. The lamination of two membranes is necessary to obtain the commercial DEA. Adapted from [9].

contact, thereby providing an extremely thin conductive layer. Owing to the absence of mechanical bonds, gold particles move relative to each other (maintaining the conductive path) when the elastomer is stretched. The experimental results presented in [14] demonstrated strains of up to 170 % before the electrodes lost their conductivity. Moreover, they sustained up to 100 000 cycles at 30 % strain keeping good DC conductivity.

The PolyPower films, on the other hand, are commercial electrodes based on corrugated PDMS membranes. These are produced using large-scale manufacturing techniques [15, 19]. The corrugated membrane is first obtained using a molding technique. Then, after curing of the elastomer material, a vacuum sputtering process is used to deposit a silver thin-film (thickness around 110 nm) on the corrugated surface. Both the corrugation depth and period are in the range of 7 μm . With this geometry, these membranes can sustain up to 80 % strain without inducing significant damages into the metal layer. These metallized films were developed aiming the implementation of DEAs, where a capacitor configuration is needed. The elastomer capacitor is obtained by laminating two films with their flat sides in contact (Fig. 2.19b). Therefore, for our scope, we needed to de-laminate the PolyPower film, in order to obtain a single PDMS membrane with the conductive layer extending only on one side.

The results corresponding to five different samples are presented in this document: two prestretched implanted membranes with equi-biaxial prestretch (*sample1* and *sample2*), two non-prestretched implanted membranes (*samples3* and *sample4*) and a Danfoss PolyPower corrugated membrane (*sample5*). The main characteristics of the considered samples are summarized in Tab. 2.1.

All available membranes were transferred to fused silica chips of dimensions $7.112 \times 3.556 \text{ mm}^2$

Table 2.1 – Main characteristics of the conductive membranes under test.

<i>Sample</i>	<i>Thickness, μm</i>	<i>Prestretch</i>
Implanted PDMS membrane	42.0	equi-biaxial, $\lambda = 1.19$
Implanted PDMS membrane	43.5	equi-biaxial, $\lambda = 1.26$
Implanted PDMS membrane	61.0	NA
Implanted PDMS membrane	69.5	NA
Danfoss PolyPower membrane	40.0	NA

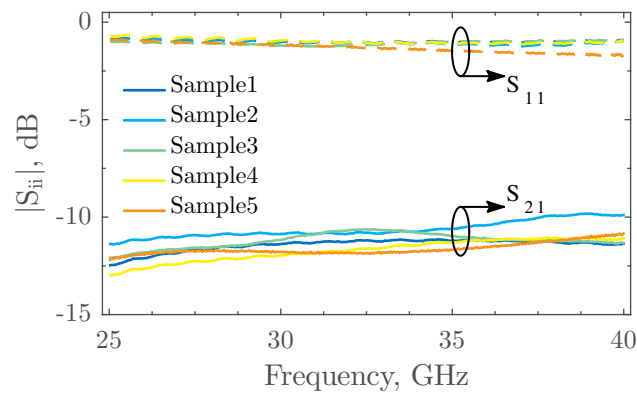


Figure 2.20 – Measured scattering parameters from the considered samples listed in Tab. 2.1. *Sample1*, *sample2*, *sample3* and *sample4* are realized using gold ion implantation in thin PDMS membranes. *Sample5* is a commercial Danfoss PolyPower corrugated membrane with thin-film metallization on the corrugated surface.

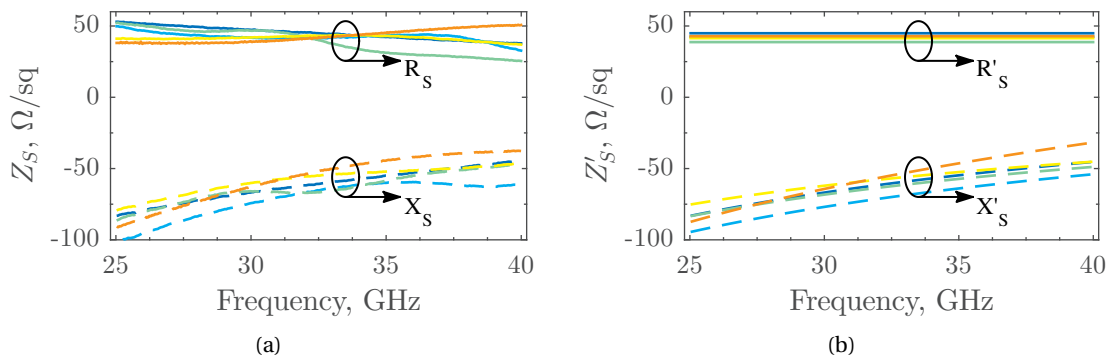


Figure 2.21 – Measured surface impedance before correction of the gap error: (a) directly extracted from the measured scattering parameters of Fig. 2.20; (b) equivalent series circuit model extraction.

(to completely fill a WR28 waveguide section), thickness $L_{glass} = 525 \pm 50 \mu\text{m}$ and permittivity $\epsilon_{glass} = 3.8 \pm 0.15$. Then, each chip was pasted on a foam substrate of same transverse dimensions, of thickness $L_{foam} = 1000 \pm 50 \mu\text{m}$ and permittivity $\epsilon_{foam} = 1.05 \pm 0.05$. The measurements setup was completed by placing the foam-glass-membrane sample within a 3 mm RWG section. Then, the RWG holder was connected to an Agilent E8361A PNA and a TRL calibration was performed. The TRL calibration allowed to place the measurement reference planes at the edges of the 3 mm RWG holder, as depicted in Fig. 2.10. Therefore, the general model of Fig. 2.9 was used for the extraction of the shunt impedance from measured scattering parameters. The approach discussed in §2.2.1 was applied and the surface impedance of the conductive membrane under test given by eq. (2.15c).

Measured scattering parameters for the considered samples of Tab. 2.1 are shown in Fig. 2.20. It is worth observing that a strong reflection (S_{11}) is available for all samples, mainly due to the conductive layer. Moreover, measured S-parameters exhibit the same trend. Thereby, as expected, neither the thickness nor the pre-stretching of the PDMS membrane affect the electromagnetic response of the test fixture. In turn, this can be also confirmed by looking at the extracted impedance for each sample.

The measured surface impedance $Z_S = R_S + jX_S$, given by eq. (2.15c), is shown in Fig. 2.21a. R_S is almost constant in the considered frequency range, whereas X_S is in the range $(-100, -50) \Omega/\square$. The imaginary part of the extracted impedance is accurately modeled by an equivalent series $L_S - C_S$ circuit, where the inductive component L_S is almost negligible (cf. §2.2.1). This series capacitance corresponds to the air gap δy between the conductive sheet and the horizontal metallic wall of the holder RWG (Fig. 2.13). This effect was studied with HFSS full-wave simulations. More specifically, a realistic measurement setup with different pure resistive layers was simulated and a parametric analysis was performed varying δy in the simulator geometry. Simulated results showed that increasing δy , the extracted equivalent R_S increases, whereas X_S decreases (negative values). Extraction examples for four assigned values of R_S are shown in Fig. 2.22. The surface impedance initially assigned in the simulator was purely real ($Z_S = R_S$), but an imaginary part different from zero was extracted for $\delta y \neq 0$. X_S is exactly fitted by a series C_S circuit, which reduced with increasing δy ($C_S \rightarrow \infty$ if $\delta y = 0$).

The extracted imaginary parts from available measurements exhibit the same capacitive behavior as retrieved from simulated data, when δy is in the range 80–160 μm (Fig. 2.22). These values of gap are realistic for the presented measurements. In fact, a minimum gap of 100 μm was present in our setup, since fused silica chips were cut 100 μm smaller than actual waveguide dimensions to take into account any size tolerance in the RWG holder. Moreover, an additional gap can be due to an imperfect manual cut of membranes after the bonding on the respective silica substrates (previously cut). Extracted *equivalent* impedances ($R - C$ series circuit model) $Z'_S = R'_S + jX'_S$ for the measurements of Fig. 2.20 are shown in Fig. 2.21b.

Therefore we can safely assume that the unknown impedance is purely resistive, while the extracted reactance is due to the gap δy , and thus a predictable effect that can be corrected.

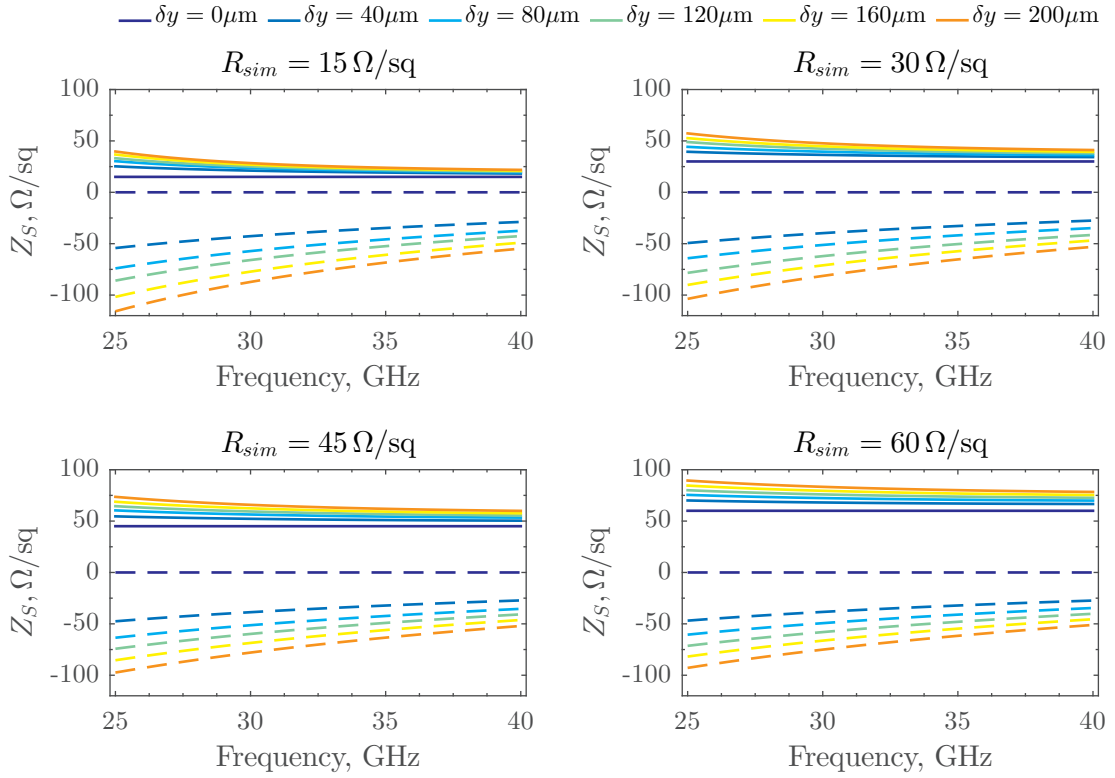


Figure 2.22 – Surface impedance Z_S extracted from simulated S-parameters when a gap between the conductive membrane and the horizontal RWG wall is introduced in the simulator. The effect of a gap δy is shown for different resistive sheets. R_S and X_S are illustrated in solid and dashed lines, respectively.

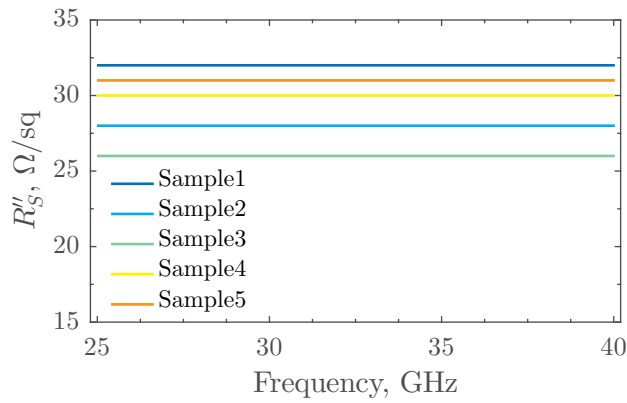


Figure 2.23 – Extracted surface resistance R''_S after correction of the gap error for the measurements of Fig. 2.20. A post-processing procedure based on simulation and least squares minimization is adopted to estimate δy and correct for the related error.

For this purpose, a post-processing procedure, based on full-wave simulations and least squares minimization has been implemented and applied to the extracted curves of Fig. 2.21b. A parametric simulation, function of δy ($0 \leq \delta y \leq 180 \mu\text{m}$) and R_S ($1 \leq R_S \leq 100 \Omega$), was performed with HFSS and all values of R_S , C_S and L_S (series circuit model), extracted from simulated S-parameters, were saved in a proper lookup table (LUT). Then, the actual values of R_S were obtained minimizing in a least squares approach the error between circuitual parameters extracted from measurements and the ones previously saved in the LUT. In this way, we were able to eliminate the gap-dependence of the extracted values of Fig. 2.21b, by reducing to zero the imaginary part X'_S and correcting the real part R'_S . Fig. 2.23 shows the actual membranes surface resistance R''_S after correction of the gap error. The final results for the analyzed samples are summarized in Tab. 2.2.

Table 2.2 – Surface resistance R''_S and estimated gap δy after the correction of the gap error.

<i>Sample</i>	$R''_S, \Omega/\square$	$\delta y, \mu\text{m}$
Sample1	32	140
Sample2	28	160
Sample3	26	140
Sample4	30	125
Sample5	31	120

2.4 Conclusions

The measurement analysis of the dielectric properties (permittivity and loss tangent) of a commercial polymer (Dow Corning Sylgard 186), often used for the implementation of dielectric elastomer actuators, has been presented. Moreover, the surface impedance of *flexible and stretchable* conductive membranes has been characterized.

The characterization of the microwave/millimeter-wave behavior of bulk PDMS and PDMS-based conductive membranes was necessary for our scopes. In fact, the design and development of any antenna device (e.g., phase shifters and antennas) require an accurate knowledge of the dielectric (i.e., permittivity and loss tangent) and electromagnetic (i.e., surface conductivity) properties of the considered materials. We needed to assess the goodness of these materials for their integration in the design and fabrication of reconfigurable millimeter-wave phase shifters and antennas based on PDMS micro-fabricated actuators.

A measurement technique based on a transmission/reflection approach has been proposed for the dielectric characterization of bulk PDMS, which allows the extraction of its permittivity and loss tangent. It is worth noting that this technique can be generally applied to any dielectric materials that can be inserted into the section of a RWG holder. All measured PDMS samples exhibit a dielectric constant (nearly constant in the frequency range of interest) in the range (2.78, 2.82) with a mean value of 2.79. A slightly bigger variability is visible for the retrieved loss tangent with extracted values between 0.033 and 0.045 and a mean

value of 0.038. The extracted values of permittivity and loss tangent are in agreement with the results presented in [8] for the Dow Corning Sylgard 184, which slightly differs from the Sylgard 186 for its mechanical properties. These results demonstrate that bulk PDMS substrates exhibit high losses at Ka-band and above, if compared to conventional substrates used for millimeter-wave antenna applications, such as commercial Rogers substrates ($\tan \delta \sim 10^{-3}$) or fused silica ($\tan \delta \sim 10^{-4}$). Thus, we can conclude that thick PDMS substrates should be avoided in the design of millimeter-wave devices, and volume micromachining techniques or membrane-based concepts should be investigated to reduce losses (e.g., [20]). However, PDMS micro-actuators are of great interest for our scopes, since they can allow to completely or partially decouple the DEA actuation from the electromagnetic (EM) active area, that is, where the EM field is stronger. This means that PDMS micro-actuators are to be isolated from the EM-active area, to reduce the interaction between the material and the electric field.

The surface impedance of flexible and stretchable PDMS-based conductive membrane (i.e., PDMS membranes implanted with gold ions and commercial PDMS corrugated films with thin silver layer deposition) has been also characterized using a non-contact measurement technique based on 2-port RWG measurements. The tested samples exhibit comparable values of surface resistance, highlighting similar performance in terms of loss and RF behaviour for the two different considered metallizations. Moreover, the prestretching of the PDMS membrane does not affect the surface impedance of the implanted layer. All analyzed samples show a considerable surface resistance (around $\sim 30 \Omega/\square$) if compared to conventional conductors, which are commonly used for the fabrication of MMW devices. Full-wave simulations demonstrated that a 50Ω microstrip realized with such a conductor, would present a loss factor of 2.4 dB/mm, while a simple printed dipole antenna on a PDMS substrate would show a radiation efficiency of only 2.3 %. These values are not acceptable in most practical applications, but the stretchable metallizations might still be used for the fabrication of small parts (e.g., flexible joints) or when antenna efficiency is not a critical parameter (for instance in interference-limited reception).

Bibliography

- [1] A. M. Nicolson and G. F. Ross, "Measurement of the intrinsic properties of materials by time-domain techniques," *IEEE Transactions on Instrumentation and Measurement*, vol. 19, no. 4, pp. 377–382, 1970.
- [2] W. B. Weir, "Automatic measurement of complex dielectric constant and permeability at microwave frequencies," *Proceedings of the IEEE*, vol. 62, no. 1, pp. 33–36, 1974.
- [3] L. F. Chen, C. K. Ong, C. P. Neo, V. V. Varadan, and V. K. Varadan, *Microwave Electronics: Measurements and Materials Characterization*. John Wiley & Sons, 2004.
- [4] D. M. Pozar, *Microwave Engineering*, 4th ed. Wiley, 2011.
- [5] J. Baker-Jarvis, E. J. Vanzura, and W. A. Kissick, "Improved technique for determining complex permittivity with the transmission/reflection method," *IEEE Transactions on Microwave Theory and Techniques*, vol. 38, no. 8, pp. 1096–1103, 1990.
- [6] A. H. Boughriet, C. Legrand, and A. Chapoton, "Noniterative stable transmission/reflection method for low-loss material complex permittivity determination," *IEEE Transactions on Microwave Theory and Techniques*, vol. 45, no. 1, pp. 52–57, 1997.
- [7] M. Driss Belrhiti, S. Bri, A. Nakheli, M. Haddad, and A. Mamouni, "Complex permittivity measurement for dielectric materials at microwave frequencies using rectangular waveguide," *European Journal of Scientific Research*, vol. 49, no. 2, pp. 234–248, 2011.
- [8] N. Tiercelin, P. Coquet, R. Sauleau, V. Senez, and H. Fujita, "Polydimethylsiloxane membranes for millimeter-wave planar ultra flexible antennas," *Journal of Micromechanics and Microengineering*, vol. 16, no. 11, p. 2389, 2006.
- [9] S. Rosset and H. Shea, "Flexible and stretchable electrodes for dielectric elastomer actuators," *Applied Physics A*, vol. 110, no. 2, pp. 281–307, 2013.
- [10] Q. Liu, K. L. Ford, R. Langley, A. Robinson, and S. Lacour, "Flexible dipole and monopole antennas," in *Proceedings of the 5th European Conference on Antennas and Propagation (EuCAP)*, April 2011, pp. 2052–2056.
- [11] S. Hage-Ali, Y. Orlic, N. Tiercelin, R. Sauleau, P. Pernod, V. Preobrazhensky, and P. Coquet, "A millimeter-wave elastomeric microstrip phase shifter," in *IEEE/MTT-S International Microwave Symposium Digest*, 2012, pp. 1–3.
- [12] P. J. Baker, R. J. Ormeno, C. E. Gough, Y. Matsushita, and I. R. Fisher, "Microwave surface impedance measurements of $Tl_xPb_{1-x}Te$: A proposed negative-U induced superconductor," *Phys. Rev. B*, vol. 81, p. 064506, 2010.
- [13] J. S. Gomez-Diaz, J. Perruisseau-Carrier, P. Sharma, and A. Ionescu, "Non-contact characterization of graphene surface impedance at micro and millimeter waves," *Journal of Applied Physics*, vol. 111, no. 11, p. 114908, 2012.

- [14] S. Rosset, M. Niklaus, P. Dubois, and H. R. Shea, "Metal Ion Implantation for the Fabrication of Stretchable Electrodes on Elastomers," *Advanced Functional Materials*, vol. 19, no. 3, pp. 470–478, 2009.
- [15] M. Benslimane, H.-E. Kiil, and M. J. Tryson, "Electromechanical properties of novel large strain PolyPower film and laminate components for DEAP actuator and sensor applications," in *Proc. SPIE, Electroactive Polymer Actuators and Devices (EAPAD)*, vol. 7642, 2010, p. 764231.
- [16] F. Bouzidi, H. Aubert, D. Bajon, and H. Baudrand, "Equivalent network representation of boundary conditions involving generalized trial quantities-application to lossy transmission lines with finite metallization thickness," *IEEE Transactions on Microwave Theory and Techniques*, vol. 45, no. 6, pp. 869–876, 1997.
- [17] "Dow corning sylgard 186," <http://www.dowcorning.com/>.
- [18] M. Niklaus and H. R. Shea, "Electrical conductivity and Young's modulus of flexible nanocomposites made by metal-ion implantation of polydimethylsiloxane: The relationship between nanostructure and macroscopic properties," *Acta Materialia*, vol. 59, no. 2, pp. 830–840, 2011.
- [19] M. Benslimane, P. Gravesen, and P. Sommer-Larsen, "Mechanical properties of dielectric elastomer actuators with smart metallic compliant electrodes," in *Proc. SPIE, Electroactive Polymer Actuators and Devices (EAPAD)*, vol. 4695, 2002, pp. 150–157.
- [20] S. Hage-Ali, N. Tiercelin, P. Coquet, R. Sauleau, H. Fujita, V. Preobrazhensky, and P. Pernod, "A Millimeter-Wave Microstrip Antenna Array on Ultra-Flexible Micromachined Polydimethylsiloxane (PDMS) Polymer," *IEEE Antennas and Wireless Propagation Letters*, vol. 8, pp. 1306–1309, 2009.

3 Reconfigurable phase shifters based on DEAs

This chapter presents the analysis, design, and implementation of mechanically reconfigurable millimeter-waves (MMW) phase shifters using dielectric elastomer actuators (DEAs). As we have discussed in the introduction, DEAs are promising candidates for the realization of mechanically tunable phase shifters and antenna devices at microwaves and millimeter-waves due to their appealing properties, and are expected to provide good results in terms of cost, insertion losses, power handling and linearity. The main properties, relevant for our scopes, can be summarized as follows [1–8]:

- Cost reduction: DEAs and devices can be fabricated in a simple and inexpensive process, without any need for advanced cleanroom activities (e.g., in contrast to RF MEMS).
- High power-to-volume ratios: smaller size actuators for most reconfigurable antenna applications compared to other mechanical reconfigurable approaches.
- Large and *analogue* mechanical displacement: availability of a significant continuous tuning range and low control complexity without the need for quantization.
- Very good linearity: the tunability is related to mechanical systems with a very low resonance frequency, and performance similar to MEMS devices are expected (e.g., [9]).
- Extremely low power consumption: driving currents are very low (in the order of μA) and the device is electrostatic in nature. Note that no power is consumed to maintain the elastomer in a stable state.

The major drawback of this technology is represented by the high voltage (in the order of kV) required for the actuation, which can be however safely obtained using driving circuit fitting in less than 1 cm^3 , as demonstrated by available commercial devices (Optotune and ViviTouchTM). Discharge is prevented by embedding the electrodes inside the polymer itself. This high actuation voltage is considered an acceptable drawback, given the above advantages in terms of functionality, as well as the expected reliability of the devices and their very low DC power consumption.

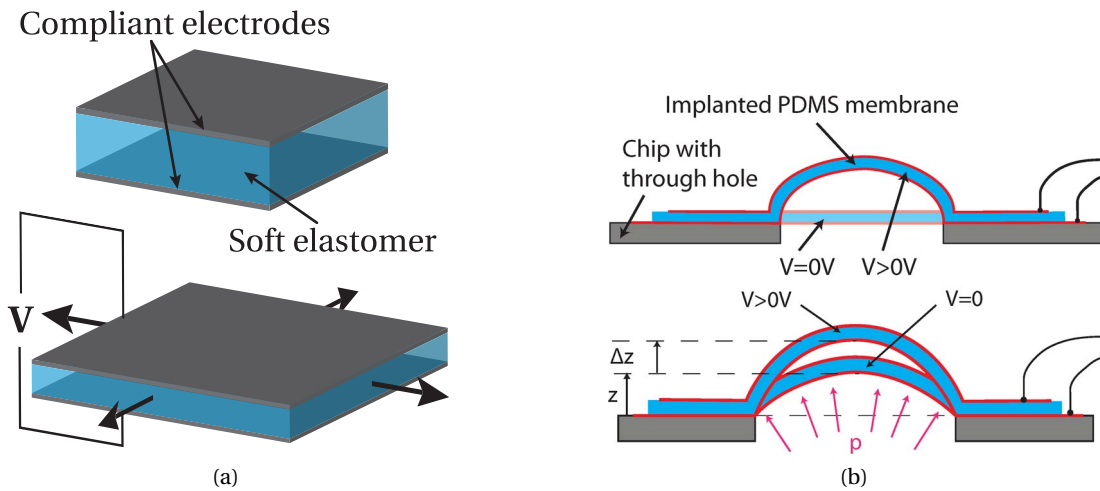


Figure 3.1 – Basic actuation principles of DEAs. (a) Generic illustration of in-plane actuation. When a voltage is applied to the compliant electrodes, the electrostatic pressure squeezes the elastomer, which contracts in thickness and expands in area. (b) Example of out-of-plane actuation implemented by a buckling-mode DEA. The membrane is initially flat, and it buckles when an external voltage is applied due to the particular geometry. The membrane is in fact clamped at its borders, preventing the in-plane area expansion. Reproduced from [5].

Dielectric elastomer actuators have been widely investigated in the last decades and many research activities are currently focused on the technological development of robust and high-performance DEAs. Different practical applications have been identified, including artificial muscles, optics and energy harvesting (cf. §1.2). However their use in the development of RF devices has not been widely investigated so far. Only basic antenna concepts, based on DEA reconfiguration, have been proved at L-band (1–2 GHz) [10, 11], but with poor performance for high complexity when compared with existing solutions. Moreover, elastomeric membranes have been used as a soft substrate for RF devices at millimeter-waves without any type of electroactive actuation [12–15].

The main objective here is the design of a reconfigurable true-time delay (TTD) phase shifter that can be mechanically tuned using DEA micro-actuators. TTD phase shifters are basic building block in many array antenna systems and are specifically required in wideband beam-squint-free scanning arrays, since they are able to provide phase shift linearly proportional to the operating frequency. The basic idea to implement the desired reconfiguration is to affect the propagation constant of a transmission line (TL) section, thereby providing true-time delay. Using micro-actuators, this can be done by changing the geometry of the device, in order to modify the effective permittivity of the equivalent TL.

Different phase shifter concepts have been under study and their preliminary performance have been assessed. Both in-plane [1, 16–18] and out-of-plane [7, 16, 19] dielectric elastomer actuators (Fig. 3.1) have been considered to implement the reconfigurable parts of the envisaged concepts. It is worth noting that the design of only one concept has been further

3.1. Existing technologies for phase shifter reconfiguration

optimized, fabricated and tested. The selected candidate exhibits the best trade-off in terms of performance and low-cost/low-complexity fabrication process, and can be easily prototyped (to speed up the testing phase) using standard manufacturing techniques and in-house available technology. The development and manufacturing of the dielectric elastomer actuators used for the implementation of the proposed device was carried out at the *Microsystems for Space Technologies Laboratory (LMTS)* at EPFL.

In order to understand the framework and to better compare the proposed reconfiguration concept with available technologies, a brief review of the state-of-the-art of MMW reconfigurable phase shifters is proposed in §3.1. All the phase shifter concepts analyzed during this study are then summarized in §3.2. This section includes a preliminary performance evaluation, a discussion about their potentials and some considerations about possible issues in their practical implementation. In §3.3 it is reported the design, manufacturing and experimental characterization of the first reconfigurable phase shifter prototype driven by dielectric elastomer actuators. A summary of the chapter, with a general comparison of the achieved phase shift performance with relevant devices from the literature is addressed in §3.4.

3.1 Existing technologies for phase shifter reconfiguration

The aim of this section is to review the main available technologies for the realization of reconfigurable millimeter-wave phase shifters, which find increasing request for instance in space-related applications. Particular attention is addressed to Ka-band (26.5–40 GHz), where great efforts are made by the European Space Agency and the industrial community for the development of new technologies for telecommunication and Earth Observation purposes. More specifically, monolithic microwave integrated circuit (MMIC), ferrite and RF-MEMS phase shifters are discussed and some available devices are presented. Moreover, a qualitative comparison between available technologies and the expected performance of DEA-based phased shifters is proposed.

3.1.1 MMIC

Phase shifters based on Monolithic Microwave Integrated Circuit (MMIC) are widely used in space application for their small size and low power consumption compared to ferrite devices. Moreover, they offer high integration with the surrounding electronics simplifying the fabrication and packaging process. They are mainly realized in GaAs FET technology (e.g., [20–23]), but devices based on SiGe (e.g., [24–26]) and InP (e.g., [27–29]) technologies have achieved good progress during the past two decades. Three types of tunable phase shifters based on MMIC can be considered:

Switched line phase shifters: use switches to direct electrical signals through transmission lines with different path length. Therefore, the achievable phase shift between different states of reconfiguration only depends on the difference between the length of the

switched lines. When the signal is switched between two lines of length L_1 and L_2 , the differential phase shift is expressed by the following relation:

$$\Delta\varphi = \beta(L_2 - L_1), \quad (3.1)$$

where β is the propagation constant of the transmission line (assuming both TLs have the same propagating properties). Phase shifters based on this principle provide a true-time-delay, meaning that the phase response is proportional to the operating frequency (the time delay is constant). FET switches or PIN diodes are generally used to toggle between different transmission lines.

One of the first switched line phase shifters developed for spaceborne phased array antennas (project supported by NASA Lewis Research Center) was proposed by Bauhahn et al. [30] in 1985. The 4/5-bit GaAs monolithic phase shifter presented in [30] was based on FET switches. The three main phase shifter bits (i.e., 45°, 90° and 180°) were implemented using switched microstrip lines, whereas a loaded transmission line approach was adopted for the remaining bits 11° and 22.5°. Experimental results demonstrated a total insertion loss lower than 10 dB over a 10 % bandwidth around the design frequency of 30 GHz. The chip size was approximately $5.5 \times 2.5 \times 0.15 \text{ mm}^3$.

More recently Maruhashi et al. [31] proposed a Ka-band monolithic phase shifter based on non-resonant FET switches, which allowed to reduce the effect of parasitic resonant elements on the phase shift performance. This phase shifter consisted of four bits (22.5°, 180°, 90° and 45°) connected in series and resulting in a chip size of around $2.5 \times 2.2 \times 0.04 \text{ mm}^3$. Phase shift performance highlighted an insertion loss lower than 14 dB in the range 32.5–35.5 GHz.

Loaded line phase shifters: generally used for achieving a phase shift lower than 90° (typically 22.5° or 45° shift bits) [32]. Conventional loaded line phase shifters consist of a transmission line section loaded by two two-states shunt admittance that can be connected or disconnected from the TL using solid states switches (generally PIN diodes). These devices generally come with low insertion losses (can be minimized with a proper design and selection of the loads) and can be actuated using only one control signal, since the loads can be biased simultaneously. For purely reactive loading elements (i.e., zero-loss), a capacitive load increases the effective length of the transmission line (the phase velocity decreases), whereas an inductive load reduces the TL length (higher phase velocity). Thus, switching from an inductive to a capacitive load, the electrical length of the device increases with a corresponding increase of the phase shift. The choice of the transmission line length is not arbitrary, but strictly depends on the adopted switching and loading elements. In the general case where loading losses are considered, a quarter-wavelength separation between the loads allows to minimize and equalize the amplitude perturbation (insertion loss minimization) in both states [32]. In contrast to switched line phase shifters, loaded line devices provide narrow-band

3.1. Existing technologies for phase shifter reconfiguration

operation with a constant phase over the frequency range.

High-pass/Low-pass phase shifters: switch the electrical signal between two circuits that have opposite phase characteristics [33]. Typically the two circuits are high-pass and low-pass filters: a low-pass filter realized by series inductors and shunt capacitors provides phase delay, while high-pass filter composed of series capacitors and shunt inductors provides phase advance. By properly arranging switch elements (PIN diodes or FET switches) to permit switching between low-pass and high-pass sections, it is possible to realize a compact phase shifter with wide-band performance. A commercial example of high-pass low-pass phase shifter at Ka-band is the TriQuint TGP2104 [34]. Series FET switches are used to toggle between the low-pass network and the high-pass network, which are both implemented by T-networks. This design utilizes a compact topology that results in 0.69 mm die area and high performance. The TGP2104 provides a 180° digital phase shift function with a nominal 3.5 dB insertion loss and maximum 15° phase shift error over a 10 GHz bandwidth centered on 30 GHz.

Another example of high-pass low-pass phase shifter can be found in the work presented by Yang and Yang [23], who proposed a 5-bit phase shifter operating at Ka-band between 26 GHz and 30 GHz. The phase shifter presented in [23] consists of five phase bits (180°, 11.25°, 22.5°, 45° and 90°) which are cascaded in series to simplify the impedance matching. The 180° phase bit was implemented by a π -type high-pass low-pass network, whereas the 22.5°, 45° and 90° was based on a T-type circuit. The switching operation was guaranteed by InGaAs PIN diodes. With the proposed design, insertion losses lower than 7.8 dB and return losses higher than 9 dB were achieved.

High-pass low-pass phase shifters are widely used whenever a constant phase shift is desired over a wide frequency range. Moreover, they offer a very compact layout because lumped elements are typically preferred to delay lines (generally bulky, especially at lower frequencies).

MMIC phase shifters are widely used in phased array antennas, due to their very small sizes (<2 mm at Ka-band) and their very good performance in terms of reliability and switching speed (in the order of nanosecond). Nevertheless, their performance in terms of radiation tolerance can be unacceptable because of the presence of solid state junctions. Moreover, their power handling capabilities are limited (in the order of tens of watt) for high power applications (e.g., SAR phased array antenna) and can exhibit high insertion loss (sometimes more than 2 dB/bit).

3.1.2 Ferrite

Ferrite phase shifters are widely used in military phased array antennas, due to their high power handling capabilities (peak power in the order of kW). They can be generally implemented in both closed (e.g., waveguides) or open (e.g., planar transmission lines) structures. Their operating principle is based on the property of non-linear dependence between the

magnetization B and the magnetic field H in ferromagnetic materials. When the ferrite is magnetized, an external magnetic field interacts with the spinning electrons in the ferrite affecting the material permeability. Therefore, when the magnitude or direction of the applied magnetic field is varied, the permeability of the ferrite changes resulting in a modified propagation constant of the specific transmission line. Thus, a variable phase shift is achieved by electronically controlling the applied magnetic field. The ferrite permeability can be tuned by changing the magnetic moment M , which increases with the magnetic bias field; the upper limit, denoted by M_s , is called the saturation magnetization and is an intrinsic property of the material. In particular, the choice of the specific ferrite and of the device geometry has to be properly selected in order to reduce losses and to guarantee correct operation in the frequency range of interest. Conductive and dielectric losses of the device, in fact, are directly proportional to its length or inversely proportional to M_s , while the magnetic loss is with good approximation directly proportional to the saturation magnetization. The full contribution of these losses (dielectric and magnetic) can be minimized selecting the material that satisfy the following relation [35]:

$$0.2 < \frac{f_m}{f} < 0.6, \quad (3.2)$$

where $f_m = \gamma 4\pi M_s$ and γ is the gyromagnetic ratio. Thereby, the choice of ferrite for a particular application is determined by selecting the operating frequency sufficiently higher than f_m .

Ferrite phase shifters can be classified in reciprocal or non-reciprocal devices. As the name suggests, the former generate a phase shift independent from the direction of propagation (as typically happens for MMIC and MEMS devices), whereas the latter differently affect opposite traveling waves. A further classification considers latching and non-latching devices, depending on the type of the applied magnetic biasing field. Three main techniques to implement ferrite phase shifters can be considered [35]:

- twin toroid devices are latching and non-reciprocal;
- dual-mode devices are latching and reciprocal;
- rotary-field devices are non-latching and reciprocal.

Theoretical models for the non-reciprocal twin toroid phase shifters were discussed by Schlo-mann [36] and Ince and Stern [37], while many other works can be found in literature. An experimental example of twin toroid phase shifter was presented by Abuelma'atti et al. [38]. The proposed phase shifter consisted of a rectangular waveguide loaded by a double toroid separated by a high permittivity dielectric. The dielectric spacer is used for matching purposes and to concentrate the RF energy in the center of the waveguide, while the walls of the toroids

3.1. Existing technologies for phase shifter reconfiguration

(those contacting the dielectric spacer) are located in the regions where the waveguide supports a circularly polarized magnetic field. Typically a current of a few ampere in a single turn coil winding can drive the ferrite into saturation. If β_+ is the propagation constant corresponding to a positive saturation and β_- is the same for negative one, the maximum achievable phase shifting is proportional to $(\beta_+ - \beta_-)$. Intermediate phase shifts are obtained reducing the bias field level. The device was optimized to operate around 10 GHz where demonstrated very low insertion loss (<1 dB) and very good return loss (>20 dB). Twin toroid phase shifters generally allow to achieve low-loss performance over a wide frequency range (up to an octave) if a given design is properly optimized. A commercial toroidal ferrite phase shifter is supplied by *Com Dev Europe Ltd* [39] and exhibits high power handling capability (peak power >1.5 kW) and low insertion loss (<1 dB) at Ka-band. The basic phase shifter consists of a 2-port rectangular waveguide, with a toroidal ferrite resonator located inside. The driving circuit is based on a single or multi coil wire wrapped around the ferrite, which induces a magnetic flux inside it when a current pulse is applied. Thus, the variable interaction between the MMW signal and the ferrite toroid generate the desired phase shift. Phase shift values in the range $-180-180^\circ$ can be achieved by varying the current pulse value. The magnitude and timing of the current is carefully controlled by sophisticated drive electronics in order to keep constant operating conditions over a wide temperature range.

Dual-mode and rotary-field phase shifters are typically used when both the transmitting and receiving chain require the same phase shift. An example of dual-mode device was presented by Boyd [40]. This phase shifter consisted of a metallized ferrite rod implementing a ferrite-filled waveguide. The principle of operation was based on the variable interaction between the partially magnetized ferrite rod and the RF field, that is a circular polarized wave with a rotating transverse magnetic field. The tunable phase shift was obtained by varying the controllable axial biasing field. Note that the phase shifter was fed by a linearly polarized field, but two non-reciprocal, quadrupole-field ferrite polarizers were placed at the input and output port to generate the conversion between the feeding input/output linear field and the circularly polarized field circulating inside the active area (i.e. where the phase shift is generated) of the device. Reciprocity was guaranteed by the two polarizers, which transform linearly polarized waves traveling in opposite directions to circularly polarized waves with opposite sense of rotation. Thus, the interaction between the RF field and the ferrite-filled section is the same for both received and transmitted wave.

Rotary-field phase shifters employ Faraday rotation to produce time delay in microwave signals. The first rotary-field device proposed by Reggia and Spencer [41] was made of a ferrite toroid placed in the longitudinal section of a rectangular waveguide. The magnetic biasing field was produced by an external magnetization circuit. The working principle of this device was based on the particular property of ferromagnetic rods to rotate the plane of polarization of a linearly polarized wave propagating in them. Therefore, if the rod is placed inside a rectangular waveguide with one of its dimension at cutoff, then the rotational effect is suppressed. This type of operation also allows to achieve the same phase shift independently from the direction of propagation (i.e., reciprocal device). Rotary-field phase shifters are

mainly used up to 20 GHz. Their realization at higher frequencies is far from being trivial, since they require a large transverse quadrupole field across the ferrite rod whose diameter decreases proportionally to the operating frequency. On the other side latching phase shifters (twin-toroid and dual-mode) have been realized for millimeter-wave applications (up to W-band), but insertion losses can become unacceptable above 60 GHz.

Ferrite phase shifters have low insertion loss and can handle significantly higher power. Nevertheless, their cost and complexity represent still a problem for many applications, and DC power consumption is higher than MMIC and MEMS devices. Semiconductor phase shifters using PIN diodes and FETs are less expensive and smaller than ferrites but their application is limited because of the high insertion loss at high frequencies and limited power handling capability.

3.1.3 MEMS

RF-MEMS phase shifters are based on standard designs (i.e., switched line, loaded line, high-pass/low-pass and reflect-line) where the PIN or FET switches are replaced by MEMS devices. This approach allows to reduce insertion losses with respect to their MMIC counterparts (up to 4 dB improvement at Ka-band) [42]. MEMS-based phase shifter are often preferred to other technologies for their light-weight, small sizes, low insertion loss, high linearity and low power consumption [43].

RF MEMS phase shifters were developed during the nineties thanks to the pioneering work of a few academic research groups (e.g. *University of Michigan*, Ann Arbor, MI with the outstanding work of Prof. Rebeiz and colleagues) and companies (e.g. *Raytheon Systems Company*, Dallas, TX and *Rockwell Science*, Thousand Oaks, CA). The first rotating type RF-MEMS switch and metal contact cantilever beam switch for microwave applications were presented for the first time by Larson et al. [44, 45]. The first MEMS-based phase shifter then arrived in 1999 [46]. This 4-bit reflection phase shifter was developed at *Raytheon Systems Company* and demonstrated good phases shift performance with an average insertion loss of 1.4 dB at 8 GHz.

Since then, RF-MEMS switches, switched capacitors and varactors could be used to replace PIN diodes and FETs in the design of loaded-line, reflect-line, high-pass/low-pass and switched-line phase shifters. Typical MEMS switches use mechanical movement to achieve a short circuit or an open circuit in the RF transmission line. They are usually realized by a metal bridge or cantilever suspended several microns above a microwave transmission line, which is actuated using an electrostatic bias. Two types of MEMS switches can be considered [47]: capacitive and contact switches. The former are generally used in a shunt configuration and employ a thin dielectric insulator (e.g., Si_3N_4) on the lower contact to avoid DC contact and stiction between the bridge and the bottom transmission line. When the metal bridge is in the up state, a very small capacitance affects the signal propagation, whereas, the actuation of the bridge generate a very large capacitance (an effective short circuit at high frequencies), which reflects the electrical signal. Thus, capacitive MEMS switches are more efficient at higher

3.1. Existing technologies for phase shifter reconfiguration

frequency. Metal-to-metal contact switches, in turn, are often fabricated as series devices that generate an open circuit in the transmission line when the switch is up, while a metal contact closes the circuit when the switch is actuated. Nevertheless, they are not effective at millimeter-wave frequency, because of the high insertion losses caused by resistive metal contacts. A considerable advantage of RF MEMS switches is that their switching performance do not depend on the characteristics of the substrate. Thereby, they can be fabricated on any material that is compatible with standard IC processing, and can be directly integrated with the transmission line bringing potential cost reduction in the fabrication of complex phased array antenna systems.

Distributed MEMS transmission lines (DMTL) offer an alternative approach to the standard reflect-line or switched-line designs. They have been widely investigated by Barker [48] and Barker and Rebeiz [49, 50] for the realization of millimeter-wave devices. The basic working principle of DMTL is to periodically load a transmission line with shunt MEMS capacitors; with this approach, the distributed capacitance of the line (and thus the propagation constant) can be varied. DMTL can be based either on analogical or digital designs. In the first case all MEMS capacitance are actuated by a single bias voltage and they operate similarly to analog varactors. However, the capacitance variation of electrostatic parallel-plate actuators is only 1.5 (theoretical) and 1.3 (practical), thereby resulting in relatively long phase shifters [42]. In general, digital DMTL are preferred, since discrete RF-MEMS switches are employed to load the TL, thereby allowing much larger loading capacitance.

Several MEMS-based switches and phase shifters have been developed for Ka-band applications over the past decades, and a few relevant examples are reported in this section. A Ka-band 4-bit switched line MEMS phase shifter was developed by *Raytheon Systems* [51] using MEMS capacitively coupled shunt switches fabricated on a $150\ \mu\text{m}$ high-resistivity silicon substrate. A variable insertion phase between 0° and 337.5° (22.5° step) was achieved with an average insertion loss of 2.25 dB and a return loss better than 15 dB for all the states at 34 GHz. *Rockwell Scientific* proposed a Ka-band 3-bit true-time-delay (TTD) switched-line network using metal-to-metal contact MEMS switches [52]. The 3-bit phase shifter (around $3.5\ \text{mm} \times 2.6\ \text{mm}$ in size) was fabricated on a $75\ \mu\text{m}$ GaAs substrate and consisted of a network of microstrip transmission lines connected by six SPDT tee junctions, each implemented by two MEMS switches. Therefore, for each reconfiguration state, the RF signal propagates through six switches, which contribute to impedance matching and insertion loss. Experimental results demonstrated an average insertion loss of 2.2 dB and a return loss higher than 15 dB at the design frequency of 35 GHz.

More recently also other MEMS switched-line phase shifters have been proposed (e.g., [53, 54]), showing performance comparable to the devices mentioned above. Moreover, also different DMTL-based phase shifter can be found in literature. An interesting example is for instance discussed in [55]. Authors presented a 2-bit Ka-band distributed phase shifter fabricated on a quartz substrate using coplanar waveguide (CPW) lines and RF MEMS metal-air-metal capacitive switches. The phase shifter consists of two sections (90° and 180° bits) with inde-

pendent biasing network and a total of 21 capacitive MEMS. In particular, the first 7 switches constitute the 90° while the 180° phase bit (double length) is composed of the remaining 14 switching elements. The measured average insertion loss was 1.5 dB and the return loss better than 11 dB (each section was designed for a maximum return loss of 15 dB) at 37.7 GHz for the maximum differential phase shift of 270° . Furthermore, low insertion loss was demonstrated in [56], where a 1-bit and a 4-bit DMTL phase shifters fabricated on a $500\ \mu\text{m}$ quartz wafer were presented. The multi-bit device (45° , 90° , 180° and 225°) included a total of 10 cascaded unit cells arranged in 5 unit cell pairs. The 4-bit phase shifter exhibited an insertion loss better than 1.4 dB and a return loss higher than 21 dB.

MEMS phase shifter have achieved a significant improvement with desirable performance for the realization of phased array antennas at millimeter-waves. The very low-loss operation of MEMS switches represent an important advantage compared to their solid-state counterparts. Moreover, they are based on electrostatic actuation bringing to a low DC power consumption, and offer a very good linearity resulting in very low intermodulation products. MEMS switches are also compatible with standard integrated circuit fabrication process, which allows high integration and compactness of the final antenna system with potential cost reduction. Nevertheless, it is still worth mentioning a few drawbacks characterizing this technology. MEMS switches are in fact typically slower (actuation speed in the order of $10\text{--}40\ \mu\text{s}$) than MMIC, since they are based on the movement of mechanical structures. However, this actuation speed is not particularly critical for many applications if we are not considering very high data rate communication systems. A more critical aspect is related to the high packaging costs, considering that MEMS switches typically need hermetic or near-hermetic seals to keep a controlled atmosphere. Therefore, although MEMS switches offer the potential for low-cost fabrication and monolithic integration, the need for a proper packaging techniques consistently affect the overall manufacturing costs. Furthermore, reliability often represents a concern, especially for very critical applications including spaceborne systems.

3.1.4 Technology comparison

The objective of this section is to draw a final comparison between the main technologies conventionally used for phase shifter reconfiguration and with respect to the expected performance achievable using DEA-based mechanical reconfiguration. Monolithic microwave integrated circuit (MMIC), ferrite and MEMS phase shifters have been discussed and some available devices presented. MMIC perform well with very good performance in terms of reliability and switching speed; moreover, they exhibit low DC power consumption, and power handling in the Watt range. The main drawback of this technology is related to the high insertion losses of the PIN or FET switches (up to 2 dB/bit). Ferrite phase shifters are the most suitable for high power applications (peak power in the order of kilowatt). Moreover, high performance in terms of reliability and radiation tolerance are achievable, while some limitations have to be considered due to their high cost and high DC power consumption. It is also worth noting that only few devices operating at Ka-band can be found in literature.

3.2. Preliminary design of DEA-based phase shifters

MEMS-based phase shifters are often preferred to other technologies for their light-weight, small sizes, low insertion loss, high linearity and low power consumption. Nevertheless, their use for critical applications (e.g., spaceborne antenna systems) is precluded by reliability issues.

A summary of the technologies discussed in previous sections is presented in Tab. 3.1, in comparison with expected performance of DEA-based devices (note that TRL stands for technology readiness level in the last row). In this framework, dielectric elastomer actuators could be good candidates for the realization of mechanically tunable phase shifters at millimeter-waves, considering the expected good results in terms of cost, losses, power handling and linearity.

Table 3.1 – Summary of available technologies for phase shifter reconfiguration and expected performance of DEA-based devices.

	Technology			
	MMIC	Ferrite	MEMS	DEA
Cost	–	--	+	++
Size	++	–	++	+
Power handling	+ (~ W)	++ (~ kW)	–	–
DC Power cons.	+ (< 10mW)	-- (~ W)	++ (current negligible)	++ (current negligible)
RF loss	–	+	++	++
Switching speed	++ (~ ns)	+ (10–100 μ s, inductance)	+ (1–50 μ s, mechanical)	– (~ ms, mechanical)
Actuation voltage	++	+	+	–
Reliability	++	++	–	+
Linearity	+	+	++	++
Radiation tolerance	–	++	++	TBD
Space compliance	++	++	+	TBD
Fabrication precision	++	++	++	TBD
TRL	++	++	+	–

3.2 Preliminary design of DEA-based phase shifters

Four different devices, based on rectangular waveguide (RWG), coplanar waveguide (CPW) and microstrip transmission lines, have been proposed and studied. These concepts have been designed and their preliminary performance evaluated through HFSS full-wave simulations. Nevertheless, the design of only one concept has been further optimized to be manufactured and tested and will be discussed in §3.3. All the conceived devices consist of a fixed transmission line (i.e., CPW, RWG, microstrip) loaded by a movable element (dielectric or metallic), which perturbs the capacitance and inductance per unit length of the equivalent TL, thus varying the related propagation constant (and so the signal phase).

When TEM or quasi-TEM transmission lines (e.g., microstrip, CPW, parallel plates) are considered, the phase constant can be written as $\beta = \omega\sqrt{\mu_0\epsilon_0}\sqrt{\epsilon_{r,eff}}$. Therefore, a given phase reconfiguration can be achieved modifying the effective relative permittivity $\epsilon_{r,eff}$ of the equivalent TL. In a TEM TL, $\epsilon_{r,eff}$ can be defined as a weighted average of the different materials' permittivity in the TL cross section, and depends on the distribution of the electric field in the involved materials. More specifically, the regions where the electric field is stronger contribute more ("heavier" weight) to the effective permittivity. The above proportional relation between β and the square root of $\epsilon_{r,eff}$ suggests that it is not sufficient to change the device geometry to generate a phase shift if this does not affect the effective permittivity itself (if the permeability μ is assumed constant). Therefore, considering a generic reconfiguration approach able to modify $\epsilon_{r,eff}$, the differential phase shift between two different states of reconfiguration A and B is expressed by:

$$\Delta\phi_{AB} = (\beta_B - \beta_A) L_{PS} = \omega\sqrt{\mu\epsilon_0} \left(\sqrt{\epsilon_{r,eff}^B} - \sqrt{\epsilon_{r,eff}^A} \right) L_{PS}, \quad (3.3)$$

where L_{PS} is the active length of the device, that is the section directly affected by reconfiguration. However, the dynamic control of β (i.e. of the phase) via the mechanical reconfiguration of the TL geometry necessarily comes with a simultaneous variation of the TL characteristic impedance, which will affect the matching of the phase shifter. Therefore, a "minimum mismatch" design approach was applied to the presented concepts. The dimensions of the fixed TL and of the loading parts in the active area were optimized to maximize the phase shift to loss figure while simultaneously minimizing the mismatch. In particular, the optimization process was based on the maximization of the two figures of merit (FoMs) defined as follows:

1. Maximum differential phase shift per unit length:

$$FoM_1 = \frac{\Delta\phi_{max}}{L_{PS}} = \frac{\phi_B - \phi_A}{L_{PS}}. \quad (3.4)$$

2. Maximum differential phase shift per unit length per maximum mismatch:

$$FoM_2 = \frac{\Delta\phi_{max}}{L_{PS} |\Gamma_{max}|}. \quad (3.5)$$

Note that Γ_{max} in eq. (3.5) is the maximum reflection coefficient between the reconfigurable and fixed sections, which is the same for the extreme states of reconfiguration, according to the minimum mismatch approach mentioned above (cf. § 3.3.1). Both $FoMs$ are normalized by the length of the active section L_{PS} , which allows to compare performance of different devices independently from their length ("per unit length"). The length of the reconfigurable section can be subsequently selected according to the phase shift requirement for a given application, since these two quantities are directly proportional (the phase shift is of TTD

3.2. Preliminary design of DEA-based phase shifters

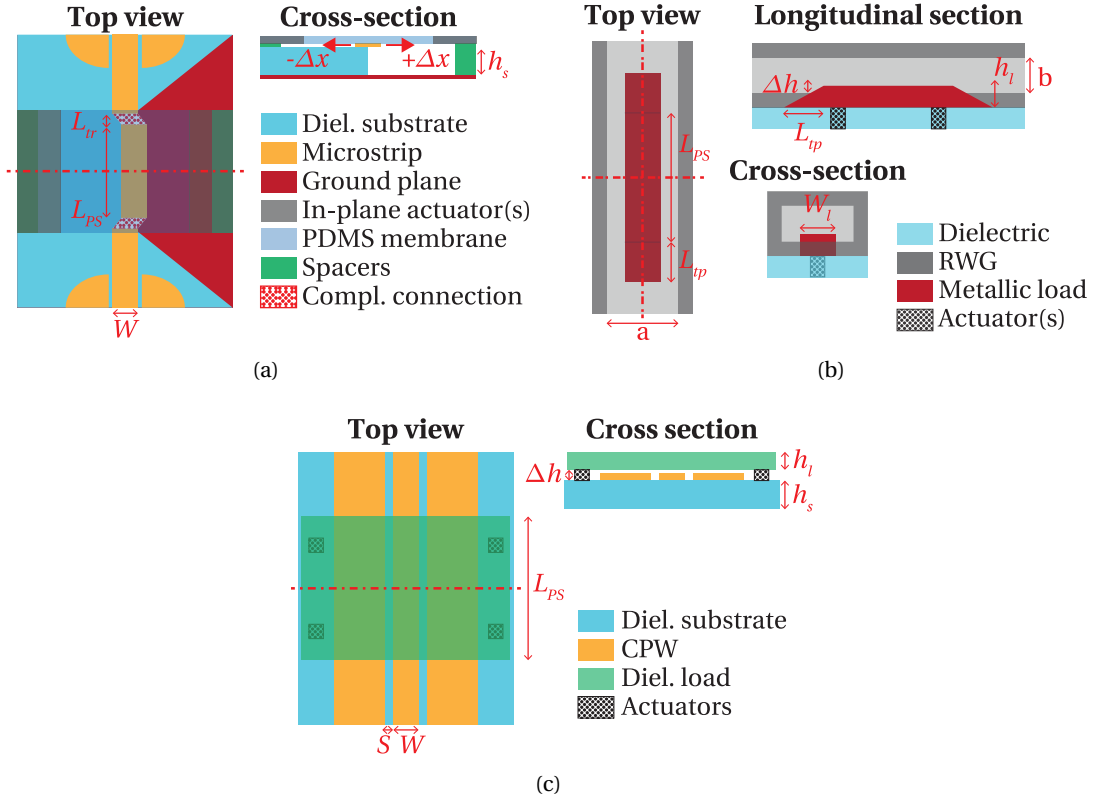


Figure 3.2 – Simplified drawing of the proposed phase shifter concepts. (a) Reconfigurable phase shifter based on a microstrip TL: the central section is displaced in-plane modifying the effective relative permittivity, due to the particular geometry of the dielectric substrate. (b) Rectangular waveguide loaded by a metallic rod that can be displaced in the vertical direction affecting the mode distribution and capacitance per unit length of the equivalent TL. (c) Reconfigurable concept based on a conventional CPW loaded by a movable high-permittivity dielectric, which is vertically displaced by out-of-plane actuators.

nature in the designs presented here). Moreover, all simulated results presented below in terms of propagation constant and differential phase shift were obtained normalizing the simulated scattering parameters to the “optimal” reference impedance Z_{opt} that satisfies the mismatch minimization. Therefore, the choice of FoM_2 is necessary to compare the performance of different devices independently from the variable mismatch between their fixed and reconfigurable sections (more details in §3.3.1).

The reconfigurable phase shifter concept of Fig. 3.2a is based on a microstrip TL (quasi-TEM) and in-plane dielectric elastomer actuation. The horizontal displacement of the central strip induces a change in $\epsilon_{r,eff}$ due to the particular shape of the bottom dielectric. When the strip is moved in the $-\Delta x$ direction, the portion of dielectric below the metal strip increases ($\epsilon_{r,eff}$ increases), while it reduces with a displacement in the $+\Delta x$ direction (the air portion below the strip increases, decreasing $\epsilon_{r,eff}$). This effect is magnified increasing the substrate permittivity,

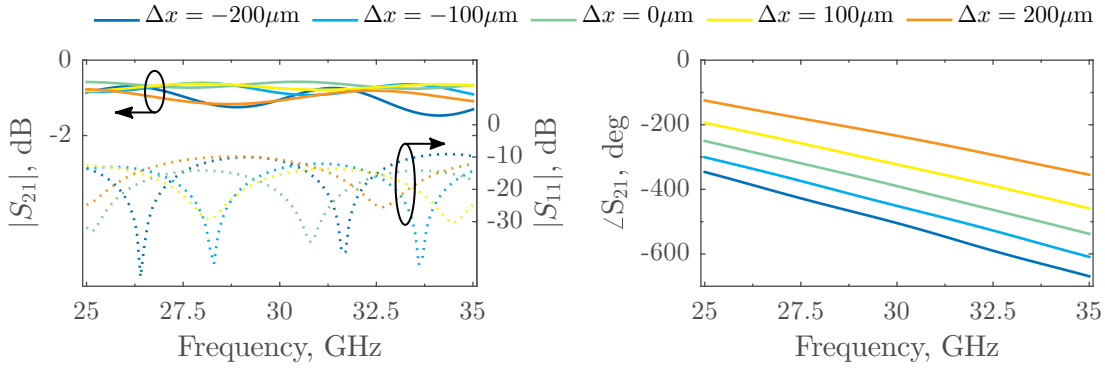


Figure 3.3 – Simulated scattering parameters for different states of reconfiguration of the concept depicted in Fig. 3.2a: $L_{PS} = 10$ mm, $L_{tr} = 200$ μ m, dielectric substrate with $\epsilon_r = 9.8$ and $\tan\delta = 0.002$ (e.g. Rogers TMM10i). Compliant connections are modeled as a resistive sheet with $R_S = 30 \Omega/\square$ [57].

since a stronger variation in $\epsilon_{r,eff}$ can be achieved for the same relative displacement. In this proposed design a relative permittivity $\epsilon_r = 9.8$ was selected, which can be easily obtained with commercial microwave laminates (e.g., Rogers TMM10). At the same time, though, also the characteristic impedance of the central section is modified: it decreases at decreasing Δx , thus increasing the mismatch with the fixed parts. It is worth noting that all the presented device exhibit a clear trade-off between maximum achievable phase shift and maximum acceptable mismatch. Further solutions (e.g., matching networks) could be introduced to improve the matching between the fixed and reconfigurable section. However, these should be reconfigurable at the same time, which is very difficult to obtain with low losses and low complexity at millimeter-waves. Therefore, for our scope, we preferred to control the mismatch (trying to minimize it) rather than increase losses and complexity. The “trapezoidal” cut of the bottom dielectric (Fig. 3.2a) was introduced to improve the matching (impedance tapering) between the the feeding (fixed) microstrip and the movable section. In a practical implementation using standard PCB fabrication, the same effect could be achieved realizing an array of holes in the dielectric to reduce its permittivity. Preliminary performance reported in Tab. 3.2 are based on a total horizontal displacement of 400μ m ($\Delta x = \pm 200 \mu$ m), which corresponds to only $0.04\lambda_0$ at the design central frequency $f_0 = 30$ GHz. This phase shifter was designed to work at the central frequency $f_0 = 30$ GHz with a 10 GHz bandwidth. The following characteristics have been chosen: dielectric permittivity $\epsilon_r = 9.8$ (e.g., Rogers TMM10i), $h_s = 500 \mu$ m, $L_{tr} = 200 \mu$ m and $L_{PS} = 10$ mm. Moreover, the compliant connections were modeled as a resistive sheet with $R_S = 30 \Omega/\square$ [57], and a conductivity $\sigma = 2.9 \times 10^7$ S/m was assigned to all the metallic parts.

Simulated scattering parameters for the device of Fig. 3.2a are shown in Fig. 3.3. Insertion loss is always lower than 1.8 dB and return loss better than 10 dB over the full 10 GHz bandwidth, with a phase shift/loss ratio of around $350^\circ/\text{dB}$ at 35 GHz. It is worth recalling that the scattering parameters of Fig. 3.3 are normalized to the optimal impedance Z_{opt} (50Ω for this

3.2. Preliminary design of DEA-based phase shifters

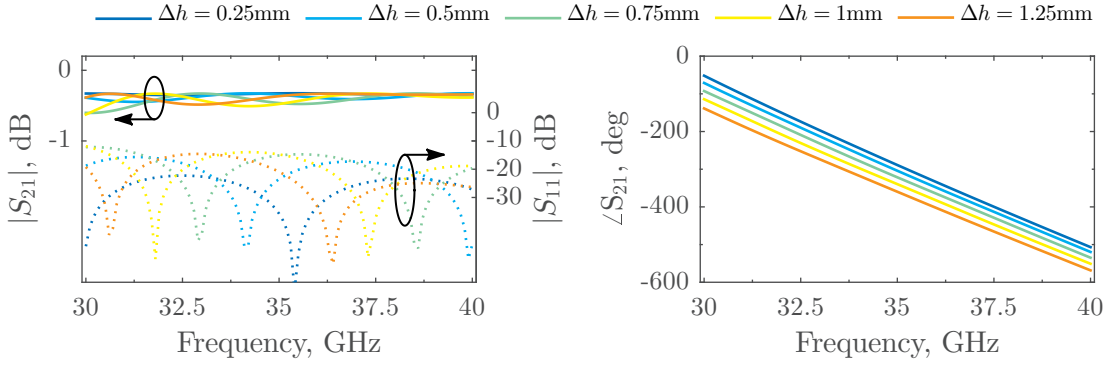


Figure 3.4 – Simulated scattering parameters for different states of reconfiguration of the concept depicted in Fig. 3.2b: $L_{PS} = 20$ mm, $L_{tp} = 5$ μ m. A conductivity $\sigma = 2.9 \times 10^7$ S/m is considered for all metallic parts (i.e., loading element and RWG), and actuators are completely shielded from the EM active area.

design) that satisfies the minimum mismatch approach. As a consequence, the mismatch generated in the two extreme states of reconfiguration (i.e., $\Delta x = -200$ μ m and $\Delta x = 200$ μ m) is the same, as it is visible from the S_{11} curves. All the remaining states are equally or better matched. The simulated performance are very good, but there remains one critical issue related to its feasibility. The main problem is represented by the need for flexible/compliant connections (Fig. 3.2a) between the fixed and the movable strip. Flexible metallizations could be used to realize these connections, but as it was showed in the previous chapter, these could dramatically increase losses degrading the nominal performance. In fact, we reported a surface resistance in the order of $30 \Omega/\square$, which can mean a loss factor of 2.4 dB/mm for a 50Ω microstrip realized with such a conductor [57]. Therefore, only a short connection ($L_{tr} = 200$ μ m selected here) was introduced in this design in order to limit the associated insertion loss. Flexible connections could be also avoided using a capacitive coupling between the two strips, but it would increase insertion losses and further degrade the mismatch. Moreover, the friction between the movable strip and the bottom dielectric should be properly accounted (or better avoided) to assure correct operation of the DEA-based actuator.

The basic idea characterizing the phase shifter concept depicted in Fig. 3.2b is the variable loading of a RWG. The size of the waveguide aperture are selected to excite the propagation of the fundamental mode TE_{10} in nominal conditions. A movable metallic bar is “pushed” inside the active area (i.e., RWG section) using one or more out-of-plane micro-actuators. This movement modifies the modal field distribution inside the RWG, thus shifting its propagation constant. The resulting propagating mode is a slightly perturbed TE_{10} , which keeps the main field configuration. The propagation constant increases if the metallic load is “pushed” inside the RWG (Δh increases), and this effect can be also modeled as an increase in the capacitance per unit length of the equivalent transmission line. At the same time the characteristic impedance of the line decreases. The loading part can be properly shaped to improve the matching between the fixed and reconfigurable sections. This device has the advantage to be a “closed” structure, which is very appealing for high power applications, and could be easily

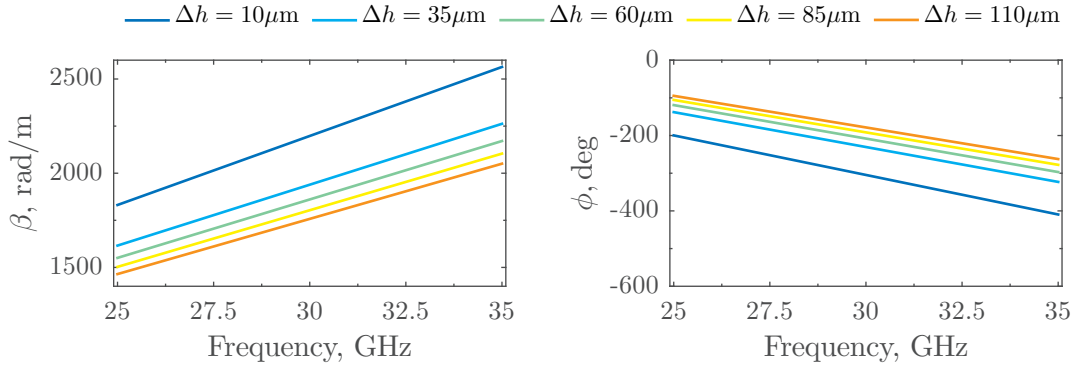


Figure 3.5 – Expected phase shift performance for the concept of Fig. 3.2c, calculated using the analytical model proposed in [58, chap. 4]. Δh is varied between $10\ \mu\text{m}$ and $110\ \mu\text{m}$ ($25\ \mu\text{m}$ step), corresponding to $\varepsilon_{r,eff} = 12.22, 9.52, 8.77, 8.24, 7.83$, respectively.

manufactured using standard micromachining techniques. Moreover, it does not comprise any dielectric in the EM active area (no dielectric losses), and does not require any connection between the fixed and the reconfigurable section (i.e., no need for flexible/compliant connections). Nevertheless, performance are poor compared to the other presented devices (cf. Tab. 3.2). Simulated performance of Tab. 3.2 refer to a total vertical differential displacement of 1 mm, starting from the initial state corresponding to $\Delta h = 0.25\ \text{mm}$. Simulated scattering parameters are reported in Fig. 3.4. These results were obtained for a WR28 waveguide with a loading element of dimensions $L_{tp} = 5\ \text{mm}$ and $L_{PS} = 20\ \text{mm}$ (note that the achievable phase shift is proportional to L_{PS} due to the TTD principle). Metallic parts were assigned a conductivity $\sigma = 2.9 \times 10^7\ \text{S/m}$, and actuators are completely shielded from the EM active area. Simulated data predict an insertion loss lower than 0.6 dB and a return loss better than 15 dB. The mean phase shift/loss ratio is around $180^\circ/\text{dB}$ at 35 GHz, which is improved (considering the poor differential phase shift) by the very low-loss behavior.

The concept of Fig. 3.2c is based on a conventional CPW whose propagation constant is perturbed by a variable dielectric load. A high permittivity dielectric is vertically displaced by out-of-plane actuators over a fixed CPW. When Δh decreases (the dielectric load is closer to the CPW) the effective permittivity increases, because the electric field starts to be more confined into the dielectric load than into the CPW substrate. As in the first concept, his effect is maximized when $\varepsilon_{r,load} \gg \varepsilon_{r,CPW}$. The phase shift performance of this concept were first evaluated using the analytical model proposed by Simons [58, chap. 4] for a CPW with a multi-layer dielectric structure. For a quasi-TEM transmission line the phase constant is directly proportional to the square root of the effective permittivity ($\beta = \omega \sqrt{\mu_0 \varepsilon_0} \sqrt{\varepsilon_{r,eff}}$). Therefore, the calculation of $\varepsilon_{r,eff}$ for the different reconfiguration states is necessary for a preliminary analysis of the desired phase shift capabilities. The analytical model presented in [58] is based on a quasi-static TEM conformal mapping technique and allows to accurately calculate the effective permittivity and the characteristic impedance of CPW sandwiched between a multi-layer dielectric substrate (both on top and bottom of the metallic lines).

3.2. Preliminary design of DEA-based phase shifters

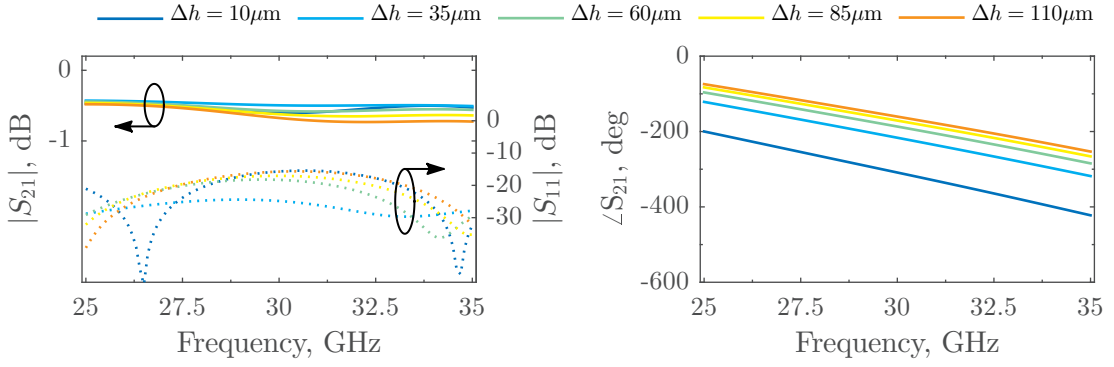


Figure 3.6 – Simulated scattering parameters for different states of reconfiguration of the concept depicted in Fig. 3.2c: $L_{PS} = 5$ mm, dielectric substrate with $\epsilon_r = 9.8$ and $\tan \delta = 0.002$ (e.g. Rogers TMM10i), dielectric load with $\epsilon_r = 50$ and $\tan \delta = 0.006$.

Assuming the propagation of a quasi-static TEM mode, the effective dielectric constant can be obtained using the following expression:

$$\epsilon_{r,eff} = \frac{C}{C_0}, \quad (3.6)$$

where C is the capacitance per unit length of the line, and C_0 is the capacitance per unit length of the line in the absence of dielectric substrates. C and C_0 are strictly dependent on the dielectric properties (dielectric constant and thickness) of the different layers and can be calculated using the formulation described in [58]. A preliminary optimization was performed using this model and the following characteristics were selected for the fixed CPW: $W = 500 \mu\text{m}$, $S = 180 \mu\text{m}$, $h_S = 500 \mu\text{m}$ and $\epsilon_r = 9.8$. In turn, the loading block was assigned a height $h_l = 500 \mu\text{m}$ and a permittivity $\epsilon_{r,load} = 50$, which can be obtained using for instance ceramic dielectrics. Figure 3.5 shows the calculated phase constant β and phase shift $\phi = -\beta L_{PS}$, where $L_{PS} = 5$ mm. In the presented results, Δh has a variation of $100 \mu\text{m}$ between $10 \mu\text{m}$ and $110 \mu\text{m}$ with a $25 \mu\text{m}$ step. The phase curves shown in Fig. 3.5 are based on the calculated effective permittivity $\epsilon_{r,eff} = 12.22, 9.52, 8.77, 8.24, 7.83$, respectively.

The predicted performance of Fig. 3.5 were then validated using HFSS full-wave simulations, in order to also evaluate the insertion loss. The values $\tan \delta = 0.006$ and $\tan \delta = 0.002$ were chosen for the loss tangent of the dielectric load and the CPW substrate, respectively. Simulated phase shifting performance corresponding to a length $L_{PS} = 5$ mm of the loading dielectric are shown in Fig. 3.6. A very good agreement is found for the calculated phase curves of Fig. 3.5 (right panel) and the simulations of Fig. 3.6 (right panel) with a maximum differential phase shift of around 147° at 35 GHz. Insertion losses are always lower than 0.7 dB and mismatch losses better than 14 dB. Insertion losses are highly dependent on dielectric losses in this concept.

The last proposed concept has been selected to be optimized, manufactured and tested.

It is based on a conventional CPW loaded by two suspended metallic strips (Fig. 3.7), and is discussed in the dedicated §3.3. However, a preliminary performance evaluation of this device is reported in Tab. 3.2 for a comparison with the other concepts described above. It is worth noting that the figure of merits reported in Tab. 3.2 allow a performance comparison between different devices independently from the length of their reconfigurable section and from the generated mismatch (cf. definition of FoM_1 and FoM_2 at the beginning of the section). This specific design has been selected among the others presented in §3.2 because it represents *the best trade-off between phase shift performance (i.e., achievable phase shift and insertion losses) and low-complexity*. In fact, it does not include any connection between the fixed and movable parts (i.e., differently from the concept of Fig. 3.2a), its performance can be easily characterized using conventional measurement techniques (e.g., using on-wafer measurements) and all its parts can be manufactured using standard PCB processes available at EPFL. It is worth noting that those concepts based on vertical actuation (i.e., Fig. 3.2b and Fig. 3.2c) were a priori discarded, since out-of-plane DEA actuators were not fully developed at the Microsystems for Space Technologies Laboratory (LMTS) and was unlikely to achieve good reliability and actuation performance in the time frame of this thesis. Moreover, although the concepts illustrated in Fig. 3.2a exhibited better performance (cf. Tab. 3.2), it presented critical technological challenges (mainly dictated by the need for a compliant connection between the fixed feed and the reconfigurable section) that would have not allowed a rapid prototyping and test of the device. Therefore, the concept illustrated in Fig. 3.7 and discussed in the next section, was preferred over the others presented above to be further optimized and fabricated. Although DEAs are considered in this thesis, the presented concepts are independent from the type of actuation, and can be potentially implemented using different technologies for mechanical reconfiguration. For instance electrostatic (e.g., [59, 60]), magnetic (e.g., [15, 61]) and piezoelectric (e.g., [62, 63]) actuators could be integrated to realize the final device.

Table 3.2 – Performance comparison for the proposed phase shifter concepts at 35 GHz.

Concept	Actuation	$\Delta\beta_{max}$ (rad/m)	FoM_1 eq. (3.4)	FoM_2^* eq. (3.5)
Fig. 3.2a	In-plane	539	30.9	563.5
Fig. 3.2b	Out-of-plane	61.9	3.5	34.3
Fig. 3.2c	Out-of-plane	513	29.4	526
Fig. 3.7	In-plane	308.5	21.5	140.6

* Note that presented performance do not include possible transitions between the fixed and reconfigurable section, differently from the full-wave simulations shown above.

3.3 The first reconfigurable TTD phase shifter using DEAs

The selected concept is depicted in Fig. 3.7. It consists of a conventional 50 Ω coplanar waveguide loaded by two suspended metallic strips (their spacing is constant), which are

3.3. The first reconfigurable TTD phase shifter using DEAs

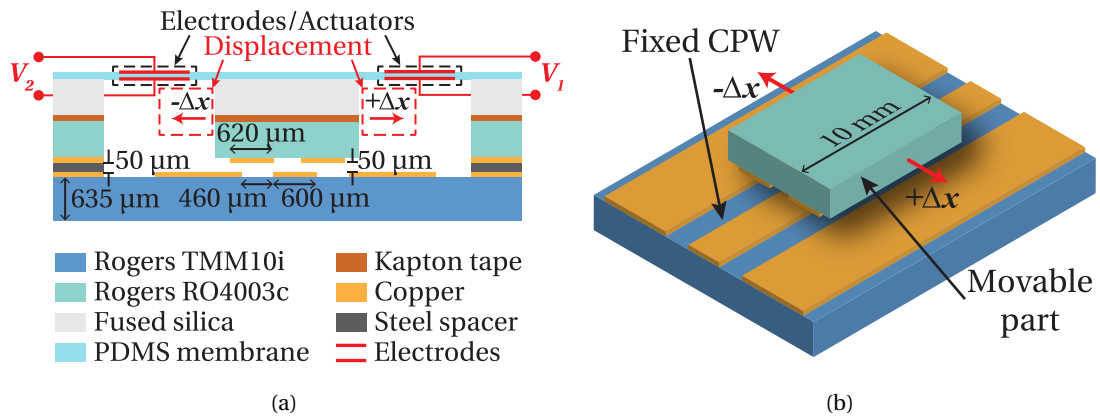


Figure 3.7 – Schematic drawing of the selected DEA-based phase shifter. (a) Cross-section view showing the device assembly and the materials used for the fabrication of the prototype. The air gap between the CPW and the loading strips is obtained using a steel spacer (same thickness as the needed air gap). (b) Simplified 3D view of the CPW and suspended loading part. The maximum differential phase shift is directly proportional to the length of the loading metal strips (here 10 mm for $\sim 180^\circ$ phase shift) due to the TTD principle.

supported and horizontally displaced in the $\pm \Delta x$ direction by DEA actuators integrated in the polydimethylsiloxane (PDMS) membrane. The actuation part also guarantees that the vertical spacing between the CPW and the loading strips keeps constant [64].

The movement in both the positive and negative Δx direction is obtained by means of two planar DEAs. Compliant electrodes are patterned on both sides of the pre-stretched PDMS membrane (excluding the EM-active area) forming two agonist planar DEAs linked by a central passive (i.e., no electrodes) PDMS segment (Fig. 3.7a). The compliant electrodes are composed of carbon black particles in a PDMS matrix and are applied using a stamping method (more details in §3.3.2). The activation of one of the electrodes increases the in-plane stretch in the activated segment and also relaxes the in-plane prestretch everywhere else in the membrane. In particular, a voltage V_1 induces a movement $-\Delta x$ proportional to the applied voltage itself, while a voltage V_2 generates a movement $+ \Delta x$ in the opposite direction. Note that only one actuator at time is active (or both inactive, i.e. $V_1 = V_2 = 0V$).

The presented concept implements a quasi-transverse electromagnetic transmission line whose propagation constant β is modified by changing its effective dielectric constant $\epsilon_{r,eff}$. In the proposed concept the horizontal displacement of the suspended lines over the fixed CPW modifies the EM field distribution inside the dielectric substrate and the air gap between the CPW and the loading lines, as qualitatively illustrated in Fig. 3.8. This variation induces a change in the effective permittivity of the equivalent TL, which results in a proportional change in the insertion phase. In *State A* (Fig. 3.8a), the loading metallic strips do not affect the nominal propagation of the fundamental CPW mode and the electric field is more concentrated in the dielectric substrate (thicker red arrows), resulting in the highest value of the effective

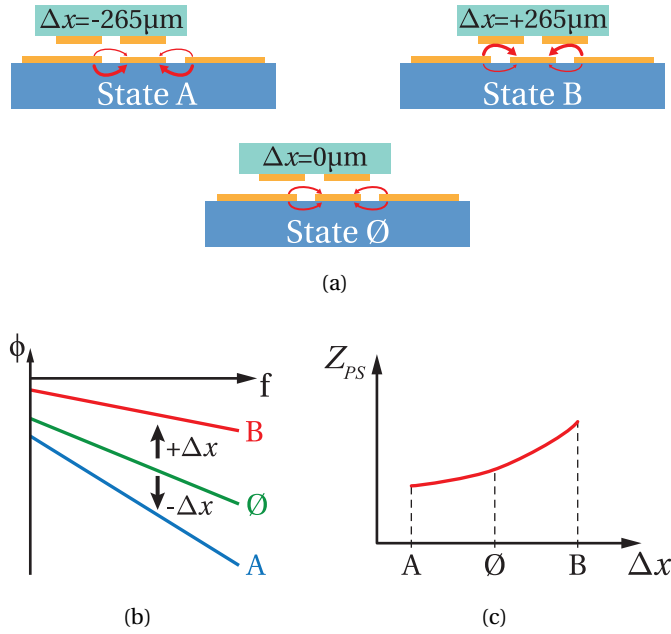


Figure 3.8 – Simplified drawing of the phase shifter reconfiguration principle. (a) Three possible states of reconfiguration with a symbolic illustration of the electric field distribution (red arrows): thicker arrows means stronger field. States A and B correspond to the minimum and maximum phase shift, respectively. State \emptyset ($V_1 = V_2 = 0V$) is the central state between A and B and corresponds to the initial assembly position. (b) Qualitative phase curves corresponding to the states shown in (a). The effective permittivity decreases moving from A to B, increasing the signal phase according to eq. (3.3). (c) Qualitative illustration of the characteristic impedance change as a function of the displacement Δx .

dielectric constant. In *State B*, on the contrary, the electric field is more concentrated in the air gap than in the substrate, owing to the perturbation of the loading element and resulting in the lowest value of $\epsilon_{r,eff}$. Thus, moving from *State A* to *State B*, $\epsilon_{r,eff}$ reduces generating a differential phase shift given by eq. (3.3) and symbolically illustrated in Fig. 3.8b. Also in this case, the effect is magnified increasing the dielectric permittivity of the bottom substrate, since this results in higher variation of $\epsilon_{r,eff}$ passing from *State A* to *State B*. For the presented design, a permittivity close to 10 was obtained using the commercial laminate Rogers TMM10i (Fig. 3.7a). The maximum differential phase shift is thereby obtained moving from A to B, generating phase curves similar to those qualitatively illustrated in Fig. 3.8b.

The design approach, the manufacturing process and the experimental characterization of this particular device are discussed in the next sections.

3.3.1 Design approach

The aim of this design was to optimize the dimensions of the CPW transmission line and of the reconfigurable loading part in order to maximize the phase shift performance. As

3.3. The first reconfigurable TTD phase shifter using DEAs

explained above, the horizontal movement of the loading lines over the fixed CPW induces a change in the effective permittivity $\epsilon_{r,eff}$ and consequently in the phase constant β of the equivalent transmission line. However, the dynamic control of the phase via the change of the effective permittivity of the quasi-TEM mode necessarily comes with a simultaneous variation of the TL characteristic impedance [65], which affects the matching of the phase shifter. Here the characteristic impedance $Z_{PS}(\Delta x)$ of the active section increases moving from state A to state B as qualitatively illustrated in Fig. 3.8c, due to the reduction of the effective dielectric constant. This effect results in increased mismatch in at least some of the phase shifter states, since the impedance Z_{CPW} of the feeding CPW is fixed (here to 50Ω). The use of matching networks between the feeding CPW and the reconfigurable section could be envisioned, but would not be advantageous in this specific concept. In fact, the matching circuit should be reconfigurable and would come with additional space, loss, and device complexity. Therefore, it is preferable to optimize the design in order to minimize the mismatch. This effect was considered in the design phase and a “minimum mismatch” approach was applied. Namely, dimensions and materials of the CPW and of the loading parts in the reconfigurable section were optimized to have the same mismatch in the extreme states of the phase shifter (A and B in Fig. 3.8a). The tuning mechanism then ensures that all intermediate states are better matched, since the impedance changes monotonically with the movement of the loading part, as symbolically depicted in Fig. 3.8c.

The transmission line model of the presented phase shifter is proposed in Fig. 3.9. The feeding CPW is represented as a TL section with constant impedance Z_{CPW} (here fixed to 50Ω) and fixed propagation constant β_{CPW} . The reconfigurable section is described by a generic TL with variable characteristic impedance $Z_{PS}(\Delta x)$ and phase constant $\beta_{PS}(\Delta x)$, functions of the horizontal displacement Δx . The optimal solution of the minimum mismatch design is achieved when the reflection coefficient in state A and B, respectively $\Gamma_{PS}(A)$ and $\Gamma_{PS}(B)$,

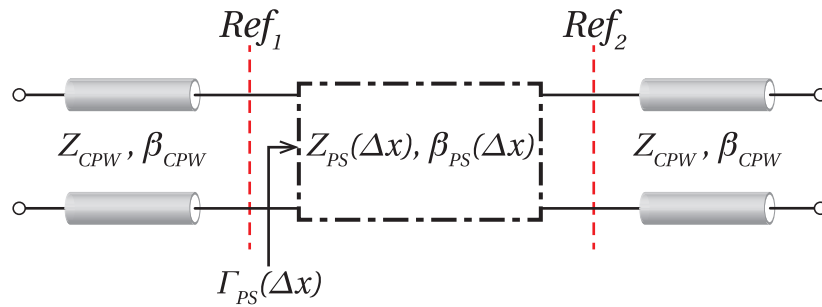


Figure 3.9 – Equivalent transmission line model of the selected phase shifter concept. The feeding CPW is represented as a TL section with constant impedance Z_{CPW} and constant propagation constant β_{CPW} . The reconfigurable section has variable characteristic impedance $Z_{PS}(\Delta x)$ and propagation constant $\beta_{PS}(\Delta x)$, which are function of the variable displacement Δx .

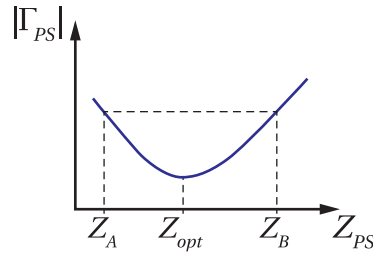


Figure 3.10 – Symbolic representation of the “minimum mismatch” principle. The maximum reflection is achieved in the extreme states A and B, and all intermediate states are better matched due to the monotonic change of Z_{PS} from A to B.

equal in magnitude. This relation is mathematically expressed by the following equation:

$$\left| \frac{Z_{PS}(A) - Z_{opt}}{Z_{PS}(A) + Z_{opt}} \right| = \left| \frac{Z_{PS}(B) - Z_{opt}}{Z_{PS}(B) + Z_{opt}} \right|, \quad (3.7)$$

where Z_{opt} is the reference impedance that satisfies the mismatch minimization. After simple calculations it is possible to demonstrate that the optimal solution in terms of characteristic impedance is given by

$$Z_{opt} = \sqrt{Z_{PS}(A) Z_{PS}(B)} = Z_{CPW} \quad (3.8)$$

It is clear from eq. (3.7) and (3.8) that the maximum reflection is achieved in the extreme states A and B, while all the intermediate states present a better matching (the minimum is reached for $Z_{PS}(\Delta x) = Z_{opt}$). A symbolical representation of this principle is illustrated in Fig. 3.10.

The design and optimization were carried out using a full-wave simulation approach. The main objective was to optimize the dimensions of the CPW TL and of the reconfigurable loading part in order to maximize the phase shift to loss figure, while simultaneously minimizing the mismatch. The characteristics of the reconfigurable section were selected in order to have $Z_{PS}(A)$ and $Z_{PS}(B)$ satisfying eq. (3.8), where $Z_{opt} = 50\Omega$ was selected. At the same time, also the maximization of the differential phase shift between the two extreme states A and B was introduced in the optimization process. In particular, the two figures of merit FoM_1 and FoM_2 defined respectively by eq. (3.4) and (3.5) were considered.

The final dimensions of the reconfigurable phase shifter were selected to maximize both eq. (3.4) and (3.5) with the constraints given by eq. (3.8). The different geometric variables taking part into the optimization process are defined in Tab. (3.3) and the main steps of the design are summarized as follow:

3.3. The first reconfigurable TTD phase shifter using DEAs

1. Z_{CPW} was set to $50\ \Omega$ and the dimensions of the feeding section were chosen accordingly [58]. The dielectric substrate is the commercial Rogers TMM10i with a permittivity of 9.8 and a thickness of $635\ \mu\text{m}$. Different commercial materials with dielectric constant close to 10 (good trade-off between achievable change in $\epsilon_{r,eff}$ and associated mismatch) were considered at this stage, but the TMM10i was chosen for its very good dielectric and mechanical stability.
2. W_{PS} and Δh_{PS} were then fixed according to preliminary simulations and some considerations concerning the manufacturing technique, the final device dimensions and the DEA limitations (e.g., fabrication precision, maximum DEA strain, total dimensions).
3. The HFSS port solver was used to evaluate the characteristic impedance Z_{PS} and the propagation constant β_{PS} for both states A and B of a realistic device. More specifically, a parametric simulation was performed as a function of S_{PS} and W_{load} with a $10\ \mu\text{m}$ step for both variables. Such a step corresponds to the maximum resolution achievable with the etching fabrication process available at EPFL. The optimal impedance Z_{opt} was then calculated for each couple ($Z_{PS}(A)$, $Z_{PS}(B)$) using eq. (3.8).

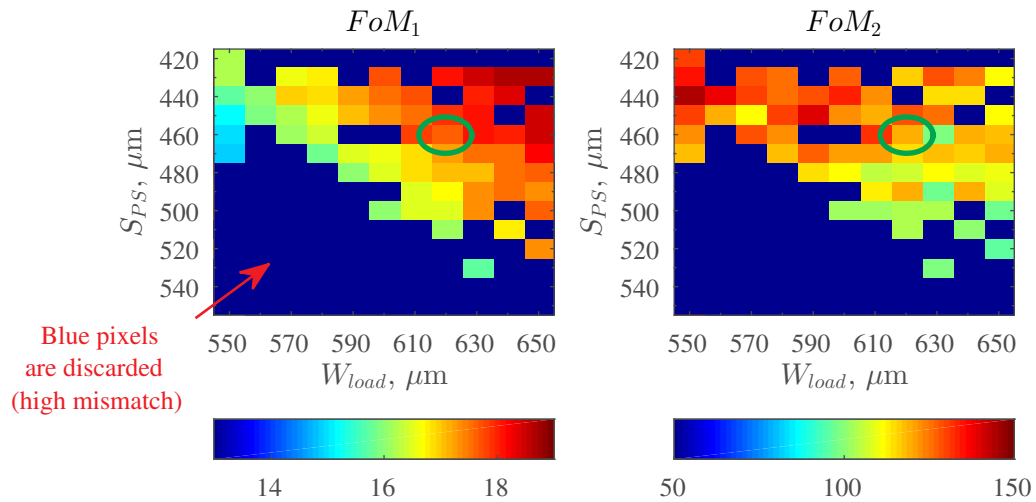


Figure 3.11 – Performance map for the design optimization of the proposed phase shifter. The optimization parameters are S_{PS} and W_{load} . Blue pixels are discarded because they correspond to unacceptable mismatch (optimal impedance different from $50.0 \pm 0.5\ \Omega$).

4. FoM_1 and FoM_2 were calculated for each couple (S_{PS} , W_{load}) with an associated $Z_{opt} = 50.0 \pm 0.5\ \Omega$. This was necessary to match the fixed impedance $Z_{CPW} = 50\ \Omega$ of the feeding CPW. Performance maps of FoM_1 and FoM_2 were generated as shown in Fig. 3.11. Blue pixels therein represent those couples (S_{PS} , W_{load}) with an associated optimal impedance different from $Z_{opt} = 50.0 \pm 0.5\ \Omega$ (i.e., higher mismatch) and thereby were discarded in the optimization process. It is worth observing the clear trade-off between FoM_1 and FoM_2 showed in Fig. 3.11: higher phase shift per unit length generally corresponds to higher mismatch (lower FoM_2) and vice versa. This relation is pretty obvious

considering that higher phase shift is achieved by means of a larger reconfiguration of the effective permittivity, which necessarily brings to a wider change in the characteristic impedance of the active section.

5. The final values of S_{PS} and W_{load} were selected by maximizing FoM_1 and FoM_2 . In particular, a minimum threshold for FoM_2 was selected and S_{PS} and W_{load} were chosen to maximize FoM_1 . Nevertheless, the available chemical etching process could introduce a $\pm 10\mu\text{m}$ error in the realization of the metallic lines and had to be considered in the selection of the final dimensions. This means that the selected optimal pixel in Fig. 3.11 needed to be surrounded by at least eight valid pixels (different from blue) with analogous figures of merit (a 5% performance reduction was accepted). From previous considerations, we can conclude that the final choice represented a “sub-optimal” solution resulting from a trade-off between *phase shift maximization*, *mismatch minimization* and *manufacturing constraints*.

The final dimensions of the presented phase shifter, together with the definition of the variables mentioned in this section, are summarized in Tab. 3.3. Figure 3.12 shows a top-view drawing of the basic CPW with the main variables defined in Tab. 3.3. It is worth observing from Fig. 3.12 that the CPW is properly shaped to have $Z_{opt} = Z_{CPW} = 50\Omega$. Moreover, a further transition (see the zoomed section) is added to comply with the measurements setup. As explained in §3.3.3, the characterization of the presented device was carried out by contacting RF ground-signal-ground (GSG) probes (*Cascade Microtech |Z| Probe*) to the CPW input/output sections, using a TRL calibration. The probes employed for measurements had a $150\mu\text{m}$ pitch, thereby the dimensions of the input section were chosen accordingly (Fig. 3.12 and Tab. 3.3).

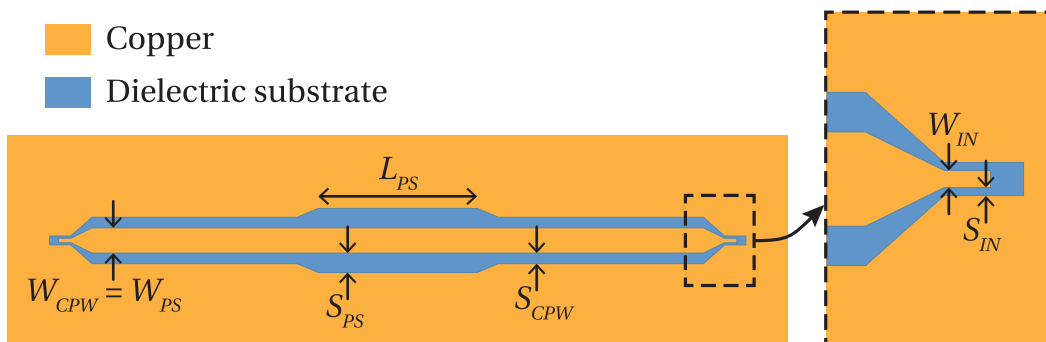


Figure 3.12 – Top-view drawing of the basic CPW transmission line constituting the fixed part of the designed phase shifter. The main dimensions reported in Tab. 3.3 are highlighted. The input and output transitions needed for the connection of the testing GSG probes are also included.

3.3. The first reconfigurable TTD phase shifter using DEAs

Table 3.3 – Main variable definitions and final dimensions of the fabricated phase shifter.

Variable name	Variable definition	Final value (μm)
W_{PS}	Width of the signal line in the reconfigurable CPW section	600
S_{PS}	Gap between signal and ground line in the reconfigurable CPW section	460
L_{PS}	Length of the loading lines. It sets the maximum phase shift	10000
W_{CPW}	Width of the signal line in the feeding CPW section	600
S_{CPW}	Gap between signal and ground line in the feeding CPW section	250
W_{IN}	Width of the signal line in the CPW section accessible to RF probes	110
S_{IN}	Gap between signal and ground line in the CPW section accessible to RF probes	50
W_{load}	Width of each loading line	620
S_{load}	Gap between the two loading lines	440
h_{diel}	Thickness of the CPW dielectric	635
Δh_{PS}	Air gap between the CPW and the loading lines	50

3.3.2 Manufacturing and assembly

The design process was carried out considering all the constraints imposed by the DEA technology in terms of possible implementation and maximum achievable strain (with respect to an assigned size of the actuator). The concept was optimized to comply with the manufacturing processes available at EPFL. In particular, all the fabrication steps relied on standard printed circuit board (PCB) manufacturing techniques (no cleanroom activity was needed) to reduce fabrication cost and complexity. The actuator part was developed at the LMETS laboratory, EPFL.

The different parts of the design were fabricated independently using commercial materials (Fig. 3.7a) and standard PCB manufacturing techniques. The fabricated pieces were then assembled manually, resulting in a very low-cost phase shifter. Moreover, the prototype was designed to be modular, allowing the use of the same fixed PCB (CPW transmission line) with different reconfigurable parts (for testing purposes) and to replace single pieces in case of local failure. A render of the assembled prototype is shown in Fig. 3.13a and its exploded view is represented in Fig. 3.13b, giving a clear idea of the modularity mentioned above. It is worth noting that the active part (i.e. the area directly affected by reconfiguration and generating a variable phase shift) is very small compared to the total dimensions of the device ($\sim 5 \times 5 \text{ cm}^2$) as represented in Fig. 3.13a. In fact, our main concern was the implementation of a first

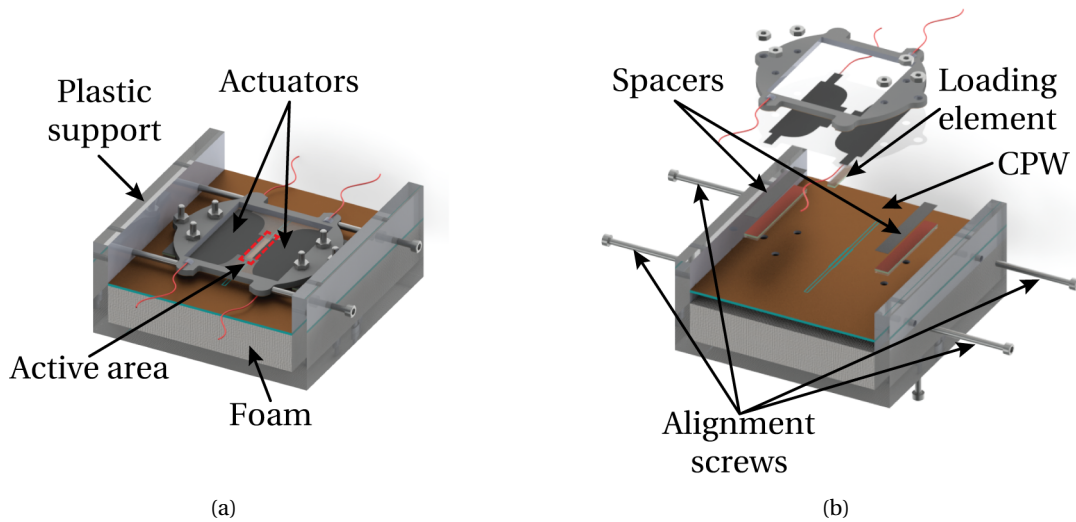


Figure 3.13 – Render of the manufactured device: (a) final assembly and (b) exploded view. The different parts constituting the modular device are labeled. The active area is highlighted with a red dashed-line rectangle, and has a dimension of $(12 \times 3 \text{ mm}^2)$.

prototype that could be easily and safely tested for a first demonstration of the DEA-based reconfiguration, while we were not particularly focusing on size minimization. Furthermore, it is important to highlight that this phase shifter was completely realized with very low cost technology.

The main manufacturing steps, together with a description of the different parts visible in Fig. 3.13, can be summarized as follow:

1. **Fabrication of the CPW:** the basic CPW transmission line was manufactured from a Rogers TMM10i laminate using a standard chemical etching technique. The choice of the TMM10i material is due to the need for a high permittivity, low losses and reliable mechanical and electrical stability.
2. **Fabrication of the loading part:** the loading strips were etched from a Rogers Duroid 4003C laminate, which presents low permittivity, low losses and good mechanical stability. In this case, though, the choice of such a material was not relevant to the phase shift performance, since the electric field in it is almost negligible. Indeed a substrate was not really needed, but it was introduced to allow an accurate, simple and inexpensive manufacturing of the loading lines. Several lines were realized on a wafer-sized (10 cm diameter) substrate, as needed by the next fabrication step. Moreover, alignment holes were drilled into the Duroid material next to the metallic lines. These holes were used to improve the horizontal alignment between the fixed CPW and the reconfigurable part, as explained later.
3. **Assembly of the loading PCB:** the substrate etched at the previous step was adhered to

3.3. The first reconfigurable TTD phase shifter using DEAs

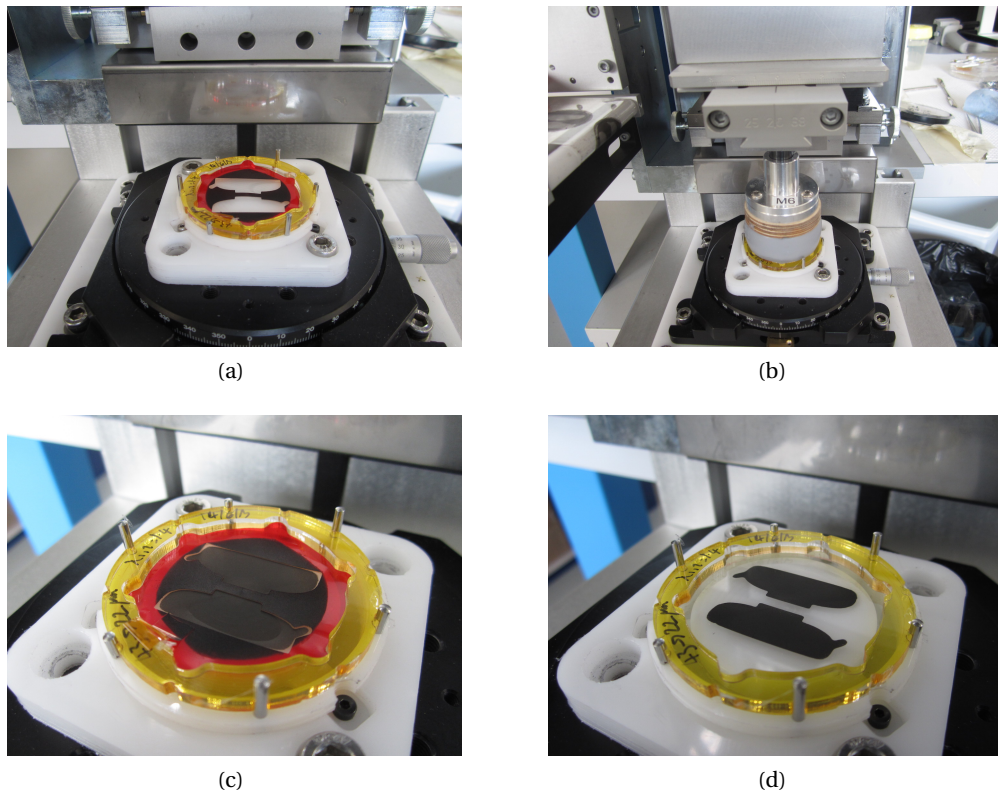


Figure 3.14 – Different steps of the electrodes printing on the PDMS membrane. (a) A laser cut PET mask with the desired electrode geometry is placed on the membrane surface. (b) A rubber pad deposit the conductive ink on the PSMS membrane through the PET mask. (c) Final result after the stamping process, and (d) after removing of the PET mask.

a fused silica wafer (thickness $525\ \mu\text{m}$, permittivity $\epsilon_r = 3.8$, loss tangent $\tan \delta = 0.0004$). This silica substrate was added to improve stiffness and flatness of the loading chip, and to simplify its bonding to the elastomer membrane using O_2 plasma activation. A plasma bonding technique allows for an irreversible bond between the fused silica surface and the PDMS membrane. The 10 cm wafer (stack of fused silica and etched Duroid PCB) was then diced to realize the needed loading chips (around $12\ \text{mm} \times 2\ \text{mm}$ when $L_{PS} = 10\ \text{mm}$).

4. **Realization of the DEA actuators:** the dielectric elastomer membrane was fabricated at LMTS [66] using a commercial two-component PDMS silicone elastomer (Dow Corning Sylgard 186) whose dielectric properties had been previously characterized (cf. §2.3). The two PDMS components were mixed at a 10:1 ratio, with the addition of a silicone solvent (Dow corning OS-20 in a 4:1 PMDS to solvent ratio) to reduce the viscosity of the mixture, using a planetary mixer (Thinky ARE-310). The mixing procedure also allowed to degas the PDMS-solvent solution in order to avoid the formation of air inclusions. The PDMS mixture was blade cast onto a PET substrate to a thickness of

approximately 60 μm using a Zehntner automatic film applicator coater, and was then allowed to cure in the oven for at least one hour at approximately 80 °C. The cured elastomer membrane was then cut into 40 mm \times 40 mm sections and pre-stretched equibiaxially of a 1.4 factor. The use of pre-stretch allows to increase the mechanical energy in the elastomer, and to improve its breakdown strength. However, this also makes the membrane stiffer requiring a slightly larger electric field to reach a given strain. The pre-stretched PDMS membrane (thickness around 30 μm) was then fixed to a plastic frame in order to maintain its pre-stretch.

Compliant electrodes were fabricated via a stamping method using a pad-printing machine (Teca Print TPM101, Fig. 3.14). The machine operates by doctor blading small amounts of conductive electrode ink (composed of carbon black particles in a PDMS matrix) onto a shallow reservoir etched into a metal plate called a cliché, which is subsequently picked up by a rubber pad (Fig. 3.14). The ink was deposited through a laser cut PET mask placed on the membrane surface (Fig. 3.14c), thereby achieving the desired electrode geometry (Fig. 3.14d). This method, in general, facilitates fast prototyping and evaluation of designs. The shape of the perimeter of the mask was cut to match the internal shape of the rigid plastic frame used to retain the membranes pre-stretch. This pad-printing methodology ensured an electrode with high resolution (feature sizes down to 50 μm were attainable), and allowed to avoid that the electrode material spilled over into the central passive zone of the membrane.

After the electrodes printing, the PDMS membrane was transferred to a plastic PCB that allowed also the electric connection between the electrodes and the electric wires necessary to apply the actuation voltage.

5. **Assembly of the reconfigurable part:** the loading PCB realized at point 3 had to be placed in the center of the active membrane, between the two agonist actuators to complete the reconfigurable part of the proposed phase shifter. Oxygen plasma was used to allow a permanent bonding of the loading chip (through the fused silica) to the center of the PDMS membrane. To complete this step, both the actuator and the loading elements were placed into a plasma chamber (Zepto, Diener electronic) and exposed to oxygen plasma for approximately 20 seconds at 100 % power (Fig. 3.15c). Radicals in the plasma first clean and then bind with the two surfaces making them highly reactive. The two activated surfaces were then removed from the chamber, placed in a custom-made jig to ensure alignment and pressed in contact with each other. The full actuator, after the bonding process, is shown in Fig. 3.15d.
6. **Assembly of the device:** the final assembly and alignment between the basic CPW and reconfigurable part was realized using a plastic support and vertical screws as illustrated in Fig. 3.13. The holes were placed to have the initial position (no applied voltage) corresponding to the 'State \emptyset ' of Fig. 3.8a. This choice allowed to completely exploit the two-direction ($\pm\Delta x$) displacement range offered by the two agonist actuators and to correct possible assembly tolerances. The needed air gap $\Delta h_{PS} = 50\mu\text{m}$ between the CPW and the loading lines was guaranteed by the introduction of proper spacers: they

3.3. The first reconfigurable TTD phase shifter using DEAs

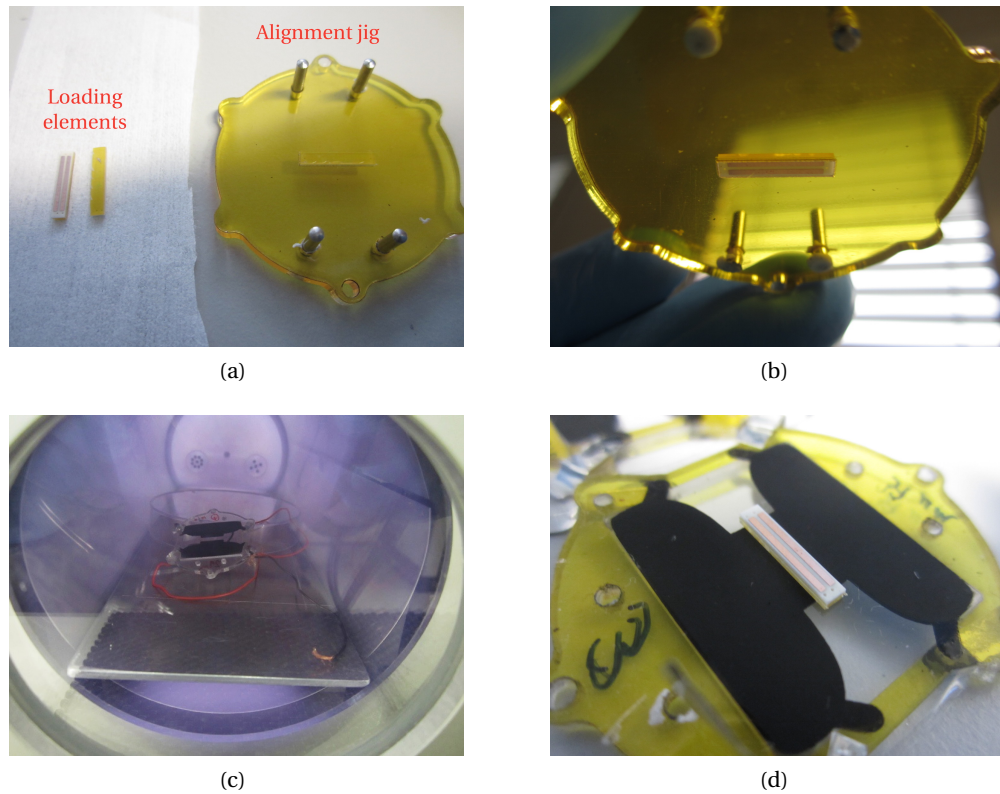


Figure 3.15 – Bonding procedure of the loading PCB to the actuator membrane by oxygen plasma activation. (a) Picture of loading elements and alignment jig with shallow recess for placing loading element. (b) Loading element placed in the alignment jig. (c) Actuator and loading element activated in the O_2 plasma chamber. (e) Bonded device.

were manufactured with the same materials used for the loading PCB, in addition to a $50\ \mu\text{m}$ steel shim (Fig. 3.7a and Fig. 3.13).

A digital holographic microscope (DHM) was subsequently used to measure and validate the vertical spacing between the two parts. DHMs are typically used for 3D real-time topography imaging at nanometric resolution. For our purposes, the DHM was used to focus on the CPW surface and then on the top surface of the glass substrate of the loading element using the available working distance tool. This tool allowed us to obtain the vertical position at which the coherence was maximized for the two planes using a 3-axes micrometer precision stage. The difference between the vertical positions of the two surfaces subtracted by the thickness of the loading element (including the glass substrate and Kapton tape) determined the spacing Δh_{PS} .

It is worth observing that a 10 mm thick Rohacell foam was placed below the CPW substrate (Fig. 3.13) in sight of the foreseen measurements setup. The Rohacell HF foam, in fact, exhibits dielectric properties similar to air ($\epsilon_r \sim 1$ and low losses), which was very convenient to separate (without affecting the device performance) the CPW and the metallic support of the employed probe station avoiding any electromagnetic coupling

between them.

7. **Horizontal alignment:** in the case of the manual assembly procedure used here, further actions were needed to improve the horizontal alignment between the loading element and the bottom CPW. The horizontal alignment was validated using an optical microscope with the aid of dedicated aligning holes in the loading PCB (drilled at step 2). Moreover, four horizontal screws were added to the plastic support (Fig. 3.13). These screws were tuned to obtain a finer adjustment of the horizontal alignment while looking at the microscope through the alignment holes. An example of microscope view is shown in Fig. 3.17. According to our setup, an aligning precision of $\pm 20 \mu\text{m}$ was estimated.

The manufacturing procedure described above required different optimizations and reiterations, especially to achieve a good vertical and horizontal alignment between the fixed transmission line and the movable loading part. The final manufactured phase shifter prototype is shown in Fig. 3.18, where the small EM-active area ($12 \times 3 \text{ mm}^2$) is highlighted. The independent electrical connections (for the actuation voltage) of each DEA actuator are also visible: red wires (positive voltage) are connected to the top electrodes, and black wires (ground) are connected to the bottom electrodes. The next section reports the experimental characterization of this specific prototype.

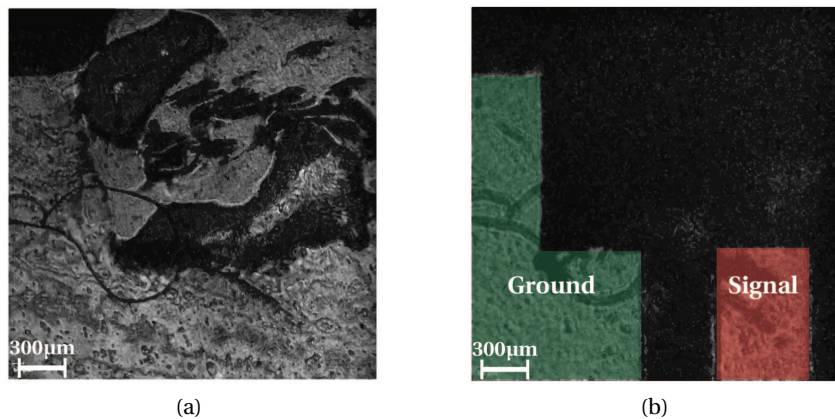


Figure 3.16 – Validation of Δh_{PS} spacing using a digital holographic microscope (DHM) (Lyncée tec). Intensity images of the surfaces as seen through the DHM: (a) fused silica plane and (b) CPW plane (green and red shading added to indicate the ground plane and signal line respectively). The machine's working distance tool obtains vertical position at which the coherence is best for the two planes using a micrometer precision stage. The difference in the vertical position is used to determine the Δh_{PS} spacing by subtracting the thickness of all the involved substrates.

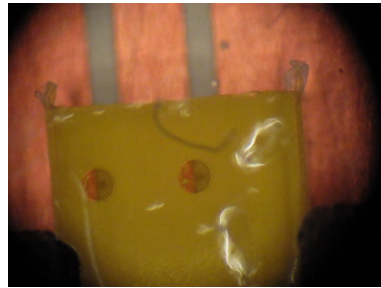


Figure 3.17 – Procedure for the horizontal alignment between the fixed CPW and the loading part. An optical microscope is used to verify the horizontal alignment through dedicated holes in the loading PCB.

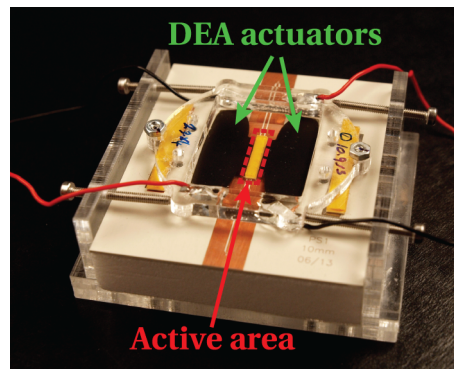


Figure 3.18 – Picture of the fabricated DEA-based phase shifter. The EM-active area is highlighted with a red dashed-line rectangle, the dimensions are $12 \times 3 \text{ mm}^2$. Two DEA segments straddle the EM-active area providing the in-plane actuation. The DEA segments have separate electrical input allowing for independent actuation. The four screws on the perimeter of the device help maintain horizontal alignment.

3.3.3 Experimental characterization

The fabricated prototype of Fig. 3.18 was characterized through conventional on-wafer measurements of the 2-port scattering parameters. The measurement setup included an Agilent E8361A network analyzer, and a Cascade Microtech CM2 manual probe station to correctly position ground-signal-ground (GSG) probes on the CPW. Cascade Microtech $|Z|$ probes with $150 \mu\text{m}$ pitch were used to access the input and output sections of the device under test. A commercial high voltage supply was used to provide the needed control voltage to the DEA actuators. A picture of the complete measurements setup is visible in Fig. 3.19a, and a detail of the device under test with connected GSG probes is proposed in Fig. 3.19b.

A TRL calibration was adopted to remove the effect of the transitions between the coaxial-based network analyzer and the CPW-based device, and to place the S-parameters reference

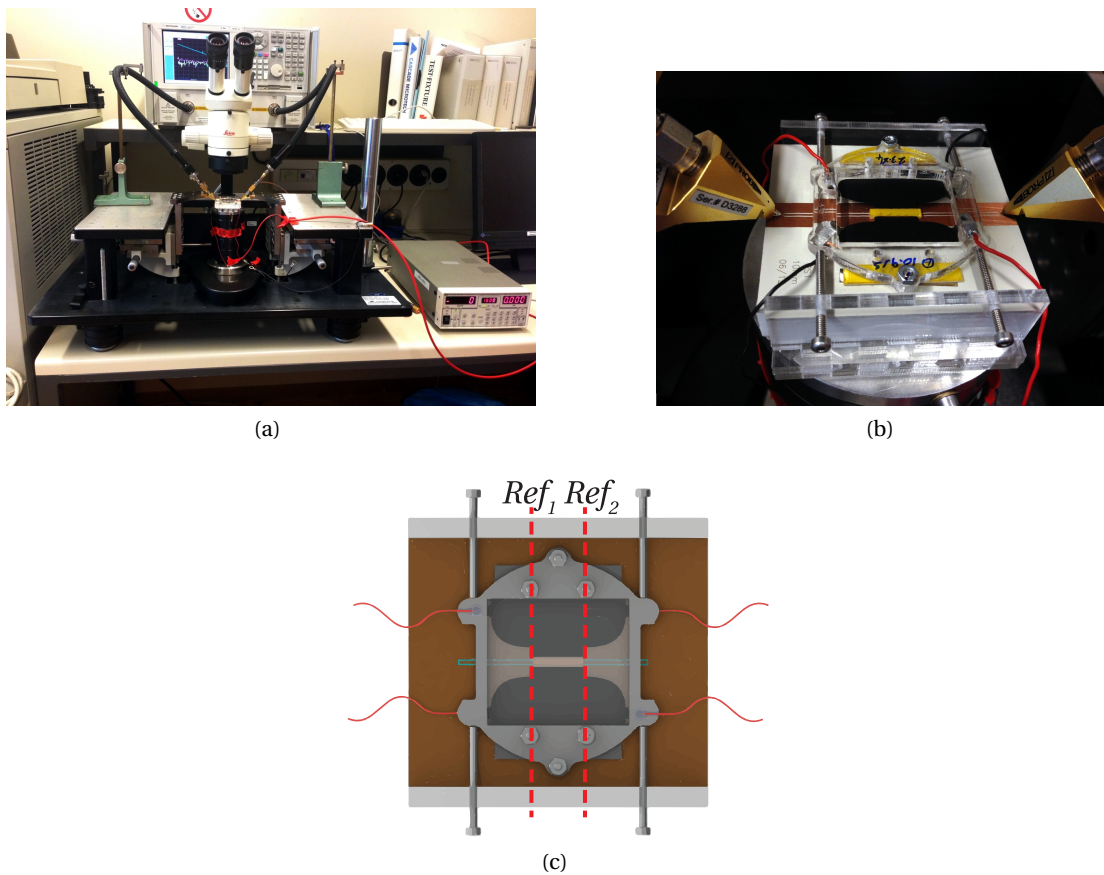


Figure 3.19 – Measurements setup used for the prototype characterization. (a) Complete setup including the Agilent PNA for 2-port S-parameters measurements, the Cascade manual probe station and the high voltage supply. (b) Detail of the phase shifter under test with connected GSG probes, conventionally used for on-wafer measurements. (c) Position of the measurement reference planes using TRL calibration.

planes at the edges of the reconfigurable section (Fig. 3.19c). It is worth noting that actuator parts extend beyond the selected reference planes over the feeding and fixed CPW. However, the effect of these parts on the propagation properties of the basic transmission line was assessed to be negligible. In fact, an air gap higher than 1 mm exists between the CPW plane and the actuator frame. Therefore, a negligible electromagnetic interaction appears in these regions (feeding CPW) between the CPW field and the actuator parts (i.e., this sections do not contribute to the signal phase shift). The particular measurement setup implemented for the MMW characterization of this first prototype did not allow for simultaneous measurement of both the horizontal displacement of the loading part and the associated scattering parameters. Therefore, the actuator displacement (Δx values, cf. Fig. 3.7) as a function of the applied voltage was determined prior to the MMW characterization using a digital camera mounted on an optical microscope. More specifically, pictures were taken at each actuation state (i.e., applied voltage) and a tracking element present in all available pictures was chosen. Then, its displacement was extracted using a pixel-based processing technique. The measured displace-

3.3. The first reconfigurable TTD phase shifter using DEAs

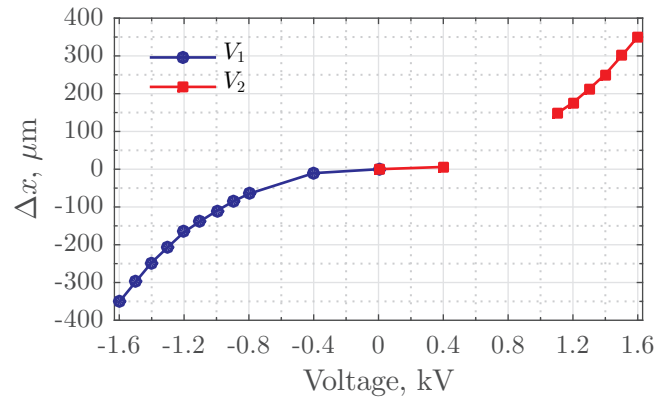


Figure 3.20 – Displacement (Δx) characterization as a function of the applied voltage performed prior to the S-parameter measurements. Note V_1 voltages are shown as negative and V_2 voltages shown as positive. A portion of V_2 curve is missing due to anomalous data extracted during the procedure.

ment for the presented phase shifter is reported in Fig. 3.20. Note that V_1 input voltages (right actuator, cf. Fig. 3.7) are shown as negative values (i.e., $V_1 = -V$) and V_2 as positive ($V_2 = V$). Figure 3.20 shows that the actuator was able to achieve the required total displacement of $530 \mu\text{m}$ well within the safe operating range defined by a maximum applicable electric field of $100 \text{ V}/\mu\text{m}$ (a maximum field of around $60 \text{ V}/\mu\text{m}$ was applied here). A small portion is missing in the ' V_2 ' curve, since anomalous data were obtained from the characterization and, thus, their values were discarded.

Phase shift performance at different actuation states were then characterized: no applied voltage ($V_1 = V_2 = 0 \text{ V}$), $V_1 = (1.1, 1.2, 1.3, 1.4, 1.5) \text{ kV}$ and $V_2 = (1.1, 1.2, 1.3, 1.4, 1.5) \text{ kV}$. It is worth observing that the initial position ($V_1 = V_2 = 0 \text{ V}$) corresponds to the 'State \emptyset ' of Fig. 3.8a, namely, the central position ($\Delta x = 0 \mu\text{m}$) between the minimum (state A) and maximum (state B) phase shift. However, due to the manual assembly, some initial displacement can be present in the manufactured prototype, and can be characterized comparing measured and simulated curves.

The measured scattering parameters in the range 25–35 GHz are shown in Fig. 3.21 (note V_1 voltages are shown as negative and V_2 voltages shown as positive). The top panels of Fig. 3.21 show the magnitude of S_{21} (left panel) and S_{11} (right panel), highlighting the very low loss and the good matching for all the reconfiguration states, respectively. The bottom panel reports the transmission phase exhibiting the typical TTD behavior. Measured curves highlight very good performance in terms of insertion loss (IL), return loss (RL), and maximum differential phase shift ($\Delta\phi_{max}$). The IL is always lower than 1.6 dB with an average value of 0.83 dB over the total frequency range. The RL is always better than 11 dB, which means good matching for all the phase shifting states in the whole 10 GHz bandwidth. A maximum differential phase shift $\Delta\phi_{max} \approx 180^\circ$ is achieved at 30 GHz, which can be increased at will by proportionally increasing the length of the active region (Fig. 3.7 and 3.18) due to the TTD working principle.

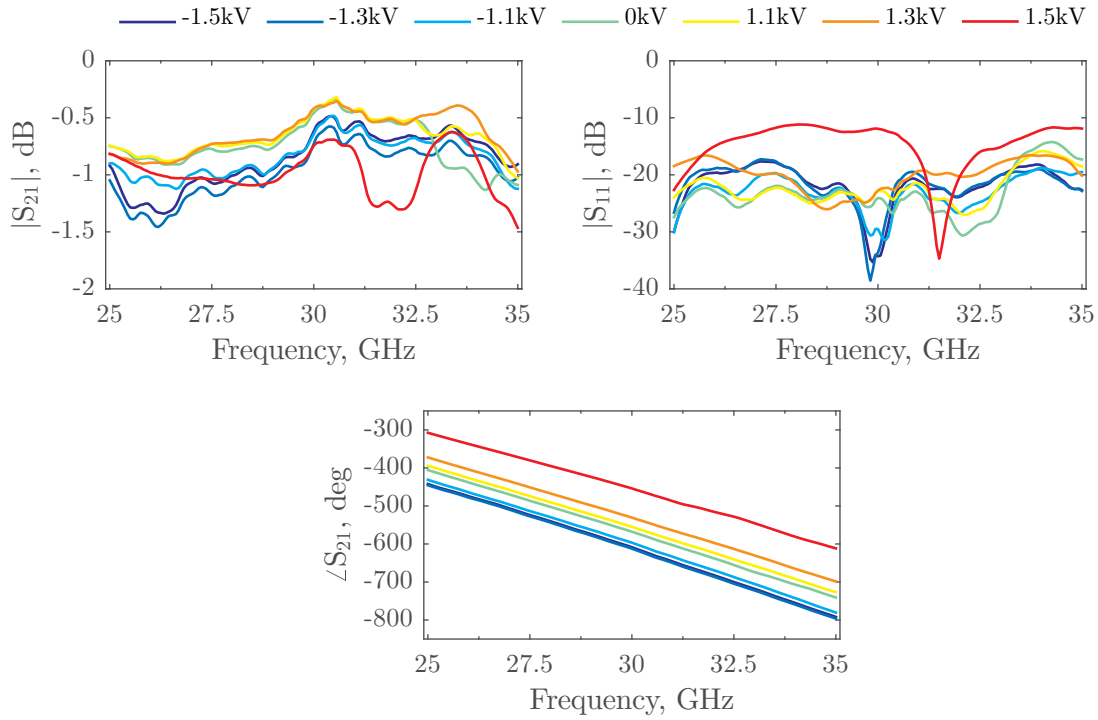


Figure 3.21 – Measured scattering parameters for different actuation states: $V_1 = V_2 = 0V$, $V_1 = (1.1, 1.3, 1.5)kV$ and $V_2 = (1.1, 1.3, 1.5)kV$. The top panels show the magnitude of S_{21} (left) and S_{11} (right) in dB. The bottom panel reports the transmission phase exhibiting the typical TTD behavior. Note V_1 input voltages shown as negative values and V_2 as positive in the legend.

These results demonstrate state-of-the-art performance in terms of the most important figure of merit for true-time delay phase shifters, namely, the phase-shift/loss ratio. Indeed, a mean value of $\sim 235^\circ/\text{dB}$ was achieved at 35 GHz, considerably outperforming MMIC phase shifters at similar frequencies (e.g., $\sim 57^\circ/\text{dB}$ at 28 GHz for a 5-bit MMIC phase shifter using InGaAs PIN diodes [23]). Moreover, similar performance as lower-loss state-of-the-art MEMS reconfigurable phase shifters were obtained. Hacker et al. [52] for instance demonstrated an average FoM of $\sim 140^\circ/\text{dB}$ at 35 GHz for a 3-bit TTD RF-MEMS network, while the 2-bit MEMS phase shifter presented by Hayden and Rebeiz [67] exhibited an average phase shift to loss of $\sim 180^\circ/\text{dB}$ at 37.7 GHz.

Measured scattering parameters are now compared with full-wave simulations from the commercial software Ansys HFSS. Figure 3.22 shows the simulated results (solid and dotted blue line) as a function of the horizontal displacement Δx , and the measured phase as a function of the input voltage (red circles and triangles) at two different frequencies, namely 25 GHz and 30 GHz. The Δx values corresponding to the measured phase data were determined prior to the device assembly and MMW characterization (Fig. 3.20), as the particular measurement setup did not allow for measurement of both quantities simultaneously (see discussion above). A good agreement can be seen between the measured and simulated results for negative

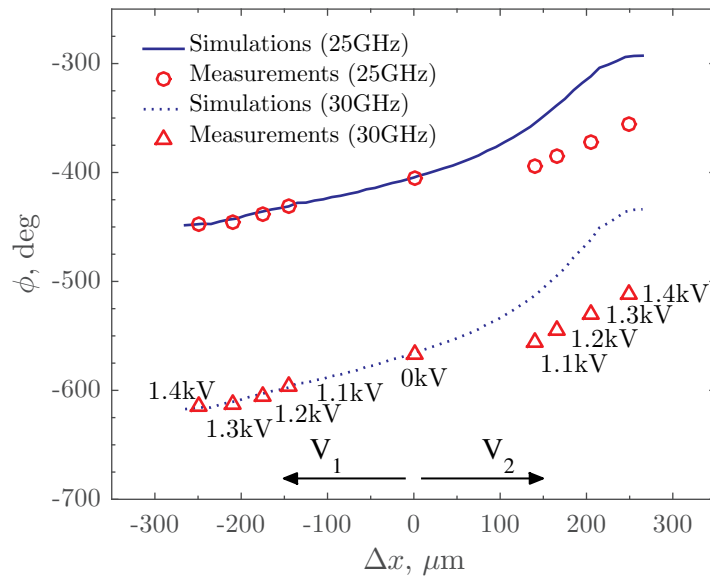


Figure 3.22 – Comparison between measurements and simulations for two different frequencies (25 GHz and 30 GHz) for actuation states $V_1 = V_2 = (1.1, 1.2, 1.3, 1.4)$ kV (V_1 input voltages shown as negative values). Full-wave simulations are performed using the commercial software Ansys HFSS. The Δx displacement values for the experiment data were measured prior to the MMW measurement.

displacements Δx (i.e., actuation of the ' V_1 ' DEA from Fig. 3.7), whilst a discrepancy exists for the positive displacements (i.e., actuation of the ' V_2 ' DEA from Fig. 3.7). This suggests that the V_2 DEA displacement during the RF measurement was different to its prior measured value, most likely due to disturbance caused during transport and test preparation. Moreover, as it has been discussed above, the ' V_2 ' actuator had an anomalous behavior during the displacement characterization (Fig. 3.20), which could be a contributing cause to this error. This type of uncertainty on the actuator displacement could be eliminated in future designs by implementing self-sensing [68] or closed-loop control capabilities [69]. Rosset et al. [69], for instance, proposed a closed-loop operation of the DEA actuator based on capacitive self-sensing. In the proposed configuration, the DEA device acts as actuator and integrated sensor simultaneously, without any need for external sensors. When a voltage is applied to a DEA segment, in fact, the compliant electrodes expand in area and the elastomer membrane is compressed in thickness, meaning that the associated capacitance increases. Thus, this capacitance is proportional to the actuation and can be used as self-sensing parameter. Rosset et al. [69] implemented this concept using a self-sensing control unit able to drive the actuator and to measure the associated capacitance at the same time. A similar approach would be definitely necessary for real applications where a precise and stable actuation displacement

is needed. Such an improvement would although necessarily come at the expense of device complexity and cost.

Figure 3.23 reports the comparison between measured and simulated scattering parameters over the full frequency range (25–35 GHz) for two of the measured phase shifter states (i.e., $V_1 = -1.4\text{ kV}$ and $V_1 = V_2 = 0\text{ V}$) shown in Fig. 3.22. The two states shown here correspond to voltages where a very good agreement was achieved in Fig. 3.22. Nevertheless, in the regions where a discrepancy exists (Fig. 3.22), the position of the movable loading part in the simulation must be logically fitted in order to compare simulations and measurements in a proper way.

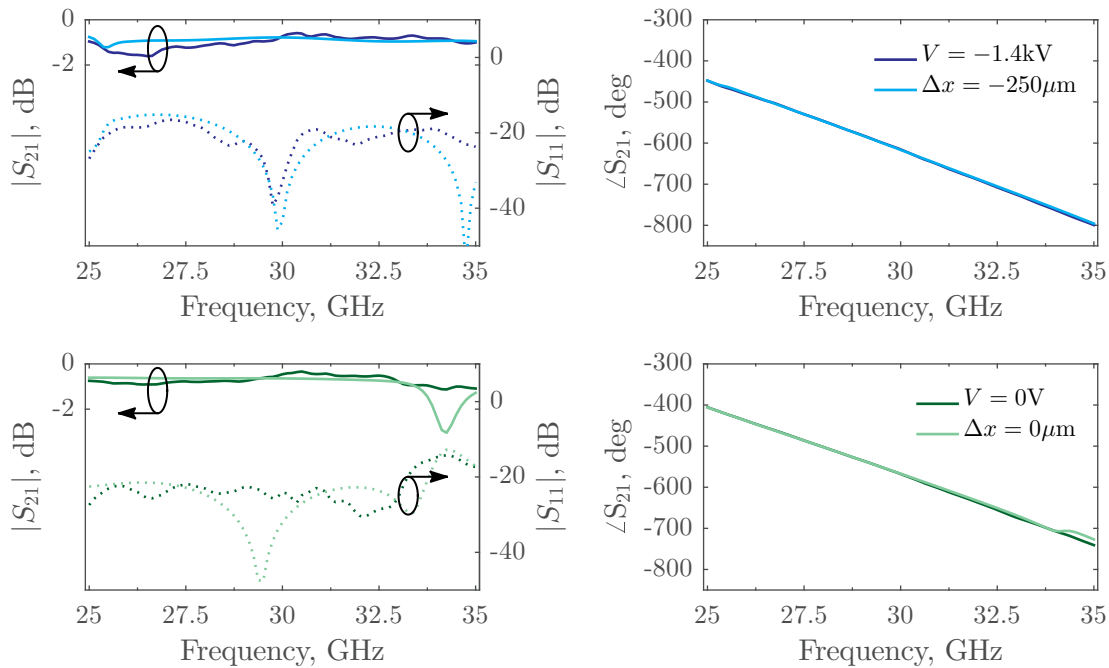


Figure 3.23 – Comparison between measurements and simulations over the complete frequency range (25–35 GHz) for two different actuation states ($V_1 = -1.4\text{ kV}$ and $V_1 = V_2 = 0\text{ V}$). The simulated curves are identified by their displacement Δx in the legend.

3.4 Conclusions

This chapter reported all the activities leading to the development of Ka-band reconfigurable phase shifters based on dielectric elastomer actuators (DEAs). Four different concepts have been proposed and their preliminary performance have been evaluated using full-wave simulations and analytical models where possible. All the proposed phase shifters consist of a fixed transmission line (i.e., CPW, RWG, microstrip) loaded by a movable element (dielectric or metallic), which perturbs the effective dielectric constant of the equivalent transmission line, thus varying the related propagation constant (and so the signal phase).

One device has been selected among the others on the basis of a trade-off between achievable performance and manufacturing complexity. The selected candidate consists of a conventional coplanar waveguide loaded by two suspended metallic strips, which are supported and horizontally displaced by a set of two agonist DEAs. The variable interaction between the fixed CPW and the movable loading strips generates a change in the effective permittivity of the line, thus modifying its propagation constant. The selected phase shifter has been optimized taking into account all the technological constraints and its final design has been manufactured using conventional PCB fabrication techniques available at EPFL and low-cost technologies. The resulting prototype has been characterized and tested in the frequency range 25–35 GHz, highlighting state-of-the-art performance in terms of phase-shift/loss figure of merit. Indeed, a mean value of $\sim 235^\circ/\text{dB}$ was achieved at 35 GHz, considerably outperforming MMIC phase shifters operating at similar frequencies and favorably comparing to lower-loss state-of-the-art MEMS reconfigurable phase shifters. The presented device represents the first proof of concept of tunable phase shifter based on DEA technology.

A comparison between the performance of the manufactured phase shifter with analogous reconfigurable devices based on conventional technologies (i.e., MEMS, MMIC, Ferrite) is reported in Tab. 3.4. These results demonstrate the potentials of DEAs for very low-loss analogue tuning of electromagnetic devices at millimeter-waves and, possibly, at higher frequencies, where available technologies (e.g., MMIC, MEMS, ferrites, liquid crystals) can come with unacceptable losses and cost. The presented DEA-based mechanical reconfiguration proved to be very efficient for the implementation of in-plane mechanical reconfiguration and could also be applied to the realization of other tunable devices in the microwave to terahertz band.

Table 3.4 – Performance comparison with tunable phase shifters available in literature and commercial devices operating in the same frequency range (i.e., Ka-band).

Device	Technology	Type	BW (GHz)	IL (dB)	RL (dB)	$\Delta\phi_{max}$ (deg)	Size (mm ²)
[23]	MMIC	5-bit	25–35	<7.8	>9	360	2.17×1.08
[70]	MMIC	5-bit	34–39	<16.5	>10	360	1.70×0.75
[71]	MMIC	4-bit	28–32	<9	>12	360	2.17×1.08
[34]	MMIC	1-bit	30–40	<4	>10	180	0.93×0.74
[39]	Ferrite	analog	22–26	<1	>23	360	–
[52]	MEMS	3-bit	25–35	<1.6	>15	315	3.50×2.60
[67]	MEMS	2-bit	32–36	<2.5	>11	270	–
<i>This work</i>	DEA	analog	25–35	<1.6	>10	180*	$50 \times 50^{**}$

* It is proportional to the length of the device due to the TTD operation (see eq. (3.3)).

** Size of the final prototype considering the manual assembly. Size minimization was not a priority for this first prototype, but dimensions could be further reduced in next design iterations.

Bibliography

- [1] R. Pelrine, R. Kornbluh, Q. Pei, and J. Joseph, "High-Speed Electrically Actuated Elastomers with Strain Greater Than 100%," *Science*, vol. 287, no. 5454, pp. 836–839, 2000.
- [2] H. Shea, "Miniaturized EAPs with compliant electrodes fabricated by ion implantation," in *Proc. SPIE 4695, Smart Structures and Materials: Electroactive Polymer Actuators and Devices (EAPAD)*, 2002, pp. 126–137.
- [3] F. Carpi, D. DeRossi, R. Kornbluh, R. Pelrine, and P. Sommer-Larsen, *Dielectric elastomers as electromechanical transducers. Fundamentals, materials, devices, models and applications of an emerging electroactive polymer technology*. Elsevier Press, 2008.
- [4] A. O'Halloran, F. O'Malley, and P. McHugh, "A review on dielectric elastomer actuators, technology, applications, and challenges," *Journal of Applied Physics*, vol. 104, no. 7, p. 071101, 2008.
- [5] S. Rosset, M. Niklaus, P. Dubois, and H. R. Shea, "Large-Stroke Dielectric Elastomer Actuators With Ion-Implanted Electrodes," *Journal of Microelectromechanical Systems*, vol. 18, no. 6, pp. 1300–1308, 2009.
- [6] S. J. A. Koh, T. Li, J. Zhou, X. Zhao, W. Hong, J. Zhu, and Z. Suo, "Mechanisms of large actuation strain in dielectric elastomers," *Journal of Polymer Science Part B: Polymer Physics*, vol. 49, no. 7, pp. 504–515, 2011.
- [7] H. Shea, "Miniaturized EAPs with compliant electrodes fabricated by ion implantation," in *Electroactive Polymer Actuators and Devices (EAPAD)*, vol. 7976, 2011, pp. 79 760R–79 760R–9.
- [8] J. Huang, T. Li, C. C. Foo, J. Zhu, D. R. Clarke, and Z. Suo, "Giant, voltage-actuated deformation of a dielectric elastomer under dead load," *Applied Physics Letters*, vol. 100, no. 4, p. 041911, 2012.
- [9] L. Dussopt and G. M. Rebeiz, "Intermodulation distortion and power handling in RF MEMS switches, varactors, and tunable filters," *IEEE Transactions on Microwave Theory and Techniques*, vol. 51, no. 4, pp. 1247–1256, 2003.
- [10] K. Daheshpour, S. J. Mazlouman, A. Mahanfar, J. X. Yun, X. Han, C. Menon, F. Carpi, and R. G. Vaughan, "Pattern reconfigurable antenna based on moving V-shaped parasitic elements actuated by dielectric elastomer," *Electronics Letters*, vol. 46, 2010.
- [11] S. J. Mazlouman, A. Mahanfar, C. Menon, and R. G. Vaughan, "A Review of Mechanically Reconfigurable Antennas using Smart Material Actuators," in *Proceedings of the 5th European Conference on Antennas and Propagation (EUCAP)*, 2011, pp. 1076–1079.
- [12] N. Tiercelin, P. Coquet, R. Sauleau, V. Senez, and H. Fujita, "Polydimethylsiloxane membranes for millimeter-wave planar ultra flexible antennas," *Journal of Micromechanics and Microengineering*, vol. 16, no. 11, p. 2389, 2006.

-
- [13] S. Hage-Ali, N. Tiercelin, P. Coquet, R. Sauleau, H. Fujita, V. Preobrazhensky, and P. Pernod, "A Millimeter-Wave Microstrip Antenna Array on Ultra-Flexible Micromachined Polydimethylsiloxane (PDMS) Polymer," *IEEE Antennas and Wireless Propagation Letters*, vol. 8, pp. 1306–1309, 2009.
- [14] S. Hage-Ali, N. Tiercelin, F. Lapierre, Y. Orlic, M. Harnois, V. Thomy, V. Preobrazhensky, P. Pernod, and P. Coquet, "An EWOD driven millimeter-wave phase shifter using a movable ultrasoft metalized PDMS ground plane," in *16th International Solid-State Sensors, Actuators and Microsystems Conference*. IEEE, 2011, pp. 522–525.
- [15] S. Hage-Ali, Y. Orlic, N. Tiercelin, R. Sauleau, P. Pernod, V. Preobrazhensky, and P. Coquet, "A millimeter-wave elastomeric microstrip phase shifter," in *IEEE MTT-S International Microwave Symposium Digest (MTT)*, June 2012, pp. 1–3.
- [16] F. Carpi, G. Frediani, and D. De Rossi, "Hydrostatically Coupled Dielectric Elastomer Actuators," *IEEE-ASME Trans. Mechatron.*, vol. 15, no. 2, pp. 308–315, 2010.
- [17] B. M. O'Brien, S. Rosset, I. A. Anderson, and H. R. Shea, "Ion implanted dielectric elastomer circuits," *Applied Physics A*, vol. 111, no. 3, pp. 943–950, 2013.
- [18] S. Akbari and H. R. Shea, "Microfabrication and characterization of an array of dielectric elastomer actuators generating uniaxial strain to stretch individual cells," *Journal of Micromechanics and Microengineering*, vol. 22, no. 4, p. 045020, 2012.
- [19] F. Carpi, C. Salaris, and D. D. Rossi, "Folded dielectric elastomer actuators," *Smart Materials and Structures*, vol. 16, no. 2, p. S300, 2007.
- [20] D. Teeter, R. Wohlert, B. Cole, G. Jackson, E. Tong, P. Saledas, M. Adlerstein, M. Schindler, and S. Shanfield, "Ka-band GaAs HBT PIN diode switches and phase shifters," in *IEEE MTT-S International Microwave Symposium Digest*, vol. 1, 1994, pp. 451–454.
- [21] A. S. Nagra, J. Xu, E. Erker, and R. A. York, "Monolithic GaAs phase shifter circuit with low insertion loss and continuous 0-360° phase shift at 20 GHz," *IEEE Microwave and Guided Wave Letters*, vol. 9, no. 1, pp. 31–33, 1999.
- [22] M. Albertini, A. Catalani, V. Guaiani, M. Migliorelli, and L. Russo, "T/R modules technology for Mobile terminals," in *Proceedings of the 5th European Conference on Antennas and Propagation (EUCAP)*, 2011, pp. 2636–2640.
- [23] J. G. Yang and K. Yang, "Ka-Band 5-Bit MMIC Phase Shifter Using InGaAs PIN Switching Diodes," *IEEE Microwave and Wireless Components Letters*, vol. 21, no. 3, pp. 151–153, 2011.
- [24] B.-W. Min and G. M. Rebeiz, "Ka-Band BiCMOS 4-Bit Phase Shifter with Integrated LNA for Phased Array T/R Modules," in *IEEE/MTT-S International Microwave Symposium*, 2007, pp. 479–482.

- [25] J.-G. Kim, D.-W. Kang, B.-W. Min, and G. M. Rebeiz, "A single-chip 36-38 GHz 4-element transmit/receive phased-array with 5-bit amplitude and phase control," in *IEEE MTT-S International Microwave Symposium Digest*, 2009, pp. 561–564.
- [26] C.-Y. Kim, D.-W. Kang, and G. M. Rebeiz, "A 44-46GHz 16-Element SiGe BiCMOS High-Linearity Transmit/Receive Phased Array," *IEEE Transactions on Microwave Theory and Techniques*, vol. 60, no. 3, pp. 730–742, 2012.
- [27] M. Dragoman, M. Block, R. Kremer, F. Buchali, F. J. Tegude, and D. Jager, "Coplanar microwave phase shifter for InP-based MMICs," in *22nd European Solid State Device Research Conference (ESSDERC)*, 1992, pp. 421–424.
- [28] R. Kremer, S. Redlich, L. Brings, and D. Jager, "A novel type of constant impedance travelling wave phase shifter for inP-based mmics," in *IEEE MTT-S International Microwave Symposium Digest*, vol. 1, 1996, pp. 265–268.
- [29] J. G. Yang, S. Choi, and K. Yang, "Highly miniaturised InP/InGaAs PIN MMIC switches using BCB-based multilayer technology," *Electronics Letters*, vol. 43, no. 18, pp. 981–983, 2007.
- [30] P. Bauhahn, C. Butter, V. Sokolov, and A. Contolatis, "30 GHz Multi-Bit Monolithic Phase Shifters," in *Microwave and Millimeter-Wave Monolithic Circuits*, vol. 85, no. 1, 1985, pp. 4–7.
- [31] K. Maruhashi, H. Mizutani, and K. Ohata, "Design and performance of a Ka-band monolithic phase shifter utilizing nonresonant FET switches," *IEEE Transactions on Microwave Theory and Techniques*, vol. 48, no. 8, pp. 1313–1317, 2000.
- [32] H. A. Atwater, "Circuit Design of the Loaded-Line Phase Shifter," *IEEE Transactions on Microwave Theory and Techniques*, vol. 33, no. 7, pp. 626–634, 1985.
- [33] R. V. Garver, "Broad-band diode phase shifters," *IEEE Transactions on Microwave Theory and Techniques*, vol. 20, no. 5, pp. 314–323, 1972.
- [34] "TriQuint TGP2104," <http://www.triquint.com/products/p/TGP2104/>.
- [35] W. Hord, "Microwave and Millimeter-wave Ferrite Phase Shifters," *Microwave Journal, State of the Art Reference*, pp. 19–31, 1989.
- [36] E. Schlomann, "Theoretical analysis of twin-slab phase shifters in rectangular waveguide," *IEEE Transactions on Microwave Theory and Techniques*, vol. 14, no. 1, pp. 15–23, 1966.
- [37] W. J. Ince and E. Stern, "Nonreciprocal remanence phase shifters in rectangular waveguide," *IEEE Transactions on Microwave Theory and Techniques*, vol. 15, no. 2, pp. 87–95, 1967.
- [38] A. Abuelma'atti, I. Khairuddin, A. Gibson, I. Morgan, and A. Haigh, "A Twin Toroid Ferrite Phase Shifter," in *IEEE/MTT-S International Microwave Symposium*, 2007, pp. 2067–2070.

-
- [39] "Ka-band high power toroidal ferrite phase shifter," <http://www.comdevintl.com/>.
- [40] C. R. Boyd, "A Dual-Mode Latching Reciprocal Ferrite Phase Shifter," *IEEE Transactions on Microwave Theory and Techniques*, vol. 18, no. 12, pp. 1119–1124, 1970.
- [41] F. Reggia and E. G. Spencer, "A New Technique in Ferrite Phase Shifting for Beam Scanning of Microwave Antennas," *Proceedings of the IRE*, vol. 45, no. 11, pp. 1510–1517, 1957.
- [42] G. M. Rebeiz, G.-L. Tan, and J. S. Hayden, "RF MEMS phase shifters: design and applications," *IEEE Microwave Magazine*, vol. 3, no. 2, pp. 72–81, 2002.
- [43] M. C. Scardelletti, G. E. Ponchak, A. J. Zaman, and R. Q. Lee, "RF MEMS phase shifters and their application in phase array antennas," in *IEEE Annual Conference on Wireless and Microwave Technology (WAMICON)*, 2005, pp. 191–194.
- [44] L. E. Larson, R. H. Hackett, and R. F. Lohr, "Microactuators for GaAs-based microwave integrated circuits," in *International Conference on Solid-State Sensors and Actuators*, 1991, pp. 743–746.
- [45] L. Larson, R. Hackett, M. Melendes, and R. Lohr, "Micromachined microwave actuator (MIMAC) technology - a new tuning approach for microwave integrated circuits," in *IEEE Microwave and Millimeter-Wave Monolithic Circuits Symposium*, 1991, pp. 27–30.
- [46] A. Malczewski, S. Eshelman, B. Pillans, J. Ehmke, and C. L. Goldsmith, "X-band RF MEMS phase shifters for phased array applications," *IEEE Microwave and Guided Wave Letters*, vol. 9, no. 12, pp. 517–519, 1999.
- [47] G. M. Rebeiz and J. B. Muldavin, "RF MEMS switches and switch circuits," *IEEE Microwave Magazine*, vol. 2, no. 4, pp. 59–71, 2001.
- [48] N. S. Barker, "Distributed MEMS Transmission Lines," Ph.D. dissertation, University of Michigan, Ann Arbor, 1999.
- [49] S. Barker and G. M. Rebeiz, "Distributed MEMS true-time delay phase shifters and wide-band switches," *IEEE Transactions on Microwave Theory and Techniques*, vol. 46, no. 11, pp. 1881–1890, 1998.
- [50] N. S. Barker and G. M. Rebeiz, "Optimization of distributed MEMS transmission-line phase shifters-U-band and W-band designs," *IEEE Transactions on Microwave Theory and Techniques*, vol. 48, no. 11, pp. 1957–1966, 2000.
- [51] B. Pillans, S. Eshelman, A. Malczewski, J. Ehmke, and C. Goldsmith, "Ka-band RF MEMS phase shifters for phased array applications," in *IEEE Radio Frequency Integrated Circuits (RFIC) Symposium*, 2000, pp. 195–199.
- [52] J. B. Hacker, R. E. Mihailovich, M. Kim, and J. F. DeNatale, "A Ka-band 3-bit RF MEMS true-time-delay network," *IEEE Transactions on Microwave Theory and Techniques*, vol. 51, no. 1, pp. 305–308, 2003.

- [53] Z. Wang, Z. Liu, and X. Li, "A Ka-band 3-bit RF MEMS switched line phase shifter implemented in coplanar waveguide," in *10th IEEE International Conference on Solid-State and Integrated Circuit Technology (ICSICT)*, 2010, pp. 1450–1452.
- [54] R. Malmqvist, C. Samuelsson, B. Carlegrim, P. Rantakari, T. Vaha-Heikkila, A. Rydberg, and J. Varis, "Ka-band RF MEMS phase shifters for energy starved millimetre-wave radar sensors," in *International Semiconductor Conference (CAS)*, 2010, pp. 261–264.
- [55] J. S. Hayden and G. M. Rebeiz, "A low-loss Ka-band distributed MEMS 2-bit phase shifter using metal-air-metal capacitors," in *IEEE MTT-S International Microwave Symposium Digest*, vol. 1, 2002, pp. 337–340.
- [56] B. Lakshminarayanan and T. M. Weller, "Design and modeling of 4-bit slow-wave MEMS phase shifters," *IEEE Transactions on Microwave Theory and Techniques*, vol. 54, no. 1, pp. 120–127, 2006.
- [57] P. Romano, S. Rosset, L. Maffli, H. Shea, and J. Perruisseau-Carrier, "Electromagnetic characterisation of flexible conductive membranes at millimetre-waves," *Electronics Letters*, vol. 49, no. 5, pp. 353–354, 2013.
- [58] R. N. Simons, *Coplanar Waveguide Circuits, Components, and Systems*. Newark, NJ: Wiley, 2001.
- [59] R. Legtenberg, A. W. Groeneveld, and M. Elwenspoek, "Comb-drive actuators for large displacements," *Journal of Micromechanics and Microengineering*, vol. 6, no. 3, p. 320, 1996.
- [60] C. Chen, C. Lee, Y.-J. Lai, and W. Chen, "Development and Application of Lateral Comb-Drive Actuator," *Japanese Journal of Applied Physics*, vol. 42, no. 6S, p. 4059, 2003.
- [61] O. Cugat, J. Delamare, and G. Reyne, "Magnetic micro-actuators and systems (MAGMAS)," *IEEE Transactions on Magnetics*, vol. 39, no. 6, pp. 3607–3612, 2003.
- [62] J. Wu, J. Lou, M. Li, G. Yang, X. Yang, J. Adams, and N. X. Sun, "Compact, low-loss, wide-band, and high-power handling phase shifters with piezoelectric transducer-controlled metallic perturber," *IEEE Transactions on Microwave Theory and Techniques*, vol. 60, no. 6, pp. 1587–1594, June 2012.
- [63] M. Mavridou, A. P. Feresidis, P. Gardner, and P. S. Hall, "Tunable millimetre-wave phase shifting surfaces using piezoelectric actuators," *IET Microwaves, Antennas Propagation*, vol. 8, no. 11, pp. 829–834, August 2014.
- [64] P. Romano, O. Araromi, S. Rosset, H. Shea, and J. Perruisseau-Carrier, "Tunable millimeter-wave phase shifter based on dielectric elastomer actuation," *Applied Physics Letters*, vol. 104, no. 2, p. 024104, 2014.

- [65] J. Perruisseau-Carrier, R. Fritschi, P. Crespo-Valero, and A. K. Skrivervik, "Modeling of periodic distributed MEMS-application to the design of variable true-time delay lines," *IEEE Transactions on Microwave Theory and Techniques*, vol. 54, no. 1, pp. 383–392, 2006.
- [66] O. A. Araromi, P. Romano, S. Rosset, J. Perruisseau-Carrier, and H. R. Shea, "A tunable millimeter-wave phase shifter driven by dielectric elastomer actuators," in *Proc. SPIE 9056, Electroactive Polymer Actuators and Devices (EAPAD)*, 2014, p. 90562M.
- [67] J. S. Hayden and G. M. Rebeiz, "Very low-loss distributed X-band and Ka-band MEMS phase shifters using metal-air-metal capacitors," *IEEE Transactions on Microwave Theory and Techniques*, vol. 51, no. 1, pp. 309–314, 2003.
- [68] T. A. Gisby, B. M. O'Brien, and I. A. Anderson, "Self sensing feedback for dielectric elastomer actuators," *Applied Physics Letters*, vol. 102, no. 19, p. 193703, 2013.
- [69] S. Rosset, B. M. O'Brien, T. Gisby, D. Xu, H. R. Shea, and I. A. Anderson, "Self-sensing dielectric elastomer actuators in closed-loop operation," *Smart Materials and Structures*, vol. 22, no. 10, p. 104018, 2013.
- [70] D.-W. Kang, J.-G. Kim, B.-W. Min, and G. M. Rebeiz, "Single and Four-Element Ka-Band Transmit/Receive Phased-Array Silicon RFICs With 5-bit Amplitude and Phase Control," *IEEE Transactions on Microwave Theory and Techniques*, vol. 57, no. 12, pp. 3534–3543, 2009.
- [71] "TriQuint TGP2100," <http://www.triquint.com/products/p/TGP2100/>.

4 A beam-scanning DEA reflectarray

This chapter presents the design and development of a reconfigurable reflectarray (RA) antenna based on dielectric elastomer actuators (DEAs) to implement 1-D beam-scanning capabilities. The proposed reconfiguration concept uses planar DEAs to achieve the mechanical tuning of the resonant length in rectangular microstrip patches on a grounded dielectric substrate. The proposed approach allows to decouple the actuation part from the electromagnetic (EM) active area, without contributing with additional losses with respect to the device fixed counterpart. The DEA-based reconfiguration principle is validated by developing an intermediate device consisting of a uniform array of tunable cells controlled by a single set of agonist DEAs, thereby generating a uniform reflection phase distribution. The final RA system is then obtained by implementing the independent control of each column of cells to realize 1-D beam-scanning in the H-plane of the antenna.

A general introduction to the reflectarray antenna system comprising a brief review of the technologies commonly used for the implementation of reconfigurable devices is presented in §4.1. The proposed reconfiguration principle based on the mechanical tuning of RA resonant elements is discussed in §4.2, and a reconfigurable reflective surface implementing and validating this approach is presented in §4.3. §4.4 reports the design of the first prototype of 1-D scanning RA using dielectric elastomer actuation. A summary of the chapter is found in §4.5.

4.1 Introduction

High-gain antennas are required in many remote sensing and communication systems, and are particularly needed for satellite applications where long distances have to be covered. Conventional high-gain antennas are typically implemented using two main configurations, namely phased arrays and reflectors [1].

Phased array antennas are generally planar structure integrating a large number of radiating elements connected to a complex beam forming network (BFN). A typical BFN includes

amplifiers and phase shifters, which allow to select the proper magnitude and phase of the electromagnetic field radiated by each element, in order to have the maximum of radiation in the desired direction. When the phase shifting properties of the BFN can be tuned (different phase profiles are realizable), beam-scanning capabilities are achieved. Moreover, magnitude control can be also introduced to obtain a particular shape of the radiated beam implementing beam-shaping functionalities. A symbolic representation of the basic phased array working principle is shown in Fig 4.1a, where a simplified 1-D linear array is depicted, although the same principle can be easily extended to a 2-D geometry. In this particular case a differential phase shift φ between adjacent radiating elements is necessary to obtain constructive interference of the field radiated by each element in the same selected direction. Phased array antennas generally offer high flexibility for antenna reconfiguration (especially beam-forming) and potentially all the possible beam directions and shapes are achievable. Nevertheless, current phased array technologies present some drawbacks related to the high-loss and complex BFN necessary to implement a given beam reconfiguration. Moreover, array antenna can become very expensive for MMW applications due to the high-cost amplifiers and phase shifter modules integrated in the BFN. Therefore, conventional phased array antennas can result in complex, heavy, and expensive structures with high power consumption, limiting their use in many practical applications.

Reflector antennas are widely used when high-gain communication links are needed. They consist of a focusing reflector illuminated by an external feed (e.g., a horn antenna). The spherical EM wave radiated by the feeding antenna impinges on the reflector and a planar wave is re-irradiated in the desired direction (the basic principle is illustrated in Fig. 4.1b). Thus, the reflected phase front is controlled by creating a difference in the path length of the field locally impinging on the reflector. Beam shaping is also possible by locally deforming the reflector surface. The position of the feed with respect to the reflector is typically fixed and beam scanning is possible through the mechanical movement of the antenna, meaning that an external motor is needed. Therefore, conventional parabolic reflectors are generally very bulky and can be inconvenient to implement advanced beam scanning functionalities, since these should be obtained through a mechanical movement of the feed and/or the reflector itself (typically small angles are achievable). Moreover, the manufacturing of this type of antennas can be complex and expensive, due to the particular needed shapes and materials of the reflecting surface.

A very interesting alternative to phased array and reflector antennas to implement a reconfigurable beam is the reflectarray (RA) antenna. RAs combine the advantages offered by both phased array (e.g., flat surface, electronic beam-forming) and reflector antennas (e.g., lack of BFN and high gain). A general description of the fixed-beam RA principle is reported in §4.1.1, and possible implementations of reconfigurable RAs are discussed in §4.1.2.

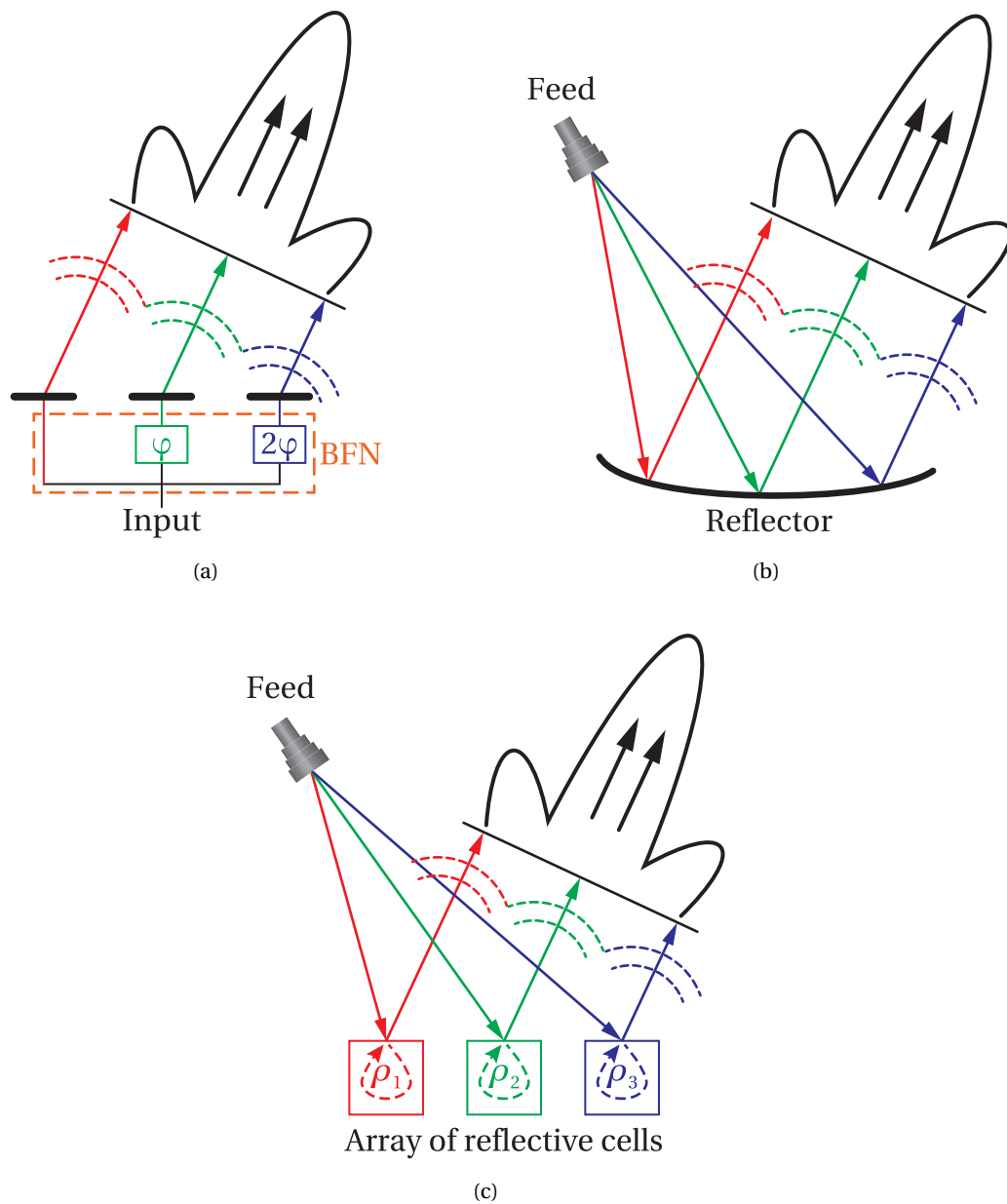


Figure 4.1 – Basic principle of conventional high-gain antenna configurations. (a) Phased array antennas use the electronic control of the different radiating elements (magnitude and phase) to point the beam in the desired direction. (b) Reflector antennas exploit the particular shape of the reflector to focus the radiation coming from the feed in a given direction. (c) RA antennas comprise a feed and a reflective surface consisting of an array of reflective cells. The reflection phase of each cell is selected to allow constructive interference of the radiated field in the pointing direction.

4.1.1 The reflectarray antenna

The principle of the reflectarray is well known and has been widely covered in literature (e.g., [2]). In brief, it consists of a reflector antenna where the usual reflector is replaced by a planar or conformal surface implemented by an array of unit cells, which allow for a local control of the reflection properties of the surface. Thus, this basic principle is very similar to the operation of conventional reflector antennas that utilize their particular curvature to compensate for the difference in the path length, in order to control the radiated beam. The desired radiation pattern is therefore obtained by properly designing the reflecting elements to generate a specific phase distribution on the reflector, which allows to coherently reflect the electromagnetic field radiated by the feeding antenna (usually a directional antenna such as a horn). The basic operating principle is schematically illustrated in Fig. 4.1c, where a 1-D array of generic unit cells is shown. Each reflecting cell is characterized by a reflection coefficient ρ_i properly selected to redirect the incident wave in the pointing direction. The reflectarray is clearly suitable to realize pencil-beam high-gain antennas; in this case, the reflector is tailored to form in the far field a planar phase front perpendicular to the desired given direction (θ_r, φ_r) . However, RAs are also a valid instrument to achieve particular contoured beams or multi-beam antennas, as needed in many satellite communications systems to realize a customized earth coverage.

The reflectarray concept was first demonstrated in the early sixties by Berry et al. [3] who proposed a reflected surface composed of a 2-D array of rectangular waveguides with the aperture directed towards the feeding antenna. The electromagnetic field radiated from the feed was coupling with the waveguide apertures and propagating inside them. The needed reflection phase distribution was achieved using short-circuited waveguides with different lengths, properly selected to compensate for the different path lengths of the feeding wave. Although the reflectarray principle was very promising, the first prototype was bulky and heavy and not particularly suitable for practical applications. Thus, advancements in this field only began a few decades later due to the development and improvement of printed circuit and planar antenna technology [4, 5]. Since then, microstrip technology has been widely utilized for the implementation of fixed-beam reflectarrays, since it allows to achieve very good antenna performance with low-profile, light-weight and low-cost structures.

Reflectarray antennas implemented with this approach consist of a planar array of printed reflecting cells, where the desired reflection phase profile is realized by varying a specific geometrical parameter in each element. In particular, three main techniques to control the reflection phase of printed unit cells can be considered. A common approach consists in using variable-size resonant elements such as rectangular patches [6], crossed dipoles [7], rings [8] and slots in a metal plane [9]. The change in the resonant length of each element allows to apply a different phase shift to the reflected wave. A further implementation is based on the use of variable-length microstrip stubs attached to the resonant patch, which act as a delay line for the impinging field that is radiated back by the reflective element [4, 10, 11]. Thus, the reflection phase is proportional to the length of the stub; however, the use of stubs generally

increases dissipative losses (due to the additional transmission line) and produce spurious radiation (since they are typically bent) that degrade the cross-polarization performance. When circular polarization is concerned, the use of identical elements with different rotation angle has been demonstrated [12]. With this approach, a given relative rotation α between different radiators allows to achieve a differential reflection phase equal to 2α for an incident circularly polarized wave.

Resonant patches of different shapes are very convenient, since they allow to obtain flat and low-profile reflectors using very low cost standard printed circuit board (PCB) techniques. Here we specifically focus on this method because it is the basic approach towards the reconfigurable reflectarray based on dielectric elastomer actuators described in §4.2 and §4.4. In particular, one possible implementation is represented by the use of resonant patches of different length: an array of rectangular metallic patches is printed on a grounded dielectric substrate, as illustrated in Fig. 4.2a, where a uniform array of square patches is shown. In this particular case, the operating principle of the RA is based on the well-known resonant behavior of the single cell shown in Fig. 4.2b. Note that square cells are illustrated in Fig. 4.2, but the same general principle applies to an array of rectangular patches. More specifically, the reflection phase can be locally controlled by changing the resonant length L_{patch} of each cell if the incident field is linearly polarized as illustrated in Fig. 4.2a. Each cell is represented by the resonant circuit reported in Fig. 4.2c, where the metallic patch is modeled by a shunt impedance ($R-C-L$ resonant circuit), the dielectric substrate by a transmission line of length H_{diel} and the ground plane by a short circuit. The values of R_p , C_p and L_p are varied depending on the size (L_{patch} for linear polarization) of the metallic patch, hence allowing to modify the resonance properties. Using rectangular or square patches, a total phase range approaching 360° can be obtained. Nevertheless, the total phase range achievable varying the length of the resonating patch strictly depends on the characteristics of the dielectric substrate (i.e., permittivity and thickness) at the design frequency. In particular, a total range of 330° can be obtained for thin substrates (less than a tenth of wavelength), but it reduces when thicker dielectrics are used.

Reflectarray surfaces based on resonant patches generally exhibit better performance in terms of losses and cross-polarization if compared to stub-based reflectarrays. However, the maximum achievable phase range is limited (in the order of 330°) and the phase dependence on the resonant length is strongly nonlinear. Moreover, this resonant behavior is quite narrow-band (relative bandwidth in the order of 3–5%), hence limiting the bandwidth of full reflectarray. Fig. 4.3 shows a typical example of reflection phase (left panel) and magnitude (right panel) curves from an infinite array of metallic rectangular patches printed on a grounded substrate. The cells are organized in a 2-D uniform lattice with period $0.5\lambda_0$ (λ_0 is the free space wavelength at the design frequency) in both directions. These results have been computed using HFSS full-wave simulations based on *Floquet* boundary conditions, which also allow to account for the mutual interaction between adjacent cells. The frequency of operation is $f_0 = 30\text{GHz}$ and the dielectric substrate ($\epsilon_r = 3.2$, $\tan\delta = 0.0018$; e.g., Rogers RO4232) is electrically thin ($H_{diel} = 500\mu\text{m}$, $\lambda_0 = 10\text{mm}$). The patch width W_{patch} (Fig. 4.2b) is fixed to

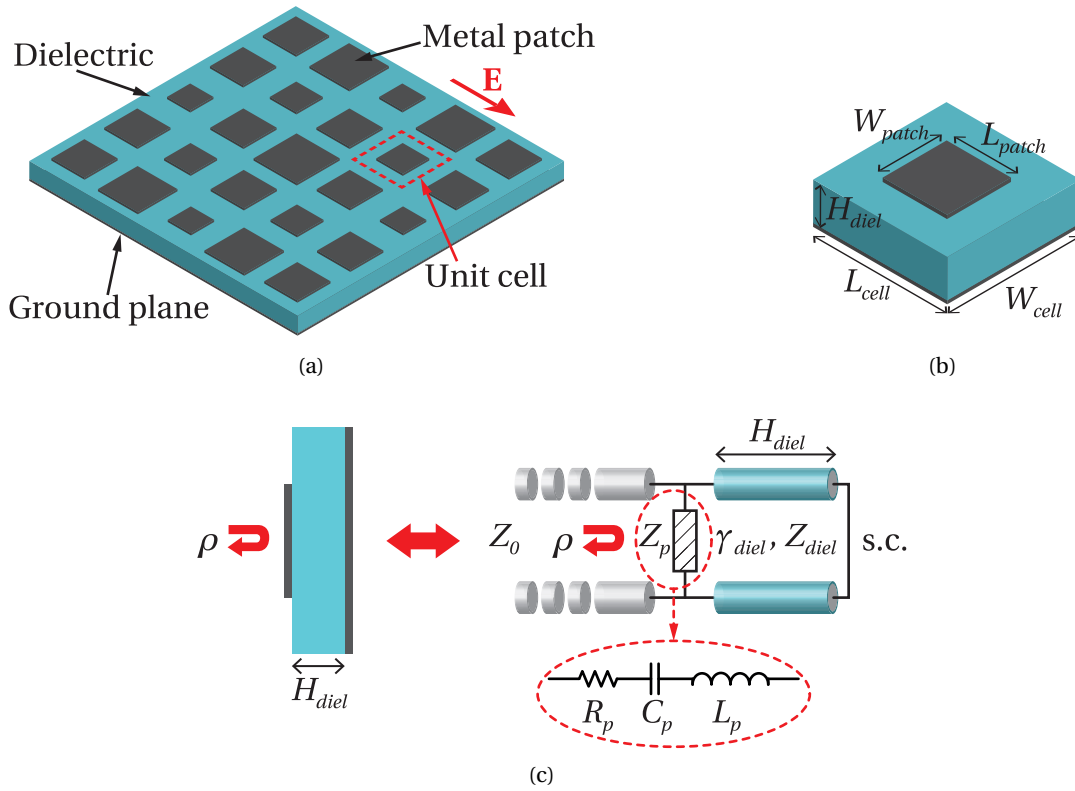


Figure 4.2 – Possible implementation of a reflectarray surface using resonant patches of different size. (a) Array of equally-spaced patches printed on a grounded dielectric substrate. Note that patches are square in the drawing, but the same principle applies to generic rectangular elements. (b) Reflectarray unit cell consisting of a square patch on grounded dielectric. The reflection phase of the cell is controlled by varying L_{patch} if a linear polarization is considered. (c) Equivalent transmission line model of the resonant patch cell. The metal patch is represented by the shunt impedance Z_p , the dielectric substrate by a TL of length H_{diel} and the ground plane by a short circuit.

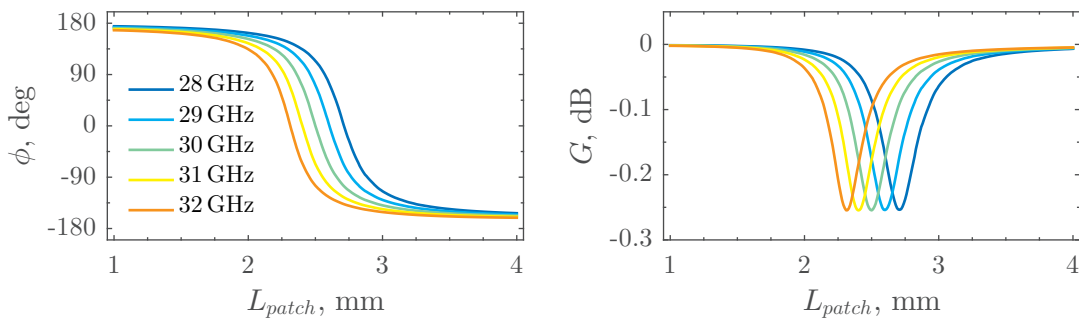


Figure 4.3 – Typical reflection phase (left) and magnitude (right) curves for an infinite array of rectangular patches under normal incidence. The curves are function of the patch length L_{patch} and W_{patch} is fixed to 2 mm. The design frequency is $f_0 = 30$ GHz, and the substrate is $500 \mu\text{m}$ thick with a permittivity of 3.2.

2 mm and the patch length L_{patch} is varied between 1 mm and 4 mm to have a phase profile centered at $L_{patch} = 2.5$ mm. As mentioned above, the phase variation as a function of L_{patch} is nonlinear (typical “S shape”), since the patch on a grounded substrate exhibits a high-Q resonant behavior. Therefore, the phase variation is steep around the resonance ($\phi = 0^\circ$) and smoother at the extremes of the length variation, making the device also sensitive to fabrication tolerances in the range where the slope is maximum. For the same principle a bigger variation of the phase response as a function of the operating frequency is generated in that region (i.e., the bandwidth is limited). A smoother slope can be obtained increasing the thickness of the dielectric substrate (the Q factor of the resonance is decreased) at the expenses of the maximum achievable phase range (a similar effect can be obtained reducing the substrate permittivity). A possible solution to realize a smoother phase response was proposed in [13, 14], and consists in implementing a stack of two or three layers of patch arrays. This technique allows to generate multiple resonances, which increase the total phase range (up to twice 360° was demonstrated in [13, 14]) without the need to use very thin substrates. In this way a smoother curve is obtained allowing also to improve the element bandwidth (up to 10 %).

The advantages and limitations of fixed-beam reflectarrays based on printed technology with respect to conventional reflectors and fixed-beam phased arrays have been extensively discussed in literature (e.g., [2]) and can be also extracted from the previous discussion. For the sake of clarity, a small summary is added here. Compared to conventional fixed-beam phased arrays, reflectarrays typically exhibit a lower complexity due to the lack of a BFN. This aspect obviously results also in reduced losses and cost, which are especially critical for high-gain and high-frequency applications. As far as standard reflectors are concerned, the reflectarray system is advantageous in terms of planarity of the reflector, weight and cost, since it is much easier to manufacture than a parabolic reflector. However, the main drawback of reflectarray antennas lies in the limited bandwidth achievable with conventional designs. Although reflectarrays generally outperform their planar phased array counterpart, they offer poor performance (in terms of bandwidth) compared to parabolic reflectors (which ideally provide infinite bandwidth, owing to their true-time-delay nature). In contrast, the cross-polarization is generally low for dual-polarized reflectarrays, which can be designed to have each polarization operating at a different frequency. In conclusion, when fixed-beam arrays are concerned, the main advantages of the reflectarray rely on size, weight and cost reduction, rather than on electrical performance. Therefore, the targeted application rules the choice of a given antenna system according to a clear trade-off between desired antenna performance (i.e., bandwidth, efficiency, cross-polarization), mechanical characteristics and cost. Different considerations can be made when reconfigurable devices are concerned (cf. §4.1.3).

4.1.2 Reconfigurable reflectarray antennas

Reflectarray antennas are particularly suitable for the implementation of reconfigurable concepts. Reconfiguration capabilities can be implemented through the adaptive control of the reflection phase in each unit cell. This way any phase distribution (i.e., any radiated beam) can be implemented real time allowing for flexible beam scanning and beam shaping functionalities. Great interest is currently addressed to RAs for the implementation of reconfigurable antenna systems, in particular for beam-steering applications. The main advantages discussed above for the fixed-beam reflectarray in terms of complexity, weight and cost (compared to conventional phased arrays and reflectors) still remain when a given reconfiguration is added. In this context, target applications for the reconfigurable RA concern space systems, where a reconfigurable radiation needs to be achieved with reliable performance while keeping very low volume and mass budget. Potential applications lie in earth observation (e.g. Synthetic Aperture Radar), atmospheric remote sensing (e.g. weather radars, radiometers) and high data-rate communications (e.g. satcom on the move, VSAT). Concerning the space segment, reconfigurable RAs could be advantageously mounted on both low earth orbit (LEO) and geosynchronous orbit (GEO) spacecrafts due to their low-weight and low-size structure, while keeping electrical performance comparable to conventional phased array and reflector antennas. Moreover, their flat structure could be more easily and safely deployed when stowed antennas are needed to arrange the whole satellite inside the launch vehicle. Regarding the Earth segment, tunable reflectarrays would be very advantageous for emerging commercial telecommunication missions at Ku and Ka-band where low-cost mobile user terminals, with possibly low profile, are needed for moving vehicles. Further applications can be identified and include automotive radar, medical imaging, airborne synthetic aperture radar and ground radar.

Different techniques and materials are currently available for the implementation of a given electromagnetic reconfiguration in the RA concept, such as semiconductors (i.e., PIN and varactor diodes), RF-MEMS, Liquid Crystal, and ferroelectrics [15]. As we have already discussed in §3.1, all these technologies come with different advantages and disadvantages, which also highly depend on the addressed frequency and reconfiguration concept. However, a common feature to all these technologies is the significant increased loss and complexity with regard to the devices fixed counterpart. Moreover, both loss and complexity further increase when high-performance reconfiguration capabilities are needed at millimeter-waves and above. The main technologies used thus far for the implementation of reconfigurable RA elements are summarized here. Moreover, relevant examples from the literature are discussed.

Semiconductor technologies, namely varactor and PIN diodes, have been extensively used for the variable loading of planar reflectarray cells and a few demonstrations can be found in [16–22]. Their wide use in the reconfiguration of reflectarrays is mainly due to their technology maturity, which allows for efficient designs based on simple and inexpensive manufacturing processes. Varactors provide a continuous (i.e., analog) capacitive load, whereas PIN diodes only implement a two-states (ON and OFF) reconfiguration resulting in digitally controlled

devices. A beam-scanning reflectarray based on varactor loading and operating at 5.8 GHz was for instance demonstrated by Hum et al. [18]. The proposed unit cell consisted of a microstrip patch divided in two segments connected in series by two varactor diodes that allowed to tune the resonance properties of the patch generating a reflection phase range of around 325° . A prototype consisting of an array of 10×7 tunable elements was manufactured and tested demonstrating very good beam-scanning capabilities. An example of X-band switched-beam reflectarray using the digital control offered by PIN diodes was presented by Carrasco et al. [20]. The reflector was divided in subarrays composed of two patches aperture-coupled to microstrip lines. The two elements were gathered in each subarray and therefore coupled to the same delay line, which was divided in two segments connected by a surface-mounted PIN diode. The proposed reflectarray used a simple control (i.e., forward biasing of half of the diodes at a time) to switch the beam between three fixed directions, namely -5° , 0° and 5° on a tilted plane with respect to the normal. An interesting example of fully functional reflectarray system can be found in [22], where a dual-reflectarray with beam-scanning functionality is presented. The prototype was developed in the frame of the ESA project RESKUE targeting a transportable ground terminal for Ku-band commercial telecommunications. The reflectarray comprises a rectangular subreflector consisting of a multilayer patch-based reflectarray and a pentagonal main tunable reflector, which is composed of an array of multiresonator cells, each one integrating two PIN diodes. The deployable reflectarray system exhibited a wide range of beam-scanning based on a 1-bit phase quantization. However, due to the high complexity of the system and large number of embedded PIN diodes, limited efficiency was achieved. The main limitation concerning semiconductor-based reflectarrays is represented by the high loss that can drastically degrade antenna efficiency especially at MMW frequency and above.

RF-MEMS offer the possibility of monolithic integration with improved performance in terms of losses (upto W-band) with respect to varactor and PIN diodes [23–28]. Moreover, they provide very good linearity and very small DC power consumption. Nevertheless, they can present reliability issues and rely on advanced cleanroom fabrication processes (complex and expensive). In addition, they do not allow for analog tuning (MEMS varactors typically suffer from reliability issue and have been barely used) which can be a limitation in specific applications. Different MEMS-based reconfigurable cells have been proposed, but only a limited number of full reflectarray systems can be found in literature, although RF-MEMS technology has improved in maturity in the last years. One of the first example of reflectarray cell controlled by MEMS switches was proposed in [23] to operate at Ka-band in circular polarization. The classical “rotation technique” (e.g., [12]) was there dynamically implemented using MEMS switches to connect dipole elements radially placed around a round patch in the middle of the cell. However, the full reflectarray was subsequently built only using static MEMS (i.e. without actuation) to prove the concept. Analog MEMS varactor were used in [24] to implement a capacitive load in resonant patch cells. The elementary cell and the reconfiguration approach was the same as previously implemented by the same author using varactor diodes [18]. The use of MEMS loading element allowed to improve loss and intermodulation performance with respect to the diode counterpart, but the measured phase

range was limited by the maximum capacitance achievable without damaging the MEMS device. Very good performance were demonstrated by Perruisseau-Carrier and Skrivervik [25] for a reconfigurable monolithic unit cell based on digital MEMS capacitor at X-band. Five pairs of MEMS switches were acting as series capacitors in a segmented ring geometry implementing 32 reconfiguration states. The experimental characterization was performed for the two extreme states (with “frozen” MEMS) demonstrating a full 360° phase distribution with very low losses in a 10 % bandwidth.

The reconfiguration techniques discussed above (i.e., semiconductor diodes and RF-MEMS) are practically based on the integration of tunable lumped elements in basic reflectarray elements. A different approach relies on the embedding of thin-film materials with particular properties that can be controlled using an external bias. In this category we can include ferroelectric thin-films [29], which allow for monolithic integration and demonstrated analog phase control with a potential for very low power consumption. Their losses though are generally higher than RF-MEMS devices. Liquid crystal have also found application as tunable substrates in reflectarray elements from microwave to sub-MMW [30–33]. Liquid crystals offer interesting tuning properties based on the variation of their effective dielectric constant when an external biasing field is applied. However, their main drawback is represented by the high losses (up to 15 dB) and complex control circuitry.

4.1.3 Basics of the reflectarray antenna

A thorough theoretical discussion on reflectarray analysis and design is clearly beyond the scope of this manuscript. However, some basic principles and performance figure of merit are summarized in the following, since are essential to evaluate the potential implementation of the reflectarray concept using DEA such as provided in the next sections.

As already mentioned above, the radiation pattern of reflectarray antennas is designed by properly choosing the reflection phase of each radiating element (once the radiation properties and the position of the feed are defined). When a pencil beam is desired in a given direction, the reflection phase of each element needs to be selected according to two principles: i) compensation of the different phase delay of the incident wave coming from the feed, and ii) radiation of a planar phase front orthogonal to the selected direction. For a generic reflectarray consisting of an array of unit cells illuminated by an offset feed, the reference system of Fig. 4.4 can be considered. When a pencil beam in the direction (θ_r, φ_r) is desired, it is possible to demonstrate that the two conditions mentioned above translate in the following reflection phase needed at the mn element ($m = 1, \dots, M; n = 1, \dots, N$):

$$\phi_{mn} = \underbrace{k_0 |\mathbf{r}_{mn} - \mathbf{r}_f|}_{\phi_{mn,1}} - \underbrace{k_0 (x_{mn} \cos \varphi_r + y_{mn} \sin \varphi_r) \sin \theta_r}_{\phi_{mn,2}}, \quad (4.1)$$

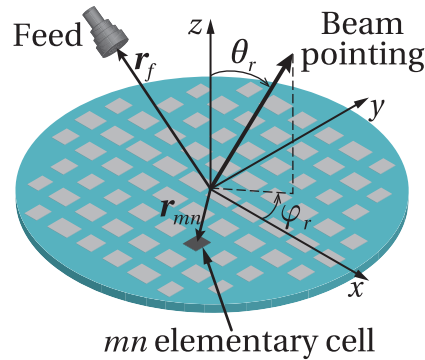


Figure 4.4 – Reference system for a generic reflectarray analysis and phase distribution calculation. The reflective surface consists of an array of $M \times N$ cell illuminated by a feed placed in $\mathbf{r}_f = [x_f, y_f, z_f]$. The radiated beam points towards the direction (θ_r, φ_r) .

where k_0 is the free space propagation constant, $\mathbf{r}_{mn} = [x_{mn}, y_{mn}, 0]$ is the position vector of the mn cell, $\mathbf{r}_f = [x_f, y_f, z_f]$ is the position vector of the feed and (θ_r, φ_r) is the pointing direction in spherical coordinates (Fig. 4.4). The first term $\phi_{mn,1}$ of eq. (4.1) allows to compensate for the different phase delays associated to the path lengths from the feed to the different array elements. $\phi_{mn,2}$ on the other hand, is calculated according to the standard phased array antenna theory and represents the phase distribution needed to realize planar phase fronts orthogonal to the direction (θ_r, φ_r) in the far field [1]. A total phase range of 360° would be ideally necessary to design a given beam. However, in practical applications, lower values (example around 300°) are totally acceptable resulting only in a very small degradation of the antenna gain (around 0.2 dB) and slightly higher side lobe levels. In fact, the total phase range is typically digitally quantized using a limited number of bits. As an example, the work presented by Rodrigo et al. [21] demonstrated a reflectarray cell providing a full phase range of 270° leading to a rms phase error of only 6.5° . The loss in directivity was evaluated to only 0.1 dB using standard array antenna theory.

It is clear from eq. (4.1) and previous discussion that an accurate characterization of the selected unit cell (i.e., reflection magnitude and phase) as a function of the control parameter (L_{patch} in the presented example) is necessary to carry out any reflectarray design. Different methods for the analysis and design of reflectarray antennas have been proposed and are extensively discussed in literature (e.g., [2]). Full-wave techniques, including Method of Moments, Finite Difference Time Domain and Finite Element Method, are by far the most used since they represent a valid approach to accurately and efficiently predict the unit cell performance. A very common full-wave technique is based on the use of an infinite array approximation with the application of the Floquet's theorem. This approach is very efficient in the case of planar arrays with a large number of elements when other methods might be computationally expensive. The analysis is in fact reduced to the single unit cell in a Floquet periodic environment, allowing to also account for the mutual coupling between adjacent cells. It is worth noting that all the designs presented in this chapter were obtained implementing

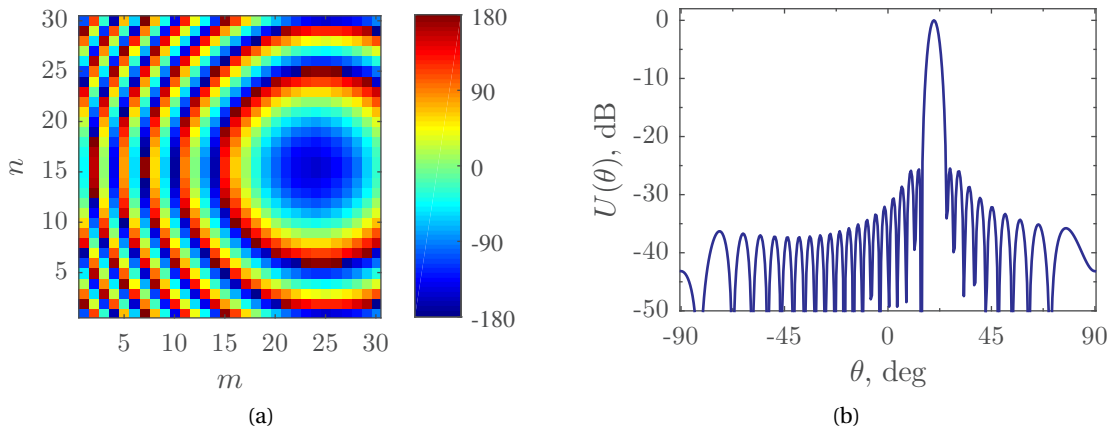


Figure 4.5 – Radiation pattern example for a planar array of 30×30 elements. (a) Phase distribution needed to generate a pencil beam in the direction $(20^\circ, 0^\circ)$ at 30 GHz. The feeding antenna is placed in the center of the array at a distance of 112.5 mm ($f/D = 0.75$). (b) Normalized radiation pattern in the principle plane xz corresponding to the reflection phase distribution illustrated in (a).

the Floquet periodicity in the commercial full-wave solver HFSS.

Once the reflection phase and losses of the unit cell have been accurately predicted (i.e., curves similar to Fig. 4.3 have been obtained), it is particularly important to evaluate the radiation pattern of the full reflectarray. This process obviously require that the position (with respect to the reflector) and radiated properties of the feed have been defined. A good approximation for the feed radiation pattern is represented by a $\cos^q(\theta)$ model, but more accurate calculations can be performed to improve accuracy. In addition, the shape and size of the reflector need to be fixed. Circular apertures are generally preferred to reduce spillover losses and consequently improve aperture efficiency, whereas the size of the reflector is selected according to the desired gain and the target application. Two main approaches can be used for the calculation of the reflectarray radiation properties [34]. The first method is based on conventional phased array antenna theory for a two-dimensional planar array consisting of $M \times N$ cells. The excitation of each element is properly calculated considering the incident field from the feed and the needed reflection phase calculated using eq. (4.1). This approach is generally accurate and allows fast computation also for large arrays. In contrast, it does not allow to calculate the cross-polar radiation. The second method is more complex and allows to calculate both the co- and cross-polar components of the radiated field. The first step consists in calculating the tangential field on the aperture, which is then integrated to obtain the far field radiated field. This last step involve a double integral which correspond to a two-dimensional Fourier transform of the tangential excitation and therefore, can be evaluated using a Fast Fourier Transform algorithm to optimize the computation. The two approaches mentioned above exhibit similar accuracy in the calculation of the co-polar radiation pattern [34]. However, when the knowledge of the cross-polarization performance

is needed, the method based on the integration of the aperture field has to be used at the expense of computation complexity and time.

Here we present an example of radiation pattern calculation for a planar array of 30×30 equally-spaced cells (e.g., rectangular patches) designed to radiate a pencil beam in the direction $(20^\circ, 0^\circ)$ at the operating frequency $f_0 = 30$ GHz. For the scope of this example, we were not interested in the cross-polarization performance, and the calculation was performed using the array antenna theory. Considering the reference system illustrated in Fig. 4.4, the far field radiation can be calculated using the following expression, where both the radiation properties of the feed and of each reflecting element are considered [12]:

$$E(\theta, \varphi) = \sum_{m=1}^M \sum_{n=1}^N \cos^{q_e} \theta \cos^{q_f} \theta_e \frac{\cos^{q_f} \theta_f}{|\mathbf{r}_{mn} - \mathbf{r}_f|} e^{-jk_0(|\mathbf{r}_{mn} - \mathbf{r}_f| - x_{mn} \sin \theta \cos \varphi - y_{mn} \sin \theta \sin \varphi)} e^{j\phi_{mn}}, \quad (4.2)$$

where θ_f and θ_e are the spherical angles (function of m and n) in the feed and array element coordinate system, respectively. Moreover, the feed radiation pattern is modeled by a $\cos^{q_f} \theta$ function, and the element radiation pattern is accounted using a $\cos^{q_e} \theta$. The reflection phase ϕ_{mn} is obtained using eq. (4.1). The phase distribution of Fig. 4.5a was calculated using eq. (4.1) for a square array of 30×30 cells spaced of $\lambda_0/2 = 5$ mm in both directions. The feed is placed in the center of the array at a distance of 112.5 mm ($f/D = 0.75$) from the reflector. The corresponding radiation pattern for the phase distribution of Fig. 4.5a is reported in Fig. 4.5b, showing the expected pencil beam at 20° in the xz plane (cf. 4.4).

An important aspect to consider in the design of reflectarray antennas lies in the choice of the proper spacing between adjacent cells to avoid the generation of grating lobes. A design rule can be easily derived from the array antenna theory and is expressed by the following relation:

$$\frac{p}{\lambda_0} \leq \frac{1}{1 + |\sin \theta_{r,i}|}, \quad (4.3)$$

where p is the array period (typically equal in both x and y direction) and $\theta_{r,i}$ is the beam pointing angle or the incidence angle of the feeding radiation, with the maximum angle ruling the relation above. It is clear from eq. (4.3) that in the case of center-fed systems, the element spacing should be selected according to the limitation imposed by the cells towards the edges of the array, where the incident angle is bigger. This condition is even more stringent for offset feeding if we consider the elements further with respect to the feed position. Therefore, the ideal choice would consist in selecting a non-uniform spacing of the elements according to their position on the array, allowing more flexibility in the design of the unit cells. However, for practical reasons a uniform lattice period is preferred in most designs. An element spacing smaller than $0.5\lambda_0$ typically represents a good design choice allowing to have a radiation free

of grating lobes for a wide range of incident/radiated angles.

4.2 Variable-size resonators RA using DEA

4.2.1 Motivation

Tunable reflectarrays are typically realized by implementing a reconfiguration mechanism within the unit cell to enable dynamic control of the reflection phase. This is for instance possible using controllable lumped loading element (e.g., semiconductor diodes) or tunable materials (e.g., ferroelectrics and liquid crystals). The main technologies currently used for the implementation of reconfigurable reflectarrays have been discussed and summarized in §4.1.2.

Here we propose a reconfigurable reflectarray based on DEAs. This device will mechanically reconfigure RA elements using a tuning approach (i.e., in-plane actuation) similar to the one successfully applied to the phase shifter discussed in the previous chapter. This choice is motivated by the appealing properties of DEAs for mechanical reconfiguration in RA systems, including inexpensive materials and fabrication, relatively large and analog displacement (due to the voltage-dependent strain output), and very low DC power consumption. Moreover, the microscale mechanical reconfiguration principle associated with DEA technology results in MMW losses comparable to those of non-reconfigurable systems. This is crucial for the concerned applications, and can represent a significant advantage over competing technologies as confirmed by the use of DEAs for the reconfiguration of MMW phase shifters [35]. Therefore the combination of the reflectarray concept and DEA actuation have the potential to address some of the most acute needs in beam scanning for millimeter-wave applications, namely:

- analog control of reconfiguration,
- relatively simple and inexpensive technology,
- potential scalability to higher frequencies (>100 GHz),
- low average electromagnetic loss,
- very low power consumption.

Within the scope of beam-scanning reflectarrays, we want to develop a first proof of concept of DEA-based reconfigurable RA implementing scanning capabilities in one plane. The conceived device should be easily manufacturable and suitable for manual assembly, in order to come up with a very low cost antenna that can be easily prototyped and tested (similarly to the approach adopted for the phase shifter of chap. 3).

4.2.2 Proposed reconfiguration concept

Considering the above constraints in terms of low-complexity and low-cost structures, we propose the implementation of a reconfigurable RA based on a planar array of tunable printed patches on a grounded dielectric substrate. In §4.1.1 we have previously shown that RA elements implemented by rectangular microstrip patches allows to achieve a phase range approaching 360° , which is a function of the patch length L_{patch} (Fig. 4.3). We have also seen in §4.1.2 that rectangular patches have been used for the implementation of electronically tunable RA cells where the resonance properties were varied using for instance varactor diodes [18] or MEMS capacitors [24].

Here we propose a mechanically reconfigurable RA patch element where the size of the patch can be dynamically changed. The envisioned reconfiguration mechanism consists in the use of in-plane DEA expansion to horizontally displace a movable patch over a fixed one. The basic operation principle is shown in Fig. 4.6a for the single cell: if the movable and fixed patches are in ohmic contact and metal thickness is small, a displacement ΔL of the moving plate with respect to the fixed one exactly corresponds to an increment ΔL of the equivalent patch length. In particular, if the two patches have the same size, the equivalent patch length is almost doubled (a given overlap has to be assured) at the maximum possible displacement. Therefore, a reflection response similar to the curves of Fig. 4.3 is achievable. The reflectarray surface is then obtained realizing an array of equally spaced reconfigurable cells as symbolically depicted in Fig. 4.6b. A 1-D scanning reflectarray can be implemented if we assume that the cells in each column are controlled by the same actuation voltage (i.e., same displacement), hence exhibiting the same reflection phase. Therefore, if the independent control of each column of cells is implemented, the radiated beam can be scanned in the principle plane xz for the linear polarization (\mathbf{E} field) shown in Fig. 4.6b. Note that Fig. 4.6 is only intended to explain the operating principle of reconfiguration, without including the actuation part.

In order to validate the envisioned beam-scanning principle based on the independent control of each column of cells (Fig. 4.6b), a simulated example is presented. Let us consider a uniform array of 30×30 cells operating at 30 GHz. The spacing between cells is fixed to $\lambda_0/2$ ($\lambda_0 = 10$ mm) and all the elements in each column operate in the same reconfiguration state (i.e. same reflection phase). The feed (e.g., a standard horn) is placed in the center of the array at a distance of 112.5 mm ($f/D = 0.75$) from the reflective surface, and its radiation pattern is modeled by a $\cos^{q_f} \theta$ function ($q_f = 6$ here). Under this assumption, two examples of realistic phase distribution are calculated using eq. (4.1) to point the radiated beam towards $(10^\circ, 0^\circ)$ (Fig. 4.7a) and $(30^\circ, 0^\circ)$ (Fig. 4.7b), respectively. With the conceived center-fed configuration the phase distribution on the full array has been selected according to the profile calculated for the central n row. The corresponding radiation pattern for the two reconfiguration states is shown in Fig. 4.7c. These results were obtained using the array theory calculation described in §4.1.3. It is worth noting that this reconfiguration approach (and related phase distribution) allows to produce a fan-beam with a narrow beamwidth in the H -plane (Fig. 4.7c) and wider beam in the E -plane. This radiation configuration depends on the particular phase distribution

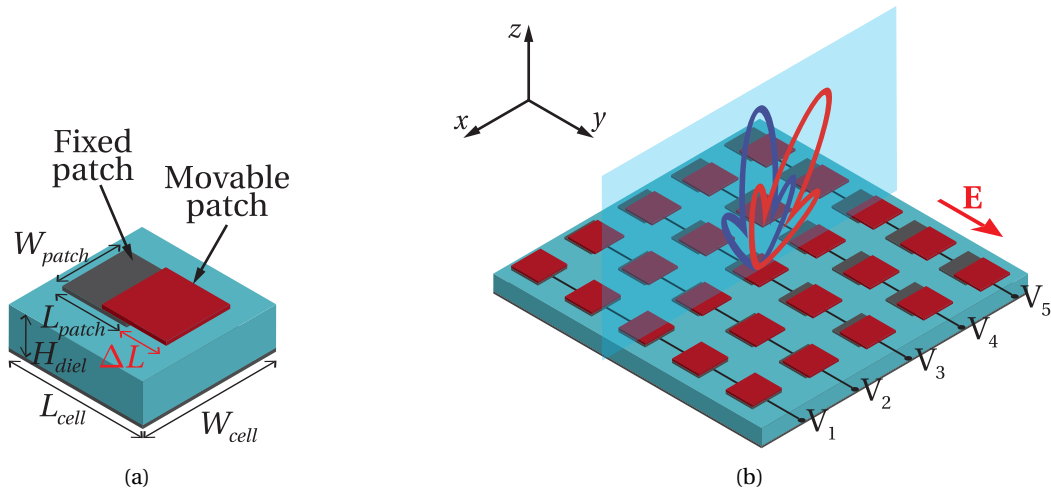


Figure 4.6 – Symbolic illustrations of a reconfigurable RA surface based on mechanically tunable resonating patches. (a) Single cell made up of a fixed metal patch on a grounded substrate and movable metal patch displaced using DEAs (not included in this simplified drawing). (b) Array of equally spaced reconfigurable cells affecting the reflection of an EM field polarized as indicated by the red arrow (E field). The number and dimensions of the cells are chosen only for illustration purposes.

(constant for each column) that does not allow to compensate for the different path length from the feed to the cells towards the edges (in the y direction) of the array. The effect of this error in the differential phase delay compensation is more evident when large arrays are considered or when a small f/D ratios are used (i.e., the path length are very similar when $f/D \rightarrow \infty$). Cross-polarization performance were not evaluated in this example, since results comparable to standard reflectarrays based on resonant rectangular patches are expected.

These simulated results demonstrate the promising opportunities for beam scanning offered by the proposed approach. The individual control of each column of unit cells allows to obtain any desired phase distribution in one given direction, offering the opportunity for 1-D beam scanning. Moreover, this would come with good expected performance and losses comparable to the analogous fixed-beam reflectarray if the simulated results were duplicated in the fabricated device. In fact, although the effect of actuators has not been considered in this example, we are targeting a DEA reconfiguration approach similar to the one described in chap. 3, and therefore allowing to completely decouple the actuation part from the EM-active area. More details about the optimization and the practical implementation of this reconfigurable reflective surface are given in the next sections. However, here a further detail of the proposed tuning approach needs to be addressed.

The reconfiguration approach symbolically illustrated in Fig. 4.6 requires good physical contact between the movable and fixed patches to achieve variation of the patch length within minimal losses. Therefore, in the static configuration (i.e., no ongoing reconfiguration) the bottom

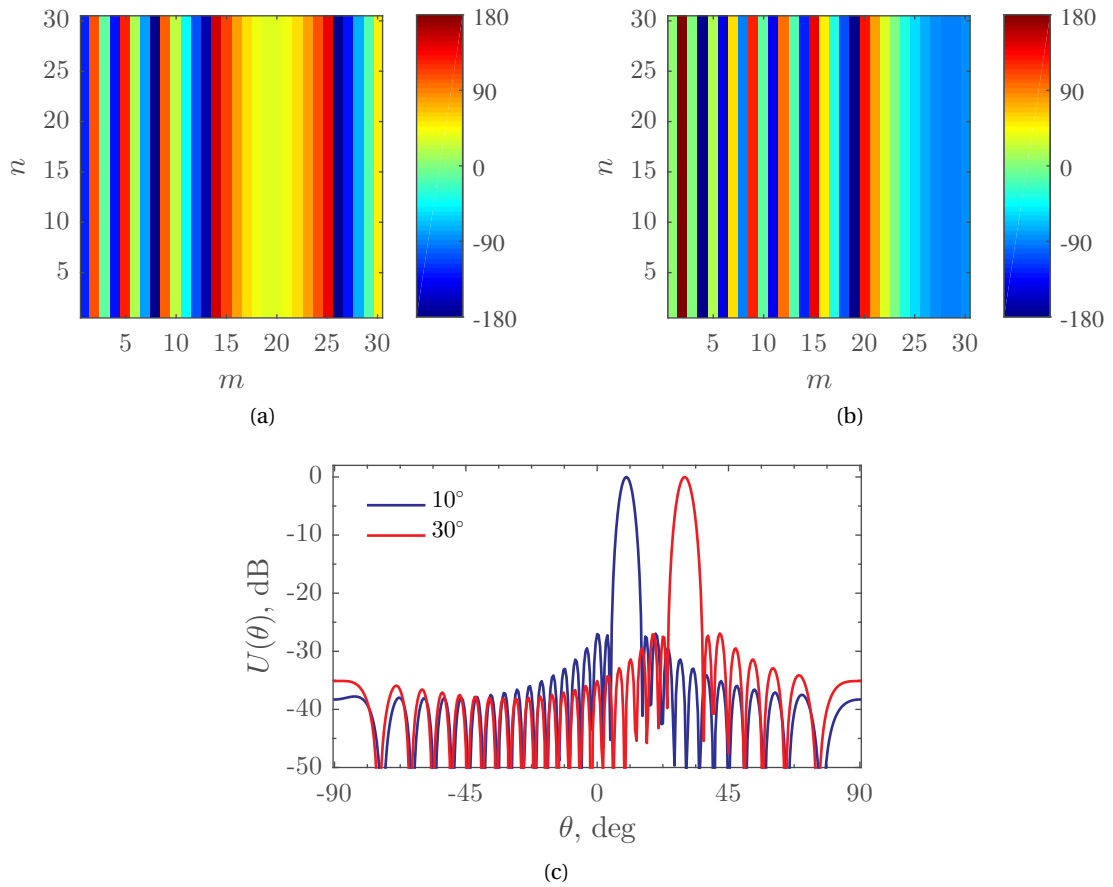


Figure 4.7 – Simulated example of a 1-D scanning reflectarray. Phase distribution needed on the reconfigurable RA of Fig. 4.6b to have the beam pointing to $(10^\circ, 0^\circ)$ (a) and $(30^\circ, 0^\circ)$ (b). The RA is composed of 30×30 (30 controlled columns) cells of the same size with a $\lambda_0/2$ spacing. (c) Calculated radiation pattern in the principle plane xz for the two phase distributions shown in (a) and (b).

surface of the movable microstrip patches and the top surface of the fix patches remain in flush contact with each other. Then, the tuning of the patch length is obtained by means of a relative horizontal displacement between the movable and fixed patches. If the patches were in constant contact with each other, this movement would generate friction and stiction effects that would negatively impact on actuation performance. To overcome this issue, a “three-step” reconfiguration procedure has been conceived. This approach is based on the integration of linear (vertical) actuators between the fixed microstrip patch array dielectric and the frame holding the movable array. These vertical actuators raise and lower the movable patches when needed, bringing them in and out of contact with the fixed ones.

To better explain the three-step reconfiguration concept, we consider an updated version of the simplified reconfigurable surface of Fig. 4.6b, where we assume that all the fixed patches have same size and are realized on the same grounded substrate (i.e., standard array of

patches), and each column of movable patches is realized on a single dielectric strip (i.e., five column PCBs). Then, we assume that the method for achieving the horizontal displacement (in the y direction) of each column is very similar to that used in the DEA-based MMW phase shifter discussed in the previous chapter. That is, each column PCB is bonded to a PDMS membrane which is pre-stretched and adhered to a rigid frame to maintain prestress. Two agonist DEA segments are implemented at the two extremities of the PDMS strip allowing in-plane displacement of the column PCB in the $\pm y$ direction. A simplified version of this reconfigurable concept is shown in Fig. 4.8 and the corresponding reconfiguration procedure is depicted in Fig. 4.9. Note that a cross section in the plane yz is represented. The top drawing (*step (0)*) of Fig. 4.9 illustrates the device static position, where the vertical actuators are conceived to assure a slight out-of-plane deflection of the PDMS membrane in order to press the movable patches towards the bottom ones (to improve contact). Hence, the beam-scanning reconfiguration is achieved in three stages:

1. activation of the vertical actuators (applying a low control voltage V_{up}) to raise the movable patches out of contact with the fixed ones;
2. application of an input voltage to the DEAs at the extremities of the PDMS strips resulting in horizontal displacement of the movable patches;
3. deactivation of the vertical actuators to bring the movable microstrip patches back into contact with the fixed ones.

It is worth noting that the control voltages of the DEAs need to be active also in a static position to keep the horizontal displacement corresponding to the desired reflection phase. However, these voltages ideally result in zero DC power consumption, due to the electrostatic nature of the DEA actuation principle (except for some leakage current). This three-step reconfiguration method may limit the scanning speed achievable with the proposed device, due to the “up” and “down” motion necessary to pass from a reconfiguration state to another. However, given the fast response time of DEAs (as low as several milliseconds), the speed performance should still be adequate for many beam scanning applications.

The size limitations for the vertical actuators are much less than those for the horizontal displacement as there is no need to place several devices very close to each other. Hence, this allowed us to explore technologies other than DEA for this purpose. Potential methods for achieving this vertical actuation may include the use of out-of-plane DEAs or commercially available multilayer piezoelectric actuators. The latter method is appealing due to the low input voltage needed for the actuation, but would require more accurate positioning and alignment of the device due to the low actuation displacements. Nevertheless, in our designs we have investigated two solutions, namely solenoid actuators and distributed pneumatic actuation as we will show in §4.3.2 and §4.3.3, respectively.

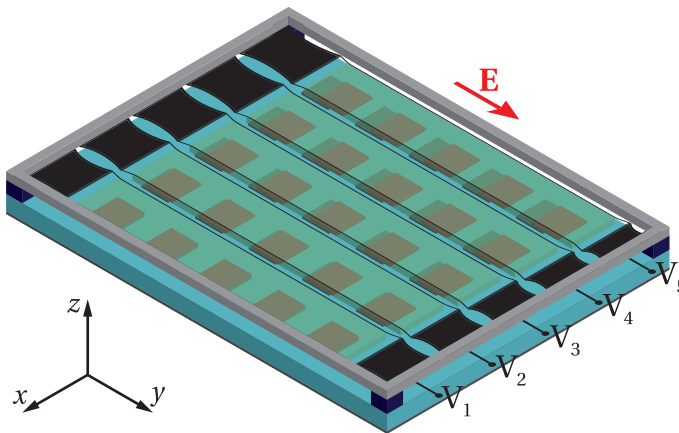


Figure 4.8 – Schematic of the DEA-driven reconfigurable reflective surface design. Movable microstrip patches (shown in red) are displaced in the y direction by the independently actuated planar DEAs at the extremities of each column.

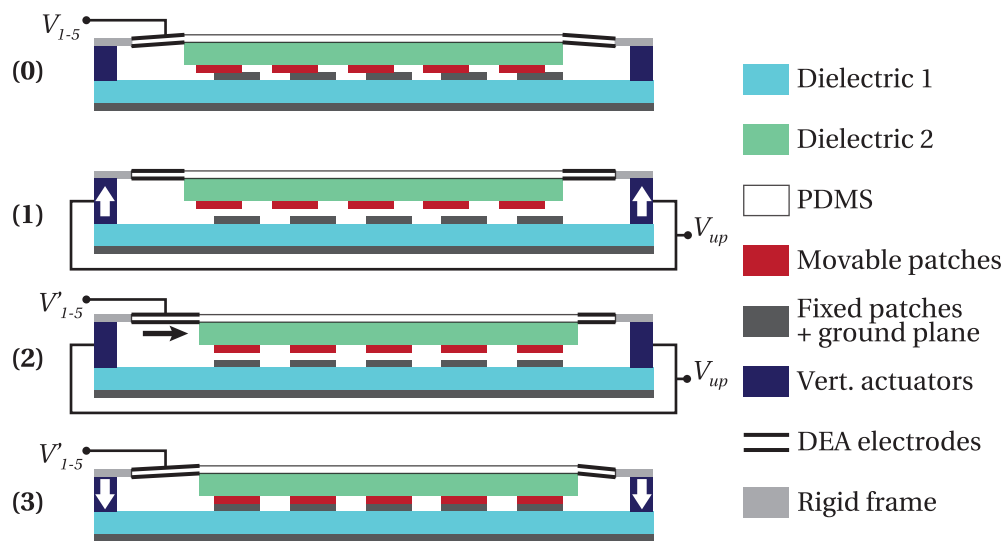


Figure 4.9 – Reconfiguration procedure for the proposed DEA-based reflectarray (cross section view). Step (0): device static and aligned such that there is a slight out of plane deflection on the PDMS membrane. Step (1): actuation of the vertical actuators to raise the movable microstrip patches out of contact with the fixed patches. Step (2): actuation of the planar DEAs to displace the movable microstrips horizontally. Step (3): deactivation of vertical actuators to bring the fixed and movable patches back into contact with each other.

4.3 A reconfigurable reflecting surface using DEA

The first step towards the development of a scanning RA has been identified in the design, fabrication and characterization of a reflective surface (array of reconfigurable patch cells) with *uniform reflection phase distribution*. This means that all patches have the same size and the reconfiguration is uniformly obtained using a single horizontal displacement, which is the same for all the unit cells (i.e., all the moving plates are controlled by the same actuator). This very first device does not provide any beam scanning capabilities since it does not allow to implement any phase profile, but only specular reflection can be obtained for the impinging wave. Nevertheless, this was conceived to proof the feasibility of the proposed reconfiguration approach and to validate the design. Moreover, this preliminary device helped us to evaluate the different issues and tolerances in the manufacturing process. The method for achieving horizontal displacement is very similar to that applied to the reconfigurable phase shifter of chap. 3, and therefore we leveraged our experience in the development and fabrication of the phase shifter for the new reconfigurable reflector. However, several technological challenges still needed to be addressed to optimize the new device design. An important aspect is related to the integration of a mechanically stable vertical actuation methodology that ensure uniform contact between movable and fixed patches and that the vertical motion does not affect the horizontal displacement. For instance, it is fundamental that when movable patches are raised and then lowered with the DEA voltage kept constant, they returns to the same horizontal position as before relative to the fixed microstrip patches.

This device has been first developed targeting Ka-band (26.5–40 GHz) considering the increasing interest of the international community for telecommunication and remote sensing systems operating in this frequency range. This choice was also particularly motivated by the performance issues concerning reconfigurable reflectarrays based on conventional technologies (e.g. semiconductors) that already exhibit significant limitations at these frequencies due to increased losses and complexity (cf. 4.1.2). The same design and reconfiguration approach can be also scaled to address higher frequencies (V-band, W-band, and low-THz range), with the maximum frequency limited by the achievable fabrication and control accuracy.

It is worth noting that the proposed reflective surface can also be seen as a functional device in the sense of a reflection phase modulator for free-space beams. An interesting development concerns the implementation of MMW tunable high impedance surfaces, which find many applications such as for instance their integration in beam-scanning and low profile leaky wave antennas [36, 37].

The practical implementation of the presented concept is discussed in the following, together with the results of the free space MMW characterization. Then, further steps to implement the scanning RA using the reconfiguration approach described above consist in the implementation of the independent control of each column of cells (Fig. 4.8), and will be discussed in §4.4.

4.3.1 Unit cell design and numerical results

We have discussed in §4.1.3 that a very common technique for the analysis and design of RA elements is based on the use of an infinite array approximation with the application of the Floquet's theorem, which allows to accurately characterize the reflection properties of the selected element taking into account also the mutual coupling between adjacent cells. With this approach, most of the efforts in the design of a RA surface lie in the optimization of the single unit cell. This method was adopted in the design of the reconfigurable reflective surface, and implemented in the commercial electromagnetic solver HFSS.

The same actuation approach developed for the phase shifter, and based on the use of two agonist planar actuators on the same PDMS membrane, was selected here to implement the horizontal displacement of the top patches. Therefore, in the following we assume that the array of movable patches is realized on the same dielectric, which is then bonded to the

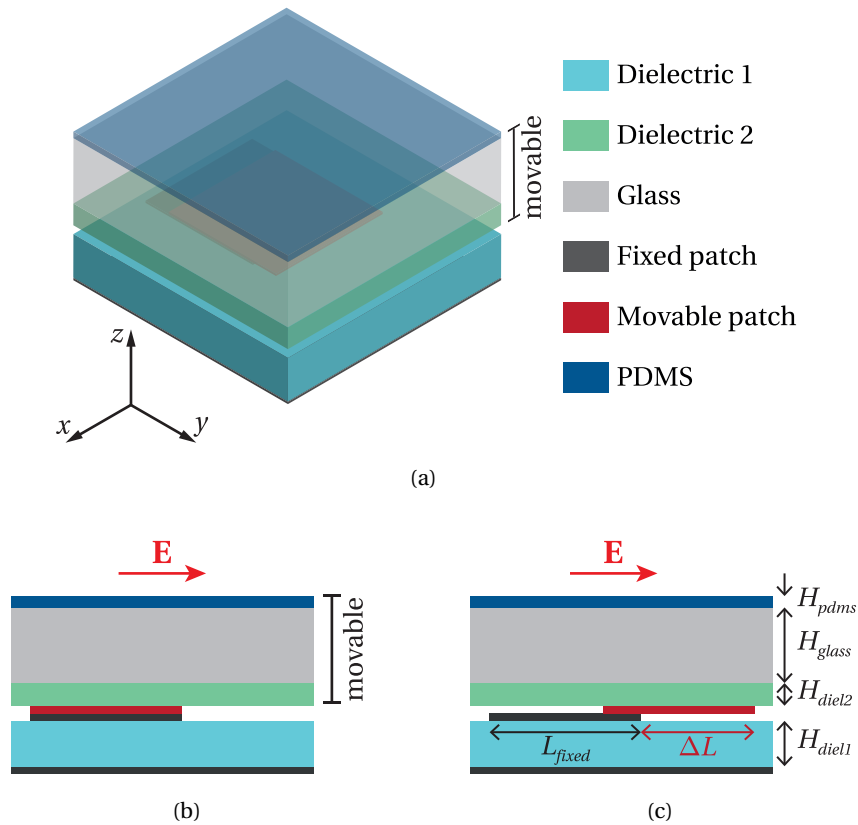


Figure 4.10 – Simplified drawing of the proposed implementation of the DEA-driven reconfigurable cell based on a tunable resonating patch. (a) Isometric view showing the different materials composing the stack. (b) Cross-section in the xz plane showing a complete overlapping between the movable and fixed patch. (c) Cross-section in the xz plane showing a movement ΔL of the movable patch with respect to the fixed one. The PDMS shown here represents only a portion of the full membrane comprising the actuator part.

PDMS membrane using an intermediate glass substrate. The proposed realization of this concept from a single cell perspective is shown in Fig. 4.10. The fixed metal patch is etched on a grounded substrate (*dielectric 1*) using standard PCB techniques and commercial materials (e.g., Rogers laminates). The movable part is a stack of different materials selected to simplify the manufacturing and assembly procedure: a dielectric substrate (*dielectric 2*) with etched movable patch bonded on a low loss glass (e.g., fused silica) substrate. The PDMS membrane is part of the DEA, which is not shown here, but will be included in the full device comprising an array of identical unit cells. The glass substrate is added to allow the plasma bonding between the PDMS membrane (i.e. actuator part) and the part to be displaced (cf. §3.3.2). Note that a bonding layer has to be considered between the glass and the dielectric 2.

The operating central frequency was fixed to 30 GHz and the design process was carried out to maximize the achievable phase range. The device geometry was defined (Fig. 4.10) and therefore the optimization procedure relied on the selection of the proper dielectric thickness and permittivity. The width and the initial length of the patch (L_{patch}) were also included in the optimization process to ensure that the total phase range at 30 GHz was centered with respect to the displacement range. That is, the maximum slope of the phase curve corresponds to the middle of the reconfiguration range. Considering the foreseen fabrication process (i.e., standard PCB technique), the range of dielectric substrates was limited to those commercially available, hence limiting the choice of their thickness and permittivity. As we have discussed in §4.1, the choice of the dielectric permittivity and thickness is fundamental since they control the properties of the resonance, and therefore the corresponding range and slope of the reflection phase when the patch length is modified. In the proposed design, this choice was made targeting a minimum phase range of 270° between the minimum and maximum displacement of the movable patch (i.e., minimum and maximum achievable patch length). This phase range (far from 360°) was selected to guarantee a smoother slope of the reflection phase curve with the main goal to mitigate fabrication and actuation tolerances, which are particularly critical in the steepest region of the curve. This design choice also allows to operate in the most efficient way the two agonist actuators, as it will be better discussed in the next section. Moreover, although the maximum differential phase is far from the ideally needed 360° , the examples reported in §4.1.3 demonstrated that such a range would allow to generate reflectarray performance with limited losses in directivity (as low as 0.2 dB with respect to a complete phase range of 360°).

To further reduce the degrees of freedom in the choice of a given dielectric, the optimization was carried out assuming that the two dielectric layer were the same (i.e., same thickness and permittivity), which mathematically translates in $H_{diel1} = H_{diel2}$ and $\epsilon_{r1} = \epsilon_{r2}$. This constraints also allowed to simplify the fabrication (reducing costs), since both the bottom and top array of patches could be realized in batch on the same laminate. The selected low-loss glass substrate was the same commercial fused silica utilized for the phase shifter, having a thickness of $525\ \mu\text{m}$ and a permittivity of 3.8. The dimensions of the unit cell need to be smaller than $0.7\lambda_0$ to limit the presence of grating lobes [2]. In this specific case, a square cell with side equal to $\lambda_0/2 = 5\ \text{mm}$ was chosen, allowing to keep low grating lobe

4.3. A reconfigurable reflecting surface using DEA

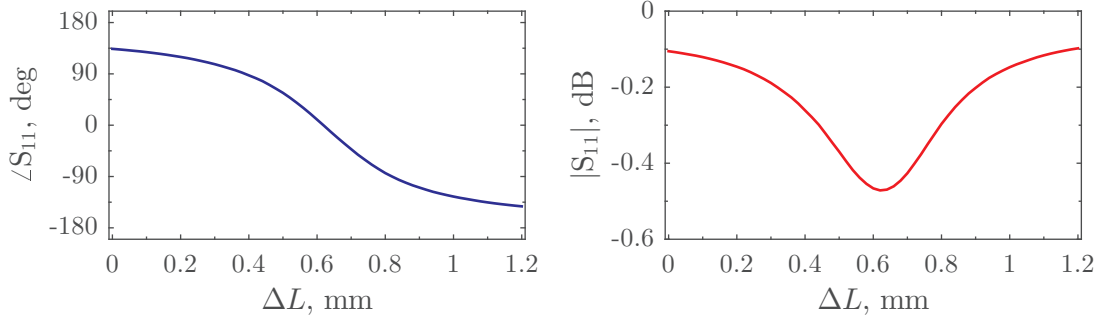


Figure 4.11 – Reflection phase (left) and magnitude (right) of the designed unit cell of Fig. 4.10. The calculation was performed using full-wave simulations in a Floquet's periodic environment at the design frequency $f_0 = 30$ GHz.

Table 4.1 – Optimized dimensions and material properties of the reconfigurable cell shown in Fig. 4.10.

Cell	$L_{cell} = W_{cell} = 5$ mm
Patches	$W_{patch} = 2$ mm $L_{patch} = 1.55$ mm $\Delta L_{max} = 1.2$ mm
Dielectric 1 and 2	$H_{diel1,2} = 305$ μ m $\epsilon_{r1,2} = 3.55$ $\tan \delta_{1,2} = 0.0027$
Fused silica	$H_{glass} = 525$ μ m $\epsilon_{glass} = 3.8$ $\tan \delta_{glass} = 0.0004$
PDMS	$H_{pdms} = 30$ μ m $\epsilon_{pdms} = 2.8$ $\tan \delta_{pdms} = 0.04$

level for a wide range of incident angles and, at the same time, to ensure enough spacing between adjacent cells in the case of the conceived independent column reconfiguration. The optimization of the single cell was carried out using a full-wave approach based on Floquet periodicity. The optimized dimensions and dielectric properties of the reconfigurable cell shown in Fig. 4.10 are summarized in Tab. 4.1. The definition of the different geometric variables can be found in Fig. 4.6 and Fig. 4.10. The selected dielectric is the commercial laminate Rogers RO4003C ($\epsilon_r = 3.55$ and $\tan \delta = 0.0027$) with a dielectric thickness of 305 μ m and a 17 μ m copper cladding.

Fig. 4.11 reports the simulated reflection magnitude and phase under normal incidence and assuming the infinite array environment for the optimized cell of Fig. 4.10. The length of both the movable and fixed patch is 1.55 mm and an overlap of 0.35 mm is considered at the

maximum displacement $\Delta L_{max} = 1.2$ mm. The maximum achievable displacement of 1.2 mm was selected after preliminary tests on the actuator performance, which took into account different constraints including the maximum size that could be realized with the considered manufacturing technique and equipment. The proposed geometry allows a reconfiguration of the patch length in the continuous range 1.55–2.75 mm. The maximum achievable phase range for this particular cell is around 280° at the design frequency $f_0 = 30$ GHz. The selected dielectric substrate allows to achieve a phase curve with a limited slope, obviously at the expense of the maximum phase range. A maximum slope of $519^\circ/\text{mm}$ is obtained close to the resonance, which happens around $\Delta L = 0.62$ mm at the design frequency. The simulated results presented here demonstrate very good performance for the implementation of a reconfigurable beam-scanning RA. In particular, an analog tuning range of around 280° is obtained with very low losses, considering the addressed reconfiguration capabilities and in comparison to available technologies. The reflection loss in fact is always lower than 0.5 dB at 30 GHz. It is worth noting that the predicted losses can be considered optimistic since the loss tangent used for the dielectric layers corresponds to the data provided at 10 GHz by the supplier, and a conductivity of 5.8×10^7 S/m (nominal value for copper) was used for patches and ground plane. Therefore, slightly higher losses can be expected in the fabricated device, and a better prediction could be obtained after the dielectric characterization of the involved materials. Nevertheless, these additional information were not considered of critical importance for this first prototype that was conceived to experimentally proof the proposed concept of reflection phase reconfiguration.

4.3.2 The first prototype: fabrication and test

This section presents the fabrication and the experimental characterization of the first prototype implementing the proposed method for the mechanical reconfiguration of microstrip patch elements. The design of the unit cell presented above was adopted to realize a uniform reflective surface where the reconfiguration of the phase was obtained using a single control based on two DEA segments allowing horizontal movement in the y direction. The implemented device consists of an array of identical fixed patches realized on a grounded dielectric, and an analogous array of patches realized on the same dielectric material. The latter array is bonded to a fused silica substrate to allow permanent adhesion to the PDMS-based actuation device. A critical aspect related to the practical implementation of the device concerned the selection of the linear vertical actuators needed to implement the three-step reconfiguration procedure shown in Fig. 4.9. According to the above discussion, these actuators have to provide up and down motion to raise and lower the movable patches when needed (step 1 and 3 of Fig. 4.9, respectively) applying a force in both directions. In the “down” position in fact a small force is needed to push the top movable patches against the fixed ones improving the physical contact between them. Commercial and off-the-shelf actuators were preferred to allow fast prototyping and validation of the concept. After a preliminary analysis of the achievable performance, push-pull solenoid actuators were selected. The chosen devices were controlled by a ± 6 V DC voltage generating a maximum stroke of 6 mm, which allowed a wide

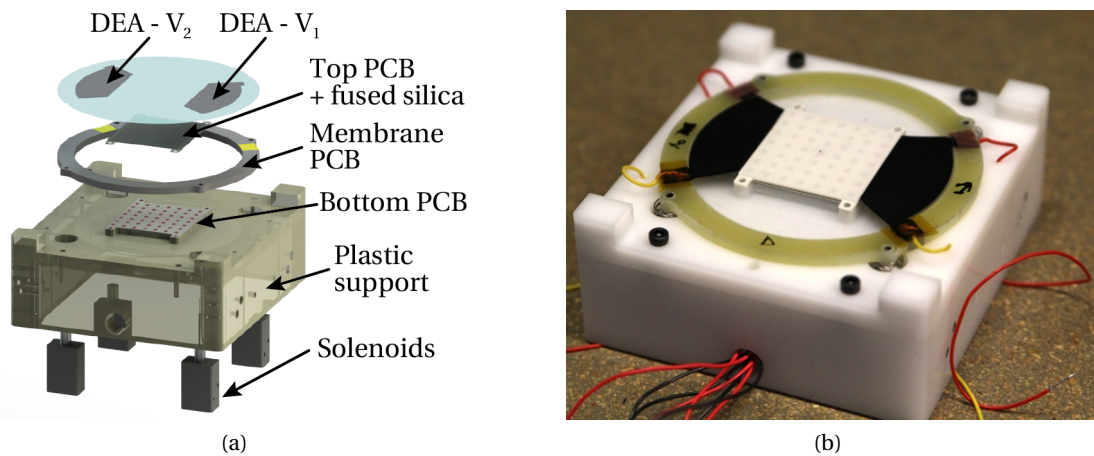


Figure 4.12 – First prototype of reconfigurable reflective surface based on dielectric elastomer actuation. (a) Render of the final design including all the parts necessary to implement the actuation procedure of Fig. 4.9. (b) Picture of the device assembly including the connections needed for the control of the DEAs and the solenoid actuators. Note the PDMS membrane is completely transparent in the picture.

and safe margin with respect to the needed vertical movement.

The design of the actuators, the manufacturing of the different parts and the assembly of the full device were carried out following the same approach used for the phase shifter. Actuators were designed and fabricated at the *Microsystems for Space Technologies Laboratory (LMTS)* considering the main requirement related to the needed stroke of 1.2 mm (plus an operating margin of 200 μm). According to the actuation principle described in chap. 3, the total desired stroke was obtained through the combination of a 0.6 mm displacement in the $+y$ direction and a 0.6 mm displacement in the opposite direction $-y$.

The manufactured prototype is shown in Fig. 4.12. The exploded view of Fig. 4.12a illustrates all the parts constituting the final device, which were assembled together using a custom-made plastic support. These parts include also the four solenoid actuators needed to implement the push-pull movement required by the actuation method (Fig. 4.9). DEAs (i.e., PDMS membrane and electrodes) were realized according to the technique described in §3.3.2, introducing only a slight difference in the pad printing of the DEA electrodes. In particular, for the device of Fig. 4.12, a standard pad printing method was used [38]. That is, the shape of the electrodes was obtained using a metal cliché (acting as a reservoir of conductive ink) directly etched with the desired electrode pattern, whereas an intermediate PET mask placed on the membrane surface was used for the phase shifter. This approach allowed to eliminate a few steps (i.e., mask fabrication, mask alignment and release) in the fabrication of the actuators, without reducing the electrode accuracy. The pre-stretched PDMS membrane with embedded electrodes was then adhered to a rigid PCB allowing the connection to the wires needed for the voltage control. The same membrane PCB was also screwed to the four solenoids (fixed to

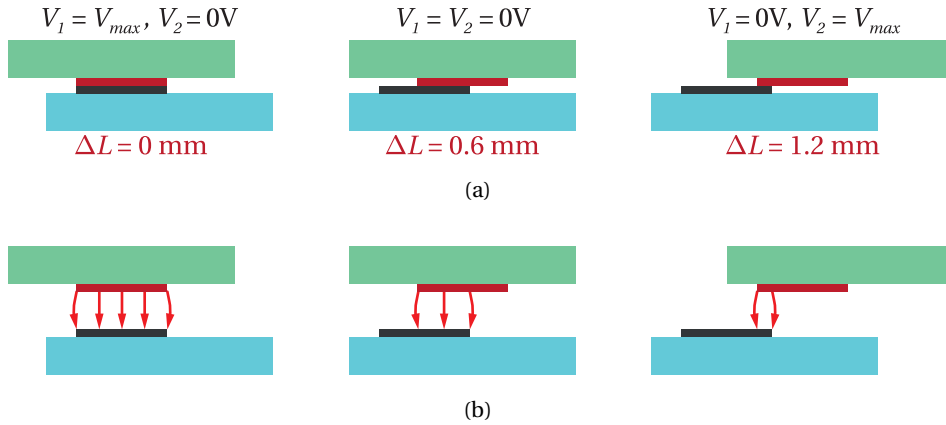


Figure 4.13 – Symbolic illustration of three main states of reconfiguration. The assembly position corresponds to the central state ($V_1 = V_2 = 0V$). (a) Nominal operation of the device, i.e. good contact between movable and fixed patches. (b) Presence of air gap between movable and fixed patches.

the plastic support) to allow the vertical movement of the top array with respect to the bottom one (glued on the plastic support).

The maximum size of the actuator part was limited by the pad-printing machine available at LMST, which allows the realization of designs fitting at the most in a circle of 80 mm diameter. This constraint explains the circular shape of the actuator part, which was selected to maximize the size of the device and DEA performance. This particular geometry and the minimum required horizontal displacement (i.e., 1.2 mm) limited the reflector to a square of $35 \times 35 \text{ mm}^2$, which was able to fit an array of 7×7 cells ($3.5\lambda_0 \times 3.5\lambda_0$) having the size reported in Tab. 4.1. The bottom (fixed) and top (movable) arrays were fabricated using standard PCB techniques on a Roger RO4003C laminate. The bottom PCB was subsequently glued to the plastic support taking care of the alignment (see alignment holes in Fig. 4.12), and the top PCB was bonded to a fused silica substrate previously cut ($35 \times 35 \text{ mm}^2$). Then the relative alignment between the actuator part, the top array and the bottom array was achieved using a custom-made alignment jig. Oxygen plasma activation of the PDMS membrane and the fused silica surface allowed permanent bonding (cf. §3.3.2) of the actuator PCB and the movable array. It is worth noting that the assembly position (i.e., $V_1 = V_2 = 0V$) corresponds to the position $\Delta L = 0.6 \text{ mm}$ of Fig. 4.13a. Starting from this inactive state, the minimum patch length ($\Delta L = 0 \text{ mm}$) is reached for the maximum V_1 voltage, whereas $\Delta L = 1.2 \text{ mm}$ is achieved controlling V_2 to the maximum displacement (V_1 and V_2 defined in Fig. 4.12a).

A monostatic measurement setup was selected for the experimental characterization of the reconfigurable reflection properties of the fabricated device under normal incidence. A monostatic setup is typically made up of a transmitting/receiving antenna pointing toward the device under test and connected to one port of a vector analyzer set up for S_{11} measurements. The reflection magnitude and phase of the device under test are then obtained by means of

relative measurements with respect to a reference metallic plate whose reflection properties are well known (i.e., ideally unitary magnitude and π phase). This setup was preferred to the commonly used rectangular waveguide simulator [39], since the particular mechanical actuation principle did not allow to place a limited number of cells inside a waveguide. The small size of the fabricated array ($3.5\lambda_0 \times 3.5\lambda_0$), however, represented a limitation for the considered measurements setup. A standard Ka-band horn antenna was in fact not suitable in this specific case due to the generally wide half power beamwidth, in the order of 25° – 30° at 30 GHz. Considering that a far field operation was needed, such a wide beam allowed to couple only a small fraction of the radiated power with the device, reducing the signal-to-noise ratio of the system. More importantly, this would have generated high diffraction effects at the edges of the device, with considerable degradation of the measurement accuracy. A better option was represented by a spot-focusing lens antenna allowing the radiation of a Gaussian beam focused at a finite distance from the lens. Gaussian lens antennas allow to concentrate the radiated energy around the axis of propagation and to consider with very good approximation a plane wave propagation at the focal plane (i.e., plane including the beam waist) [40]. In particular, both the field distribution and the power density of the fundamental Gaussian beam mode are maximized at the beam waist, where about 87 % of the total power in the fundamental mode is concentrated [41].

The reflection phase characterization of the prototype shown in Fig. 4.12b was performed using the free-space quasi-optical test facility available in the Compact Antenna Test Range (CATR) at ESA ESTEC (European Space Research and Technology Centre), and shown in Fig. 4.14. A Gaussian beam radiation is there generated using an offset reflector illuminated by a circular corrugated horn. A wire-grid polarizer is introduced in front of the reflector to select a single linear polarization, ensuring a cross-polarization level 50 dB lower than the co-polarized component. The relative position between the antenna and the sample holder is completely adjustable (including rotation) using the integrated positioning system, which is particularly convenient for the correct alignment of the setup (Fig. 4.14). The adopted quasi-optical system, however, generates a beam waist diameter in the order of $5\lambda_0$ (i.e., 50 mm at 30 GHz) at the focal distance of 1 m, which is bigger than the active surface of the device under test ($3.5\lambda_0 \times 3.5\lambda_0$). Therefore, diffraction effects at the edge of the sample were unavoidable, although better performance than those achievable with a standard horn antenna were expected. Flat absorbers (ECCOSORB AN72) were placed around the sample to reduce these edge diffraction and to shadow all the supports and the actuation part needed to implement the reconfiguration. The selected absorbers ensured a reflectivity lower than -20 dB, but needed a metal backing for proper operation. Therefore, an aluminium sample holder with a flat front surface was designed and manufactured to allow the alignment of the device in the center of the antenna beam and the correct installation of the absorbers (Fig. 4.14). A square window with size of 35×35 mm² was left in the aluminium plate to allow the illumination of the device. The thickness of the aluminium plate in correspondence of the window was 1 mm. An important aspect in the preparation of the measurement setup consisted in the development of a LabVIEW software able to remotely control and synchronize

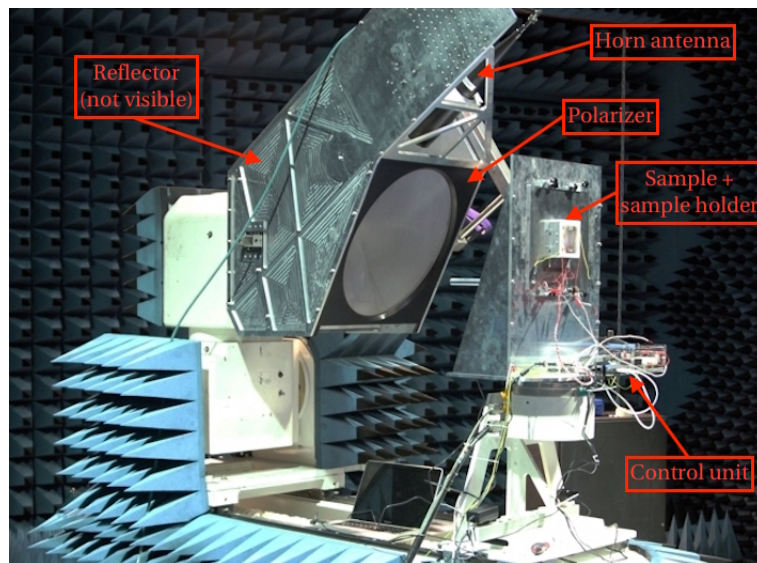


Figure 4.14 – Free-space quasi-optical test facility available at ESA ESTEC. The picture includes the transmitting/receiving antenna (comprising the circular horn, the reflector and the polarizing grid), the sample holder and the device control unit.

the full system comprising the network analyzer, the high voltage controller for the DEAs and the low voltage control for the vertical solenoid actuators. This software allowed to completely automatize the MMW measurements requiring operator inputs only at the beginning of the procedure. The high voltage controller for the planar DEAs was also specifically developed (designed and fabricated) for the particular application considering the need for a simple and efficient remote operation. Its main core was a commercial DC-DC voltage converter (American High Voltage SC-50) generating a high voltage (up to 5 kV) directly proportional to the input voltage in the range 0–12 V. The input voltage was generated and regulated by a custom-made adjustable low voltage supply based on a microcontroller unit which allowed the serial communication with the controlling computer.

The considered setup did not allow the simultaneous characterization of the horizontal displacement generated by DEAs and the corresponding reflection properties of the device. Therefore, like in the case of the phase shifter (cf. §3.3.3), the actuator displacement as a function of the applied voltage was determined prior to the MMW measurements. For this mechanical characterization we used a digital microscope (Dino-Lite AM4113TL) placed on a dedicated holder (fixed to the aluminium sample holder) to point normally at the device surface, and controlled by the same LabVIEW software mentioned above. The software was programmed to operate the device following the reconfiguration approach illustrated in Fig. 4.9 and, at the same time, to measure the horizontal displacement of the movable top array for each applied voltage by tracking a reference feature on the array surface. This procedure was repeated three consecutive times (i.e., without moving or touching the sample) to assess the repeatability of the reconfiguration approach. The results of the displacement characterization (3 consecutive runs) for the considered prototype are reported in Fig. 4.15,

where V_1 input voltages (right actuator, Fig. 4.12a) are shown as negative values (i.e., $V_1 = -V$) and V_2 as positive ($V_2 = V$). The values Δy are referred to the assembly position where no voltage is applied ($V_1 = V_2 = 0V$), meaning that the positions $\Delta y = 0$ mm, $\Delta y = -0.6$ mm and $\Delta y = 0.6$ mm correspond to the states $\Delta L = 0.6$ mm, $\Delta L = 0$ mm and $\Delta L = 1.2$ mm of Fig. 4.13a, respectively. The measured values of Fig. 4.15 demonstrate a good repeatability for the proposed actuation method showing a slightly higher variability at low voltages, but with errors that are always smaller than $20 \mu\text{m}$. Once the displacement characterization is completed, the microscope and its holder are removed without moving the device that remains fixed in the sample holder. Then, the MMW reflection characterization can be started programming the LabVIEW software to implement the same procedure (i.e., applied voltage and reconfiguration speed) previously used for the displacement measurements. Under these assumptions and considering the good repeatability of Fig. 4.15, we can safely assume that the horizontal displacement of the movable array obtained during the MMW characterization corresponds to the one previously measured for the same applied voltage.

The desired reflection properties (magnitude and phase) are therefore obtained after different consecutive steps that are summarized in the following, assuming that the full device is fixed to the sample holder and all the electrical and computer cables are connected:

1. The digital microscope is placed and fixed normal to the aluminium sample holder, and the automatic displacement characterization is performed (3 consecutive runs) for a given set of actuation voltages V_1 and V_2 .
2. The microscope and its holder are removed and automatic S_{11} measurements are carried out for the same set of voltages chosen for the displacement characterization.
3. The reconfigurable reflector is removed and a metallic plate of same size is placed at the same distance to obtain the reference reflection measurement.
4. Measurements are processed normalizing the reflection from the reflectarray device with respect to the reference metal plate that acts as a short standard.

Figure 4.16a shows the measured reflection magnitude (top) and phase (bottom) as a function of the frequency and the applied voltages V_1 and V_2 for the device of Fig. 4.12, after normalization to the reference plate. A time-gating procedure was applied to remove the effect of unwanted reflections due for instance to the cables and the feeding horn antenna. The frequency range (28–38 GHz) shown in Fig. 4.16a is limited by the single mode operation of the feeding antenna (26–40 GHz) and by the applied time gating that generates artifacts in the first and last ~ 2 GHz of the frequency range, which therefore need to be discarded. Measurements can be compared with simulations (function of the frequency and ΔL) of Fig. 4.16b which were obtained in HFSS for a single cell under normal incidence and in a periodic boundary condition. Curves with same color in Fig. 4.16a and Fig. 4.16b correspond to the same reconfiguration state since the values of ΔL employed in simulations were retrieved from the

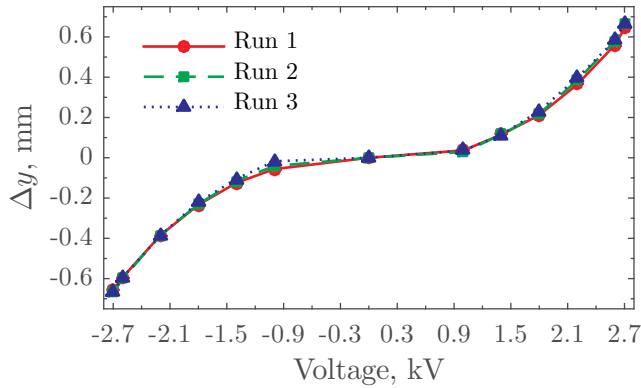


Figure 4.15 – Displacement Δy characterization as a function of the applied voltage for the prototype of Fig. 4.12b performed prior to the MMW reflection measurements. Note V_1 voltages are shown as negative and V_2 voltages shown as positive.

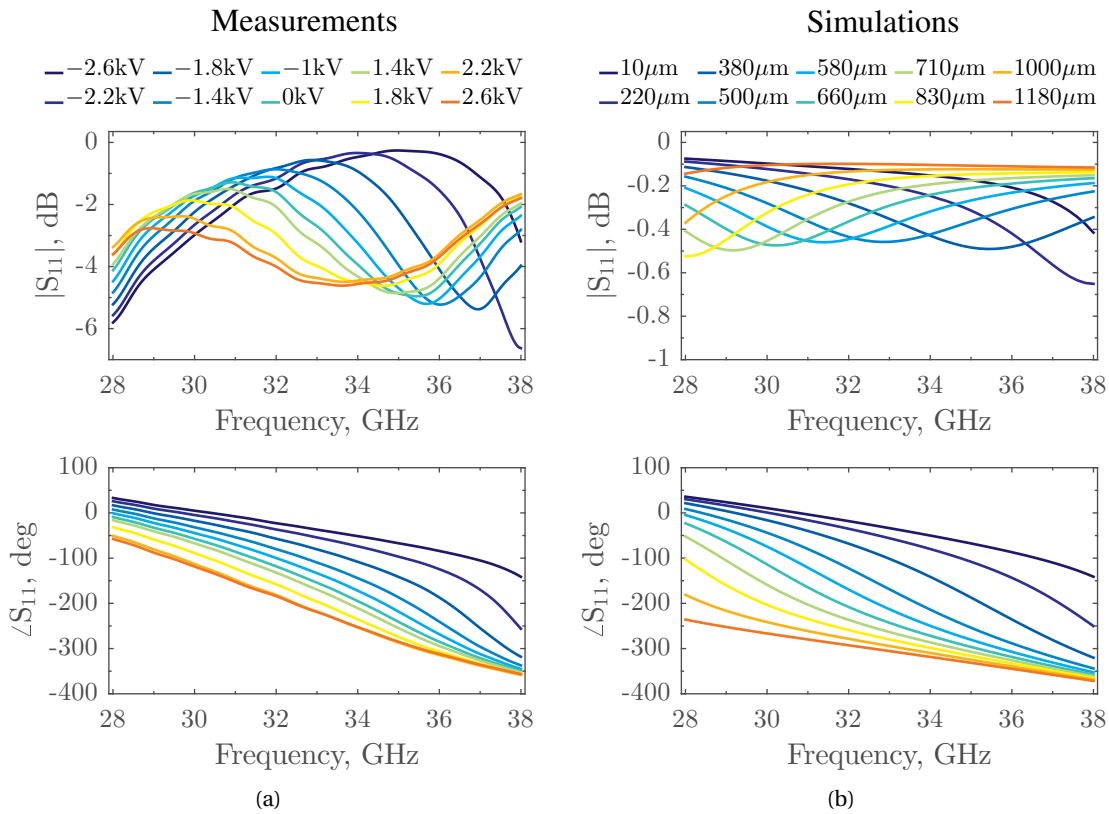


Figure 4.16 – Comparison between measurements and simulations of the reflection magnitude (top) and phase (bottom) for the prototype of Fig. 4.12. (a) Measurements as a function of the actuation voltage and (b) full-wave simulations as a function of the displacement ΔL . Note V_1 voltages are shown as negative and V_2 voltages shown as positive. ΔL values in (b) correspond to the applied voltages in (a) according to the experimental curve of Fig. 4.15.

experimental curve of Fig. 4.15 for each voltage applied during measurements. Note that the displacements of Fig. 4.15 are expressed as Δy values that can be converted to ΔL by simply adding 0.6 mm. A first look at the results of Fig. 4.16 suggests that the fabricated prototype does not provide the expected performance as it is clearly visible comparing simulations and measurements. The main effects are a shift of the resonance towards higher frequencies and a consequent “shrink” of the phase curves, which therefore do not allow the designed 280° of differential phase at 30 GHz. A more careful analysis of these results allows to observe that the visible degrading effect is more emphasized at lower frequencies and for higher values of ΔL (i.e., smaller overlap between movable and fixed patches), suggesting a frequency and geometry-dependant issue.

After different studies and evaluation of the results, we concluded that this performance degradation was generated by an irregular contact between the movable and fixed patches, hence preventing the ohmic contact between them. Two main reasons for this irregular contact were identified in the fabricated prototype: i) oxidation of the copper patches considering that several weeks passed from the array manufacturing and the MMW characterization (moreover their storage and handling was not particularly careful); ii) non-uniform contact of all the cells, meaning that an air gap was present for a number of them between the top and bottom patch (i.e., no physical contact). This latter issue was difficult to control and to correct for the considered prototype since it was not possible to assure precise uniform thickness of the copper and perfect flatness of all the involved surfaces (i.e., top and bottom arrays, plastic support and fused silica substrate). Moreover, the force applied by the out-of-plane deflection of the PDMS membrane (see Fig. 4.9) was not sufficient to guarantee uniform pressure over the whole array. These hypothesis were verified through full-wave simulations which allowed to observe a behavior similar to that shown in Fig. 4.16, namely a shift of the resonance frequency and a compression of the phase distribution when an air gap is introduced. Moreover, we observed also in simulations the same dependence on frequency and displacement. This phenomenon can be qualitatively explained through the symbolic drawings of Fig. 4.13b: if an air gap is present, there remains still a capacitive coupling (red arrows) between the movable and fixed patch, which increases for higher frequencies and/or for larger overlaps between the two patches (i.e., small ΔL). This qualitative analysis, also verified by simulations, justifies the fact that a quite good agreement is found in Fig. 4.16 at high frequencies and for large overlaps, whereas performance degrades moving towards the lower part of the bandwidth and for bigger displacements.

For a final validation of this assumption, we now compare the measured reflection phase with a simulated reflection phase of a cell where an air gap is present. Figure 4.17 shows a comparison between the measured reflection phase of Fig. 4.16a and the corresponding simulations where an air gap of $20\ \mu\text{m}$ has been added in the simulated geometry between the fixed and the movable patch. Simulations exhibit the same compression of the phase response at lower frequencies and are in quite good agreement with measured curves. It is worth noting that this is not a very rigorous comparison, since the simulation geometry corresponds to an infinite array of identical cells (all with the same gap), whereas different contact irregularities

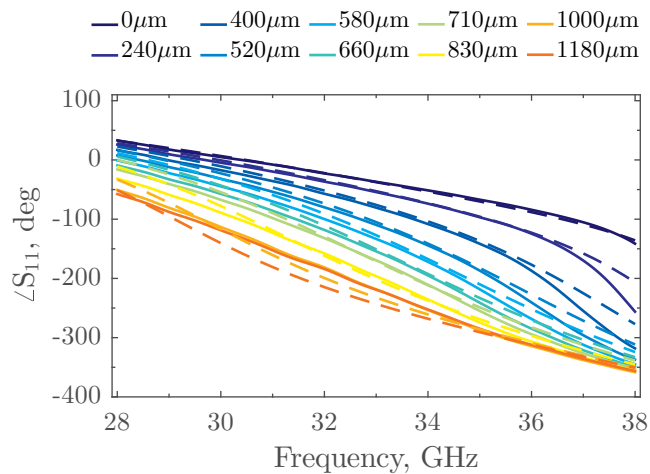


Figure 4.17 – Comparison between measured reflection phase of Fig. 4.16a (solid lines) and simulations when an air gap of $20\mu\text{m}$ is added between the fixed and movable patch (dashed lines). The agreement between measurements and simulations validate the hypothesis of irregular contact between movable and fixed patches.

can be present in the fabricated prototype. However, these simulated results can be considered a good approximation of an average effect in the whole real array, and therefore a validation of the encountered phenomenon. An improved version of the proposed prototype is presented in §4.3.3 where two simultaneous solutions have been adopted to avoid the above “contact issue”.

4.3.3 Prototype optimization: fabrication and test

The prototype discussed above exhibited degraded performance with respect to the results predicted with full-wave simulations, and the reason for that has been identified in an irregular contact between movable and fixed patches. Here we present the design, manufacturing and characterization of an improved prototype targeting the solution of the two main phenomena affecting the performance of the previous device, namely copper oxidation and non-uniform contact of the top and bottom arrays.

The solution of the former issue was easy to implement applying a gold plating to the copper elements. This step was added to the standard PCB fabrication process and allowed to avoid the oxidation of the metal parts, hence keeping a low contact resistance between the touching patches. In practice, this coating was obtained by covering the copper cladding with a layer of nickel ($\sim 5\mu\text{m}$) and a subsequent top gold metalization ($\sim 200\text{nm}$). The solution of the latter problem (i.e., non-uniform contact), on the other hand, was address by investigating different approaches to implement the vertical actuation. In particular, the ideal actuation method had to allow a push-pull mechanism generating a small uniform force during the “push” movement and a uniform pressure of the top array over the bottom one during the “pull” movement, allowing to overcome the effects related to the imperfect flatness of the

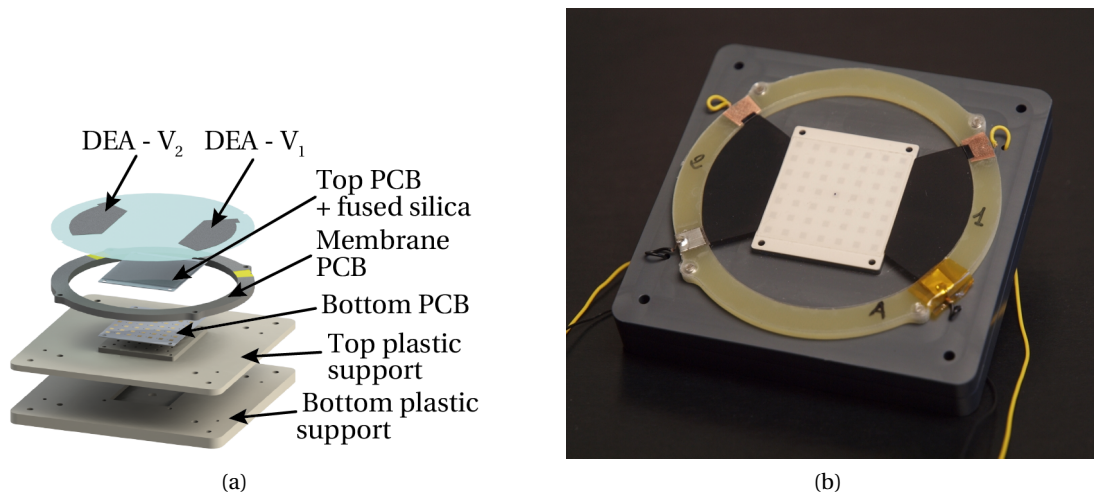


Figure 4.18 – Optimized prototype of reconfigurable reflective surface based on dielectric elastomer actuation. (a) Render of the final device showing the air chamber needed to implement the vertical pneumatic actuation. (b) Picture of the device assembly including the connections needed for the control of the DEAs. Note the PDMS membrane is completely transparent in the picture.

involved substrates. These characteristics were identified in a technique based on the use of distributed pneumatic actuation. More specifically, this approach envisages the integration of a mechanism in the bottom part of the device, which allows to invert an air flow switching from a pumping state (“push” movement) to a suction state (“pull” movement). Obviously such a mechanism needs to be properly shielded to avoid any interaction with the electromagnetic signal. This approach was implemented in the new device by drilling a uniform array of small holes (500 μm diameter) in the bottom PCB, coupled to an air chamber in the plastic support. This chamber was then connected to the pneumatic control systems through a standard tube. A render of the new version of the reconfigurable reflective surface is shown in Fig. 4.18a. The design and fabrication process of the actuator part, including DEAs, membrane PCB and movable array, was completely inherited from the previous prototype (cf. Fig. 4.12), whereas a significant modification had to be introduced to implement the proposed pneumatic actuation. The main plastic support of the device was manufactured in two pieces for an easy realization of the needed air chamber ($43 \times 36 \times 2 \text{ mm}^3$) that was integrated in the bottom part of the plastic support (Fig. 4.18a)). In turn, a uniform array of holes (aligned with the corresponding holes in the bottom patch array) was drilled in the top part of the support to let the air flowing from the air chamber to the interface between the fixed and movable arrays. The two pieces were then sealed together to make the chamber airtight.

In order to allow a compact and efficient demonstration of the concept, the pneumatic control system was implemented using a miniaturized 3-way valve whose output was directly connected to the device, and the two inputs were connected respectively to a low-pressure compressed air source and to a miniaturized Venturi vacuum pump. The valve was remotely

actuated by a modified version of the LabVIEW software and the control unit mentioned above, allowing to switch from a positive air flow (i.e., from the air supply to the device) to a negative one (i.e., air suction from the vacuum pump). The former condition generates a uniform pressure (slightly higher than the atmospheric one) between the two arrays which gently pushes the top one releasing the contact between the patches. The top plate therefore remains in a steady vertical position due to the equilibrium between the force applied by the airflow and the opposite force generated by the PDMS membrane. When the pneumatic valve is actuated, the air flow is inverted and a quasi-vacuum condition is induced between the movable and fixed array of patches.

The design of the unit cell was also slightly modified to account for the new geometry including the holes in the bottom PCB, which were placed between adjacent cells aligned in the y direction (i.e., 2 half holes for each cell). Moreover, the new design was also carried out targeting a wider phase range ($>300^\circ$) at the expense of a steeper slope. However, this aspect was not particularly critical considering that the previous prototype highlighted good fabrication accuracy and reliable DEA actuation. The increased differential phase between the two extreme states of reconfiguration was achieved reducing the thickness of the dielectric layers to $203\ \mu\text{m}$ (i.e., commercial standard for Rogers RO4003C), and consequently the initial patch length L_{patch} was properly adjusted to center the 30 GHz resonance to $\Delta L = 0.6\ \text{mm}$. As the actuator part remained unchanged with respect to the previous device, the design optimization was carried out considering a maximum achievable displacement of 1.2 mm. To have a better estimation of the losses we also considered a more realistic geometry in the simulator, where the metallic ground plane and patches were modeled as 3-dimensional elements realized by a stack of copper, nickel and gold as in the real fabricated device. Furthermore, the dielectric properties of the array substrate (Rogers RO4003C, $203\ \mu\text{m}$ thick) were measured using a commercial setup based on an open resonator technique. Measurement results demonstrated an average loss tangent of 0.0051, higher than the 0.0027 value provided by the manufacturer for 10 GHz operation. The updated geometrical and dielectric properties of the unit cells are reported in Tab. 4.2 considering the geometry illustrated in Fig. 4.10. The corresponding reflection phase and magnitude as a function of the displacement ΔL at 30 GHz are shown in Fig. 4.19, which highlight a phase range of 310° for an increase of 1.2 mm in the patch length (i.e., from 1.8 mm to 3 mm). Reflection losses are higher with respect to the cell designed for the previous prototype (cf. Fig. 4.11) due to two main reasons, namely the introduction of higher dielectric and metal losses in the full-wave calculation and the use of a thinner substrate generating a stronger resonance peak (i.e., higher Q factor). However, the real gain loss in reflectarray antennas due to the reflection losses of the single unit cell does not correspond to the peak loss, but rather to a weighted average of the reflection losses corresponding to the different available reflection phases, considering that in real reflectarrays unit cells will operate in different reflection states (i.e., magnitude and phase). Moreover it is important to point out that the losses exhibited by the designed cell are only due to the involved materials, whereas the actuation mechanism is completely isolated from the EM active area and thereby does not contribute to the loss budget.

4.3. A reconfigurable reflecting surface using DEA

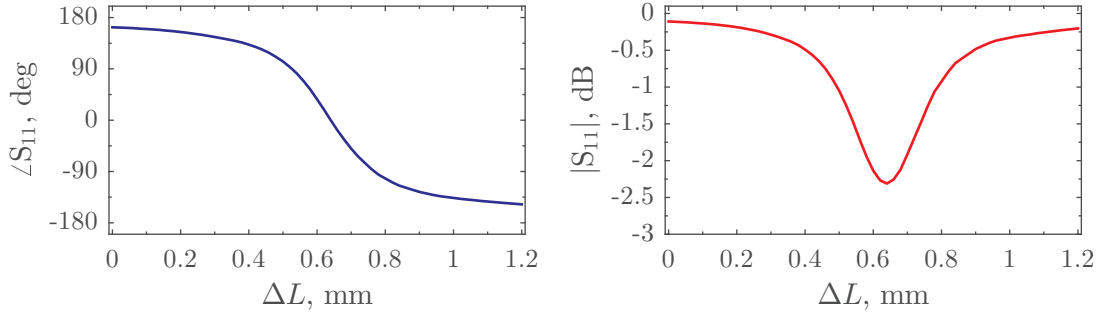


Figure 4.19 – Reflection phase (left) and magnitude (right) of the designed unit cell of Fig. 4.10 for the optimized prototype. The calculation was performed using full-wave simulations in a Floquet’s periodic environment at the design frequency $f_0 = 30$ GHz.

Table 4.2 – Optimized dimensions and material properties of the reconfigurable unit cell constituting the new prototype of Fig. 4.18.

Cell	$L_{cell} = W_{cell} = 5$ mm
Patches	$W_{patch} = 2$ mm $L_{patch} = 1.8$ mm $\Delta L_{max} = 1.2$ mm
Dielectric 1 and 2	$H_{diel1,2} = 203$ μ m $\epsilon_{r1,2} = 3.55$ $\tan \delta_{1,2} = 0.0051$
Fused silica	$H_{glass} = 203$ μ m $\epsilon_{glass} = 3.8$ $\tan \delta_{glass} = 0.0004$
PDMS	$H_{pdms} = 30$ μ m $\epsilon_{pdms} = 2.8$ $\tan \delta_{pdms} = 0.04$

The experimental characterization of the new prototype was performed adopting the same monostatic measurement technique discussed in the previous section. Nevertheless, we used a newly-developed setup which was built in our laboratory (Laboratory of Electromagnetics and Antennas) at EPFL. The new setup was based on a commercial customized Gaussian optics lens antenna from the American company Millitech, which generated a linearly polarized Gaussian beam with a $4\lambda_0$ beamwaist diameter on the focus plane located 35 cm from the lens. The antenna and the new sample holder were placed on a steel optical rail, and their alignment was performed by means of a custom-made system comprising a laser and a set of mirrors. Differently from the characterization of the previous prototype, we used a plastic sample holder that was again covered with flat absorbers baked by a thin (~ 100 μ m) aluminium foil to comply with the guidelines of the supplier. The full control and synchronization of the measurement system (i.e., network analyzer, DEA and vertical actuation) was achieved using

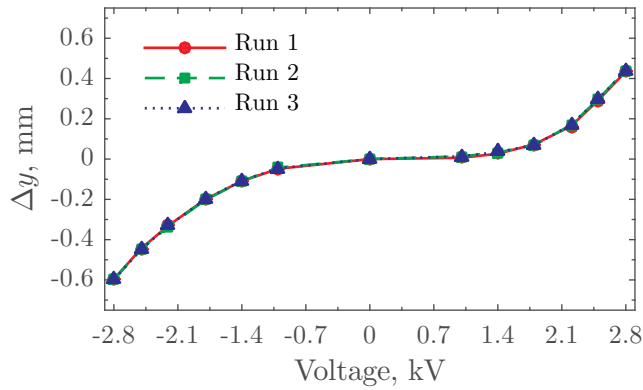


Figure 4.20 – Displacement Δy characterization as a function of the applied voltage for the prototype of Fig. 4.18b performed prior to the MMW reflection measurements. Note V_1 voltages are shown as negative and V_2 voltages shown as positive.

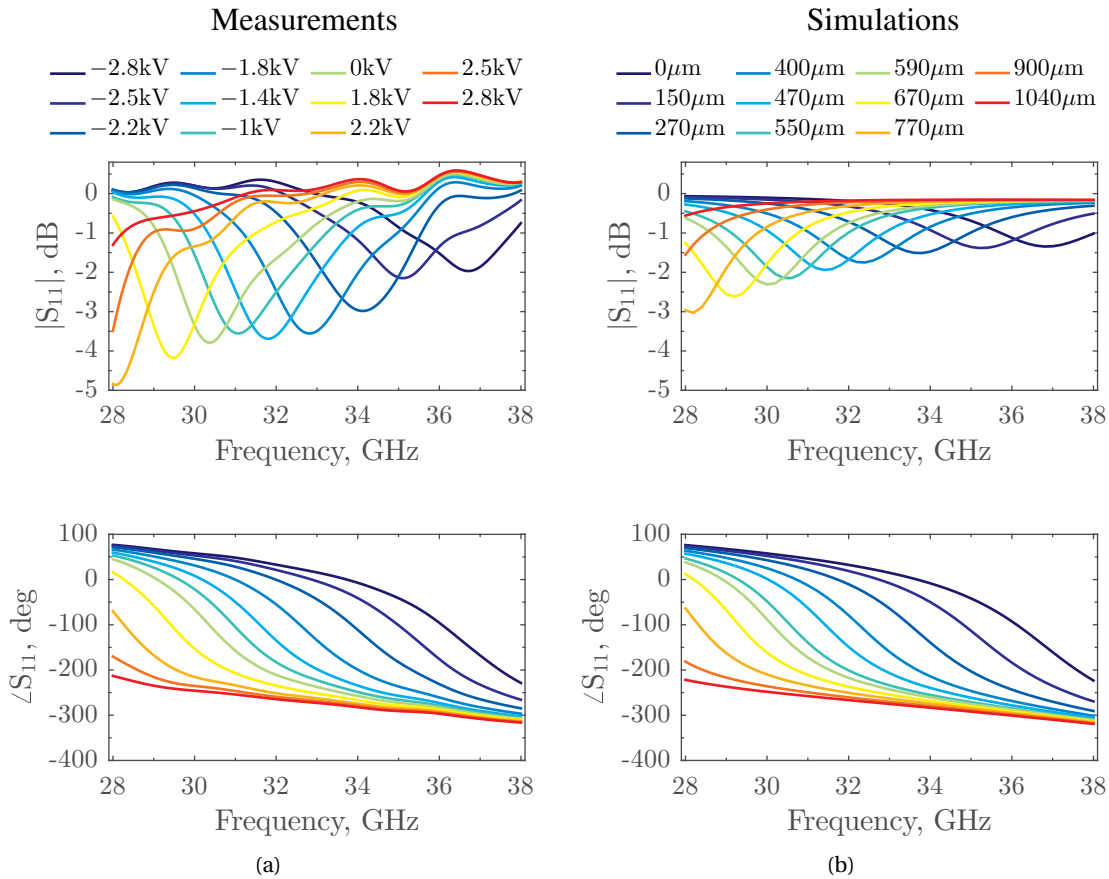


Figure 4.21 – Comparison between measurements and simulations of the reflection magnitude (top) and phase (bottom) for the prototype of Fig. 4.18. (a) Measurements as a function of the actuation voltage and (b) full-wave simulations as a function of the displacement ΔL . Note V_1 voltages are shown as negative and V_2 voltages shown as positive. ΔL values in (b) correspond to the applied voltages in (a) according to the experimental curve of Fig. 4.20.

the LabVIEW software mentioned above and properly modified to account for the new vertical pneumatic actuation.

The measurement procedure followed the same approach previously adopted for the first prototype and described in the previous section, and therefore will not be repeated here. The first step consisted in measuring the displacement Δy as a function of the applied voltage using the digital microscope and the real time LabVIEW processing. The results of this characterization for the prototype of Fig. 4.18b are shown in Fig. 4.20. We can observe very good repeatability of the displacement for the same applied voltage, demonstrating enhanced actuation performance compared to the solenoid-based version of the previous device (cf. Fig. 4.15). This improvement is due to the adopted approach implementing a distributed pneumatic actuation, which allows to generate a uniform force (in both up and down directions) over the whole surface of the array. The MMW measurement results, after normalization to the reference plate, are reported in Fig. 4.21a, which can be compared with the corresponding simulated data of Fig. 4.21b. This time, a very good agreement is found between measurements and simulations, completely validating the proposed reconfiguration approach. Moreover, these results further confirm the assumption of irregular contact adopted to justify the results from the previous device. The main difference between measurements and simulations relates to the reflection magnitude since higher losses are extracted from measurements, with a difference that increases as the frequency decreases. The main reason for these extra losses has been identified in the contribution of different factors related to the measurements system. A few test measurements of a simple mono-layer array of patches (very simple device), in fact, demonstrated the same increase in the peak loss. Moreover, we found that the application of different time gating windows can affect quite considerably the measured magnitude, but only marginally affects the phase of the measured signal. Another aspect to consider is the angular orientation of the device and the reference plate with respect to the measuring antenna. In particular, if a small misalignment exists, the array and the reference reflect the impinging radiation in a slightly different direction with a loss in the measured magnitude. The same loss is observed if the patches are not perfectly aligned with the linear polarization of the impinging field.

Nevertheless, the observed loss issue is not particularly critical, especially considering the MMW reconfiguration potential offered by the proposed concept. These results demonstrate better performance than conventional technologies, such as semiconductors (varactor and PIN diodes) and liquid crystals in the same frequency range. This last statement is justified by the poor loss performance exhibited by reconfigurable RA antennas integrating PIN and varactor diodes. Reflection losses are typically higher than 5 dB for devices operating at C-band (4–8 GHz) [18] and X-band (8–12 GHz) [19], whereas worse performance are achieved at higher frequencies due to the higher losses and parasitic effects introduced by semiconductor diodes. Reflectarrays based on tunable liquid crystals exhibit similar performance with losses higher than 10 dB at Ka-band and above [33, 42].

The proposed reconfigurable design can be also scaled to operate at higher frequencies, such

as V-band (40–75 GHz) and W-band (75–110 GHz), which are of particular interest for high data-rate communications, automotive radar, security screening, and remote sensing. This frequency upgrade would be achieved without degrading the loss performance, since the actuation part does not directly interact with the electromagnetic signal, and only conventional dielectric materials are present in the active area (except for the PDMS that is however very thin).

4.4 DEA-based 1-D scanning RA

The results presented in the previous section allowed to validate the concept for the implementation of a reflectarray device based on rectangular resonant patches where the patch length is mechanically tuned using planar DEAs. The device presented above only allows the reconfiguration of uniform reflection phase of the surface, without providing any beam-scanning capabilities. The evolution of this uniform reflector is represented by the simplified concept of Fig. 4.8, where we envisage the use of agonist DEAs to implement the independent control of each column. This type of control allows to tailor a phase distribution on the reflector surface similar to that shown in the examples of Fig. 4.7, hence implementing beam-scanning in the H-plane of the reflectarray.

This section reports the activities carried out towards the first demonstrator of 1-D beam-scanning reflectarray. The transition between the uniform reconfigurable device of Fig. 4.18 to the column-based reconfiguration of Fig. 4.8 would ideally consist in cutting the top PCB into columns so that they can move independently with respect to each other. Each column would then need to be equipped with its own set of planar actuators to implement the desired bidirectional displacement in the y direction. The schematic concept of Fig. 4.8 would however limit the size of the actuators (maximum width of 5 mm) making impossible to achieve the needed 1.2 mm of bidirectional displacement demonstrated in the previous device, where the size of each actuator was in the order of 40 mm \times 20 mm. This restriction is due to the particular properties of the DEA technology where the achievable strain is clearly strongly dependent on the size of the actuators, in addition to other boundary conditions [43]. The strip actuators depicted in Fig. 4.8 have two free edges, being less effective than other DEA configurations. A DEA with two free edges is unconstrained and does not allow a uniform prestretch of the PDMS membrane. This lack of prestretch (demonstrated by the necking of the actuators), results in a loss of displacement and reduced DEA performance. Another challenge related to the configuration of Fig. 4.8 is represented by the high-voltage operation of DEAs. Owing to the high voltage, adjacent electrodes would need to be properly spaced to prevent the breakdown of air (3 kV/mm). In practical design a safe limit of 1 kV/mm is adopted to ensure that breakdown does not occur because of conductive residues between the electrodes.

In order to overcome the limitations discussed above and to allow more flexibility in the design of the DEAs, we investigated a new concept, slightly different from the one shown in

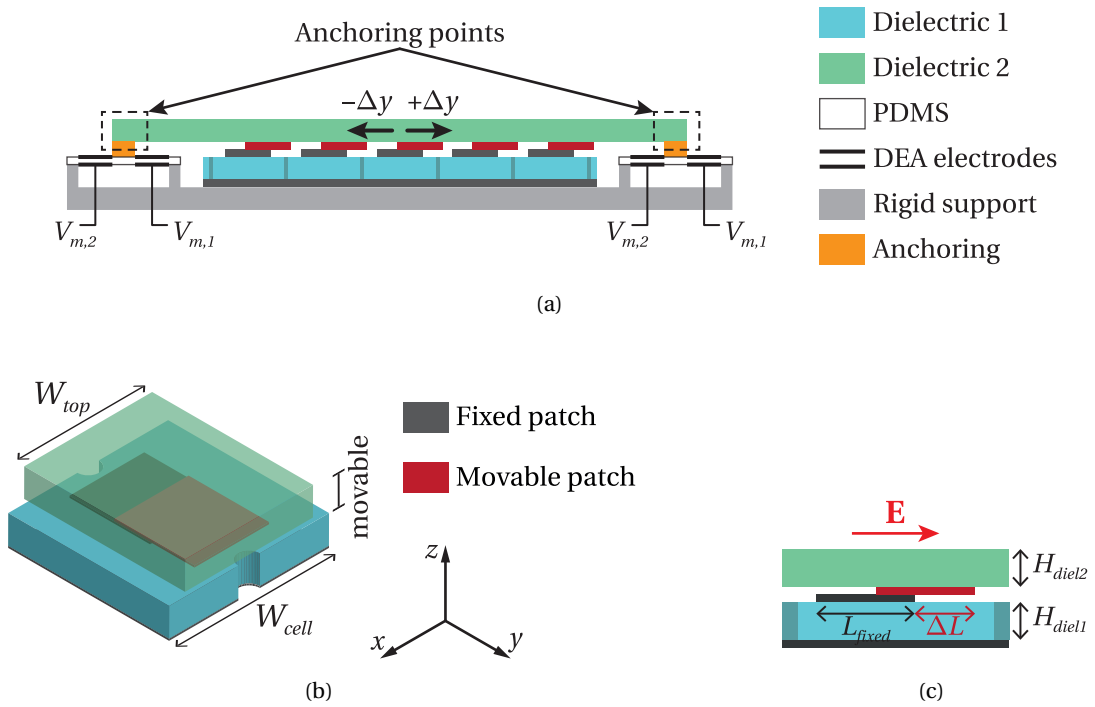


Figure 4.22 – Simplified drawing of the final concept for independent column reconfiguration. (a) yz longitudinal section showing the DEA reconfiguration approach for one column of the reflectarray surface. (b) Isometric view and (c) yz longitudinal section of the unit cell constituting the final reflectarray device. The holes in the bottom array are used to implement the discussed pneumatic vertical actuation.

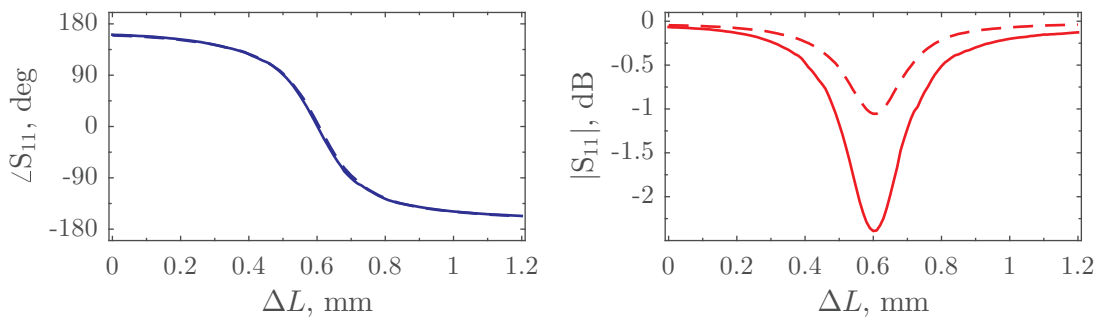


Figure 4.23 – Reflection phase (left) and magnitude (right) of unit cell of Fig. 4.22b designed for the realization of the beam-scanning RA. The calculation was performed using full-wave simulations in a Floquet's periodic environment at the design frequency $f_0 = 30$ GHz.

Table 4.3 – Optimized dimensions and material properties of the reconfigurable unit cell constituting the beam-scanning concept of Fig. 4.22.

Cell	$L_{cell} = W_{cell} = 5 \text{ mm}$ $W_{top} = 4 \text{ mm}$
Patches	$W_{patch} = 2 \text{ mm}$ $L_{patch} = 1.78 \text{ mm}$ $\Delta L_{max} = 1.2 \text{ mm}$
Dielectric 1 and 2	$H_{diel1,2} = 305 \mu\text{m}$ $\epsilon_{r1,2} = 3.55$ $\tan \delta_{1,2} = 0.0051$

Fig. 4.8. The new approach is based on the use of rigid-frame actuators, where the whole PDMS membrane is bound to a rigid frame, and all the edges are supported maintaining a uniform prestretch. The actuator parts are therefore confined at the edges of the array, and the movable strips are anchored to them at their extremities. This means that no PDMS, and consequently no fused silica, are needed in the EM active area to allow the bonding between the movable part and the corresponding DEAs. A schematic illustration of this concept is depicted in Fig. 4.22a, showing the longitudinal cut of one reconfigurable column. In this new configuration, each extremity of the movable strip is fixed to a set of two agonist DEA segments by means of a rigid anchoring element. Homologous actuators (i.e., $V_{m,1}$ and $V_{m,2}$ in Fig. 4.22a) on the two sides of the m -th column are connected and actuated in parallel to optimize the actuation output. This geometry in fact avoids that a passive region on the opposite side could reduce the achievable strain. An actuation voltage $V_{m,1}$ generates a displacement $-\Delta x$ reducing the patch length, whereas a voltage $V_{m,2}$ produces a movement $+\Delta x$ in the opposite direction which increases ΔL . The vertical movement to implement the three-step actuation procedure of Fig. 4.9 is still obtained using the pneumatic actuation described in §4.3.3, for which an array of holes is considered in the bottom array (Fig. 4.22).

A new design of the unit cell was necessary to account for the modifications applied to the reconfigurable concept discussed above. The new RA element is shown in Fig. 4.22b (isometric view) and Fig. 4.22c (yz cut). The first difference with respect to the cell of Fig. 4.10 consists in the absence of the PDMS membrane and the related fused silica bonding layer. Moreover, the width W_{top} of the column PCB is smaller than the actual width W_{cell} of the unit cell to avoid any contact (and consequent friction) between adjacent movable strips. Therefore, the reflection properties are modified with respect to the previous design. The selected dielectric and geometric parameters of the cell shown in Fig. 4.22b are summarized in Tab. 4.3. In this case both the top and bottom arrays are realized using a $305 \mu\text{m}$ thick Rogers RO4003C laminate. The corresponding full-wave simulations (reflection phase and magnitude) are reported in Fig. 4.23. Note that two curves are shown in each panel: 1) dashed lines correspond to a simulation where metallic parts are characterized by a nominal copper conductivity ($\sigma_{cu} = 5.8 \times 10^7 \text{ S/m}$) and dielectric losses are modeled by a loss tangent of 0.0027

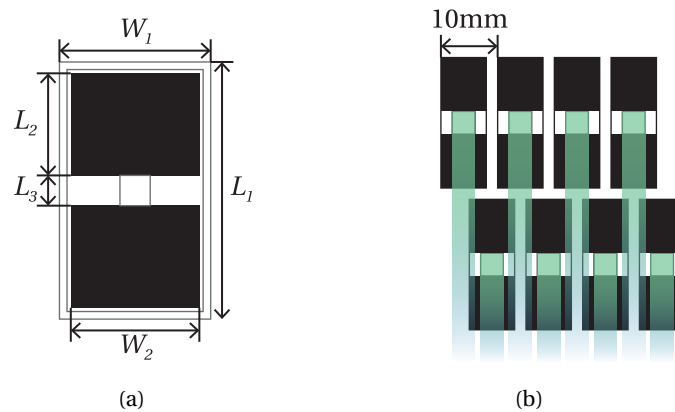


Figure 4.24 – Final geometry of the DEA actuators integrated in the beam-scanning reflectarray. (a) Single actuator comprising 2 agonist DEA segment to optimize the achievable displacement. (b) Example of 8 actuators staggered on two rows, implementing the independent displacement of just as many columns (in shaded green).

(provided by the supplier for 10 GHz operation); solid lines correspond to a more realistic situation where a metal stack of copper, nickel and gold implements the metallic parts and the datasheet loss tangent is replaced by the measured one (0.0051). A difference of around 1.3 dB is found in the resonance peak which is due to the increased dielectric and conductor losses. The reflection phase remains unchanged and allows a reconfigurable range of around 315° centered at $\Delta L = 0.6$ mm.

Figure 4.22 shows that the single column PCB and the associated DEAs are not bound to the same PDMS membrane, hence offering more degrees of freedom to design the actuators and allowing to optimize their size and their position with respect to the moving arrays. As we have mentioned above, a 5 mm wide actuator (comprising 2 agonist DEAs) would not be able to comply with the requirement of 1.2 mm displacement. However, it is clear that it is impossible to increase the size of the actuators if these remain aligned one next to each other. This issue was overcome by considering a staggered configuration of the actuators, which are placed and aligned on different rows. It is clear that this disposition still needs to ensure the independent movement of adjacent column arrays that are spaced 5 mm apart. Therefore, considering the actuator geometry of Fig. 4.24a, the maximum width of the actuator (W_1 in Fig. 4.24a) strictly depends on the maximum number of rows that are acceptable in the final device. An implementation example is shown in Fig. 4.24b where 8 actuators are divided in 2 rows. In this particular case the maximum W_1 allowing enough spacing to move the independent columns ($W_{top} = 4$ mm) is 10 mm. Preliminary actuator designs and tests carried out at LMTS demonstrated that a minimum value $W_1 = 20$ mm was necessary to obtain the required displacement of 1.2 mm. The remaining dimensions of the actuator depicted in Fig. 4.24a were selected as follows: $L_1 = 34$ mm (total length of the actuator), $W_2 = 17$ mm (width of each electrode), $L_2 = 13.5$ mm (length of each electrode) and $L_3 = 4$ mm (size of the rigid anchoring element placed in the center of the actuator). A staggered configuration based

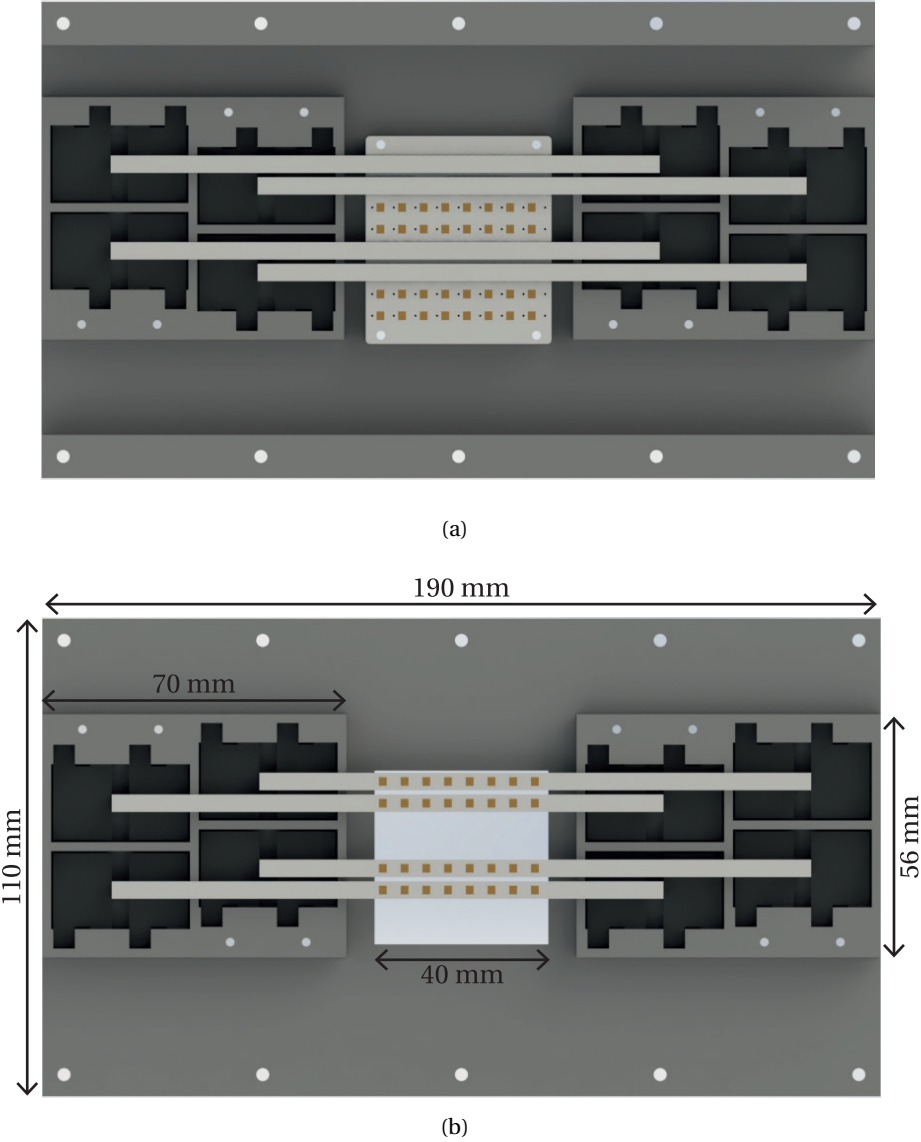


Figure 4.25 – Render of the 1-D beam-scanning RA consisting of an array of 8×8 cells. (a) Top view of the bottom part integrating the array of fixed patches and a full set of 4 DEAs allowing the independent control of just as many RA columns. (b) Bottom view of the top part including the remaining set of 4 actuators with corresponding moving arrays.

on the selected size would produce a set of DEAs divided in four rows and, therefore, a total length of 136 mm. The same set of actuator would then need to be duplicated on the opposite side of the movable columns (cf. Fig. 4.22a) resulting in a long device, not really practical for our scopes.

To reduce the size of the full reflectarray device we investigated alternative approaches permitting to increase the size of the single actuator without affecting the total size and the manufacturing complexity of the final prototype. The identified solution relies on the implementation of a three-dimensional staggered configuration where the single actuators are laid out in different rows and multiple layers. For an assigned size of the single actuator, it is for instance possible to halve the number of needed rows by placing the same number of actuators on two stacked layers. We selected this approach for our first prototype to implement independent column reconfiguration of an array of 8×8 cells. To this purpose we divided the 8 actuators in 2 layers, each one comprising 2 rows of 2 actuators (size 20 mm \times 34 mm). The maximum size of the array was again limited by the pad-printing machine currently used for the realization of the electrodes, assuming that the 4 actuators in each layer are printed at the same time on a single PDMS membrane. This choice allowed to reduce the number of fabrication steps and to avoid any issue in the alignment of the actuators in the same layer. The independent control of each actuator was then obtained by adhering the printed membrane to a rigid frame including apertures corresponding to the position of the different actuators.

A render of the designed 1-D scanning reflectarray is shown in Fig. 4.25. The device is realized in two parts, each one integrating 4 full sets of actuators (i.e., a single layer). The two parts are then assembled together to implement the final device consisting of an array of 8×8 cells where each column is independently controlled. The bottom part (Fig. 4.25a) integrates the fixed array of patches and the air chamber required to implement pneumatic vertical actuation validated with the uniform reconfigurable reflector of §4.3.3. Also here the same pneumatic approach is realized drilling an array of small holes in the bottom PCB to convey the bidirectional flow controlled by the external pneumatic valve. Obviously all the strips are moved together in the vertical direction, whereas an independent horizontal displacement can be obtained for each of them by actuating the corresponding DEAs. The alignment between the different parts is a critical aspect in the assembly of the device, since it is important to ensure a precise overlap between each movable strip and the corresponding bottom line of cells. Moreover, the assembly position needs to coincide to the state $\Delta L = 0.6$ mm for all the RA columns. However, the use of precise micro-fabrication techniques and of properly designed alignment jigs permit to obtain good accuracy in the final assembly, and consequently performance are expected in good agreement with the prediction. The final prototype is currently under development, but preliminary mechanical experiments performed on an intermediate device demonstrated correct operation of the actuation principle, able to produce the total displacement of 1.2 mm for a single column.

The final reflectarray will operate in single linear polarization with the electric field aligned in the y direction of Fig. 4.22 and will be controlled to achieve beam-scanning in the H -plane

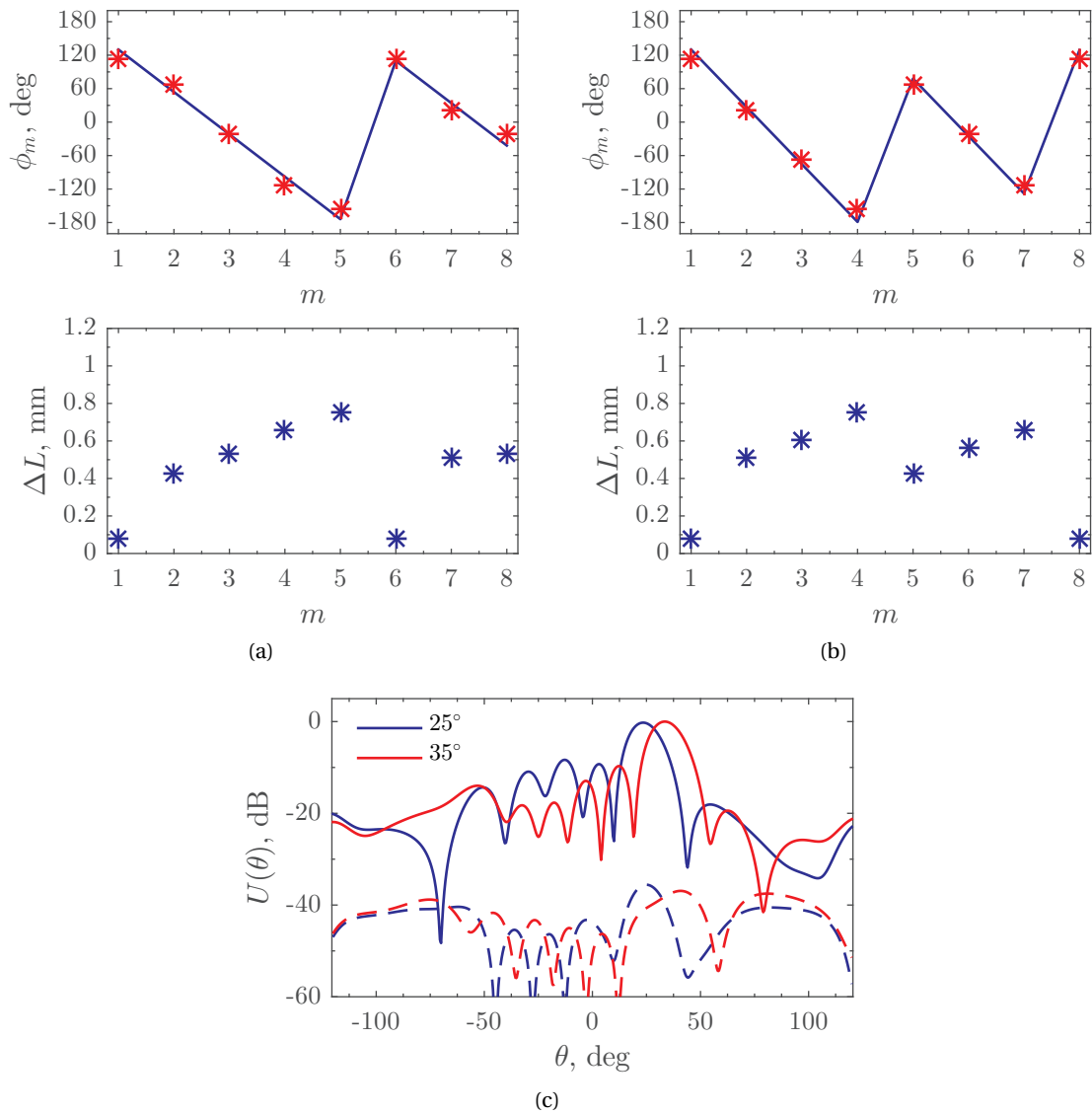


Figure 4.26 – Simulated beam-scanning example for the final RA prototype consisting of an array of 8×8 cells grouped in 8 reconfigurable columns. Top panels of (a) and (b): calculated phase profile (solid lines) and related phase quantization (markers) to point the beam at $\theta = 25^\circ$ and $\theta = 35^\circ$, respectively. Bottom panels of (a) and (b): corresponding displacement ΔL to realize the needed phase profile. (c) Computed co- (solid lines) and cross-polar (dashed lines) radiation pattern.

(xz plane). To obtain a fully operative antenna, the prototype of Fig. 4.25 will be illuminated by a linearly polarized feed that shall be placed in the H -plane of the array to minimize the cross-polarization and the dependence of the reflection phase on the relative position of the element in the array. This geometry translates in a TE-polarized incident field and a wave vector in the H -plane of the array element. Here we present a simplified example based on full-wave simulations able to predict the beam-scanning performance of the final reflectarray prototype. Simulated data were generated considering an array of 8×8 cells of the type shown in Fig. 4.22 and with the properties selected for the final design (cf. Tab. 4.3). The device model implemented in the simulator did not include the actuator parts, which will be screened in the final device to avoid any coupling with the feeding wave (this is necessary considering the small size of the array). Moreover, the array was illuminated by a normally impinging plane wave. The reflection phase profile needed in the x direction to point the beam at $\theta = 25^\circ$ and $\theta = 35^\circ$ was calculated and is reported in the top panels of Fig. 4.26a and Fig. 4.26b, respectively. Solid lines represent the calculated phase, and markers are the values generated by a 3-bit phase quantization, which produces a maximum quantization error of 21.5° . It is worth noting that an arbitrary phase bias can be added to the calculated profile. In particular, this principle was here used to minimize the phase quantization error. These phase values were then converted in displacement ΔL (bottom panels of Fig. 4.26a and Fig. 4.26b) using the phase curve of Fig. 4.23. The corresponding radiation patterns are shown in Fig. 4.26c including both the co- (solid lines) and cross-polarization (dashed lines) components. The cross-polarization level is always lower than 35 dB with respect to the radiation maximum. However, sidelobes are only 10 dB below the maximum, which is mainly due to the small electrical size of the considered aperture (only $4\lambda_0 \times 4\lambda_0$). Sidelobe performance are in fact typically degraded at decreasing the reflector size, due to the increased amounts of edge diffraction and specular reflection [2].

4.5 Conclusions

This chapter discussed the design, manufacturing and characterization of reconfigurable reflectarray devices operating at Ka-band and integrating a mechanical tuning mechanism based on planar dielectric elastomer actuators (DEAs). The proposed reconfiguration approach relies on a DEA-based actuation principle similar to that successfully applied to the tunable phase shifter presented in the previous chapter. The reconfigurable unit cell discussed here consists of a fixed rectangular patch on a grounded dielectric substrate and a movable patch realized on a second dielectric layer, which is horizontally displaced by the in-plane DEA expansion. When the movable and fixed patch are in ohmic contact, a given displacement of the moving plate with respect to the fixed one exactly corresponds to an equal increment of the equivalent patch length. With this approach the actuation part is confined at the extremities of the array and therefore does not interfere with the EM propagation, resulting in losses comparable to the device fixed counterpart.

The proposed reconfiguration concept has been validated by designing and fabricating a

reflective surface with uniform phase distribution where the reconfiguration of all the cells was realized using a single horizontal displacement. A prototype was manufactured using commercial materials and standard PCB fabrication techniques available at EPFL. The experimental characterization demonstrated very good agreement with simulations, confirming the predicted performance in terms of losses and phase reconfiguration capabilities. Based on these promising results, the design of a 1-D beam-scanning reflectarray has been proposed. This concept is based on the independent control of each column of cells to implement beam-scanning functionality in the H -plane of the antenna. The radiating performance of this device have been evaluated using full-wave simulations, and further activities will be carried out to manufacture a fully functional prototype that can be tested using conventional radiation pattern measurements.

Bibliography

- [1] C. A. Balanis, *Modern Antenna Handbook*. John Wiley & Sons, Inc., 2008.
- [2] J. Huang and J. A. Encinar, *Reflectarray antennas*. John Wiley & Sons, Inc., 2007.
- [3] D. Berry, R. Malech, and W. Kennedy, "The reflectarray antenna," *IEEE Transactions on Antennas and Propagation*, vol. 11, no. 6, pp. 645–651, 1963.
- [4] J. Huang, "Microstrip reflectarray," in *Antennas and Propagation Society International Symposium Digest*, June 1991, pp. 612–615.
- [5] D. M. Pozar and T. A. Metzler, "Analysis of a reflectarray antenna using microstrip patches of variable size," *Electronics Letters*, vol. 29, no. 8, pp. 657–658, 1993.
- [6] D. M. Pozar, S. D. Targonski, and H. Syrigos, "Design of millimeter wave microstrip reflectarrays," *IEEE Transactions on Antennas and Propagation*, vol. 45, no. 2, pp. 287–296, 1997.
- [7] D. M. Pozar and S. D. Targonski, "A microstrip reflectarray using crossed dipoles," in *IEEE International Symposium on Antennas and Propagation Society*, vol. 2, 1998, pp. 1008–1011.
- [8] N. Misran, R. Cahill, and V. F. Fusco, "Design optimisation of ring elements for broadband reflectarray antennas," *IEE Proceedings on Microwaves, Antennas and Propagation*, vol. 150, no. 6, pp. 440–444, 2003.
- [9] M. R. Chaharmir, J. Shaker, M. Cuhaci, and A. Sebak, "Reflectarray with variable slots on ground plane," *IEE Proceedings on Microwaves, Antennas and Propagation*, vol. 150, no. 6, pp. 436–439, 2003.
- [10] D.-C. Chang and M.-C. Huang, "Multiple-polarization microstrip reflectarray antenna with high efficiency and low cross-polarization," *IEEE Transactions on Antennas and Propagation*, vol. 43, no. 8, pp. 829–834, 1995.
- [11] R. D. Javor, X.-D. Wu, and K. Chang, "Design and performance of a microstrip reflectarray antenna," *IEEE Transactions on Antennas and Propagation*, vol. 43, no. 9, pp. 932–939, 1995.
- [12] J. Huang and R. J. Pogorzelski, "A Ka-band microstrip reflectarray with elements having variable rotation angles," *IEEE Transactions on Antennas and Propagation*, vol. 46, no. 5, pp. 650–656, 1998.
- [13] J. A. Encinar, "Design of two-layer printed reflectarrays using patches of variable size," *IEEE Transactions on Antennas and Propagation*, vol. 49, no. 10, pp. 1403–1410, 2001.
- [14] J. A. Encinar and J. A. Zornoza, "Broadband design of three-layer printed reflectarrays," *IEEE Transactions on Antennas and Propagation*, vol. 51, no. 7, pp. 1662–1664, 2003.

- [15] S. V. Hum and J. Perruisseau-Carrier, "Reconfigurable Reflectarrays and Array Lenses for Dynamic Antenna Beam Control: A Review," *IEEE Transactions on Antennas and Propagation*, vol. 62, no. 1, pp. 183–198, 2014.
- [16] D. F. Sievenpiper, J. H. Schaffner, H. J. Song, R. Y. Loo, and G. Tangonan, "Two-dimensional beam steering using an electrically tunable impedance surface," *IEEE Transactions on Antennas and Propagation*, vol. 51, no. 10, pp. 2713–2722, 2003.
- [17] M. Riel and J. Laurin, "Design of an Electronically Beam Scanning Reflectarray Using Aperture-Coupled Elements," *IEEE Transactions on Antennas and Propagation*, vol. 55, no. 5, pp. 1260–1266, 2007.
- [18] S. V. Hum, M. Okoniewski, and R. J. Davies, "Modeling and Design of Electronically Tunable Reflectarrays," *IEEE Transactions on Antennas and Propagation*, vol. 55, no. 8, pp. 2200–2210, 2007.
- [19] J. Perruisseau-Carrier, "Dual-Polarized and Polarization-Flexible Reflective Cells With Dynamic Phase Control," *IEEE Transactions on Antennas and Propagation*, vol. 58, no. 5, pp. 1494–1502, 2010.
- [20] E. Carrasco, M. Barba, and J. A. Encinar, "X-band reflectarray antenna with switching-beam using pin diodes and gathered elements," *IEEE Transactions on Antennas and Propagation*, vol. 60, no. 12, pp. 5700–5708, 2012.
- [21] D. Rodrigo, L. Jofre, and J. Perruisseau-Carrier, "Unit Cell for Frequency-Tunable Beam-scanning Reflectarrays," *IEEE Transactions on Antennas and Propagation*, vol. 61, no. 12, pp. 5992–5999, 2013.
- [22] S. Montori, F. Cacciamani, R. Vincenti Gatti, R. Sorrentino, G. Arista, C. Tienda, J. A. Encinar, and G. Toso, "A Transportable Reflectarray Antenna for Satellite Ku-band Emergency Communications," *IEEE Transactions on Antennas and Propagation*, vol. 63, no. 4, pp. 1393–1407, 2015.
- [23] H. Legay, B. Pinte, M. Charrier, A. Ziaei, E. Girard, and R. Gillard, "A steerable reflectarray antenna with MEMS controls," in *IEEE International Symposium on Phased Array Systems and Technology*, Oct 2003, pp. 494–499.
- [24] S. V. Hum, G. McFeetors, and M. Okoniewski, "Integrated MEMS reflectarray elements," in *1st European Conference on Antennas and Propagation (EuCAP)*, Nov 2006, pp. 1–6.
- [25] J. Perruisseau-Carrier and A. K. Skrivervik, "Monolithic MEMS-Based Reflectarray Cell Digitally Reconfigurable Over a 360° Phase Range," *IEEE Antennas and Wireless Propagation Letters*, vol. 7, pp. 138–141, 2008.
- [26] H. Rajagopalan, Y. Rahmat-Samii, and W. A. Imbriale, "RF MEMS Actuated Reconfigurable Reflectarray Patch-Slot Element," *IEEE Transactions on Antennas and Propagation*, vol. 56, no. 12, pp. 3689–3699, 2008.

-
- [27] C. Guclu, J. Perruisseau-Carrier, and O. Civi, "Proof of Concept of a Dual-Band Circularly-Polarized RF MEMS Beam-Switching Reflectarray," *IEEE Transactions on Antennas and Propagation*, vol. 60, no. 11, pp. 5451–5455, 2012.
- [28] T. Debogovic and J. Perruisseau-Carrier, "Low Loss MEMS-Reconfigurable 1-Bit Reflectarray Cell With Dual-Linear Polarization," *IEEE Transactions on Antennas and Propagation*, vol. 62, no. 10, pp. 5055–5060, 2014.
- [29] R. R. Romanofsky, "Advances in Scanning Reflectarray Antennas Based on Ferroelectric Thin-Film Phase Shifters for Deep-Space Communications," *Proceedings of the IEEE*, vol. 95, no. 10, pp. 1968–1975, 2007.
- [30] M. Y. Ismail, W. Hu, R. Cahill, V. F. Fusco, H. S. Gamble, D. Linton, R. Dickie, S. . Rea, and N. Grant, "Phase agile reflectarray cells based on liquid crystals," *IET Microwaves, Antennas Propagation*, vol. 1, no. 4, pp. 809–814, 2007.
- [31] W. Hu, R. Cahill, J. A. Encinar, R. Dickie, H. Gamble, V. Fusco, and N. Grant, "Design and Measurement of Reconfigurable Millimeter Wave Reflectarray Cells With Nematic Liquid Crystal," *IEEE Transactions on Antennas and Propagation*, vol. 56, no. 10, pp. 3112–3117, 2008.
- [32] G. Perez-Palomino, P. Baine, R. Dickie, M. Bain, J. A. Encinar, R. Cahill, M. Barba, and G. Toso, "Design and Experimental Validation of Liquid Crystal-Based Reconfigurable Reflectarray Elements With Improved Bandwidth in F-Band," *IEEE Transactions on Antennas and Propagation*, vol. 61, no. 4, pp. 1704–1713, 2013.
- [33] S. Bildik, S. Dieter, C. Fritsch, W. Menzel, and R. Jakoby, "Reconfigurable folded reflectarray antenna based upon liquid crystal technology," *IEEE Transactions on Antennas and Propagation*, vol. 63, no. 1, pp. 122–132, 2015.
- [34] P. Nayeri, A. Z. Elsherbeni, and F. Yang, "Radiation Analysis Approaches for Reflectarray Antennas," *IEEE Antennas and Propagation Magazine*, vol. 55, no. 1, pp. 127–134, 2013.
- [35] P. Romano, O. Araromi, S. Rosset, H. Shea, and J. Perruisseau-Carrier, "Tunable millimeter-wave phase shifter based on dielectric elastomer actuation," *Applied Physics Letters*, vol. 104, no. 2, p. 024104, 2014.
- [36] R. Guzman-Quiros, J. L. Gomez-Tornero, A. R. Weily, and Y. J. Guo, "Electronically Steerable 1-D Fabry-Perot Leaky-Wave Antenna Employing a Tunable High Impedance Surface," *IEEE Transactions on Antennas and Propagation*, vol. 60, no. 11, pp. 5046–5055, 2012.
- [37] R. Guzman-Quiros, J. L. Gomez-Tornero, A. R. Martinez-Ros, Alejandro J Weily, and Y. J. Guo, "Novel and Simple Electronically Reconfigurable Fabry-Perot Antennas," in *XXVIII Simp. Nac. URSI, Santiago de Compostela*, vol. 1, 2013, pp. 2–5.

- [38] S. Rosset and H. R. Shea, "Towards fast, reliable, and manufacturable DEAs: miniaturized motor and Rupert the rolling robot," in *Proc. SPIE*, vol. 9430, 2015, p. 943009.
- [39] P. W. Hannan and M. A. Balfour, "Simulation of a phased-array antenna in waveguide," *IEEE Transactions on Antennas and Propagation*, vol. 13, no. 3, pp. 342–353, 1965.
- [40] L. E. R. Petersson and G. S. Smith, "An estimate of the error caused by the plane-wave approximation in free-space dielectric measurement systems," *IEEE Transactions on Antennas and Propagation*, vol. 50, no. 6, pp. 878–887, 2002.
- [41] F. Goldsmith, Paul, *Quasioptical systems*. Wiley-IEEE Press, 1998.
- [42] S. Bildik, C. Fritzsche, A. Moessinger, and R. Jakoby, "Tunable liquid crystal reflectarray with rectangular elements," in *German Microwave Conference*, March 2010, pp. 1–4.
- [43] S. Rosset, O. A. Araromi, and H. R. Shea, "Maximizing the displacement of compact planar dielectric elastomer actuators," *Extreme Mechanics Letters*, *in press*, vol. 3, pp. 72–81, 2015.

5 Stretchable reflectarray antennas for THz applications

The results presented in the previous chapters have demonstrated the potential of dielectric elastomer actuators to implement low-loss reconfiguration of antenna devices at millimeter-waves. In particular, previous activities have focused on Ka-band, owing to the increasing evolution of emerging telecommunication systems operating in this frequency range. In parallel, recent years have also seen a growing interest for terahertz applications where the technological development is of paramount importance.

Within this context, the objective of this chapter is to present the activities carried out for the development of THz antenna devices with reconfiguration capabilities. After a brief introduction to THz systems and applications (§5.1), an efficient approach for the fabrication of flexible and stretchable conductors based on gold ion implantation is presented in §5.2. The design, fabrication and test of a fixed-beam reflectarray operating at 1 THz and integrating an implanted ground plane are discussed in §5.3. Based on previous results, §5.4 proposes the first experimental demonstration of THz beam-scanning reflectarray based on mechanical stretching that can be realized using DEAs. A summary of the chapter is found in §5.5.

5.1 Introduction

Terahertz radiation is typically located in the frequency range 0.3–10 THz, falling between the microwave and infrared electromagnetic spectrum (Fig. 5.1). This frequency band has also been defined as the “terahertz gap” due to the poor availability of efficient technology (particularly sources and detectors) that has influenced for more than two decades the development of practical applications, with respect to the well-established microwave and optical regions. The “gap”, clearly highlighted in Fig. 5.1, is progressively reducing due to the technological development initially ignited by emerging applications in the space field. With the improvement achieved by the semiconductor industry, the development of new materials and the increasing advancement of micro and nano-fabrication techniques, several terrestrial applications have been also identified and are currently addressed by the international scientific community. Terahertz science is currently undergoing a rapid advancement especially driven by the avail-

ability of emitters and detectors (e.g., femtosecond lasers and photoconductive antennas) and the development of commercially available spectroscopy and imaging systems. Several applications in the THz region are under investigation and can be summarized as follow:

- **Space observations:** this macro-area comprises several targets, including atmospheric remote sensing, astronomy, planetary and cometary science. These applications are motivated by the particular properties of the THz radiation allowing to detect variations in the thermal, rotational or vibrational state of the interacting media [1–3].
- **Security screening:** based on the ability to penetrate several non-conductive materials such as polymers, paper, clothing, ceramics, chemical powders that can be opaque in the visible range. These properties are therefore particularly appealing for the non-invasive identification of hidden objects (e.g., concealed weapons) [4]. Moreover, THz spectroscopy can be successfully used for the identification of specific explosives or drugs, which present particular spectral lines when illuminated by THz radiation [5].
- **Non-invasive medical imaging:** THz radiation is particularly suitable to medical application since it exhibits a low photon energy that allows safe and high resolution imaging without ionization of biological tissues (in contrast to X-rays for instance) [6, 7].
- **Communication systems:** potential for high data rate (up to Tbit/s) links operating in the lower THz band (between 300 GHz and 1 THz), where an atmospheric window exists. Possible applications include indoor femto-cellular networks, wireless local area networks (WLAN) and wireless personal area network (WPAN), high-speed connection of computer devices, kiosk download, and satellite-to-satellite links [8–10].

The activities presented in this chapter have been carried out targeting a contribution to the development of THz antenna technology. The use of high-gain antennas, together with high-power sources and efficient detectors, plays a critical role in all the applications mentioned above, with a special focus on communication systems, where high performance are needed to cope with the high free-space attenuation that heavily affect the link budget. Moreover, advanced capabilities, such as beam-scanning could be very advantageous in particular applications where a real time optimization of the communication link is needed (e.g., indoor femto-cellular networks, kiosk download, satellite-to-satellite communications). Related to the antenna development, it is worth to consider the evolution of metamaterials that are experiencing a growing interest due to the need to compensate for the poor performance of conventional materials that instead are typically used at lower frequencies (microwave to millimeter-wave) or in the optical region [11–13]. In this framework we integrate our activities targeting the development of conformal and reconfigurable antenna devices based on stretchable conductors and that can potentially benefit from the use of dielectric elastomer actuators.

5.2. Stretchable conductors based on gold ion implantation

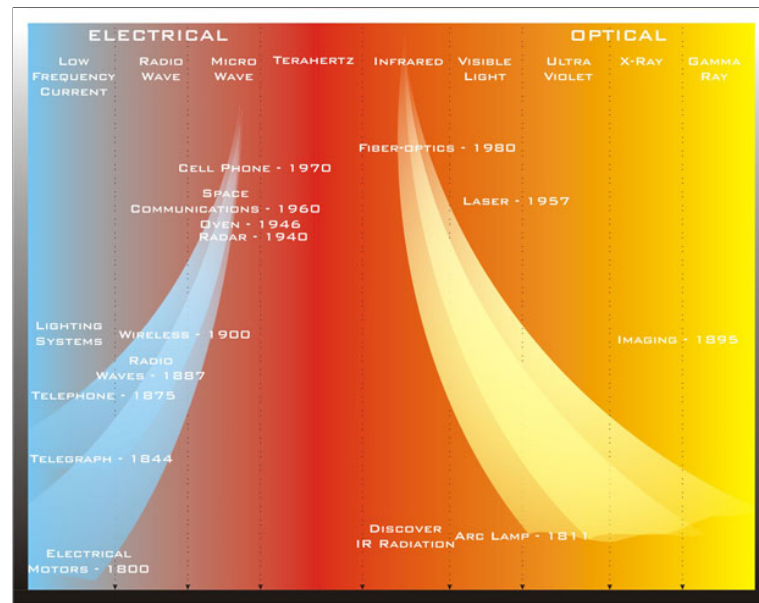


Figure 5.1 – Electromagnetic spectrum spanning from microwave to optical frequencies and highlighting the lack of established applications within the “THz gap”. Courtesy of Teraphysics Corporation.

5.2 Stretchable conductors based on gold ion implantation

This section presents a practical and efficient approach for the implementation of flexible and stretchable conductors targeting terahertz applications. The proposed technique is based on low-energy gold ion implantation in thin PDMS membranes. The same method has been already discussed in chap. 2, where we investigated its possible utilization at millimeter-waves. We have experimentally demonstrated a surface conductivity of around $30 \Omega/\square$ at Ka-band resulting in high ohmic losses and limiting the practical application of implanted PDMS membranes to the realization of small compliant connections. Nevertheless, better performance are expected at THz frequencies due to the smaller wavelength of the considered radiation (more than 30 times smaller with respect to 30 GHz) associated with the particular structure of the conceived metallization. It is worth recalling that this technique was initially developed for the realization of compliant electrodes in dielectric elastomer actuators [14–16], where reliable electrical conduction needs to be maintained at high strains (up to 100%). Thin stretchable conductive layers are obtained using a low-energy filtered cathodic vacuum arc (FCVA) that allows to confine the implanted gold ions within the top 50 nm from the PDMS surface. This type of implantation does not generate a continuous rigid film, but leads to the formation of gold nano-clusters into the polymer matrix which are in physical contact, thereby generating a conductive path. When the polymer is stretched, these particles move with respect to each other keeping electrical conductivity providing that a continuous path or capacitive coupling exists. Therefore, qualitative considerations suggest that better conductivity is achievable at THz with respect to Ka-band as the higher frequency allows a stronger coupling.

This technology allows a rapid and efficient manufacturing, which is highly compatible with standard micro-fabrication techniques and allows the realization of precise patterns up to the micrometer scale using micro-fabricated shadow masks. The shadow-mask patterning method can be a limiting factor for the realization of micrometer elements, since the aspect ratio of the mask can affect the concentration of gold ions into the elastomer [16]. However, if very small patterns need to be realized, nano-stencil lithography techniques represent a very effective solution allowing the precise patterning of sub-micrometer features (e.g., [17, 18]). This fabrication technique would find wide application at THz frequencies, including the realization of flexible and conformal devices, or tunable metamaterials in general, based on the mechanical deformation of the substrate or the composing unit elements [13, 17, 19–23].

The applicability of gold ion implantation for the realization of THz stretchable devices has been assessed characterizing the surface conductivity of several samples realized with different concentration of the gold ions. Measurements were performed for different stretching ratio of the implanted zone in order to evaluate the corresponding change in conductivity. The analyzed samples were prepared at the *Microsystems for Space Technologies Laboratory (LMTS)* using pulsed-mode FCVA to realize low-energy implantation allowing uniform concentration of gold nano-particles within the first 50 nm of the PDMS layer. A detailed description of the equipment and the implantation procedure can be found in [15]. Considering the utilized FCVA equipment, the implantation dose (in ions/cm²) is directly proportional to the number of arc pulses used during the implantation. The relation between dose level and number of pulses can be typically obtained using a Rutherford backscattering spectroscopy calibration. Nevertheless, the size of the samples considered here required the use of a motorized scanning stage to realize the implantation of the full area, making this type of calibration not valid [14]. The ion concentration is therefore expressed in terms of arc pulses per unit area (pulses/cm²). Each sample consists of a thin PDMS membrane (Sylgard 186) with size of 50 mm × 30 mm and thickness ranging between 40 and 50 μm (uniform for each sample). The PDMS membrane is adhered to a laser-cut frame and gold ion implantation is performed on one side of the membrane covering a square area of 20 × 20 mm². Half of the membrane is left free from any implantation to allow a reference measurement of the PDMS material on the same membrane as needed by the extraction technique described in the following. A render of the test sample is shown in Fig. 5.2. It is worth noting that the rigid elements needed for the connection to the mechanical stretcher are placed exactly at the top and bottom edges of the implanted square. This precaution is necessary to ensure that a given stress applied to the membrane in the *y* direction corresponds to an effect of the same amount in the implanted area.

Measurements were carried out using a time domain spectroscopy (TDS) technique, which is widely used for material characterization at THz frequencies [24, 25]. More specifically, a commercial fiber-coupled TDS setup (TERA K15 from Menlo Systems) was adopted to perform transmission measurements through the sample under test. This setup employs a femtosecond laser operating at 1560 nm and coupled to two photoconductive antennas based on InGaAs/InAlAs technology that implement the emission and detection of the THz signal. The generated beam is focused by a set of polymer lenses placed in the THz path. The

5.2. Stretchable conductors based on gold ion implantation

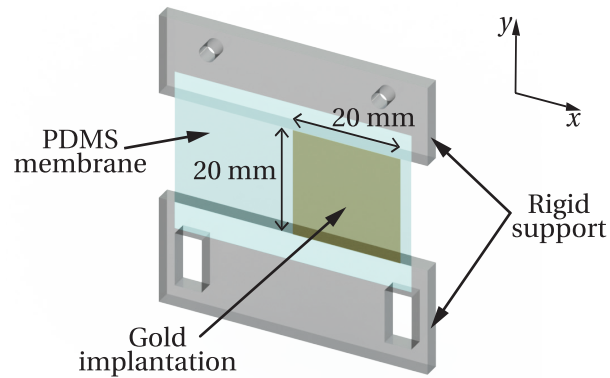


Figure 5.2 – Illustration of the test sample composed of a PDMS membrane partially implanted with gold ions. The membrane is adhered to rigid supports to allow the mounting on the measurement setup.

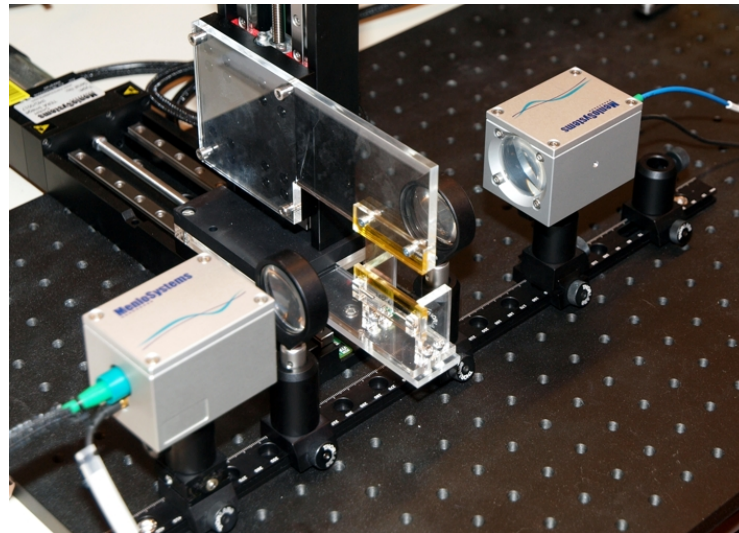


Figure 5.3 – Picture of the THz TDS measurement setup used for the conductivity characterization of gold ion implantation in a PDMS membrane for different stretching conditions.

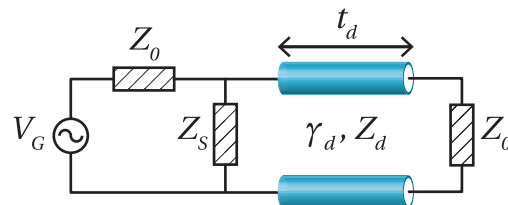


Figure 5.4 – Equivalent transmission line model representing the implanted PDMS membrane under normal plane wave illumination. The PDMS membrane is described by a transmission line section of length t_d , propagation constant γ_d and characteristic impedance Z_d . The implanted layer is modeled by the shunt impedance Z_S .

measurements presented here have been collected in focused mode that allows a beam waist diameter of less than 1 mm at the sample position. In this configuration, four lenses were used, namely two for the emitter and one for the detector units. The desired stretching of the PDMS membrane in the y direction was obtained using the motorized linear stage (generally used for imaging applications) available in our TDS setup. The bottom frame of the sample was bound to a fixed anchoring point and the top frame to the moving plate of the motorized stage. A detail of the measurement setup including the sample under test is shown in Fig. 5.3.

The employed setup configuration involves the propagation of a Gaussian beam focused at the sample position (i.e., beam waist location), where the propagating phase front can be considered planar. Thus, a plane wave illumination is assumed and the propagation through the sample under test is described by the transmission line model shown in Fig. 5.4. The PDMS membrane is represented by a transmission line section characterized by a complex propagation constant γ_d , a characteristic impedance Z_d and a length t_d corresponding to the PDMS thickness. In turn, the gold implantation is represented by the shunt impedance Z_S . The transmission line model of Fig. 5.4 allows to exactly describe the THz wave propagation through the sample under test, considering that the conductive layer is electrically very thin (i.e., $t/\lambda < 10^{-4}$). In frequency domain the transmission line model of Fig. 5.4 can be described using a transmission matrix approach [26] allowing to mathematically express the plane wave transmission through the sample as the concatenation of two matrices:

$$ABCD_{tot} = \begin{bmatrix} 1 & 0 \\ \frac{1}{Z_S} & 1 \end{bmatrix} \begin{bmatrix} \cosh(\gamma_d t_d) & Z_d \sinh(\gamma_d t_d) \\ \frac{1}{Z_d} \sinh(\gamma_d t_d) & \cosh(\gamma_d t_d) \end{bmatrix}. \quad (5.1)$$

The transmission coefficient T_{tot} is then calculated using the $ABCD$ parameters of eq. (5.1) by the following equation:

$$T_{tot} = \frac{2}{\left(2 + \frac{Z_0}{Z_S}\right) \cosh(\gamma_d t_d) + \left(\frac{Z_d}{Z_0} + \frac{Z_0}{Z_d} + \frac{Z_d}{Z_S}\right) \sinh(\gamma_d t_d)}, \quad (5.2)$$

where Z_0 is the vacuum characteristic impedance. Equation (5.2) allows to relate the measured transmission signal with the dielectric properties of the PDMS material and the conductivity characteristics of the implanted layer. The signal directly measured from the TDS setup, however, is a time-domain pulse that is attenuated and delayed with respect to the free-space transmission according to the properties of the measured material. The measured time pulse is then converted to frequency domain applying a Fourier transformation in order to apply the transmission line model discussed above. Equation (5.2) expresses the measured transmission coefficient as a transcendental function of the PDMS dielectric properties and the desired

5.2. Stretchable conductors based on gold ion implantation

Table 5.1 – Measurement procedure needed to extract the surface resistance of the implanted layer.

Step	Measurement	Measured quantity	Output
1	Free-space transmission	T_{fs}	system calibration
2	PDMS only	T_{pdms}	$\epsilon_{r,d}$
3	Implantation	T_{tot}	Z_S

surface impedance, and need to be solved using regression techniques. The PDMS complex permittivity $\epsilon_{r,d} = \epsilon'_{r,d} - j\epsilon''_{r,d}$ is typically unknown and is retrieved by means of a separate transmission measurement through the non-implanted region of the membrane under test (cf. Fig. 5.2) solving the following equation:

$$T_{pdms} = \frac{2}{2 + \cosh(\gamma_d t_d) + \left(\frac{Z_d}{Z_0} + \frac{Z_0}{Z_d}\right) \sinh(\gamma_d t_d)}. \quad (5.3)$$

The PDMS thickness is a known parameter since it is previously measured using a visible spectrometer that allows an accurate thickness characterization of free-standing PDMS membranes. A measurement of the free-space transmission coefficient T_{fs} is also needed to calibrate the setup removing the typical frequency-dependent response of TDS systems and the effects of the THz propagation in air. The conductivity characterization of a single sample consists of different steps that are summarized in Tab. 5.1, including the corresponding output parameter. Step 3 of Tab. 5.1 is repeated for different points over the implanted area to evaluate the uniformity of the conductive layer.

The results from three samples with different implantation doses are presented here. Two consecutive stretching cycles were performed for each sample. More specifically, the strain applied to the tested membrane was increased from 0 to 10 % with 0.5 % increment and then reduced to 0 again with 0.5 % decrement. The same cycle was repeated right after to have a basic information on the repeatability of the measurement. However, Rosset et al. [14] already demonstrated a good stability of the DC resistance after more than 10^5 cycles at a maximum strain of 10 %. The extracted values of surface resistance reported in Fig. 5.5a–5.5c correspond to an implantation rate of 80, 100 and 110 pulses/cm², respectively. The presented results confirm that higher implantation doses generate better conductivity (lower resistance), which reduces while the membrane is stretched. A good overlap is found between values extracted from different cycles, and a similar increment of the resistance with the applied strain can be observed for the different samples, independently from their ion concentration. Moreover all the analyzed samples exhibit an abrupt variation of the extracted resistance at the beginning of the strain range, which can be explained by the fact that the membrane was not perfectly

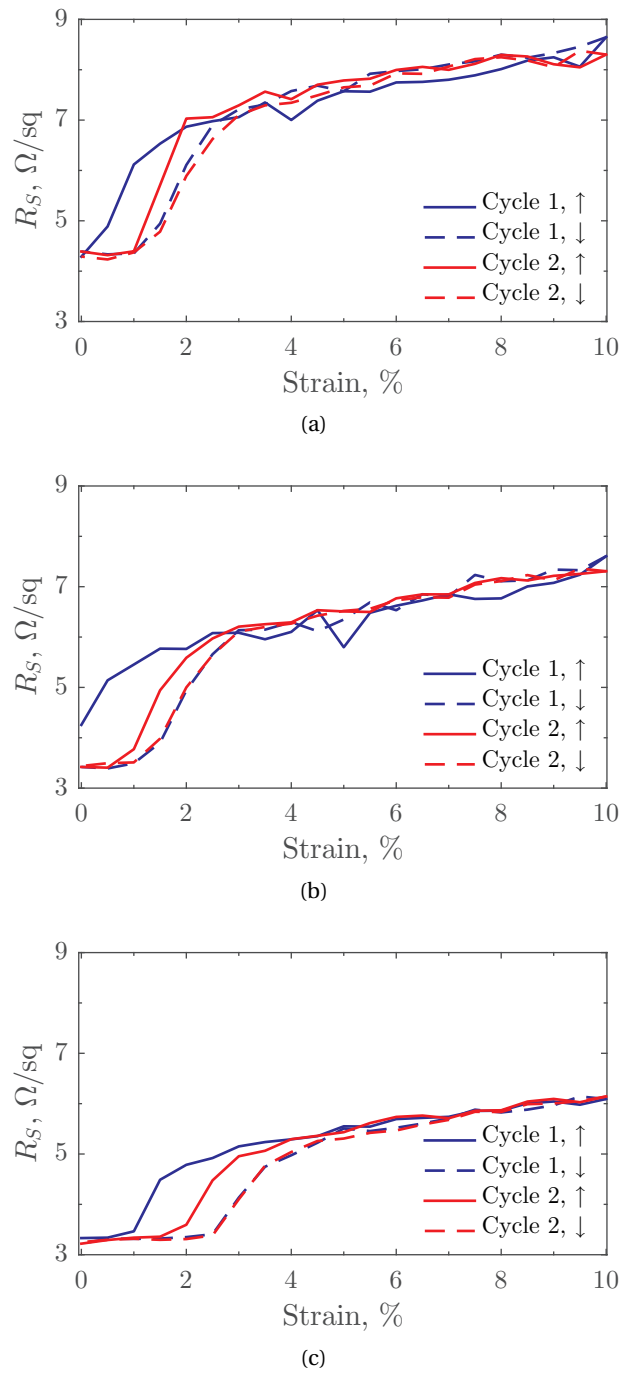


Figure 5.5 – Surface resistance extracted from TDS measurements of 3 samples implanted with different gold ion concentrations: (a) 80 pulses/cm², (b) 100 pulses/cm², (c) 110 pulses/cm². Two strain cycles (from 0 to 10%) and back to 0 are performed for each samples.

strained when the samples were mounted on the stretcher. The extracted values allow to target the realization of stretchable conductors for THz applications using the proposed gold ion implantation technique, although higher losses should be expected with respect to solid metals (e.g., gold) commonly used for the micro-fabrication of THz devices. Nevertheless, this approach offers the unique potential for the implementation of flexible and stretchable patterns that would find wide application in emerging THz systems as it has been previously discussed. Higher conductivity can be obtained increasing the implantation dose as it was demonstrated in [14] where concentration of up to 800 pulses/cm² were investigated. This improvement in conductivity would obviously come at the expense of a higher stiffening of the implanted membrane and bigger variation of the resistance with the strain [14]. A practical application of the considered gold ion implantation is proposed in §5.3 and §5.4 for the implementation of a stretchable reflectarray with beam-scanning capabilities.

5.3 A fixed-beam stretchable reflectarray

The objective of this section is to present the results achieved in the design and implementation of a stretchable reflectarray at terahertz frequencies based on PDMS and gold ion implantation. The proposed device demonstrates the practical integration of the results discussed in the previous section validating the potential of gold ion implantation to implement stretchable conductors for THz applications.

These activities were motivated by the important role played by antenna components in THz systems and the consequent growing interest in the improvement and development of antenna technology, which is particularly driven by the need to overcome the high path loss characterizing THz communication and sensing systems [27]. The free-space loss at 1 THz is for instance 60 dB higher with respect to the same system at 1 GHz. Therefore the use of high-efficiency and high-gain antennas becomes an important means to partially compensate for these losses or to mitigate the requirements of the other components constituting the transmitting/receiving chain. In this framework reflectarray antennas represent good candidates for the generation of high-gain and narrow-beam radiation, which is typically required in most of the high resolution imaging systems and communication applications. The main advantages of reflectarrays over conventional phased arrays and reflector antennas discussed in the previous chapter still remain and can be even more evident in the THz frequency band. The realization of focusing reflectors becomes very critical and expensive at THz due to the precision needed to account for the very small wavelength (300 μm at 1 THz). Moreover, the power loss generated by the beam forming network in phased array antennas is even more critical together with the technology limitations currently characterizing THz systems.

Although the reflectarray concept has been widely developed at microwaves and millimeter-waves, with the experimental demonstration of several prototypes (cf. §4.1), only a few devices have been proposed at THz frequencies. The first contribution related to reflectarrays at THz can be found in the work of Ginn et al. [28] who experimentally investigated the use of

square resonant patches at infrared frequencies (28.3 THz more specifically). Several uniform arrays with different patch size were fabricated using electron beam lithography on a zirconium dioxide substrate, and were then characterized using an infrared interferometer, proving the feasibility of the concept. The same authors then proposed a 1-bit reflectarray using the same principle [29]. A relevant example of reflectarray operating around 1 THz is represented by the device realized by Niu et al. [30] who proposed the experimental demonstration of a RA based on resonant square patches on a PDMS grounded substrate. The same research group also proposed a RA beam splitter with polarization-dependent characteristics [31] based on the same technology and fabrication process demonstrated in [30], and further validating the potential of reflectarrays for efficient radiation at THz frequencies. Other examples of RA devices can be found at higher THz frequencies (i.e., visible), such as the concept based on spherical plasmonic particles with a dielectric core [32], the design using a perforated silver plate [33], and the manufactured device based on dielectric resonator elements [34].

Considering this increasing interest in the reflectarray concept for terahertz applications and in sight of potential reconfiguration capabilities, we propose a novel approach for the implementation of THz reflectarray based on square resonant patches on a PDMS substrate backed by a stretchable ground plane realized by gold ion implantation (cf. §5.2). The selected unit cell and the operating principle of the proposed reflectarray are very similar to the device presented in [30], but a significant difference exists, namely the high potential for the implementation of reconfiguration capabilities offered by the stretchable structure implementing the concept described here. Moreover, a different fabrication approach is proposed for the realization of the reflectarray and is detailed in §5.3.1. In [30] the PDMS polymer was spin coated on a metalized wafer and then metallic patterns were defined with standard optical lithography. Here instead we spin coat the PDMS on a water-soluble polymer which allows the subsequent release of the PDMS membrane (having thickness in the order of 25 μm) after the fabrication of the metal pattern. The ground plane is then implemented using gold ion implantation on the opposite side of the membrane. In addition, we also propose an alternative method to implement the metal patches, namely electron-beam metal evaporation through a shadow mask. The implementation of beam-scanning capabilities based on the mechanical stretching of the whole reflectarray is then discussed in §5.4.

5.3.1 Reflectarray design and fabrication

The reflectarray design discussed here was developed using the well-known approach based on resonant square patches of variable size over a grounded dielectric substrate [35]. PDMS was selected to implement the dielectric layer for three main reasons: i) possibility to realize stretchable devices in combination with the gold ion implantation discussed in §5.2, targeting the integration of dielectric elastomer actuators to implement reconfiguration functionalities; ii) PDMS is a low-cost material implying simple and inexpensive fabrication processes; iii) PDMS exhibits relatively low losses ($\tan \delta \sim 0.04$) at THz frequencies [36] and is therefore a suitable material for the fabrication of efficient antenna devices. The unit cell selected for

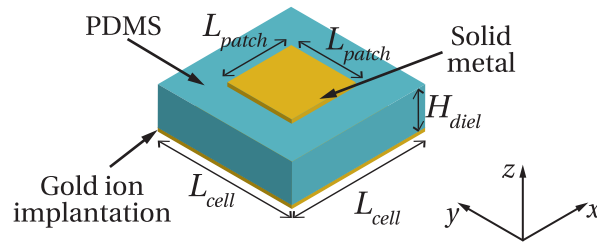


Figure 5.6 – Drawing of the unit cell composing the THz stretchable reflectarray. The square resonant patch is made up of solid metal and the stretchable ground plane realized using gold ion implantation.

the conceived reflectarray is illustrated in Fig. 5.6. The reflection phase distribution over the array is tailored by varying the size of the square patches, which need to be realized using solid metal to avoid that their size varies when the array (i.e., the PDMS) is stretched. Here a gold layer of 300 nm thickness is considered in the design phase.

The design and optimization of the reflectarray was carried out following the same full-wave simulation approach discussed in the previous chapter for the MMW device. The reflection properties of the unit cell of Fig. 5.6 were computed as a function of the patch size L_{patch} implementing a Floquet's periodic environment in Ansys HFSS. At the design frequency of 1 THz a square cell of $140\ \mu\text{m}$ side ($< 0.5\lambda_0$), and a thickness of $20\ \mu\text{m}$ for the PDMS layer were selected for this first prototype. The PDMS material chosen for this application is the Sylgard 184, which is the commercial standard available at the EPFL Center of Micronanotechnology (CMI), where the full fabrication process was developed. The dielectric properties of this particular elastomer were characterized using the TDS setup discussed in §5.2, although different studies on the same material were available in literature [22, 36, 37]. Average values of 2.37 and 0.035 were respectively extracted for the dielectric constant and the loss tangent. These results are in agreement with the values found in literature and also very similar to the dielectric properties of the Sylgard 186 discussed in chap. 2. Regarding the conductivity of the gold patches, the Drude model adopted in [30] was considered and a surface impedance of $0.287 + j0.335\ \Omega/\square$ was assigned in the electromagnetic solver. The geometric characteristics of the designed cell and the electromagnetic properties of the involved materials are summarized in Tab. 5.2. The corresponding reflection phase and magnitude are shown in Fig. 5.7, assuming linear polarization with the electric field directed along y . A phase range of around 300° is achieved with losses lower than 2 dB, which are mainly due to the PDMS substrate ($\tan \delta = 0.035$).

The results shown in Fig. 5.7 for the designed unit cell have been used to implement a full reflectarray allowing to deflect the incident wave towards an off-normal direction in the H -plane (xz plane). In order to simplify the fabrication process discussed below, the number of phase states was reduced to three for this first prototype. In particular, a differential phase of -120° was chosen between the three states, corresponding to a patch length of 62, 83 and $102\ \mu\text{m}$, as highlighted in Fig. 5.7 (red markers). To obtain a deflection of the beam in the

Chapter 5. Stretchable reflectarray antennas for THz applications

Table 5.2 – Geometric and electromagnetic properties of unit cell of Fig. 5.6 for the fixed-beam RA prototype.

Cell	$L_{cell} = 140\mu\text{m}$
Patches	$L_{patch} = 30 - 130\mu\text{m}$
	$H_{diel} = 20\mu\text{m}$
PDMS	$\epsilon_r = 2.37$
	$\tan\delta = 0.035$

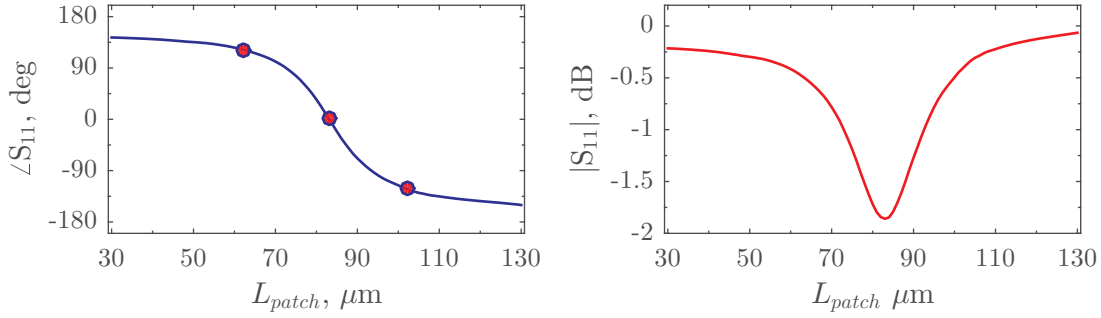


Figure 5.7 – Reflection phase (left) and magnitude (right) of the resonant unit cell designed for the fixed-beam RA prototype. The calculation was performed using full-wave simulations in a Floquet periodic environment at the design frequency $f_0 = 1$ THz and considering the properties of Tab. 5.2.

xz plane, these 3 cells were periodically arranged along the x direction, whereas a uniform repetition of the same elements was considered in the y direction. The proposed arrangement is symbolically illustrated in Fig. 5.8 for a sample array of 24×24 cells. Assuming a center-fed RA with normal plane wave excitation (i.e., realistic case in a THz TDS setup) with TE polarization, the assigned phase shift of -120° between adjacent cells results in a beam pointing angle $\theta_r = 45.6^\circ$ at 1 THz. The radiation pattern of the proposed design was evaluated using HFSS full-wave simulations. In order to reduce the simulation complexity only a limited number of cells was modeled in the simulator. More specifically a 1-D array consisting of 33 cells (i.e., 11 repetitions of the 3 cells shown in the inset of Fig. 5.8) in x direction was considered. On the other hand periodic boundary conditions were used on the two sides of the cells in the y direction to emulate the array behavior. The illumination of the array was implemented using a normally incident plane wave. The normalized far-field radiation pattern obtained from HFSS is reported in Fig. 5.9 (blue solid line).

The simulated structure clearly radiate a pencil beam with the maximum at $\theta_r = 45.6^\circ$, as expected from the assigned phase profile. Nevertheless, two undesired lobes with a relative level of -17 dB and -12 dB with respect to the maximum appear respectively at 0° (specular direction) and -45.6° ($\theta = -\theta_r$). This phenomenon was evaluated and modeled in [38] for a similar geometry. These parasitic lobes are generated by a periodic error in the assigned phase profile with respect to the ideal one. This phase distortion is typical of reflectarrays based

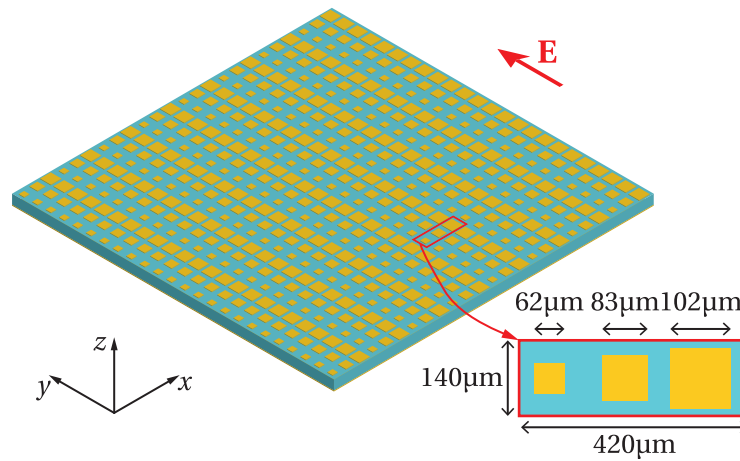


Figure 5.8 – Symbolic illustration of the designed fixed-beam RA. A beam radiated at $\theta_r = 45.6^\circ$ in the xz plane is obtained via the periodic repetition of 3 cells (62, 83 and 102 μm) generating a -120° phase slope in the x direction. All the rows in y direction are identical. The array is illuminated by a normal plane wave polarized along y (i.e TE wave excitation).

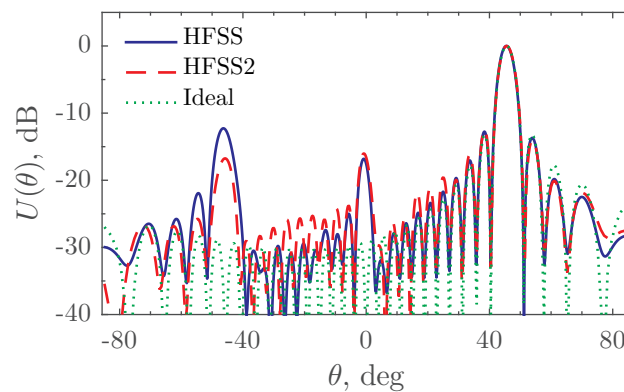


Figure 5.9 – Simulated radiation pattern in the H-plane for the designed fixed-beam RA. Blue solid curve is the far-field pattern obtained from HFSS. Red dashed curve is calculated from the near-field reflection phase profile extracted from HFSS. Green dotted curve is the ideal pattern expected from the assigned phase profile.

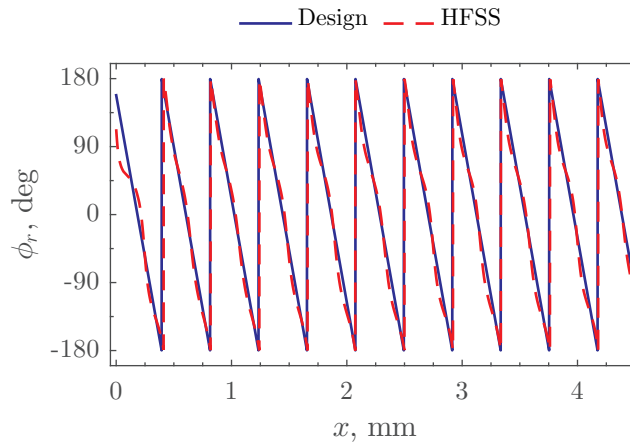


Figure 5.10 – Reflection phase profile selected for the fixed-beam RA. Blue solid curve represents the ideal phase profile needed to realize a pencil beam pointing at 45.6° . Dashed red line is the phase of the reflected near field extracted from HFSS.

on variable size resonators where a linear phase profile is assigned, resulting in a progressive change of the elements size and the related presence of abrupt variations due to the 2π phase wrapping. A phase error arises because the reflection properties of the unit cell are computed using a Floquet periodic environment, which considers an infinite array of identical elements with consequent identical mutual coupling between adjacent cells. This condition, however, is not exactly verified when the reflectarray is considered since a different coupling exists between the cells, which will behave differently with respect to the Floquet calculation. The produced phase error is obviously periodic due to the 2π periodicity of the desired phase profile and the corresponding repetition of the elements, hence contributing to the radiation towards undesired directions. To validate this assumption for the specific design presented here, we used an approach similar to the analysis proposed in [38]. The reflection phase of the scattered near-field was extracted from HFSS and compared with the desired phase profile having a slope of -120° between adjacent cells. The results of Fig. 5.10 clearly show that a periodic perturbation of the phase is generated in HFSS by the cell repetition illustrated in Fig. 5.8. To further confirm this effect, we also computed the far-field radiation pattern from the phase of the scattered near-field shown in Fig. 5.10 (red dashed line in Fig. 5.9). A very good agreement is observed with the radiation pattern directly calculated in HFSS (blue solid line), confirming that the undesired lobes are generated by the perturbed phase profile. For the sake of completeness the ideal radiation pattern is also included in Fig. 5.9 (green dotted line), confirming that a periodic perturbation of the phase generates a negligible effect on the main lobe. The presence of these parasitic lobes was not considered a critical aspects for the demonstration of the stretchable RA as they are far from the main beam and their level is comparable to sidelobes.

The reflectarray design presented above has been fabricated to test the use of gold ion implantation for the realization of the stretchable ground plane. The small features constituting the device required the use of precise micro-fabrication techniques in a clean room environment.

In particular, the facilities available at the EPFL Center of Micronanotechnology were used to develop a fabrication process based on electron-beam metal evaporation through a silicon (Si) shadow mask. This approach was preferred to other techniques based for instance on standard lithography (e.g., [30]) to avoid that the PDMS came into contact with solvents. The particular PDMS polymeric structure, in fact, allows the absorption of many chemicals that are commonly used during lithographic processes and can generate significant swelling of the material (e.g., [39]). In addition, the permanent inclusion of chemicals into the PDMS matrix would also alter its dielectric properties. These aspects are particularly important in light of the potential device reconfiguration involving the integration of dielectric elastomer actuators (cf. §5.4). In this specific case a degradation of the PDMS dielectric constant would affect the designed antenna performance, whereas a variation of the mechanical properties would drastically degrade DEA performance. The proposed method exhibits also the advantage that a photolithographic process is only needed for the realization of the mask, which can be ideally reused for an unlimited number of times. A new process is only needed if a different pattern is desired.

The developed fabrication process is organized in three main steps that are detailed in the following:

1. realization of the Si shadow mask using optical lithography and dry etching techniques;
2. evaporation of the metal patches on the PDMS surface and release of the membrane from the sacrificial wafer;
3. implantation of the ground plane on the opposite side of the PDMS membrane as described in §5.2.

The procedure adopted for the fabrication of the Si shadow mask is based on standard photolithography and dry etching techniques, and is illustrated in Fig. 5.11a. The process starts with a 4-inches Si test wafer which is first treated with hexamethyldisilazane (HMDS) to promote the adhesion of the resist and then coated with the positive resist AZ9200 (step a.1). A thickness of 4 μm is obtained using a standard recipe. The cured photoresist is exposed and developed to obtain the desired aperture pattern (step a.2). The apertures in the shadow mask are then realized using a Bosch process able to produce a 240 μm etching of the Si with sharp vertical edges (step 1.3). This dry etching also removes almost the totality of the resist and therefore allows to avoid an additional removing step. The shadow mask with a final thickness of 150 μm is subsequently obtained using a grinding process that allows to remove the remaining silicon on the bottom part of the wafer (step a.4).

The shadow mask fabricated using the technique discussed above is then used to realize the metallic pattern on the PDMS surface, following the process depicted in Fig. 5.11b. The first action consists in the spin coating and curing of a thin layer (<1 μm) of Poly(acrylic acid) (PAA) on a Si test wafer (step b.1). PAA is spin-coated at a speed of 2500 rpm and baked at 90 °C

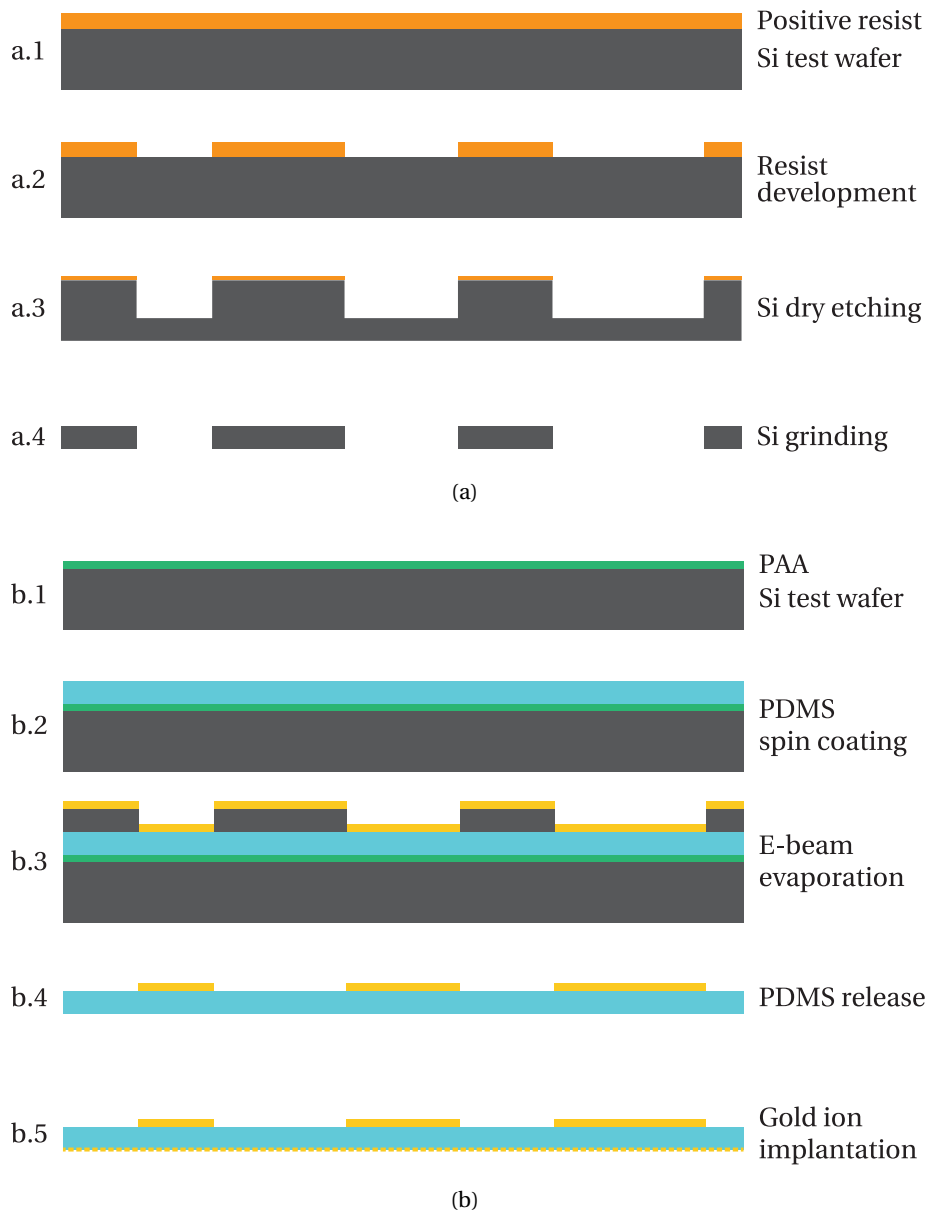


Figure 5.11 – Fabrication process developed for the realization of the stretchable RA. (a) Realization of the shadow mask from a Si test wafer using standard lithography and dry etching techniques. (b) Main steps to obtain a standalone stretchable reflectarray based on e-beam evaporation of the patches and implantation of the ground plane using gold ions.

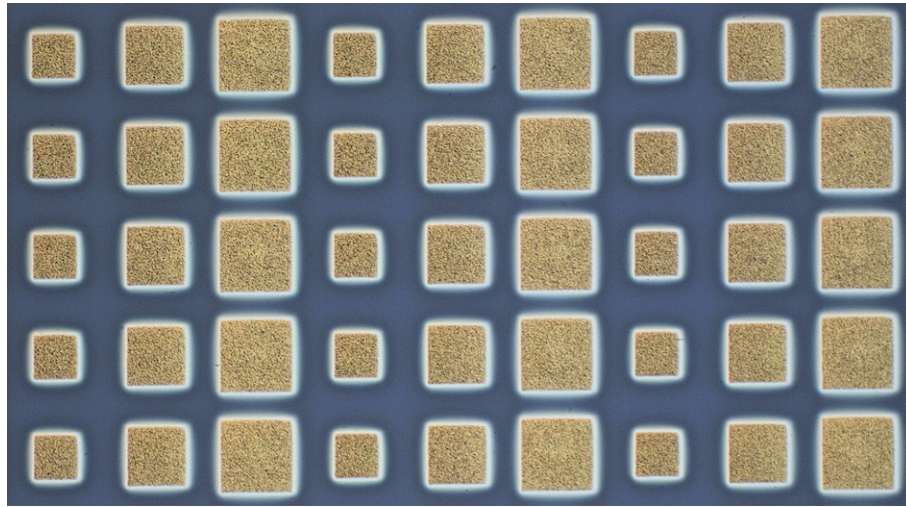


Figure 5.12 – Detail of fabricated fixed-beam reflectarray operating at 1 THz. A beam deflected towards 45.6° in the H -plane is obtained via the periodic repetition of 3 cells, as represented in Fig. 5.8.

for 5 min to achieve a thickness of around $0.8\ \mu\text{m}$. PAA is used as a water-soluble sacrificial layer allowing the final release of the PDMS membrane before the implantation of the ground plane. The PDMS substrate (Sylgard 184) is realized by spin coating of the unpolymerized mixture (step b.2) prepared using the standard procedure suggested by the supplier (i.e., PDMS monomer with the curing agent in a 10:1 mass ratio). A spin-coating speed of 4000 rpm is used to realize a thickness of around $20\ \mu\text{m}$, and the curing of the PDMS is accelerated by a baking phase at 80°C for 120 minutes. The shadow mask is then placed in contact with the PDMS layer and electron beam evaporation is performed to realize the metallic patches (step b.3). A chromium adhesion layer is first evaporated on the PDMS, followed by a 300 nm layer of gold. After the evaporation, the mask is removed and a plastic frame is adhered to the PDMS to allow the release of the PDMS membrane (keeping the array geometry) by dissolving the PAA sacrificial layer in water (step b.4). The final step of the proposed fabrication process relies on the realization of the stretchable ground plane on the opposite side of the PDMS membrane using the gold ion implantation discussed in §5.2 (step b.5).

The process discussed above and illustrated in Fig. 5.11 was validated with the manufacturing of the reflectarray design shown in Fig. 5.8. A prototype comprising 71×71 cells was realized, fitting in an active area of around $10 \times 10\ \text{mm}^2$. Metal patches of this first prototype were realized by evaporating on the PDMS surface a 10 nm thick adhesion layer of chromium, followed by 200 nm of silver and a 40 nm protective layer of gold. This metal stack was selected to reduce fabrication costs allowing to validate the concept at the same time. The ground plane was realized at LMTS using an implantation rate of 100 pulses/ cm^2 obtaining a surface resistance of around $4\ \Omega/\square$ according to the experimental results presented in §5.2. A detail of the fabricated device is shown in the optical microscope picture reported in Fig. 5.12. The experimental characterization of this first prototype is discussed in the next section.

5.3.2 Experimental characterization

The fabricated reflectarray prototype shown in Fig. 5.12 has been measured using the same time-domain spectroscopy setup adopted for the characterization of the ion implantation, with the addition of a motorized rotation stage to implement pattern measurements. A schematic of the measurement setup is depicted in Fig. 5.13. The system was utilized in collimated mode to allow the illumination of the full array. The THz source antenna and the respective collimating lens were placed on a fixed support pointing at the device under normal incidence, that is $\theta = 0^\circ$ in the RA reference system. The THz detector and the associated lens were mounted on a different rail fixed on the rotary stage and allowing a wide range of angular movement for radiation pattern measurement. The measurements presented here were obtained scanning the detector from 25° to 90° , with the minimum angle selected to ensure a safe distance between the transmitting and receiving lenses. Moreover, an angle resolution of 0.25° was considered.

The presented measurement results were obtained normalizing the reflection spectrum measured at each scanning angle by the spectrum of the free-space reference thru (i.e., transmission measurement). This operation allows to eliminate the frequency-dependent response of the TDS setup. Experimental data are reported in Fig. 5.14. Figure 5.14a shows the normalized amplitude of the deflected wave as a function of the frequency and the scanning angle θ (cf. Fig. 5.13). Presented values are expressed in logarithmic scale referred to the free-space transmission measurement. These results clearly show the deflection capabilities of the proposed device with the maximum of radiation that moves towards higher angles when the frequency decreases. Obviously the radiated beam becomes wider and weaker (i.e., lower antenna efficiency) moving away from the design point. The reflection magnitude at the design frequency of 1 THz as a function of the angle is shown in Fig. 5.14b. The maximum of deflection is reached at 47° , very close to the 45.6° expected from the design. This difference is certainly due to fabrication and operation tolerances in the tested prototype. Three main aspects need to be considered: i) tolerances in the patch size, ii) variation in the PDMS thickness, and iii) planarity of the PDMS membrane. In particular, we evaluated that a maximum error of around $1.5\ \mu\text{m}$ was obtained for the fabricated patches, confirming the effectiveness of the proposed fabrication technique. On the other side, the fabricated PDMS substrate had a thickness of around $24\ \mu\text{m}$ (measured using a visible spectrometer), despite the targeted $20\ \mu\text{m}$. This difference was generated by an inaccurate optimization of the spin-coating procedure for this first prototype. However, a very good uniformity of the thickness was observed over the full membrane. The third aspect relates to the planarity of the array originated by a possible relaxation of the standalone PDMS membrane after release from the sacrificial wafer and implantation of the ground plane. Moreover, it was difficult to ensure perfect alignment of the the normal to the reflectarray surface with the pointing direction from the THz source.

The experimental results presented above validate the deflection capabilities of the proposed reflectarray device embedding a flexible and stretchable ground plane based on gold ion implantation. Full-wave simulations demonstrated that the same device with a solid gold

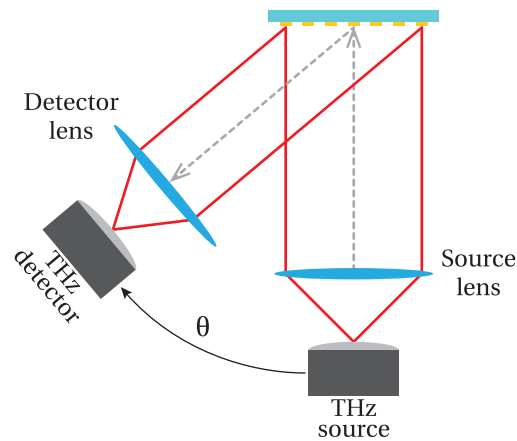


Figure 5.13 – Schematic illustration of the THz TDS setup used for the characterization of the fixed-beam RA of Fig. 5.12. The RA is fed by the source antenna along the normal direction and the detector is moved by a motorized rotary stage.

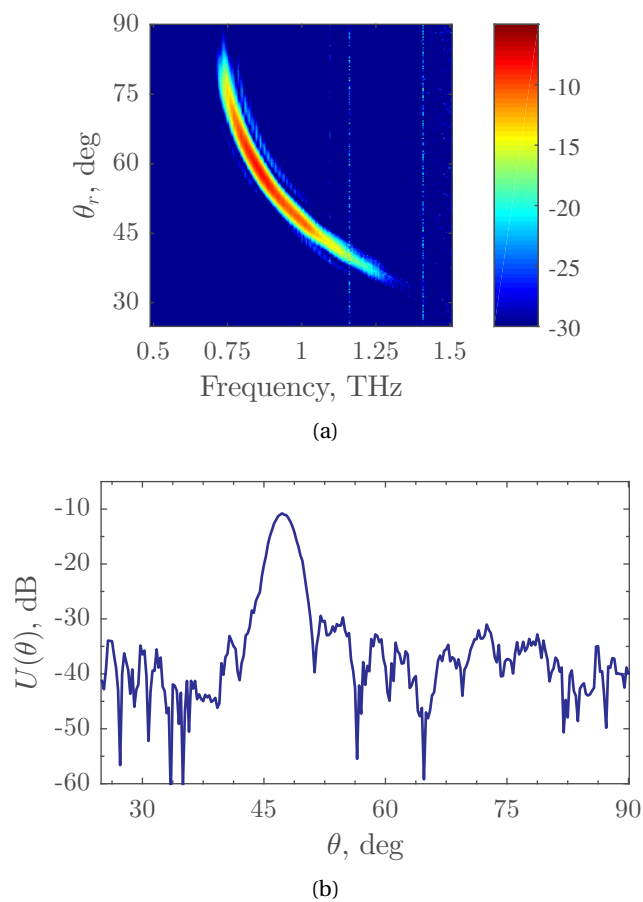


Figure 5.14 – Experimental characterization of the fabricated THz RA. (a) Normalized radiation pattern as a function of the frequency and the scanning angle. (b) Normalized radiation at the design frequency of 1 THz.

ground plane replacing the ion implantation, would only produce a 0.4 dB improvement in the peak directivity. The particular mechanical properties offered by the integration of gold ion implantation, combined with the related electromagnetic response, pave the way for the implementation of adaptive functionalities based on stretching or the easier realization of conformal devices. A beam-scanning concept based on the stretchability of the device is experimentally demonstrated in the next section.

5.4 A beam-scanning stretchable reflectarray

This section presents the experimental demonstration of a 1-D beam-scanning reflectarray operating at THz frequencies. The proposed reconfiguration concept is based on the mechanical stretching of the reflectarray device, which is made possible by the integration of a ground plane realized by gold ion implantation.

As we have discussed above, the development of reconfiguration capabilities in antenna systems is considered of strategic importance to comply with the performance requirements of emerging terahertz applications, such as communication systems. Indoor femto-cellular communication systems and WLAN/WPAN networks, for instance, would strongly need automatic beam-scanning terminals able to adapt to propagation conditions that are dynamically changing due to the indoor nomadic users or multiple reflections between transmitter and receiver [8]. Therefore, the implementation of beam-scanning concepts would represent an important milestone for the development of THz applications, and reflectarrays are again appealing candidates for this scope. To our best knowledge, no beam-scanning reflectarrays have been experimentally proved at THz so far, although different technologies for reconfiguration have been demonstrated for the realization of tunable metamaterials (or periodic surfaces, more generally), as it is discussed in several review papers [11–13]. During the last few years graphene has been proposed as a tuning material for the realization of reconfigurable antenna devices. A design of a fixed-beam reflectarray operating at 1.3 THz and based on graphene resonant patches over a grounded dielectric has been proposed in [40] and the implementation of a graphene-based reconfigurable cell for beam-scanning applications has been investigated by the same authors in [41]. Moreover, a beam-scanning leaky-wave antenna concept has been proposed in [42], where graphene was used to realize an adaptive sinusoidally modulated reactance surface able to affect the leaky mode propagation and the corresponding beam pointing. Reconfiguration capabilities are realized in [40] and [41] exploiting the particular 2-D graphene structure that allows to tune its surface conductivity when a DC bias voltage is applied. Nevertheless, the proposed graphene-based reconfigurable antenna devices are still far from a practical implementation and consequent experimental demonstration, mainly due to technology and fabrication limitations.

Here we propose a THz reconfigurable reflectarray concept based on resonant patches on grounded dielectric and implementing beam-scanning capabilities in one plane via the mechanical stretching of the array realized on PDMS and backed by an implanted ground plane.

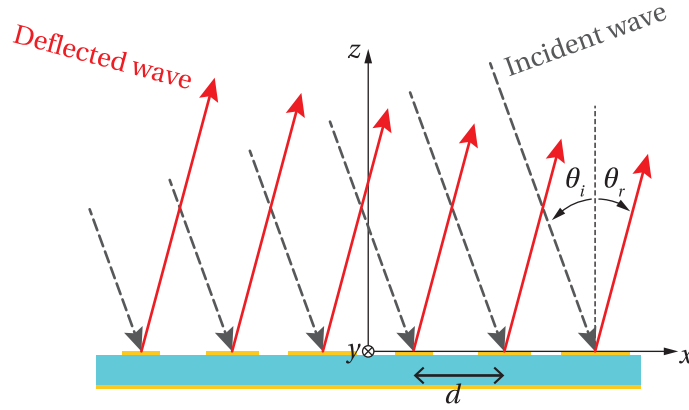


Figure 5.15 – Schematic illustration of the operation principle of a 1-D RA. The reflector surface is illuminated by a plane wave with incident angle θ_i and TE polarization. The phase profile in the x direction is selected to deflect the beam towards the direction θ_r .

In order to easily explain the proposed reconfiguration approach, let us consider the schematic illustration of Fig. 5.15, showing the operating principle of a 1-D reflectarray (i.e., allowing the deflection of the beam on the plane xz) under plane wave illumination. We assume that the reflectarray is fed by a plane wave incident with an angle θ_i with respect to the normal z , and the reflection phase profile is tailored to deflect the beam in the θ_r direction. θ_i and θ_r are signed angles and are considered negative and positive, respectively. According to this scenario, the differential reflection phase between adjacent array elements needed to deflect the beam towards θ_r can be easily calculated and is expressed by the following relation:

$$\Delta\phi_r = -k_0 d (\sin\theta_i + \sin\theta_r), \quad (5.4)$$

where k_0 is the free-space wave number and d is the array period (i.e., distance between adjacent cells). Inverting eq. (5.4) and expressing the reflection angle as a function of the other design parameters θ_i , d and $\Delta\phi_r$, we can write

$$\theta_r = -\arcsin\left(\frac{\Delta\phi_r}{k_0 d} + \sin\theta_i\right). \quad (5.5)$$

In typical reconfigurable reflectarray designs (such as the MMW device discussed in chap. 4), beam-scanning is realized by tuning $\Delta\phi_r$ to achieve a variation of θ_r as clearly visible from eq. (5.5). In this chapter we propose an alternative approach relying on the variation of the array period d , assuming that all the other design parameters (i.e., operation frequency, $\Delta\phi_r$ and θ_i) are kept constant. It is worth noting that the reflection properties of the RA unit cell are dependent on the cell size (i.e., d) and the corresponding mutual coupling between adjacent

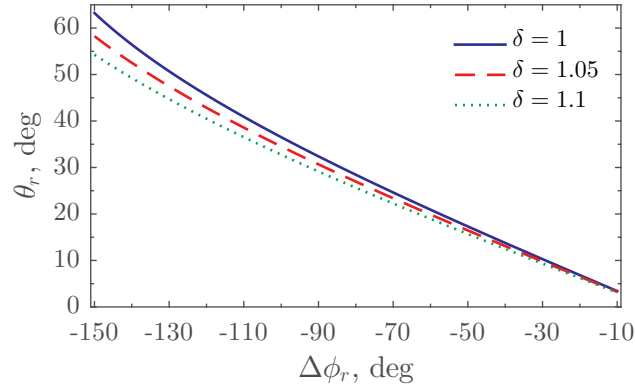


Figure 5.16 – Deflection angle θ_r as a function of the differential reflection phase $\Delta\phi_r$ and the cell stretching ratio δ for a 1-D RA. The illumination of the array is realized by a plane wave normally impinging on the surface ($\theta_i = 0^\circ$), the operation frequency is 1 THz and the initial period $d = 140\mu\text{m}$.

elements. However, we want to keep constant the reflection phase when d is modified, in order to maximize the proposed reconfiguration. Therefore, the previous assumption is valid for small variations of d (e.g., $\leq 10\%$), hence allowing for maximum scanning angles in the order of 10° . However, this is an efficient technique to realize beam-scanning, since this can be obtained with a single control (i.e., uni-axial stretching) that does not interact with the electromagnetic active area nor introduce additional losses. These features are particularly important at terahertz frequencies and are difficult to realize for currently available technologies based for instance on tunable materials, such as liquid crystals [43], photo-excited semiconductors [44], vanadium dioxide [45] and graphene [41].

Figure 5.16 is a graphical representation of eq. (5.5) for a RA operating at 1 THz and an array period $d = 140\mu\text{m}$. This example shows the variation of the deflection angle θ_r as a function of the differential phase between adjacent cells and the stretch ratio δ . Note that δ is defined as the ratio between the stretched and the initial cell size (i.e., $\delta > 1$ when the device is stretched). According to the proposed reconfiguration approach, the reflectarray presented in the previous section ($\Delta\phi_r = -120^\circ$) allows a 5° deflection of the beam with respect to the initial pointing angle (45.6°) for a 10% stretching (and corresponding increase in the array period) along the x direction (cf. Fig. 5.8). The scanning angle achievable with this approach is limited to a maximum of around 10° if the feed angle θ_i and the phase distribution are properly selected. However, this scanning capabilities are still attractive for particular line-of-sight communication systems requiring beam-scanning to electronically correct small perturbations in the alignment of the transmitting and receiving units [10]. Moreover, this scanning functionality would come without significant degradation of the antenna radiation properties.

The conceived method for the implementation of 1-D beam-scanning at THz frequencies has been first validated using full-wave simulations. The reflectarray design discussed in

5.4. A beam-scanning stretchable reflectarray

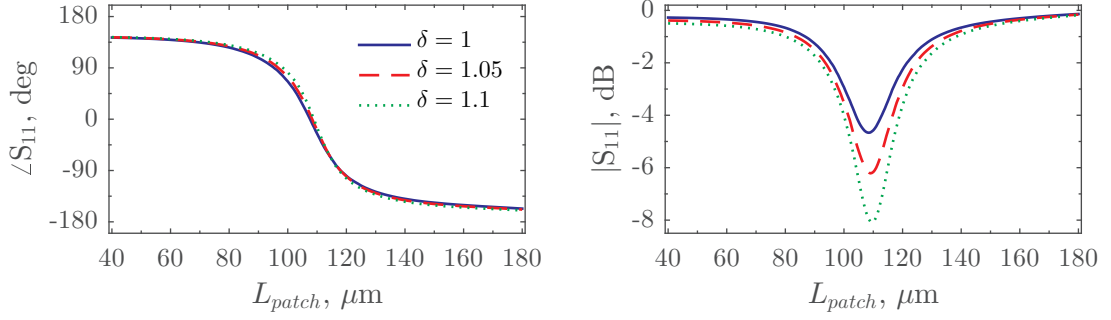


Figure 5.17 – Reflection phase (left) and magnitude (right) of the resonant unit cell designed for the stretchable beam-scanning RA. The calculation was performed using full-wave simulations in a Floquet’s periodic environment at the design frequency $f_0 = 0.75$ THz as a function of the patch size and the stretch ratio.

the previous section was properly optimized to operate at 0.75 THz. To accomplish this goal, a PDMS thickness of $25 \mu\text{m}$ and an array period of $190 \mu\text{m}$ in both x and y directions were selected for the unit cell of Fig. 5.6. With this geometry, a phase range of around 300° was achieved varying the patch size between 40 and $180 \mu\text{m}$.

The performance of the new design were then evaluated when a uni-axial stretching is applied along the x direction, with the main goal to modify only the array period without affecting the reflection phase (i.e., the patch size remains unchanged). In particular, this approach is based on the assumption that the size of the metallic patch is not affected by the stretching, which is a good approximation of the real case if the evaporated metal is “thick enough” (i.e., $>200 \text{ nm}$) [23]. The solid metal patches, in fact, behave as rigid islands on the soft elastomer and the uni-axial stress only acts on the unpatterned PDMS membrane, owing to the considerable difference in the Young’s modulus between the two regions (i.e., patterned and unpatterned PDMS).

The stretching of the PDMS membrane obviously generates also a variation in its thickness and a contraction of the cell in the direction orthogonal to the applied stretching (i.e., y). These additional variations were taken into account through an ideal model for dielectric elastomers [46]. In the case of the considered uni-axial stretching, a stretch ratio δ along the x direction generates a variation of $1/\sqrt{\delta}$ in y direction and in thickness (i.e., the polymer is incompressible and the volume is conserved). The stretching of the reflectarray also produces a variation of the ground plane conductivity, which is modeled in the electromagnetic solver according to the experimental results presented in §5.2.

The reflection properties of the designed unit cell consisting of a resonant patch on a stretchable PDMS substrate are shown in Fig. 5.17. The cell has initial size of $190 \times 190 \mu\text{m}$, and a thickness of $25 \mu\text{m}$ is chosen for the PDMS substrate. The reflection curves corresponding to two different uni-axial stretch ratio (i.e., 1.05 and 1.1) are shown in Fig. 5.17, in addition to the nominal condition (i.e., no stretching). As expected, the reflection phase is marginally affected

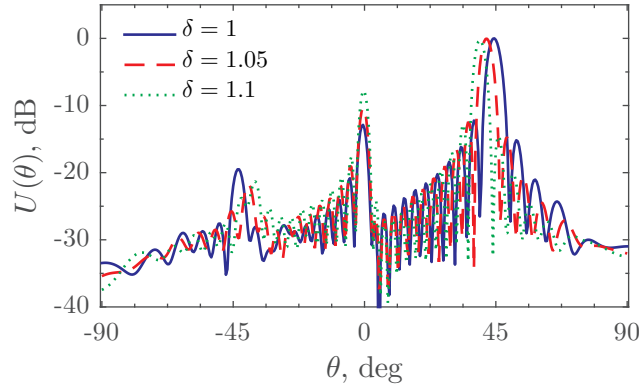


Figure 5.18 – Calculated radiation pattern in the H -plane for the designed stretchable RA for different stretch ratio δ . A beam deflection of around 5° with respect to the nominal design is achieved increasing the array period of 10 %.

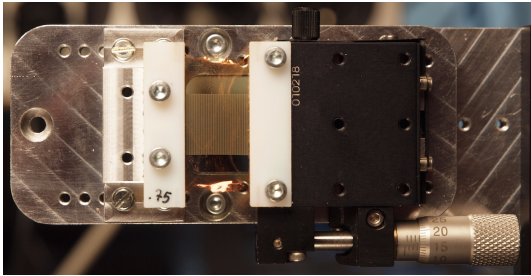
by a stretching of the array in the x direction. A maximum phase error of 19.5° is observed between the two extreme curves ($\delta = 1$ and $\delta = 1.1$) in correspondence of the resonance, but it rapidly decreases to values lower than 4° at the extremes of the L_{patch} range. The average phase error is 5.3° , which is not considered a critical value for the addressed reconfiguration, especially considering the conceived phase quantization (i.e., only 3 states). A larger variation of the reflection magnitude arises and it is particularly evident around the resonance peak. These increased losses are only due to the reduced conductivity of the ground plane, but are not expected to significantly affect the radiation performance, since the losses of the full reflectarray are evaluated considering a weighted average of the unit element losses at different states. A limited variation of the reflection magnitude (around 0.2 dB) is in fact observable towards the extremes of the L_{patch} range.

The unit cell design and the corresponding calculated results of Fig. 5.17 have been used to design a full reflectarray following the same approach discussed in the previous section. Also in this case the deflection of the beam towards an off-normal direction in the H -plane is obtained by periodically repeating a group of three cells in the x direction. The size of the three patches was selected to implement a differential phase of -120° between consecutive cells ($\theta_r = 44.5^\circ$ for normal plane wave excitation at 0.75 THz). These condition resulted in the following patch lengths for the nominal array condition ($\delta = 1$): 86, 108 and $128\ \mu\text{m}$. To assess the effect of the array stretching, the radiation pattern of the full reflectarray was computed using HFSS full-wave simulations. In analogy with the results presented in §5.3, a 1-D array composed of 33 cells in the x direction was considered, and periodic boundary conditions were applied on the two faces orthogonal to the y direction. Simulated radiation patterns for three values of δ , namely 1, 1.05 and 1.1, are shown in Fig. 5.18. The presented results are normalized with respect to the maximum of the beam calculated for $\delta = 1$. A relative beam deflection of around 5° with respect to the nominal design is obtained when a 10% stretching is applied to the array along the x direction, as predicted by eq. (5.5). Moreover, this beam-scanning is realized without any influence on the radiation performance of the

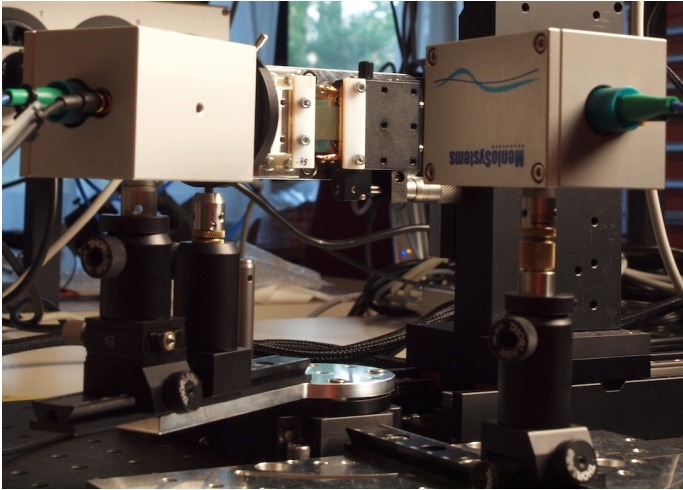
main beam, while it generates an increase in the specular reflection at $\theta_r = 0^\circ$ passing from -13 dB to -8 dB. This effect have been discussed in the previous section and is generated by the difference between the real phase profile and the assigned ideal phase calculated using Floquet's periodicity. In this particular case this error increases when the array stretching is applied, since the cell size and the mutual coupling between consecutive cells is modified.

The reconfiguration approach discussed above was demonstrated through the experimental characterization of a fabricated prototype operating at 0.75 THz. An array of 78×78 cells (around 15×15 mm²) was manufactured using the fabrication process described in §5.3.1 and illustrated in Fig. 5.11. Gold patches were realized using shadow-mask evaporation and the ground plane was implanted after releasing the PDMS membrane from the sacrificial wafer. The mechanical stretching of the fabricated prototype was implemented by a custom-made stretcher based on a linear micrometer stage (Fig. 5.19a), which allowed precise reconfiguration of the array period. The radiation pattern of the fabricated prototype (fixed on the manual stretcher) was measured using the TDS setup discussed in §5.3.2, where the source antenna illuminated the RA under normal incidence, and the detector antenna was placed on a motorized rotary stage (Fig. 5.19b). The radiation pattern was measured in collimated mode between 25° and 70° with an angle resolution of 0.25° . In analogy with the experimental results presented in §5.3.2 for the fixed-beam reflectarray, the radiation pattern was obtained normalizing the reflection spectrum measured at each scanning angle by the free-space transmission measurement (i.e., reference thru). The same pattern measurement was repeated for different stretching conditions of the array. Figure 5.20 shows the measured radiation pattern (normalized by the reference measurement) corresponding to three reconfiguration states, namely $\delta = 1$, $\delta = 1.05$ and $\delta = 1.1$. Measurement results are in very good agreement with simulations of Fig. 5.18 (note that a different scale is used for θ). As predicted from eq. (5.5) and from full-wave simulations, a 5° scanning of the main beam (i.e. from 44.5° to 39.5°) is achieved for a 10 % stretching of the array in the x direction. These results completely validate the addressed reconfiguration concept, representing *the first experimental demonstration of beam-scanning functionality at THz frequencies*.

The proposed reconfiguration approach is independent from the technique used for the mechanical stretching of the PDMS membrane. A possible implementation for automatic stretching is represented by the use of dielectric elastomer actuators, which would allow high integration of the actuation part within the reflectarray resulting in a very compact device. We have discussed throughout this manuscript the many advantages offered by DEA technology to generate in-plane displacement. In this particular case, the in-plane expansion offered by DEAs could be used to reduced the strain of a pre-tensioned PDMS membrane. With such an approach, the assembly configuration (i.e., no applied voltage) corresponds to a stretched states (i.e., $\delta > 1$), whereas the nominal condition $\delta = 1$ is reached for an actuation voltage different from zero. The integration of DEAs into the device discussed above would obviously require additional steps in the fabrication process described in §5.3.1 and illustrated in Fig. 5.11b. Starting from the release of the PDMS membrane from the sacrificial wafer (step b.4 of Fig. 5.11b), the actuator part can be added adopting the following procedure:



(a)



(b)

Figure 5.19 – Measurement setup of the THz beam-scanning RA. (a) Fabricated prototype fixed to the custom-made stretcher. The mechanical stretching in the x direction is implemented by the micrometer linear stage. (b) TDS setup used for radiation pattern measurements of the fabricated prototype.

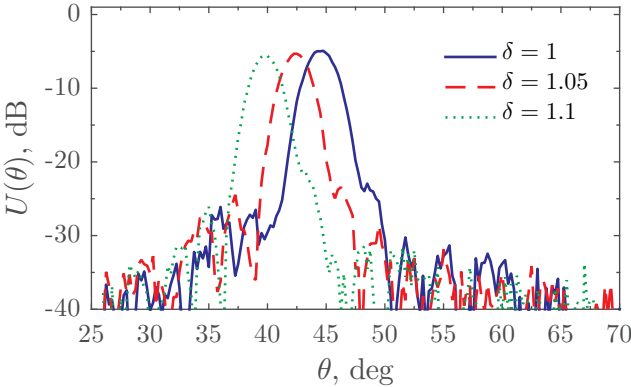


Figure 5.20 – Experimental characterization of the fabricated beam-scanning RA operating at 0.75 THz. Normalized radiation patterns corresponding to different stretch ratios are shown. The main beam is deflected towards lower angles when δ increases.

1. The PDMS membrane is adhered to a temporary rigid frame before the release from the sacrificial wafer to keep the original fabricated geometry.
2. The released PDMS membrane is placed on a uni-axial stretcher to apply the initial pre-stress that increases the separation between the cells (i.e., $\delta > 1$).
3. A new rigid frame is adhered to the membrane to keep the applied pre-stretch.
4. The ground plane is realized through ion implantation on the PDMS face opposite to the array of gold patches.
5. Compliant electrodes are realized on one side of the device close to the array and along the x direction using gold ion implantation [15, 16]. A portion of the ground plane can be used as a bottom electrode.

The practical realization of a fully-functioning device would require the optimization of the additional fabrication steps synthesized above and of the calibration of the actuation procedure (i.e., relation between applied voltage and the achieved stretching state). Nevertheless, a successful demonstration of this reconfiguration principle would surely represent an attractive means to implement reconfiguration capabilities in antenna devices. The same approach could be also applied to the implementation of tunable periodic surfaces, such as metamaterials, frequency selective surfaces, polarizers or spatial beam modulators in general, where the performance reconfiguration is obtained through the variation of the array lattice or the mutual coupling between element parts (e.g., [23, 47–50]).

5.5 Conclusions

In this chapter we have proposed an efficient approach for the practical implementation of flexible and stretchable conductors with high potential for the realization of adaptive antenna devices operating at terahertz frequencies. The technique discussed in the previous sections is based on the implantation of gold ions into a PDMS substrate. This technique was originally developed by LMTS for the realization of compliant electrodes needed in dielectric elastomer actuators. It is based on the use of low-energy and high-flux filtered cathodic vacuum arc allowing the implantation of a quasi-continuous layer of gold nano-clusters confined in the top 50 nm from the PDMS surface. These clusters are not bound, but free to move relatively to each other, making this layer capable to sustain high strain while keeping good electrical conductivity. We have first fabricated several test samples with different ion concentration and assessed the conductivity variation as a function of the applied strain. All the presented samples exhibited a surface resistance in the range $3\text{--}8 \Omega/\square$ and a relative variation of around 1.8 for a maximum applied strain of 10 % with respect to the initial value (i.e., no applied strain). The extracted values clearly imply higher ohmic losses with respect to solid metals in the same frequency range, but offering several advantages related to the stretchable nature of the conductor. The applicability of this technique was experimentally validated by the design,

fabrication and test of a fixed-beam reflectarray based on resonant patches (solid metal) over a PDMS substrate with the ground plane realized using gold ion implantation. A prototype operating at 1 THz was designed and fabricated using a shadow mask evaporation technique to realize the solid patches. The radiation pattern of the manufactured device was measured using a THz TDS setup, validating the results obtained in simulation. Based on these promising results, we have then proposed and experimentally demonstrated a reflectarray concept able to realize beam-scanning in one plane, based on the mechanical stretching of the array. This capability was made possible by the presence of a stretchable ground plane that allows to modify the array period without affecting the size of the solid resonant patches. Experimental results were in very good agreement with simulations and allowed to demonstrate for the first time beam-scanning at THz frequencies. The proposed concept is also particularly suitable to the integration of DEAs to implement an electromechanical control of the stretching.

The results presented in this chapter set the basis for the realization of flexible and stretchable THz devices offering attractive mechanical and electromagnetic properties for the implementation of reconfiguration capabilities, which can be achieved with relatively low losses. The combination of gold ion implantation in a PDMS substrate and the use of precise nano-stencil lithography techniques represents an effective means for the realization of precise patterns allowing the fabrication of very small features down to the micrometer scale [17, 18]. This capability can be favorably applied to the realization of several adaptive devices, such as metamaterials and reflectarray antennas implementing reconfiguration functionality based on mechanical stretching. The particular properties of the involved materials (i.e., PDMS and implanted gold ions) make such devices highly compatible with DEA planar actuation, since DEAs can be directly embedded into the device resulting in very compact and integrated structures.

Bibliography

- [1] P. H. Siegel, "THz Instruments for Space," *IEEE Transactions on Antennas and Propagation*, vol. 55, no. 11, pp. 2957–2965, Nov 2007.
- [2] P. de Maagt, "Terahertz Technology for Space and EARTH Applications," in *International Workshop on Antenna Technology: Small and Smart Antennas Metamaterials and Applications, 2007*, pp. 111–115.
- [3] S. U. Hwu, K. B. deSilva, and C. T. Jih, "Terahertz (THz) Wireless Systems for Space Applications," in *IEEE Sensors Applications Symposium (SAS), 2013*, pp. 171–175.
- [4] S. R. Murrill, E. L. Jacobs, S. K. Moyer, C. E. Halford, S. T. Griffin, F. C. De Lucia, D. T. Petkie, and C. C. Franck, "Terahertz imaging system performance model for concealed-weapon identification," *Appl. Opt.*, vol. 47, no. 9, pp. 1286–1297, Mar 2008.
- [5] W.-t. Liu, J.-w. Li, and W. Yang, "Detection and identification of explosives and illicit drugs by terahertz spectroscopy technology," in *IEEE International Geoscience and Remote Sensing Symposium (IGARSS), July 2010*, pp. 3576–3579.
- [6] P. H. Siegel, "Terahertz technology in biology and medicine," *IEEE Transactions on Microwave Theory and Techniques*, vol. 52, no. 10, pp. 2438–2447, 2004.
- [7] A. J. Fitzgerald, S. Pinder, A. D. Purushotham, P. O'Kelly, P. C. Ashworth, and V. P. Wallace, "Classification of terahertz-pulsed imaging data from excised breast tissue," *Journal of Biomedical Optics*, vol. 17, no. 1, pp. 016 005–1–016 005–10, 2012.
- [8] T. Kleine-Ostmann, Thomas Nagatsuma, "A review on terahertz communications research," *Journal of Infrared, Millimeter, and Terahertz Waves*, vol. 32, no. 2, pp. 143–171, 2011.
- [9] H.-J. Song and T. Nagatsuma, "Present and future of terahertz communications," *IEEE Transactions on Terahertz Science and Technology*, vol. 1, no. 1, pp. 256–263, 2011.
- [10] I. F. Akyildiz, J. M. Jornet, and C. Han, "Terahertz band: Next frontier for wireless communications," *Physical Communication*, vol. 12, no. 0, pp. 16–32, 2014.
- [11] I. B. Vendik, O. G. Vendik, M. A. Odit, D. V. Kholodnyak, S. P. Zubko, M. F. Sitnikova, P. A. Turalchuk, K. N. Zemlyakov, I. V. Munina, D. S. Kozlov, V. M. Turgaliev, A. B. Ustinov, Y. Park, J. Kihm, and C.-W. Lee, "Tunable metamaterials for controlling thz radiation," *IEEE Transactions on Terahertz Science and Technology*, vol. 2, no. 5, pp. 538–549, 2012.
- [12] A. Q. Liu, W. M. Zhu, D. P. Tsai, and N. I. Zheludev, "Micromachined tunable metamaterials: a review," *Journal of Optics*, vol. 14, no. 11, p. 114009, 2012.
- [13] H. Tanoto, L. Ding, and J. H. Teng, "Tunable terahertz metamaterials," *Terahertz Sci. Technol.*, vol. 6, no. 1, pp. 1–25, 2013.

- [14] S. Rosset, M. Niklaus, P. Dubois, and H. R. Shea, "Metal Ion Implantation for the Fabrication of Stretchable Electrodes on Elastomers," *Advanced Functional Materials*, vol. 19, no. 3, pp. 470–478, 2009.
- [15] —, "Large-Stroke Dielectric Elastomer Actuators With Ion-Implanted Electrodes," *Journal of Microelectromechanical Systems*, vol. 18, no. 6, pp. 1300–1308, 2009.
- [16] S. Akbari and H. R. Shea, "Microfabrication and characterization of an array of dielectric elastomer actuators generating uniaxial strain to stretch individual cells," *Journal of Micromechanics and Microengineering*, vol. 22, no. 4, p. 045020, 2012.
- [17] S. Aksu, M. Huang, A. Artar, A. A. Yanik, S. Selvarasah, M. R. Dokmeci, and H. Altug, "Flexible plasmonics on unconventional and nonplanar substrates," *Advanced Materials*, vol. 23, no. 38, pp. 4422–4430, 2011.
- [18] L. G. Villanueva, C. Martin-Olmos, O. Vazquez-Mena, J. Montserrat, P. Langlet, J. Bausells, and J. Brugger, "Localized Ion Implantation Through Micro/Nanostencil Masks," *IEEE Transactions on Nanotechnology*, vol. 10, no. 5, pp. 940–946, 2011.
- [19] H. Tao, A. C. Strikwerda, K. Fan, C. M. Bingham, W. J. Padilla, X. Zhang, and R. D. Averitt, "Terahertz metamaterials on free-standing highly-flexible polyimide substrates," *Journal of Physics D: Applied Physics*, vol. 41, no. 23, p. 232004, 2008.
- [20] X. G. Peralta, M. C. Wanke, C. L. Arrington, J. D. Williams, I. Brener, A. Strikwerda, R. D. Averitt, W. J. Padilla, E. Smirnova, A. J. Taylor, and J. F. O'Hara, "Large-area metamaterials on thin membranes for multilayer and curved applications at terahertz and higher frequencies," *Applied Physics Letters*, vol. 94, no. 16, p. 161113, 2009.
- [21] C. Zaichun, M. Rahmani, G. Yandong, C. T. Chong, and H. Minghui, "Realization of Variable Three-Dimensional Terahertz Metamaterial Tubes for Passive Resonance Tunability," *Advanced Materials*, vol. 24, no. 23, pp. OP143–OP147, 2012.
- [22] I. E. Khodasevych, C. M. Shah, S. Sriram, M. Bhaskaran, W. Withayachumnankul, B. S. Y. Ung, H. Lin, W. S. T. Rowe, D. Abbott, and A. Mitchell, "Elastomeric silicone substrates for terahertz fishnet metamaterials," *Applied Physics Letters*, vol. 100, no. 6, 2012.
- [23] J. Li, C. M. Shah, W. Withayachumnankul, B. S.-Y. Ung, A. Mitchell, S. Sriram, M. Bhaskaran, S. Chang, and D. Abbott, "Mechanically tunable terahertz metamaterials," *Applied Physics Letters*, vol. 102, no. 121101, 2013.
- [24] P. H. Bolivar, M. Brucherseifer, J. Gomez Rivas, R. Gonzalo, I. Ederra, A. L. Reynolds, M. Holker, and P. de Maagt, "Measurement of the dielectric constant and loss tangent of high dielectric-constant materials at terahertz frequencies," *IEEE Transactions on Microwave Theory and Techniques*, vol. 51, no. 4, pp. 1062–1066, 2003.
- [25] M. Naftaly and R. E. Miles, "Terahertz Time-Domain Spectroscopy for Material Characterization," *Proceedings of the IEEE*, vol. 95, no. 8, pp. 1658–1665, 2007.

- [26] D. M. Pozar, *Microwave Engineering*, 4th ed. Wiley, 2011.
- [27] T. Schneider, A. Wiatrek, S. Preussler, M. Grigat, and R.-P. Braun, "Link budget analysis for terahertz fixed wireless links," *IEEE Transactions on Terahertz Science and Technology*, vol. 2, no. 2, pp. 250–256, 2012.
- [28] J. C. Ginn, B. A. Lail, and G. D. Boreman, "Phase Characterization of Reflectarray Elements at Infrared," *IEEE Transactions on Antennas and Propagation*, vol. 55, no. 11, pp. 2989–2993, 2007.
- [29] J. C. Ginn, B. A. Lail, J. Alda, and G. D. Boreman, "Planar infrared binary phase reflectarray," *Opt. Lett.*, vol. 33, no. 8, pp. 779–781, 2008.
- [30] T. Niu, W. Withayachumnankul, B. S.-Y. Ung, H. Menekse, M. Bhaskaran, S. Sriram, and C. Fumeaux, "Experimental demonstration of reflectarray antennas at terahertz frequencies," *Opt. Express*, vol. 21, no. 3, pp. 2875–2889, 2013.
- [31] T. Niu, W. Withayachumnankul, A. Upadhyay, P. Gutruf, D. Abbott, M. Bhaskaran, S. Sriram, and C. Fumeaux, "Terahertz reflectarray as a polarizing beam splitter," *Opt. Express*, vol. 22, no. 13, pp. 16 148–16 160, 2014.
- [32] A. Ahmadi, S. Ghadarghadr, and H. Mosallaei, "An optical reflectarray nanoantenna: The concept and design," *Opt. Express*, vol. 18, no. 1, pp. 123–133, 2010.
- [33] S. H. Zainud-Deen, H. A. El-Azem Malhat, S. M. Gaber, and K. H. Awadalla, "Perforated nanoantenna reflectarray," *Progress In Electromagnetics Research M*, vol. 29, no. 1, pp. 253–265, 2013.
- [34] L. Zou, W. Withayachumnankul, C. M. Shah, A. Mitchell, M. Bhaskaran, S. Sriram, and C. Fumeaux, "Dielectric resonator nanoantennas at visible frequencies," *Opt. Express*, vol. 21, no. 1, pp. 1344–1352, Jan 2013.
- [35] D. M. Pozar, S. D. Targonski, and H. D. Syrigos, "Design of millimeter wave microstrip reflectarrays," *IEEE Transactions on Antennas and Propagation*, vol. 45, no. 2, pp. 287–296, 1997.
- [36] A. Podzorov and G. Gallot, "Low-loss polymers for terahertz applications," *Appl. Opt.*, vol. 47, no. 18, pp. 3254–3257, 2008.
- [37] S. C. Nemat-Nasser, A. V. Amirkhizi, W. J. Padilla, D. N. Basov, S. Nemat-Nasser, D. Bruzewicz, and G. Whitesides, "Terahertz plasmonic composites," *Phys. Rev. E*, vol. 75, p. 036614, 2007.
- [38] R. El Hani and J.-J. Laurin, "Specular Reflection Analysis for Off-Specular Reflectarray Antennas," *IEEE Transactions on Antennas and Propagation*, vol. 61, no. 7, pp. 3575–3581, 2013.

- [39] J. N. Lee, C. Park, and G. M. Whitesides, "Solvent Compatibility of Poly(dimethylsiloxane)-Based Microfluidic Devices," *Analytical Chemistry*, vol. 75, no. 23, pp. 6544–6554, 2003.
- [40] E. Carrasco and J. Perruisseau-Carrier, "Reflectarray Antenna at Terahertz Using Graphene," *IEEE Antennas and Wireless Propagation Letters*, vol. 12, pp. 253–256, 2013.
- [41] E. Carrasco, M. Tamagnone, and J. Perruisseau-Carrier, "Tunable graphene reflective cells for thz reflectarrays and generalized law of reflection," *Applied Physics Letters*, vol. 102, no. 10, 2013.
- [42] M. Esquiús-Morote, J. S. Gomez-Diaz, and J. Perruisseau-Carrier, "Sinusoidally Modulated Graphene Leaky-Wave Antenna for Electronic Beamscanning at THz," *IEEE Transactions on Terahertz Science and Technology*, vol. 4, no. 1, pp. 116–122, 2014.
- [43] J. Bossard, X. Liang, L. Ling, S. Yun, D. Werner, B. Weiner, T. Mayer, P. Cristman, A. Diaz, and I. Khoo, "Tunable Frequency Selective Surfaces and Negative-Zero-Positive Index Metamaterials Based on Liquid Crystals," *IEEE Transactions on Antennas and Propagation*, vol. 56, no. 5, pp. 1308–1320, May 2008.
- [44] M. Kafesaki, N. H. Shen, S. Tzortzakis, and C. M. Soukoulis, "Optically switchable and tunable terahertz metamaterials through photoconductivity," *Journal of Optics*, vol. 14, no. 11, p. 114008, 2012.
- [45] S. Vegesna, Y. Zhu, Y. Zhao, Z. Fan, A. Bernussi, and M. Saed, "Terahertz frequency selective surface with reconfigurable polarization characteristics using vanadium dioxide," *Journal of Electromagnetic Waves and Applications*, vol. 28, no. 1, pp. 83–90, 2014.
- [46] Z. Suo, "Theory of dielectric elastomers," *Acta Mechanica Solida Sinica*, vol. 23, no. 6, pp. 549–578, 2010.
- [47] W. M. Zhu, A. Q. Liu, X. M. Zhang, D. P. Tsai, T. Bourouina, J. H. Teng, X. H. Zhang, H. C. Guo, H. Tanoto, T. Mei, G. Q. Lo, and D. L. Kwong, "Switchable Magnetic Metamaterials Using Micromachining Processes," *Advanced Materials*, vol. 23, no. 15, pp. 1792–1796, 2011.
- [48] C. W. Berry, J. Moore, and M. Jarrahi, "Design of reconfigurable metallic slits for terahertz beam modulation," *Opt. Express*, vol. 19, no. 2, pp. 1236–1245, 2011.
- [49] W. Zhang, A. Q. Liu, W. M. Zhu, E. P. Li, H. Tanoto, Q. Y. Wu, J. H. Teng, X. H. Zhang, M. L. J. Tsai, G. Q. Lo, and D. L. Kwong, "Micromachined switchable metamaterial with dual resonance," *Applied Physics Letters*, vol. 101, no. 15, p. 151902, 2012.
- [50] W. M. Zhu, A. Q. Liu, T. Bourouina, D. P. Tsai, J. H. Teng, X. H. Zhang, G. Q. Lo, D. L. Kwong, and N. I. Zheludev, "Microelectromechanical Maltese-cross metamaterial with tunable terahertz anisotropy," *Nature Communications*, vol. 3, no. 1274, pp. 1–6, 2012.

6 Conclusion and perspectives

6.1 Summary

Several communication and remote sensing systems are rapidly expanding in the region of the electromagnetic spectrum ranging between millimeter-waves (MMW) and terahertz (THz), which have been almost unexplored with respect to microwave frequencies, owing to the performance limitations of available technologies for higher frequency operation. The progress of MMW and THz applications is simultaneously generating an increasing demand for advanced performance and reconfiguration capabilities in antenna devices, which represent critical components in all these systems.

The objective of this research was to overcome the limitations in terms of losses, cost and complexity affecting available technologies when high-performance reconfiguration capabilities are addressed at MMW and above. Within this scope, the use of dielectric elastomer actuators (DEAs) has been proposed to implement mechanical reconfiguration in antenna devices operating at MMW and THz frequencies. DEAs have been selected for their unique properties which are particularly suited to the realization of adaptive antenna systems, notably large strain, analog control, very low power consumption, low-cost materials and inexpensive fabrication process. The application of DEAs to MMW and THz antenna reconfiguration has never been investigated thus far. Therefore, the electromagnetic characterization of DEA-based materials was necessary to allow an accurate modeling of the actuator parts embedded in the proposed designs.

The application of DEAs for the implementation of MMW tunable phase shifters has been demonstrated for the first time. A true-time-delay phase shifter operating at Ka-band has been designed and fabricated targeting the realization of a low-loss and low-cost device with dynamically controllable insertion phase. The proposed device exploits the in-plane expansion offered by DEAs to horizontally displace a suspended loading element over a conventional coplanar waveguide, thereby inducing a change in the propagation of the transmission line. This approach allowed to completely isolate the actuation part from the electromagnetic active area resulting in a very low-loss reconfiguration. A prototype was manufactured using stan-

standard PCB fabrication techniques available at EPFL highlighting state-of-the-art performance in terms of the phase-shift/loss figure of merit.

The successful application of DEAs to the reconfiguration of the Ka-band phase shifter encouraged the development of more complex devices targeting the development of MMW beam-scanning capabilities. To this end, a reconfigurable reflectarray (RA) concept integrating a mechanical tuning mechanism based on planar DEAs has been proposed. In-plane DEA displacement was adopted to mechanically modify the resonant length of microstrip patches on a grounded dielectric substrate. The proposed concept has been validated by designing and fabricating a reflective surface with uniform phase distribution where the reconfiguration of all the cells was realized using a single DEA control. Similarly to the phase shifter, the actuation part was confined at the extremities of the array and therefore did not interfere with the EM propagation, resulting in losses comparable to the device fixed counterpart. The design of a 1-D beam-scanning RA has been also proposed. This concept is based on the independent control of each column of cells to implement beam-scanning functionality in the H -plane of the antenna. The combination of this RA concept and DEA actuation has the potential to address some of the most acute needs in beam scanning, providing a low-cost and pseudo-planar device with low loss, low power consumption and analogue control. Although the RA device has been optimized to operate at Ka-band, the same tuning approach can be down-scaled targeting higher frequency of operation without introducing additional losses, and with the potential to further reduce the device size and improve actuator integration. In this case, the maximum achievable frequency would be defined by fabrication tolerances and actuation accuracy.

Finally, the possible application of DEAs to THz devices has been investigated. DEAs are particularly attractive for the implementation of THz reconfigurable concepts due to the electromagnetic and mechanical properties of the involved materials. In particular they can be directly embedded into the EM device producing relatively low losses and resulting in very compact and integrated structures. We have first proposed an efficient approach for the practical implementation of flexible and stretchable conductors with high potential for the realization of adaptive antenna devices operating at THz frequencies. This technique, originally developed by LMTS for the realization of compliant DEA electrodes, is based on the implantation of gold ions into a PDMS substrate. A fixed-beam reflectarray embedding a stretchable ground plane and operating at 1 THz was experimentally demonstrated. The proposed RA consisted of an array of variable-size resonant patches (solid metal) realized on a PDMS substrate, with the addition of an implanted ground plane. Based on these results, a beam-scanning reflectarray operating at 0.75 THz has been proposed and experimentally demonstrated. The reconfiguration concept is based on the mechanical stretching of the array (integrating an implanted ground plane) with the scope to modify the array period without affecting the size of the solid resonant patches. Experimental results were in very good agreement with simulations demonstrating for the first time beam-scanning at THz frequencies. The experimental results allowed to validate the use of gold ion implantation in a PDMS substrate for the realization of THz devices. In particular, the combination of this

technique with nano-stencil lithography represents an effective means for the realization of precise patterns allowing the fabrication of very small features down to the micrometer scale. Such an approach can be favorably applied to the realization of several adaptive devices, such as for instance metamaterials and reflectarray antennas implementing reconfiguration functionality based on mechanical stretching.

6.2 Perspectives

The results achieved in this thesis allowed to confirm the potential of DEA technology for the realization of low-cost, low-complexity and efficient antenna devices based on mechanical reconfiguration. In addition to the devices developed during this research work, the use of planar DEAs can be extended to other electromagnetic concepts where the reconfiguration of a given parameter is obtained by the variable interaction of moving surfaces and/or via the mechanical stretching of the device to modify the spacing between radiating elements. These approaches could be for instance applied to the realization of tunable frequency selective surfaces, filters and polarizers. Moreover, DEA electrodes could be directly used as variable radiators or resonant elements in THz devices (e.g., using gold ion implantation), with the possibility to realize localized deformation as for instance demonstrated in the single-cell stretcher developed at EPFL-LMTS. The unique flexible and compliant nature of these actuators allows the realization of devices and structures that are unattainable by other technologies keeping the same fabrication complexity and cost.

However, despite the field of DEAs is rapidly growing as demonstrated by the extensive literature on the topic and the wide range of applications, considerable work is still needed to achieve the maturity level necessary for their immediate integration in commercial antenna systems (i.e. compared to well-established micro-actuator technologies). DEA evolution requires a combination of material development, electronic advancement and optimization of the manufacturing techniques. The main challenge is to attain commercially available DEA micro-actuators that are not only low-cost, but also allow for high-quality and repeatable performance. Regarding DEA development for antenna applications, two main points need to be addressed in future activities: 1) realization of precise and repeatable actuation output possibly associated with closed-loop control capabilities; 2) optimization (i.e., reduction) of the control voltage.

The first point has been discussed in chapter 3, but the same principle obviously applies to all the devices proposed during this work as well as to any future development. The addition of self-sensing and closed-loop operation is clearly an improvement and would definitely represent a breakthrough towards the realization of precise and stable actuators. The inherent electrostatic nature of DEA actuators and the strong link between the applied field and the realized displacement, make them suitable to the realization of capacitive self-sensing capabilities. This property, in combination with a feedback control, would allow to eliminate the uncertainty on the actuator displacement and to compensate for possible performance

Chapter 6. Conclusion and perspectives

degradation arising during the actuator lifetime (e.g., elastomer stiffening, temperature effects). In such a configuration, the DEA device acts as actuator and integrated sensor simultaneously, without any need for external sensors. However, this improvement requires the integration of a control unit able to drive the actuator and to measure the associated capacitance at the same time.

The second point is not in contradiction to what it has been repeatedly stated throughout this thesis. Driving voltages in the kV range are not a critical aspect as different commercial systems (e.g., Optotune's laser speckle reducer and ViviTouch™) have demonstrated the safe implementation of DEAs and related control circuitry in very small devices. However, the use of lower control voltages would further reduce system complexity and cost, and would certainly widen the interest of the antenna community towards DEA technology. The reduction of the actuation voltage can be addressed proposing two main solutions: i) increasing the dielectric permittivity of the elastomer or ii) reducing the elastomer thickness. Both solutions are a direct consequence of the eq. (1.2) governing the electromechanical response of DEAs. A common approach to modify the elastomer permittivity consists in the addition of a filler with higher dielectric constant in the polymer matrix (i.e., realization of a random composite). However, this method typically comes with an increased stiffness (or modified mechanical properties in general) that degrades actuation performance acting against the improved actuation voltage. Another technique is represented by the synthesis of new materials complying with the desired mechanical and dielectric requirements. Although this might seem the best approach, it is by far the most demanding since it requires higher development time and costs. Thus, the main challenge is to develop a low-cost technique able to increase the material permittivity while keeping low Young's modulus, high breakdown field, low dielectric losses (i.e., loss tangent), very good ability to sustain large and reversible deformations, and good thermal stability. Regarding the reduction of the elastomer thickness, the main approach consists in the realization of multi-layer structures where ultra-thin elastomer membranes are alternated with electrodes connected in parallel. Here the main challenge is clearly the development of reliable techniques enabling the realization of very thin (up to the molecular monolayer structure) and defect-free membranes, and the interconnection between the different layers.

Future advancements involving the two points discussed above (i.e., uncertainty-free actuation and voltage reduction) would definitely allow DEA technology to compete on equal terms (with the addition of unprecedented capabilities) with well-established technologies that are currently integrated in commercial antenna systems.

List of Publications

Journal papers

- [J1] P. Romano, S. Rosset, L. Maffli, H. Shea, and J. Perruisseau-Carrier, “Electromagnetic characterisation of flexible conductive membranes at millimetre-waves,” *Electronics Letters*, vol. 49, no. 5, pp. 353–354, 2013.
- [J2] P. Romano, O. Araromi, S. Rosset, H. Shea, and J. Perruisseau-Carrier, “Tunable millimeter-wave phase shifter based on dielectric elastomer actuation,” *Applied Physics Letters*, vol. 104, pp. 024104, 2014.
- [J3] P. Romano, S. Capdevila-Cascante, S. Rosset, H. Shea, and J. R. Mosig, “A practical approach to the realization of stretchable conductors for terahertz applications,” *in preparation*.
- [J4] P. Romano, S. Rosset, S. Schlatter, O. Araromi, T. Debogovic, H. Shea, and J. R. Mosig, “A reconfigurable millimeter-wave reflective surface driven by dielectric elastomer actuators,” *in preparation*.

International conferences and workshops

- [C1] P. Romano, S. Rosset, L. Maffli, H. Shea and J. Perruisseau-Carrier, “Surface impedance measurements of thin flexible metallization at millimeter-waves”, *7th European Conference on Antennas and Propagation (EuCAP)*, Göteborg, Sweden, April 8-12, 2013.
- [C2] O. Araromi, P. Romano, S. Rosset, J. Perruisseau-Carrier, and H. Shea, “Towards reconfigurable RF devices based on dielectric elastomer actuators,” *3rd International Conference on Electromechanically Active Polymer (EAP) transducers & artificial muscles*, Dübendorf, Zürich, Switzerland, June 25-26, 2013.

List of Publications

- [C3] O. Araromi, P. Romano, S. Rosset, J. Perruisseau-Carrier, and H. Shea, “A tunable millimeter-wave phase shifter driven by dielectric elastomer actuators,” *Proc. SPIE 9056, Electroactive Polymer Actuators and Devices (EAPAD)*, San Diego, California, USA, March 9, 2014.
- [C4] P. Romano, O. Araromi, S. Rosset, H. Shea and J. Perruisseau-Carrier, “Electroactive polymer based reconfigurable phase shifter at millimeter-waves,” *8th European Conference on Antennas and Propagation (EuCAP)*, The Hague, The Netherlands, April, 6-11, 2014.
- [C5] P. Romano, O. Araromi, S. Rosset, H. Shea and J. Perruisseau-Carrier, “Microwave to terahertz reconfiguration of antenna devices using dielectric elastomer micro-actuators,” *9th ESA round table on micro and nano technologies*, Lausanne, Switzerland, June 10-13, 2014.
- [C6] P. Romano, O. Araromi, S. Rosset, J. Perruisseau-Carrier, H. Shea, and J. R. Mosig, “Low-loss millimeter-wave phase shifters based on mechanical reconfiguration,” *36th Progress In Electromagnetics Research Symposium*, Prague, Czech Republic, July 6-9, 2015. *Selected as finalist for the best student paper award.*
- [C7] P. Romano, M. Tamagnone, S. Capdevila-Cascante, S. Rosset, H. Shea, and J. R. Mosig, “Stretchable and transparent THz reflectarrays based on PDMS,” *6th International Conference on Metamaterials, Photonic Crystals and Plasmonics*, New York City, NY, USA, August 4-7, 2015.
- [C8] M. Tamagnone, S. Capdevila, H., P. Romano, W. A. Vitale, C. F. Moldovan, A. M. Ionescu, A. Skrivervik, J. Perruisseau-Carrier, and Juan R. Mosig, “Performance evaluation of novel technologies for terahertz reflectarrays”, *European Microwave Week*, Paris, France, September 6-11, 2015.

Provisional patent

- [P1] International Patent Application (provisional) n° PCT/IB2015/052363, March 31, 2015.
Title: “Millimeter-wave beam scanning reflectarray antenna using artificial muscles”
Inventors: P. Romano, J. Perruisseau-Carrier, S. Rosset, H. Shea, O. Araromi.

Technical reports and proposals

- [T1] P. Romano, and J. Perruisseau-Carrier, “State-of-the-art of millimeter-wave phase shifters: Ka-band applications,” European Space Agency – ESTEC, NPI deliverable D1, July 2012.
- [T2] P. Romano, and J. Perruisseau-Carrier, “Electromagnetic characterization of EAP materials at millimeter-waves,” European Space Agency – ESTEC, NPI deliverable D2, January 2013.

- [T3] P. Romano, and J. Perruisseau-Carrier, “EAP-based phase shifters: Design Fabrication and Test,” European Space Agency – ESTEC, NPI deliverable D3, July 2013.
- [T4] P. Romano, J. Perruisseau-Carrier, H. Shea, S. Rosset, O. Araromi, “Dynamically reconfigurable antennas and surfaces for pico and nanosatellites – millimeter-wave beam scanning using artificial muscles,” SERI/SSO Call for Ideas, December 2013.
- [T5] P. Romano, and J. Perruisseau-Carrier, “Millimeter-wave reconfigurable PRS antennas using EAP actuators: preliminary design,” European Space Agency – ESTEC, NPI deliverable D4, January 2014.
- [T6] J. Perruisseau-Carrier, P. Romano, H. Shea, S. Rosset, O. Araromi, F. Bongard, C. Lyttle, F. Tiezzi, “Artificial Muscles for Reconfigurable Millimeter-wave Antennas (AMRA),” Swiss Space Center, Project Proposal, April 2014.

Pietro Romano

Address Rue de Lyon 62, 1203 Geneva, Switzerland
Phone +41 78 868 83 78
Mail pietromano@gmail.com
Nationality Italian
Birth May 18th, 1986



Education

PhD in Microsystems and Microelectronics

École Polytechnique Fédéral de Lausanne (EPFL), Switzerland

Thesis directors: Prof. H. Shea and Prof. Juan R. Mosig

Feb 2012–Aug 2015

Postgraduate course in Satellites and Orbiting Platforms

La Sapienza University of Rome, School of Aerospace Engineering, Italy

Final grade: 110/110 summa cum laude.

Jan 2011–Dec 2011

MSc. in Electronic Engineering for Telecommunications and Remote Sensing

La Sapienza University of Rome, Italy

Final grade: 110/110 summa cum laude.

Sep 2008–Dec 2010

BSc. in Electronic Engineering

La Sapienza University of Rome, Italy

Final grade: 110/110 summa cum laude.

Sep 2005–Dec 2008

Professional experience

Research engineer

École Polytechnique Fédéral de Lausanne (EPFL), Lausanne, Switzerland

- Design, fabrication and test of millimeter-wave and THz reconfigurable antenna devices
- Involved in the scientific and management tasks for the REACT (European Space Agency) and AMRA (Swiss Space Center) projects
- Co-authored a 270000 CHF project proposal, accepted by the Swiss Space Office
- Lecturer and project supervisor for B.Sc. and M.Sc. students

Feb 2012–Aug 2015

System engineering intern

Thales Alenia Space Italia, Rome, Italy

- Involved in system engineering tasks, development of algorithms and software tools, preparation of user requirements and technical documentation
- Provided the company with a novel processing tool for high resolution spaceborne SAR images

Jun 2011–Dec 2011

System engineering intern

Rheinmetall Italia S.p.a., Rome, Italy

- Analysis, feasibility study and technical proposal of a spaceborne atmospheric remote sensing mission using millimeter-wave radar aboard the ISS
- Definition of mission and scientific requirements, system specifications and preliminary design

Oct 2010–Dec 2010

Short-term researcher

Jul 2010–Aug 2010

NASA Goddard Space Flight Center, Greenbelt (MD), USA

- Active participation in the NASA Global Precipitation Measurement (GPM) mission
- Development of software simulators and algorithms to estimate precipitation from satellite radar observations

Summer intern

Jul 2009–Aug 2009

University of Washington, Seattle (WA), USA

- Development and software implementation of processing algorithms for spaceborne weather radars

Skills

<i>Languages</i>	Italian (mother tongue), English (proficient user, level C1), French (independent user, level B1).
<i>Technical</i>	Electromagnetics, modelling and design of microwave devices, full-wave electromagnetic simulations, RF/Microwave measurements and characterization, standard PCB fabrication, clean room fabrication, signal processing, algorithm development and software implementation, technical/scientific writing.
<i>Software</i>	Microsoft Windows, Mac OS X, Microsoft Office Suite, C, Fortran, Python, Matlab, Wolfram Mathematica, Ansys HFSS, \LaTeX . Computer skills have been gained through dedicated courses, training and during the work and research activities.
<i>Social</i>	Excellent team spirit and ability to establish and maintain effective working relations with people of different national and cultural backgrounds. Very good oral and written communication and presentation skills.
<i>Organizational</i>	Extremely organized person with end-oriented work capability, proactive problem-solving attitude and strong wish to learn more, good ability for synthetic and global views. Experience in coordinating different groups and work packages.

Additional information

<i>Awards</i>	2011: recipient of a 7500€ scholarship awarded by the University of Rome “La Sapienza” and sponsored by Thales Alenia Space Italia to attend the second level Master (postgraduate) in “Satellites and orbiting platforms”. 2010: recipient of a 6000\$ scholarship (only 2 students selected) awarded by the Italian Scientists and Scholars of North America Foundation (ISSNAF) and sponsored by the Italian Space Agency (ASI) for a 2-months internship at NASA Goddard Space Flight Center, Greenbelt, MD (USA).
<i>Activities</i>	2001–2008: : Administrative assistant at a local branch of the Italian Football Referees Association (AIA). 2001–2011: Professional football referee up to the Italian national level. 2008–2010: Library assistant at the Department of Electronic Engineering, La Sapienza University
<i>Interests</i>	Road cycling, skiing, amateur photography, cooking.

References

Available upon request.